UNIVERSITY of ABERTAY DUNDEE

Analysis of Tomographic Images:

Quantitative Methods for Soil Pore Structure

Alasdair Neil Houston

Submitted in partial fulfillment
of the requirements of the
University of Abertay Dundee
for the award of
Doctor of Philosophy

May 2013

Declarations

I the undersigned doctoral candidate, declare that this thesis contains my own original work none of which has previously been submitted in pursuit of any academic qualification, and any content that is not my own original work is clearly identified as such:

Signed:  Date: 31st Oct 2013

As an appointed representative of the University I the undersigned declare that this work is a true and accurate copy of the thesis approved by the examiners:

Signed:  Date: 31st Oct 2013

Abstract

Soil is a material of tremendous importance to the sustainability of complex life on planet Earth and X-ray computed micro-tomography permits the minimally invasive study of 3D soil pore structure at appropriate scales. However, the tremendous variety of materials and their complex spatial arrangement that may be found within soil, in addition to the vast quantity of information present within a tomographic image, lead to significant difficulty in the accurate interpretation of these images. This thesis deals with problems of acquisition, assessment, processing and measurement for such images, applying unsupervised (fully automatic) methods as a means of dealing with very large data in a consistent fashion. Existing methods of image analysis are assessed, refined, extended and applied in novel ways to meet the challenges posed by soil.

Noise resulting from X-ray scattering is a significant problem when samples having a substantial mineral content (i.e. most soils) are the subject of tomographic imaging. Further compounding this problem is the high degree of heterogeneity seen in the spatial distribution of material within soil, covering scales from the sub-micron level up to those obvious to the naked eye. Reliable automatic identification of pore versus solid structure requires sensitivity to coherent evidence yet robustness against noise. It is shown that this very significant technical challenge is robustly addressed via the consideration of spatial correlation, but this involves potentially very high computational cost . This latter problem is addressed through developing a novel algorithm that extends the indicator kriging approach, greatly reducing computational cost and simultaneously improving the quality of results.

Subsequent to the identification of coherent structure within an image, that structure is measured using Minkowski functionals applied in conjunction with concepts of topological connectivity. This novel combination of analyses facilitates investigation of fine structural detail while also permitting more general information to be efficiently summarised and presented. As well as being applied to soil pore structure, such analyses are applied for the first time to simulated fungal biomass and water distributions and also to the study of in-vitro tumour formation.

Acknowledgements

Firstly, thanks go to my supervisory team:

Simona Hapca for patience and attention to detail,

Wilfred Otten for objectivity and scientific balance,

Philippe Baveye for stimulating discussion.

An especially big thank you to my "fourth supervisor",

life coach, personal manager and soul mate:

Ruth Falconer

for keeping reality in perspective

(fungi and arachnids notwithstanding).

Thanks also to John Palfreyman and Nia White

for opportunities then and now

and many others within the university

for their good humoured help and support.

Glossary

ART Algebraic Reconstruction Technique (tomographic reconstruction)

AWIK Adaptive Window Indicator Kriging (image segmentation)

CT Computed Tomography

EM Expectation Maximisation (model fitting)

FBP Filtered Back Projection (tomographic reconstruction)

MAP Maximum A Posteriori (Bayesian inference)

MF Minkowski Functional (structural analysis)

MRF Markov Random Field

OM Organic Matter

PDF Probability Density Function (continuous)

PMF Probability Mass Function (discrete)

POM Particulate Organic Matter

PSD Pore Size Distribution (structural analysis)

PSF Point Spread Function (imaging)

SOM Soil Organic Matter

Contents

Figures

Tables

1.0 Introduction

Considered on a planetary scale, soil is a rare and precious resource; a layer of biologically active material, often just a few metres deep, covering only a fraction of the Earth's surface (Richter and Markewitz, 1995). This is the outermost layer of the Earth's *critical zone*, so named because of it's importance in sustaining life. In addition to the soil layer or *pedosphere* the critical zone includes two successively deeper layers known as the *vadose zone* and then the *phreatic zone*. The phreatic zone is characterised by groundwater saturation hence the fluid pressure increases with depth, whereas the vadose zone is a transitional region containing pockets of both air and water at atmospheric pressure. The availability of fresh water is dependant upon processes occuring in these three successive layers.

The importance of the pedosphere is discussed in more detail in the section following, but here it suffices to say that understanding the full range of processes within soil is fundamentally important to arriving at management policies that can sustain human life in the long term. Despite an unassuming appearance at the macroscopic scale, soil is a remarkably complex material (Young and Crawford, 2004) and hence extremely difficult to investigate in a comprehensive fashion. Micro-scale X-ray computed tomography is just one investigative tool, but one that is very important because it can reveal the interior structure of soil with little or no disturbance. This thesis addresses some of the problems that arise within soil science when images, obtained by X-ray CT (Figure 1.1) or otherwise, are used to investigate soil structure.

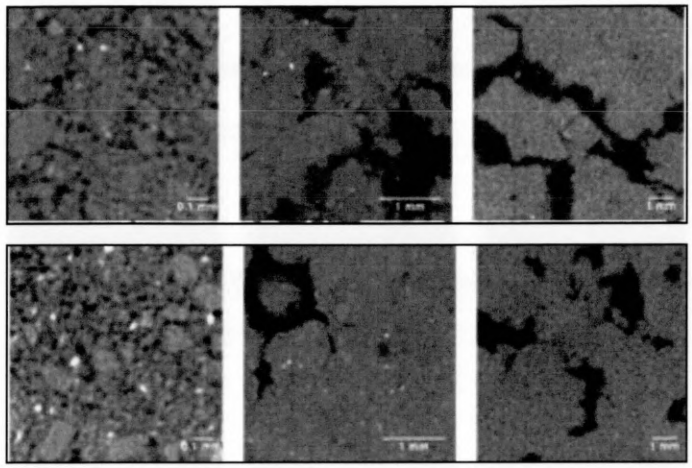

Figure 1.1 X-ray CT soil images.
Three replicates (horizontal axis) of two experimental treatments are shown.
Adapted from Juarez et al. (2013).

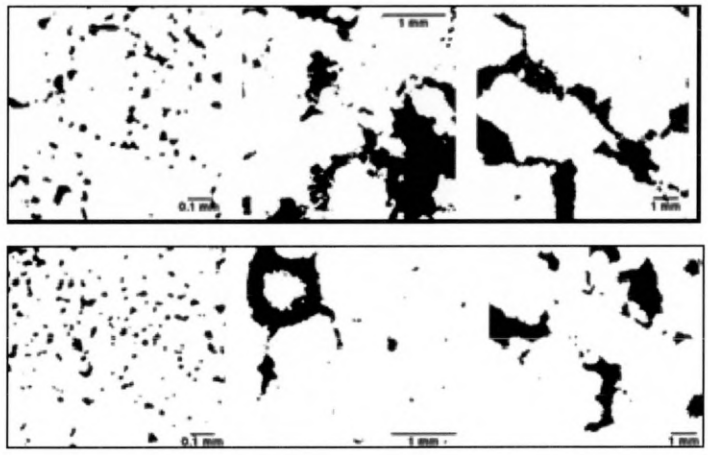

Figure 1.2 Segmented X-ray CT soil images.
These correspond to the images shown in figure 1.1.
Black pixels are pore, white are solid.
Adapted from Juarez et al. (2013).

The broad aim of this work is to select, develop and evaluate methods appropriate for understanding soil pore structure as represented in the form of a digital image. This is a specific application of *digital image analysis* which is generally defined as the process of extracting meaningful information from an

image. At the core of this process is a sequence of image processing operations that transform and reduce the information content of the soil image, ultimately obtaining a set of measures describing pore structure. A common approach to image analysis, and the one adopted for this work, first applies image segmentation as a distinct step prior to measure calculation. In the case of this project, this means that all elements within a soil image have been classified as either pore or solid; information which simplifies the subsequent calculation of measures. Figure 1.1 X-ray CT soil images.

Three replicates (horizontal axis) of two experimental treatments are shown. Adapted from Juarez et al. (2013).(above) shows X-ray CT images used as part of a study (Juarez et al. 2013) that investigated links between the micro-structure of soil and microbial activity. Figure 1.2 shows the corresponding segmented images in which pores are shown in black, solid in white.

The key project objectives were firstly to improve the accuracy and robustness of soil image segmentation and secondly to obtain measures of soil pore structure meeting requirements of both accuracy and relevance to the soil scientist. In addition, a general aim was to obtain computationally efficient implementations of analysis tools, such that these tools are widely applicable without requiring specialised computing resources.

1.1 Motivation: The Importance of Soil

Soil is fundamentally important to sustaining complex terrestrial life such as humans: it facilitates the conversion of solar energy into biochemical resources on a vast scale. Without food obtained from plants growing in soil, the survival of humans and many other land animals is not sustainable. Without the raw materials similarly obtained, it is difficult to conceive how technology and culture might exist in a recognisable form. In short, without productive soil and the incredible variety of life it supports, the surface of planet Earth would be dramatically less interesting.

The formation of soil is a process spanning millennia, from the weathering of rock to form silicate and other mineral particles, to the gradual enrichment of this particulate matter with animal and plant detritus. Inevitably this is a climate dependant process; precipitation and temperature are important factors both in the weathering of rock and for the rate of biological activity. Biological processes can themselves contribute to the production of particulate matter: plant roots and fungal hyphae can each exert gradual pressure sufficient to fracture rock. However perhaps the most significant effect of plants and fungi is their ability to bind and reinforce soil structure, which helps to limit erosion by wind and water.

Catastrophic changes to the soil layer can occur as a result of natural processes (e.g. volcanic activity) but these have been sufficiently localised and infrequent that colonisation by humans has been affected only to a limited

degree. The unrelenting expansion of human populations and their growing power to change the environment through technological means, represent a significant threat to soil health (Ellis & Mellor, 2010). Public concern in this respect is focused mainly on changes visible at the macroscopic scale e.g. rainforest clearance leading to soil erosion. It is however equally important to consider effects at the microscopic scale as these may lead to an insidious deterioration of soil quality. Loss of Soil Organic Matter (SOM) and declining biodiversity are such phenomena with important large scale impact (Dobie et al, 2011) and while causes have been hypothesised, the underlying mechanisms have yet to be established.

Soil carbon transformations have been investigated using global carbon models such as RothC (Coleman and Jenkinson, 2008) and CENTURY (Parton et al. 1987), however the predictions of these models can conflict with each other. Studies explicitly considering spatial heterogeneity suggest that it is the microscopic properties of soils, the scale relevant to microbes that critically effect soil function e.g. fertility and respiration (Stoyan et al. 2000). Spatial disconnection between soil carbon, energy sources and decomposer organisms has been suggested as a more significant factor in SOM turnover than chemical recalcitrance, contrary to previous assumptions (Dungait et al. 2012). Alternative hypotheses that physical isolation of fine, intra-aggregate Soil Organic Carbon (SOC) from microbial decomposers are now proposed as the limiting factor for microbial mineralisation. A greater understanding of soil microstructure and mechanisms governing microbial interaction with SOM is

required, so that global models of carbon turnover can be formulated appropriately.

Other studies highlighting the driving force of pore geometry on chemical and biological distributions include (De Gryze et al. 2006) who provide evidence linking pore structure and the distribution of organic matter to the activity of microorganisms. Understanding the complex interplay of physical and biochemical processes within soil therefore requires an understanding of pore structure at fine scales.

1.2 Traditional Methods of Soil Analysis

Soil structure has previously been studied through gradation i.e. sieving a sample so as to obtain separate fractions, each of which has a distinct range of particle sizes (Barnes, 2010). This is a physical means of estimating particle size distribution which, via a model of particle packing, can be used to infer pore size distribution. Gradation is a relatively simple approach that is fundamentally limited in accuracy by the number of size fractions obtained (i.e. the number of sieves employed) and also by simplifications or generalisations of particle shape inherent in the packing model. Also of concern is the dis-aggregation of particles that can occur due to repeated impact with a sieve, thus the measured size distribution may not accurately reflect that of the undisturbed sample prior to sieving. Gradation is however useful for microcosm construction in which the constituents, their particle size distribution and their packing density may be

deliberately manipulated as part of an investigation (Harris et al. 2003) and (Pajor et al. 2010).

Another technique used to study soil structure is serial sectioning, in which the sample is physically sliced into a number of parallel thin sections (Hall and Dalrymple, 1979). This has the advantage of being able to map mineral, organic matter and microbial colonies along with soil structure (Nunan et al. 2003) and (Harris et al. 2003). Applying this technique to soil generally requires that the sample is impregnated with wax or resin to stabilise its structure during cutting and for subsequent handling (Ringrose-Voase, 1996). Each slice is typically recorded as a digital photographic image, from which the spatial distribution of solid and pore components are estimated. From measurements made in 2D it is possible to estimate 3D measures by applying the techniques of stereology (Ringrose-Voase and Nortcliff,1987) and other forms of statistical data reconstruction (Hapca et al. 2011). In addition to being labour intensive and suffering from errors caused by distortion of the structure during cutting, the main limitation of serial sectioning is in the thickness of sections that can be achieved. This leads to limited reliability of 3D pore size estimates, for example it has been shown that rare events such as large cracks cannot be recovered by this approach (Blair et al. 2007).

1.3 CT Imaging of Soil Samples

The application of X-ray computed tomography to soil is perhaps the greatest step towards understanding the internal structure of soil; it is a minimally invasive technique, unlike the alternatives of grading or serial sectioning. Imaging thus yields the great advantage of being able to periodically assess the internal structure of a sample within an on-going experiment. A CT reconstructed volume image typically has a monochromatic appearance, that is the X-ray attenuation coefficient estimates are mapped as a grey-scale for presentation. Solid regions within the image are conventionally represented using white, whereas pore is black, and between these two extremes are grey levels representing various densities. The quality of image information is however marred by the presence of systematic problems such as the partial volume effect, beam hardening and perhaps most significantly by noise resulting from X-ray scattering and other sources (Seibert and Boone, 2005).

Despite the noticeable imperfections in image quality which are evident when CT is applied to soil, the overall quality of information acquired via CT is superior to that from other methods presently available. Within the next decade, there is promise that innovations in X-ray detector technology, along with corresponding advances in information processing techniques, will substantially improve the quality of information available from CT images. This implies that time and effort directed towards the development of analysis techniques for CT images represents a good investment that should provide long term benefits.

Both human and technological challenges exist in processing and interpreting the very large quantity of information contained within a 3D image. The computational cost of transforming and then distilling this information into a concise description of structure dictates the type of information that can be obtained in practice. Although the mathematical tools for describing the elements of 3D form have been in existence for well over a century (Gauss 1827) and (Reimann, 1854) the resulting descriptions are difficult to interpret in the case of very complex structures, such as pore networks in soil. Hence it is necessary to summarise information in the form of integral measures, sacrificing detail in order to gain a more general characterisation of structure. These measures are not necessarily intuitive and may embody assumptions or approximations made in the development of a particular analysis technique. Understanding the algorithm employed is therefore advisable, so that results can be interpreted without bias.

Beyond such "abstract" forms of analysis, the real objective of the soil scientist is to understand the effect of structure on physical processes such as transport of water and nutrients and the subsequent effect on biochemical processes. This is in principle achievable through spatially explicit modeling and simulation approaches (e.g. Lattice Boltzmann computational fluid dynamics). The result of such a 3D simulation is (often multivariate) spatial data, which can be interpreted in the form of an image. Thus the process of image analysis is again applicable in order to summarise simulation data in the form of integral measures (e.g. the flux through a plane).

1.4 Digital Image Analysis

A survey (Rosenfeld, 1969) perhaps marks the first widespread recognition of digital picture processing (as it was then known) as a distinct research topic. The book of the same name (Rosenfeld & Kak, first edition 1976, revised 1982) provides extensive references that serve to illustrate much of the early progress within this subject. Important work by Georges Matheron and Jean Serra at the Paris School of Mines during the 1960's receives almost no attention from Rosenfeld, however. The collaborative efforts of Matheron and Serra gave rise to the theory of mathematical morphology, which arose from difficulties in applying geostatistical analysis (Matheron, 1963) to mineral resource problems. Mathematical morphology is today recognised as being a fundamentally important basis for the interpretation of digital images, but this does not seem to have been widely appreciated (outwith the Paris School of Mines, that is) until published in the English language (Serra, 1982). The morphological approach underlies concepts of connectivity in binary classified digital images (Pfaltz and Rosenfeld, 1967) and thus provides the theoretical basis for the discrete skeleton (Rosenfeld, 1967) which is a form of medial axis (Blum, 1967). Matheron and Serra are also responsible for naming the Minkowski functionals and for developing practical methods for their estimation from images, although these fundamentally important measures date back to the quer-mass integrals (Hadwidger, 1957).

In addition to (Rosenfeld, 1976), perhaps the most significant work in the field during the 1970's is the classic text (Duda and Hart, 1973) which provides a

comprehensive treatment of statistical methods for image analysis. This era is also notable for the contribution of (Otsu, 1979) which is perhaps the globally most cited method for threshold calculation, and a method that seems especially popular in the life sciences. Many of the processing and analysis methods developed in this early period have stood the test of time as far as practical application is concerned, as they are in many cases sufficient to solve a problem, without being overly complex to implement. The time period from the 1970's to early 80's is also significant for the development of commercial systems for X-ray CT (or computerised tomography as it was then known). The huge benefits this offered for medical diagnosis led to its rapid adoption and gave new impetus to research in digital image processing and analysis. The need for improved image definition and faster tomographic reconstruction was one of the driving forces behind development of dedicated digital signal processor (DSP) systems which offered high performance at lower cost than a mainframe computer, but sacrificed flexibility.

The 1980's marked the transition to personal computers from mainframe systems, and the wider availability of resources for researchers, developers and practitioners of digital image analysis. It should however be borne in mind that the digital representation of images was at this time quite unusual outside of a few specialised application areas (mainly military, aerospace and medical). Much effort was directed towards improving the quality of image information through noise reduction and more robust segmentation methods. In this respect (Geman and Geman, 1984) produced important results in the interpretation of

images as random fields, with applications to noise reduction. Also notable was the survey (Haralick and Shapiro, 1985) categorising image segmentation methods with practical examples. Based on the approach of (Geman and Geman, 1984), the iterated conditional modes (ICM) method for recovering information from images corrupted by noise was deleoped (Besag 1986). Robust and accurate edge detection in images with variable levels of noise was achieved by (Canny, 1986). In (Kittler and Illingworth, 1986) a threshold calculation method similar to Otsu's method but with reduced inherent bias was described. A Bayesian approach to local threshold calculation was developed by (Mardia and Hainsworth, 1988) and this, by considering local spatial information, provided better robustness against noise. A near-optimal quality image segmentation method was developed based on the minimisation of an energy functional (Mumford and Shah, 1989) but this has remained a computationally difficult problem in the general case. Making use of spatial information or otherwise requiring expensive calculations per image element was at this time very difficult without mainframe type computer systems. This was particularly true in the case of 3D images, hence a 2D slice-by-slice approach was prevalent.

1.5 Digital Imaging Practice in Soils Research

During the 1990's digital imaging steadily became ubiquitous as relatively affordable digital cameras, based on high quality CCD sensors, became available. One of the early attempts at digital analysis of soil images was by (Terribile and FitzPatrick, 1992) who captured then digitised colour images of soil thin sections using specific illumination such as polarised light, but noted the unreliability of unsupervised analysis techniques. The guide to image analysis (Glasbey and Horgan, 1995) specifically targets the life sciences, but does not discuss segmentation methods specifically for soil structure. A significant development in this respect is due to (Vogel and Kretzschmar, 1996) who suggested applying bi-level thresholding to soil images, defining an unclassified or hysteresis interval between pore and solid, and then completing segmentation by region growing. This marks an important point in the divergence between "mainstream" segmentation methods (e.g. applied to general photographic images) and methods developed specifically for an imaging technique (e.g. X-ray and ultrasound) applied to a particular material. The gulf between theory and practice of image analysis was also widening as exemplified by work such as (Berthod et al. 1995 and 1996) and (Kato et al. 1996 and 1999) in which iteratively convergent Bayesian and Markov Random Field approaches were applied to image segmentation. Although such methods are robust and can yield results of high quality, their computational cost means they are difficult to apply to high definition volume images and their repeatability is undermined by the need for operator supervision. At the end of the decade

(Oh and Lindquist, 1999) proposed applying the geostatistical approach of indicator kriging to image segmentation of geo-materials.

The introduction of commercial "bench" X-ray micro-tomography scanners at the end of the 20th Century allowed 3D images of soil pore structure to be obtained relatively easily via a "turnkey" solution. The major market for these scanners was (and remains) industrial and this is reflected in the commercially available analysis software, such as VGStudio Max (Volume Graphics GMBH) which is well suited to engineering applications but lacks image segmentation appropriate for geo-materials. The software 3DMA (Lindquist et al. 1999) was an open source package developed originally for the analysis of rock samples in oil-exploration. This software provided methods applicable to soil (e.g. segmentation by indicator kriging) but seems not to have been widely accepted within the soils research community. More specialised software for soil image analysis was developed in the form of DXSoil (Delerue and Perrier, 2002) which is a closed source library module for the open source application OpenDX (IBM Research, 1999). Also developed specifically for soil science is the image analysis software QuantIm4 (Schlüter et al, 2010) which is entirely open source, but not entirely self-contained, relying on the open source *Qt* framework and some other modules (e.g. graph plotting). It has however proven difficult to find evidence (in peer reviewed articles) of these software applications being used except by the original authors or by institutional affiliates.

Contrastingly, ImageJ (Abramoff et al. 2004) is perhaps the most widely used scientific image analysis application. This is by virtue of the fact that it is easily obtained free of charge, in an immediately usable form, is reasonably well documented and supported by a large community (Schneider et al. 2012). However ImageJ does not provide specific tools for the analysis of soil pore structure, but is flexible enough to be applied to such problems, although this may require technical computing skills. In the opinion of the present author, the major issue underlying all of these software is a lack of published verification of method reliability. This problem affects even the most basic level of measurement on images, for example the location of the interface between adjacent solid and pore elements. In the case of ImageJ, the interface is not interpreted as being mid-way between the two, but rather is assumed to lie on the solid element, assigning the pore element a distance of 1 unit. This is a biased interpretation of image information (Serra, 1982) that has been implemented without explanation or caution to prospective users. There is therefore a pressing need for widespread agreement within the soil science community regarding both the definition and appropriate methods of calculation of measures to characterise soil pore structure. This thesis represents the authors first steps on a journey towards resolving this problem by developing, adapting or refining methods of analysis and then assessing their suitability for soils research.

1.6 Thesis Structure

Following this introductory chapter is an overview of some fundamental aspects of digital image analysis, presented as chapter two. This is intended to highlight essential information (such as image processing techniques) that are referenced in the remaining body of work. This includes material on the use of a geostatistical approach, which is rarely considered in the main body of image analysis literature. Following chapter two is a sequence of chapters that reflect the natural workflow of image acquisition, segmentation and analysis.

Chapter three, on the topic of image acquisition, presents original work on the assessment of image quality using numerical measures. This is an important aspect of the acquisition process as it dictates the selection of suitable parameters and also permits early accept/reject decisions, these being necessary for efficient workflow. Chapter four reviews a number of existing image segmentation methods selected from literature. These are assessed using synthetic image data as this provides a known reference point. Chapter five presents original work on image segmentation where an existing approach is reworked and extended yielding significant benefits. This novel work is assessed in the same fashion as the methods of chapter four.
Chapter six covers methods of analysis distinct from segmentation i.e. the subsequent calculation of numerical measures on segmented images. This reviews some published work, conducting a limited degree of verification on the accuracy of measure calculation. Some novel work is presented based on combining distinct approaches (functional measures with connectivity) within a

single analysis process, yielding advantages of accuracy and more general descriptive power.

Chapter seven presents a selection of image analysis work (either published or in press) to which the present author has made a significant contribution. As well as summarising the investigative processes, results determined by the present author are presented.

Chapter eight concludes the thesis, reiterating and discussing the important findings of the research project. A significant body of work is proposed for future investigation and development. This list of work is far from exhaustive but represents a prioritisation of objectives based on a perception of both relevance and achievability within a limited time scale (one to two years).

2.0 Digital Image Fundamentals

This chapter briefly summarises what is meant by a digital image and introduces some notation and concepts that are used throughout the thesis.

2.1 Digital Image Representation

The digital images subjected to analysis during this project are all examples of a discrete scalar field i.e. a scalar valued function that is known only at discrete spatial locations. The function is therefore sampled at these locations. By far the most common means of spatial discretisation uses a Cartesian grid which provides a point support for the image function. Such grids are particularly convenient because they directly match the high level programming language concept of the array whose elements are indexed by a tuple of coordinates (Knuth, 2011). This is certainly not the only means of defining an image e.g. a hexagonal grid offers advantages of geometric symmetry and topological consistency (Middleton and Sivaswamy, 2005) but must be explicitly implemented in software. The number of elements measured along each principal axis of an image array describes the definition of each axis; the total definition of an image may be quoted in terms of the axial element count tuple e.g. "1280 by 1024" or simply as a product e.g. "1.2 Megapixels". The resolution of a digital image can be interpreted in various ways, but in this work it is used to mean the separation between points on a physical object that are projected to axially adjacent image elements. In other words this is the size of the smallest physical feature that an imaging system might resolve, ignoring any limitations in the ability to achieve precise focus. The resolution is typically the

same for all axes in the case of tomographic images, this is however not true for image acquisition techniques such as confocal laser scanning microscopy. The product of both definition and resolution for any given axis therefore measures a span of physical space captured within the image.

This work is exclusively concerned with the analysis of scalar valued image functions, more commonly referred to as intensity or grey-scale images. Multispectral image information such as RGB colour (represented as a 3 component vector function) is important in many applications but has not been investigated in any detail for this project. This is more a consequence of the current technological limitations of X-ray computed tomography equipment, rather than any scientific principle.

The elements of a digital image array are finite not only in spatially, but also in terms of their value; a certain number of bits (binary digits) is allocated for the storage of each element. These bits may be interpreted as representing either natural numbers (including zero), integers or real numbers but in all cases the range of values is limited by the finite number of bits. In modern programming languages (such as the C family) the natural numbers are referred to as unsigned integers (Kernighan and Ritchie, 1972) emphasising the inclusion of zero. Similarly, real numbers are implemented in floating point representation, the format specified in the standard (IEEE-754,1985) being almost universal for hardware implementation. For integers, 2's complement number representation and processing (Tanenbaum, 1976) is provided by modern hardware and

languages. It is of course possible to define other forms of number in software, a typical example being fixed point numbers (Smith, 1997) which are basically integers, but implicitly scaled so as to represent fractional numbers (this requires some software implementation of arithmetic operations). The issue of numeric range and precision of image elements versus their storage and processing cost is an important consideration for any practical implementation of 3D image manipulation software. High precision image elements may limit the spatial dimensions of an image that can be easily handled, whereas low precision elements may introduce quantisation of intensity and are more vulnerable to information loss through rounding and truncation (Smith, 1997).

2.2 Digital Image Processing

In the most general terms image processing refers to methods that transform the information content of an image. In the case of digital images this usually means obtaining a new image whose elements are some function of elements in the original image. In the case where each new element is a function of exactly one original element, this is said to be a point function of the image, as illustrated in fFigure following. An example of a point function is applying a linear mapping to the image elements so as to uniformly lighten or darken the image.

In the more general case where a new element is a function of multiple elements of the original image, this said to be a vector function of the image. Typically a vector function operates on image elements within a local neighbourhood of the original image, as illustrated in Figure following.

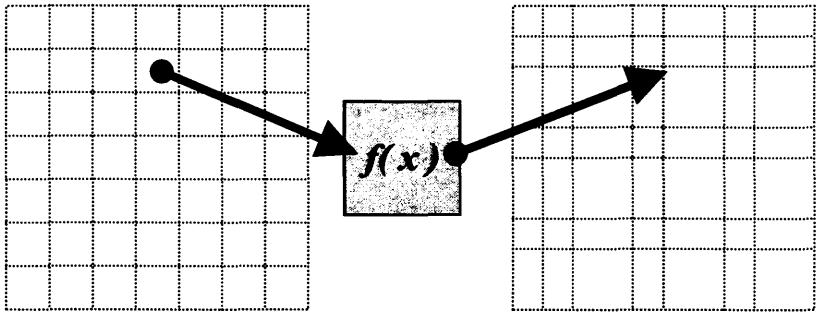

Figure 2.1 Point function of image.

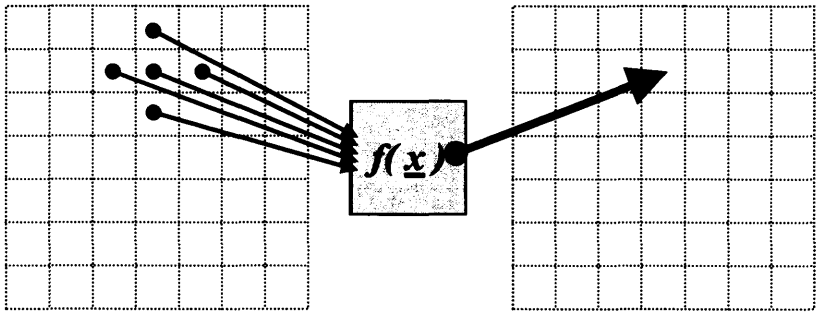

Figure 2.2 Vector function of image.

Vector functions are often referred to as filtering operations and may take the mathematical form of a discrete convolution operator applied to the image elements i.e. a localised product over the image with another spatially discretised function. In the context of signal and image processing the discrete form of a convolving function is typically referred to as a convolution kernel (O'Gorman et al. 2008). In 2D image processing applications a convolution kernel may be presented in the form of a matrix but considering 3D images it becomes clear that convolution kernels are more generally tensor quantities,

having a rank equal to the dimensionality of the space in which they are applied. An important point, omitted from some literature, is that coefficients within a convolution kernel should generally be standardised so as to sum to one. In this way the "energy" or mean grey level within an image is preserved. However, coefficients are often presented in literature as integers with the standardising factor omitted e.g. (Kroon, 2009). Although convenient for presentation purposes, and possibly yielding a faster implementation due to the use of integer arithmetic (Davies, 2005) this does mean that caution is required on the part of the implementer.

The use of a convolution kernel is not the only means of defining an image operator, there are many other useful vector functions on images. Operators that more generally make use of image elements within a local neighbourhood are described in terms of the shape and size of moving window. Reserving the term kernel for use only in the context of convolutional operations helps avoid confusion.

2.2.1 Digital Filters

Digital image filters that have been investigated as part of the soil image analysis project are described following. These were assessed initially for their ability to reduce noise and thus improve the extraction of information from soil images. However some filters can affect the location of edges within an image. As the accurate location of interfaces is precisely the objective of analysing porous media, such filters are of limited value.

2.2.2 Gaussian

The Gaussian filter is a form of weighted average, but unlike the uniformly weighted mean filter, is ideally suited for the purpose of smoothing digital images due to it's non-oscillatory nature (Marr and Hildreth, 1980). Although it can be applied to reduce noise in an image, the potential loss of edge definition through smoothing can make this impractical. A more general use of the Gaussian filter stems from it's close resemblance to the Point Spread Function (henceforth PSF) typically seen in imaging systems (Rawlins and Shaw, 1991). This fact is applied in the "un-sharp mask" operation (originally a technique of analogue photographic printing) where differences between blurred and original images are amplified to enhance the appearance of detail. In this project the simulation of the defocus or blurring characteristic of an imaging system is of interest in order to synthesise the effect of a PSF for verification and assessment purposes. This was implemented using discrete convolution for which the parameters are the shape and radius of the kernel plus the standard deviation of the Gaussian function. The shape can be specified as spherical or cubic while the remaining parameters are specified in image elements. A radius of at least one is required to have any filtering effect, a cubic kernel of radius one results in a cube with length of side three, whereas a sphere of radius one is a cruciform shape (essentially a cube with edge and vertex elements removed).

2.2.3 Median

The median filter is well known in signal processing and is simply the median average of values within a moving window of a particular width, conventionally an odd number so that the median is exactly defined. Extension to 2D and 3D image processing simply involves defining a window and then taking the median average of data points within the window applied at every location within an image. This has the effect of removing texture on scales less than the window size and results in a filtered image exhibiting regions with a typically "flattened" appearance. Although this is highly effective in removing many types of noise from an image, it has the disadvantage of distorting edges. Used in a fashion similar to the Gaussian filter based "un-sharp mask" operation, the median has the potential to isolate or enhance textural information (but also noise) which might be useful for types of analysis not considered in this thesis. Parameters of this filter type, as implemented by the author, are the shape of the window (either spherical or cubic) and the radius given in image elements.

2.2.4 Pseudomedian

The pseudo-median filter preserves edges while giving a quality of noise reduction similar to the median. The pseudomedian filter used in signal processing (distinct from the definition of pseudomedian in more general descriptive statistics) is defined in (Pratt et al. 1985) on a 1D signal by dividing the filter window into a number of overlapping sub-windows. The minimum and maximum values are taken within each sub window and then the overall maximum of sub-window minima and also minimum of sub-window maxima are

determined. Taking the mean average of these two provides the result of the filter. Extending this procedure to a square window applied to 2D images was one aspect of work by (Schulze, 1990). In this work it is noted that the 2D square window proposed in (Pratt et al. 1985) is not properly consistent with 2D information: the 2D window is collapsed into 1D form and sub-windows are defined that, viewed in terms of the 2D window, "wrap-around" from the right edge of a row to the left edge of the next lower row. This practice clearly violates principles of locality and continuity in 2D space. Instead (Schulze, 1990) proposes a set of overlapping 2D sub-windows which preserve the spatial properties of the data. This scheme was extended by the author to 3D using a cubic window measuring three image elements along each principal axis of the image, and within this window were defined eight overlapping cubic sub-windows (measuring two elements in each direction). The remaining min-max processing is carried out exactly as for lower dimensional versions of the filter, taking the result as the mean of the maximum of all sub-window minima with the minimum of all sub-window maxima. This filter was also parameterised in terms of shape (sphere or cube) but not radius, which is presently fixed at one. The spherical (i.e. cruciform) shape was evaluated as part of the development process i.e. extending from a 2D to a 3D implementation. Due to the small number of image elements it considers, the pseudomedian based on a sphere of radius one has a very limited filtering effect. For this reason, only the cubic form has been used for work presented in this thesis.

2.2.5 Majority

This is an extended form of the mode average applied within a moving window. The classical mode average is not particularly useful in the context of grey-scale images as it does not guarantee a fair representation of the image element population within a window (Davies, 2005). This is because the most frequently occurring value may represent a window population fraction as little as 2/N for a window containing N elements when all but two elements have unique intensity values. To address this problem, the majority filter applies a test to decide whether the most populous element is significant. This test involves comparing the mode population fraction against a majority threshold parameter, typically a value of at least 50% of total window population size is used. When the mode reaches the threshold it is accepted as a valid result, otherwise the original image element at the centre of the window is by default accepted as the result. For grey-scale images containing a great many intensity levels, the majority filter is of limited value because there is rarely a significant local majority - the resulting majority filtered image is almost indistinguishable from the original. When the number of levels is small however, as in the case of a quantised or classified image, the majority filter can provide a very effective means of removing isolated values i.e. noise.

2.2.6 Visual Assessment of Filtering

Examples of the effect of these filters applied to a 2D CT image of soil are shown on the pages following. Each image is shown in 8bit precision (i.e. using 256 grey levels) while the corresponding histogram (to the right of each image) is shown using 128 bins. The first to be shown in figure 2.3 is the unmodified soil image, which has a significant noise content. The histogram of this unmodified image shows evidence of bimodality but the degree of overlap between pore and solid modes is significant.

Each of the filters previously described (except mode or majority which are inappropriate for grey-scale images) is applied to the unmodified soil image of figure 2.3 and the resulting image and histogram are shown (figures 2.4 - 2.9). Also shown in each case is a difference image formed by subtracting the unmodified image from the filtered image. The difference images are encoded using a biased 8bit representation so that black corresponds to a difference of -128, white to +127 and mid-grey to zero. The histograms of the difference images are also shown to the right in each case.

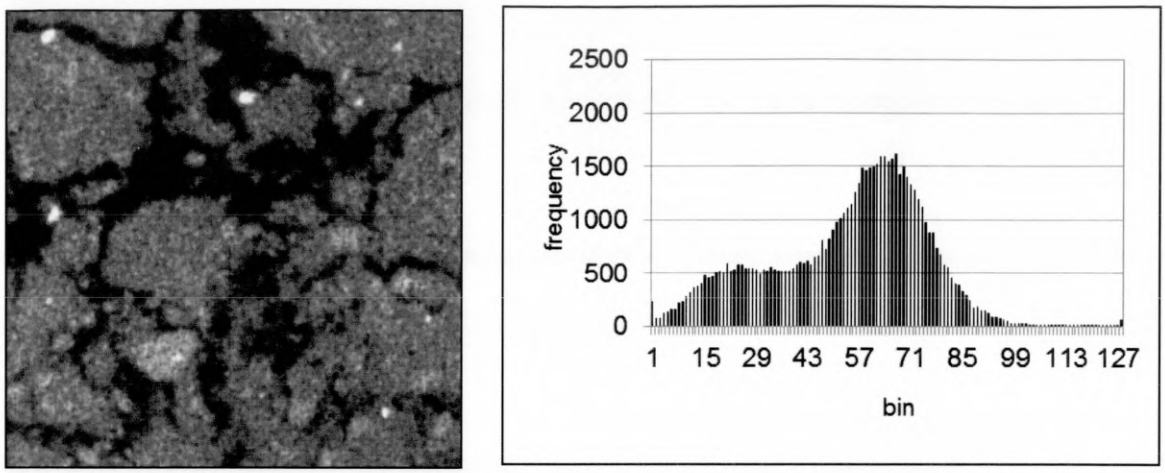

Figure 2.3 Soil image.
2D slice from a CT reconstructed image of soil (left) with its histogram (right).
Bimodality is discernable in the histogram, but not particularly clear.

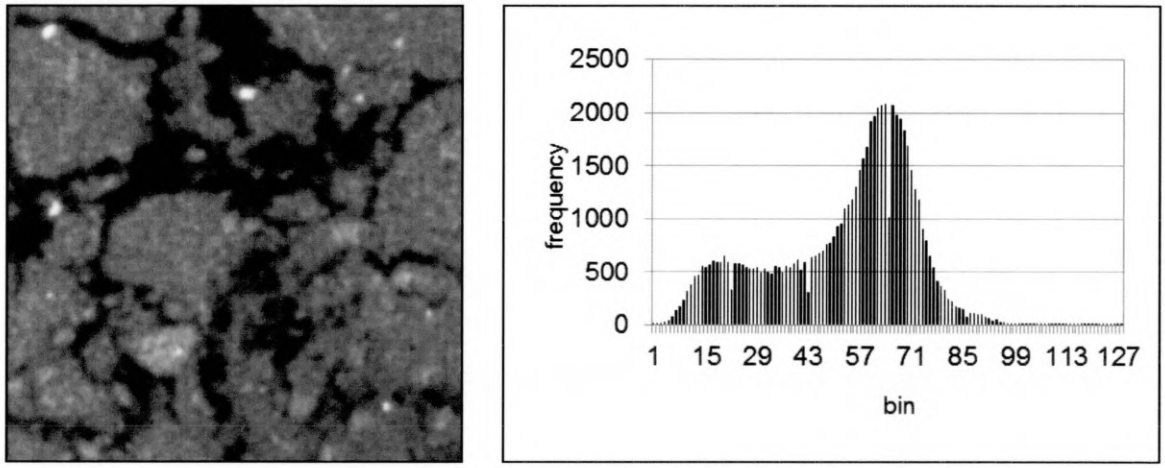

Figure 2.4 Gaussian filtered soil image.
Parameters r=2, σ=1, yields smoother image but blurring of object edges.
Improved separation of modes is evident in histogram.

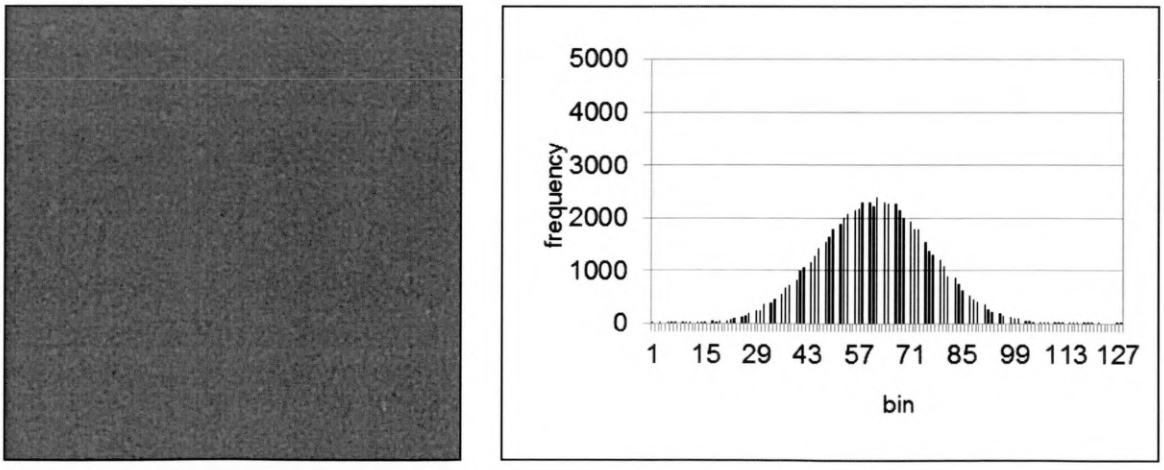

Figure 2.5 Difference between original and Gaussian filtered soil image.

The faintly visible pore edges suggest edge information has been lost by filtering.

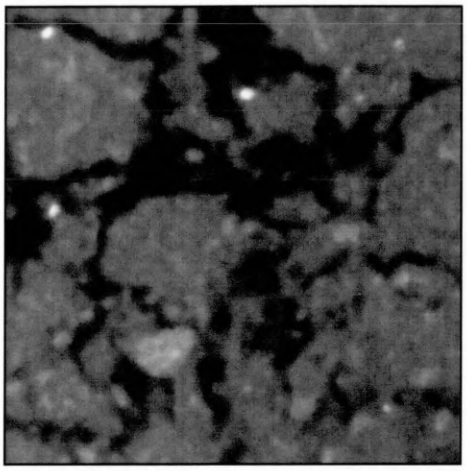

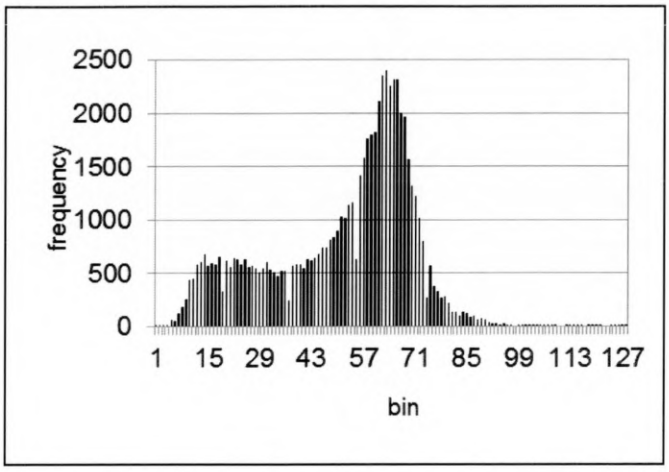

Figure 2.6 Median filtered soil image.
This yields yields a "flattened" appearance with better local homogeneity.
Mode separation in histogram is improved noticeably.

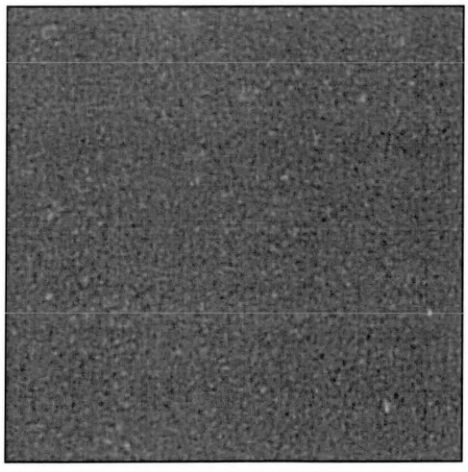

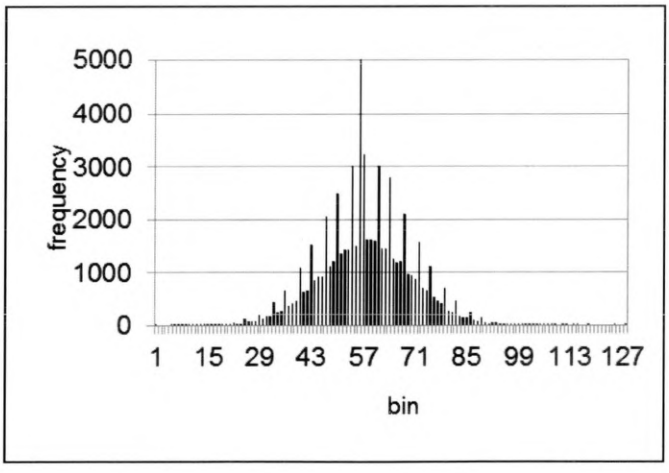

Figure 2.7 Difference between original and median filtered soil image.
Some partly fragmented edge information is discernable amid the noise.
The histogram indicates that a significant proportion of image elements have remained unchanged.

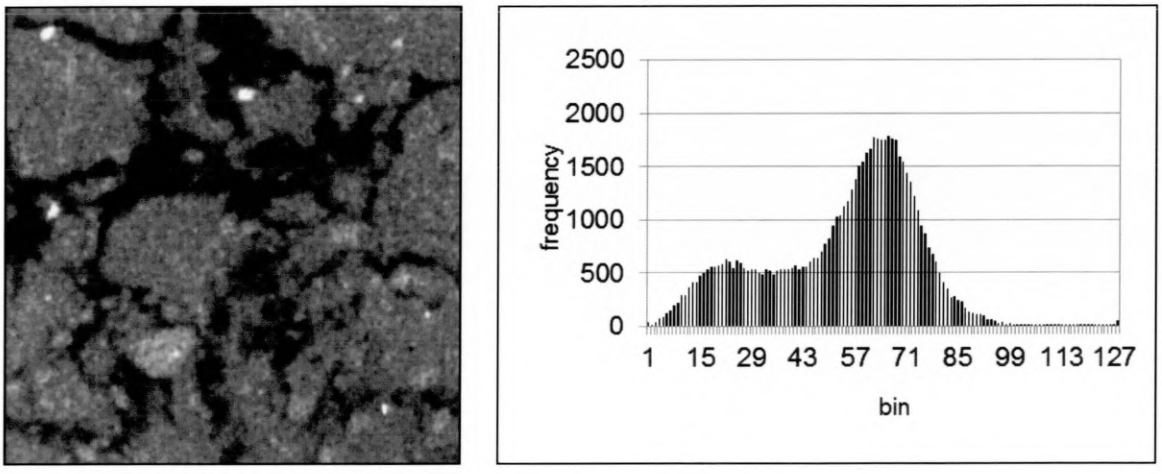

Figure 2.8 Pseudo-median filtered soil image.
(r=1) "softens" the appearance of noise but provides good edge contrast.
The histogram appears slightly smoother than the original with improved separation of modes.

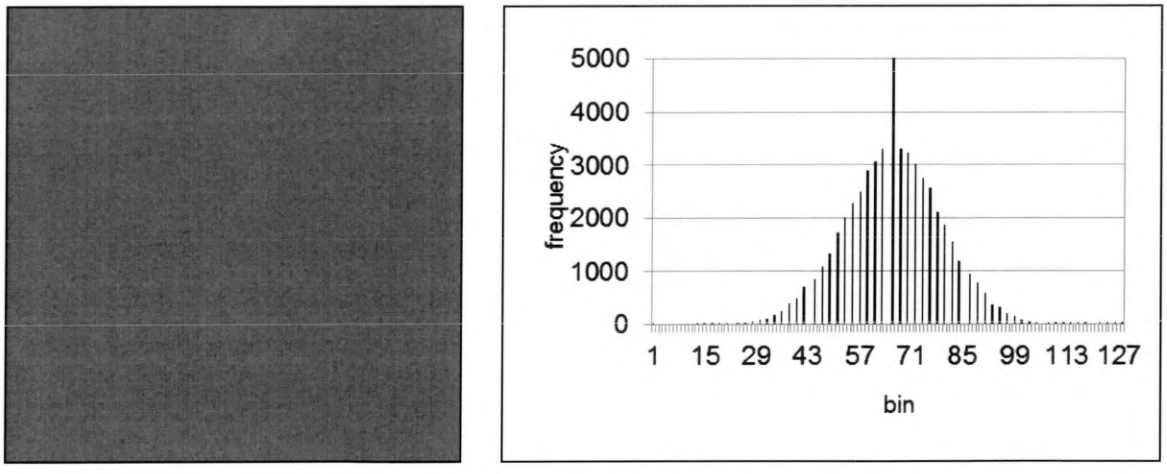

Figure 2.9 Difference between original and pseudo-median filtered soil image.
It is difficult to discern correlated structure amid the noise and the histogram indicates most image elements have changed only slightly.

2.3 Basic Tools for the Analysis of Grey-scale Images

The most basic analysis tool is undoubtedly the image histogram, which shows the frequency distribution of categories of image intensity (i.e. numerical values of image elements). This information is also commonly shown in the form of a Probability Density Function (henceforth PDF) which shows the probability of occurrence per category (defined in equation 2.1 below, where **m** is the histogram frequency). This completely describes one fundamental aspect of image information (it's intensity distribution) but conveys nothing regarding spatial structure.

$$p_i = \frac{m_i}{\sum m}$$

(equation 2.1)

The natural partner to the histogram is the semivariogram which describes the variation in image intensity by classes of distance (and possibly direction). The empirical semivariogram, also called the experimental or sample semivariogram (Goovaerts, 1997) can be determined using the estimator proposed in (Matheron, 1962) which, in principle, considers all possible pairs of image elements over all positions ***x***:

$$\gamma_{\underline{h}} = \frac{1}{2N} \sum_{i=1,N} \left(f(\underline{x}_i + \underline{h}) - f(\underline{x}_i) \right)^2$$

(equation 2.2)

Where the lag vector ***h*** between a pair of elements defines the direction and distance class to be computed. When the data is considered isotropic then classes of lag distance are used instead. For images containing millions of elements, it becomes impractical to calculate a full semivariogram due to the

$O(n^2)$ cost in the number of pair-wise combinations. Instead a cutoff distance is applied so that only lags within this distance are actually evaluated. The software developed by the author is parameterised by this cutoff distance and in the case of the 2D examples shown in this chapter, a cutoff lag of 100 image elements has been applied. All semivariograms shown in the form of a conventional 2D graph are necessarily limited to presenting either isotropic data or some other mapping of directional information. If significant anisotropy is present within the image data then multiple 2D semivariogram graphs are required to assess the extent of the anisotropy. The work presented in this thesis treats all images as being isotropic hence only a single graph is presented.

2.4 Image Synthesis

The use of synthetic images allows image processing operations to be assessed with respect to a *ground truth* image. This is particularly important for an application such as soil image analysis where a true image, unaffected by physical handling and image acquisition artifacts, cannot be obtained. As the objective is to identify potential flaws and weaknesses in the processing of images, it is argued that a ground truth image should exhibit a simple and easily identifiable structure to facilitate comparison. Therefore theoretical methods for simulating complex soil structure such as the pore-solid fractal model (Perrier et al. 1999) are best avoided; figure 2.10 (below) illustrates the visually complex results produced by this model. Instead a 2D ground truth image is generated by creating a single black (pore) disk on a white (solid) background (figure 2.11). The area of the circle is defined to be 25% of the image leading to a radius of 72 image elements within an image of 256^2 elements. This image is shown overleaf in figure 2.10 along with its histogram and semivariogram. While the histogram is singularly uninteresting and shown only for completeness, the semivariogram clearly indicates the presence of spatial correlation within the image.

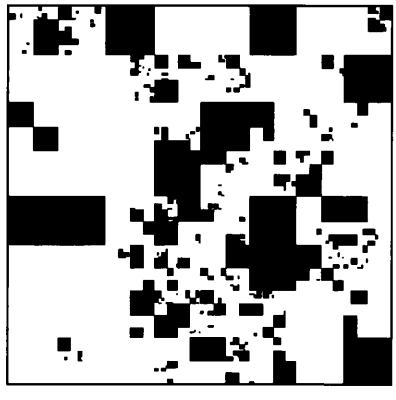

Figure 2.10 Pore Solid Fractal

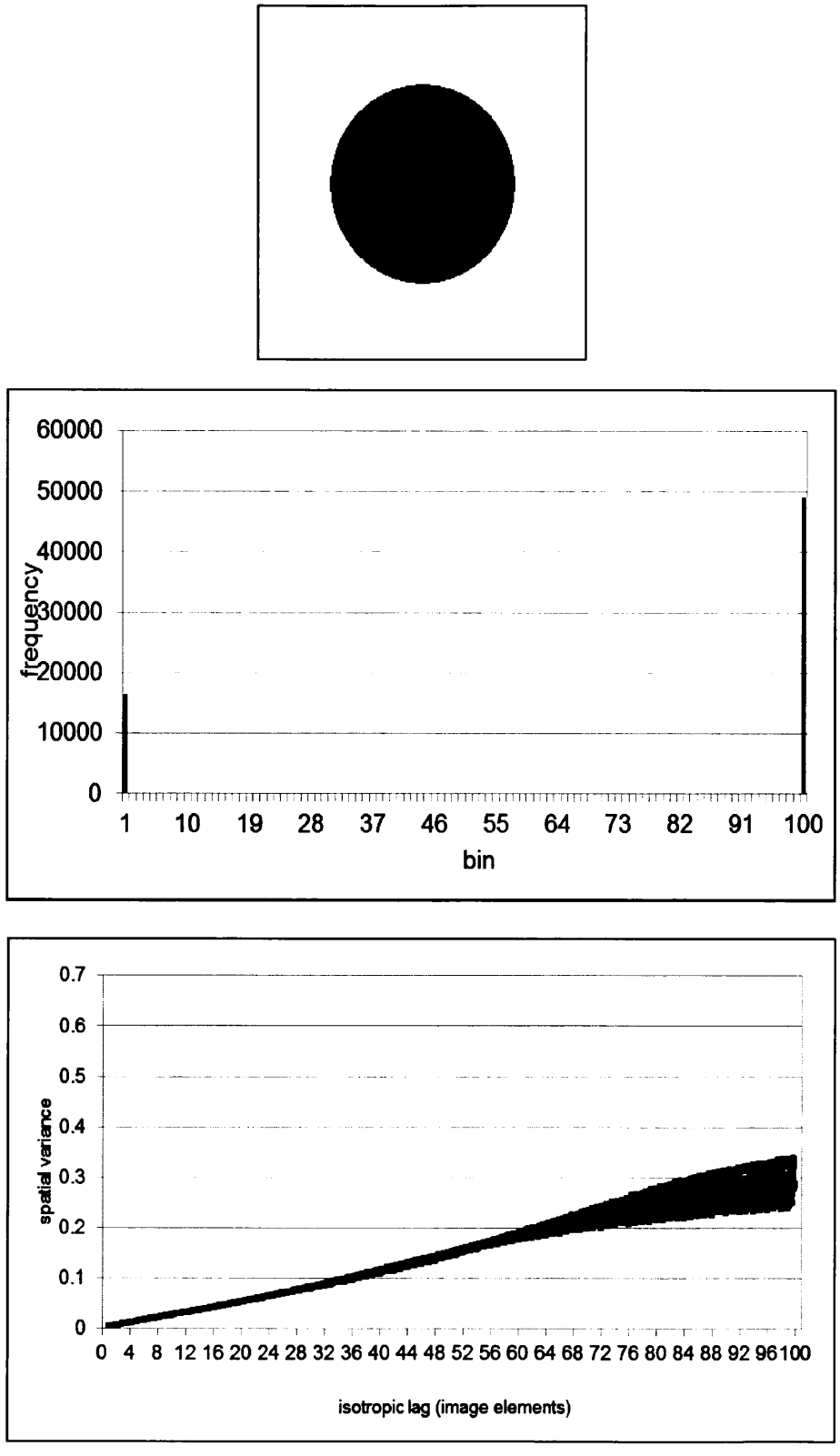

Figure 2.11 Synthetic 2D test image.
Image (top) shows 25% pore area (value 0.0) against a background of solid (value 1.0). Histogram (middle) shows 1:3 ratio of pore to solid. Semivariogram (bottom) shows gradual decline in spatial correlation with increasing lag distance. This pattern is typical of long range correlated structure.

2.4.1 Noise Synthesis

Two forms of noise were synthesised, the first form is intended to represent general random errors while the second is intended to approximate the effect of X-ray scattering. The first noise function was generated using random deviates drawn from a normal distribution, yielding an independent and identically distributed 2D image of noise. These deviates were obtained using the *ziggurat* algorithm (Marsaglia and Tsang, 2000).

The second noise function was obtained according to the Asymptotic Discrete Spot Noise (henceforth ADSN) principle described in (Galerne et al. 2011). The noise image was first set entirely to zero and then disks of constant radius but random intensity were added to random locations within the image. Both intensity and position were determined by sampling a uniform random distribution such that each disk was independent and identically distributed. As the disks accumulate, a normal distribution of intensity emerges within the image (as a consequence of summing many random variables) and also spatial correlation is evident on a scale corresponding to the diameter of the disks. This is therefore a method for generating spatially correlated noise with normally distributed intensity.

An example of each type of noise image is shown in figures 2.12 and 2.13 along with histograms and variograms. The normal distribution is clearly identifiable in both histograms and the variograms clearly illustrate the difference in spatial correlation. The "pure nugget effect" visible in the uncorrelated noise

semivariogram (figure 2.12) indicates that there is no correlation at any lag distance. The steady increase in the correlated noise semivariogram (figure 2.13) which reaches its "sill" value at a lag distance of four image elements, indicates widespread spatial correlation (i.e. coherent structure) ending at this distance.

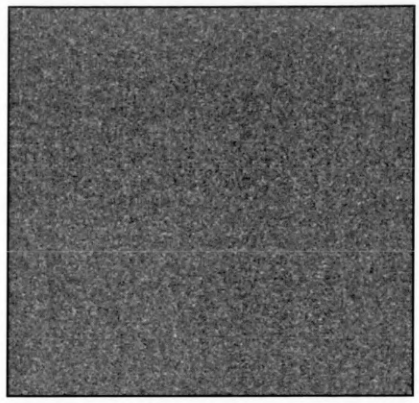

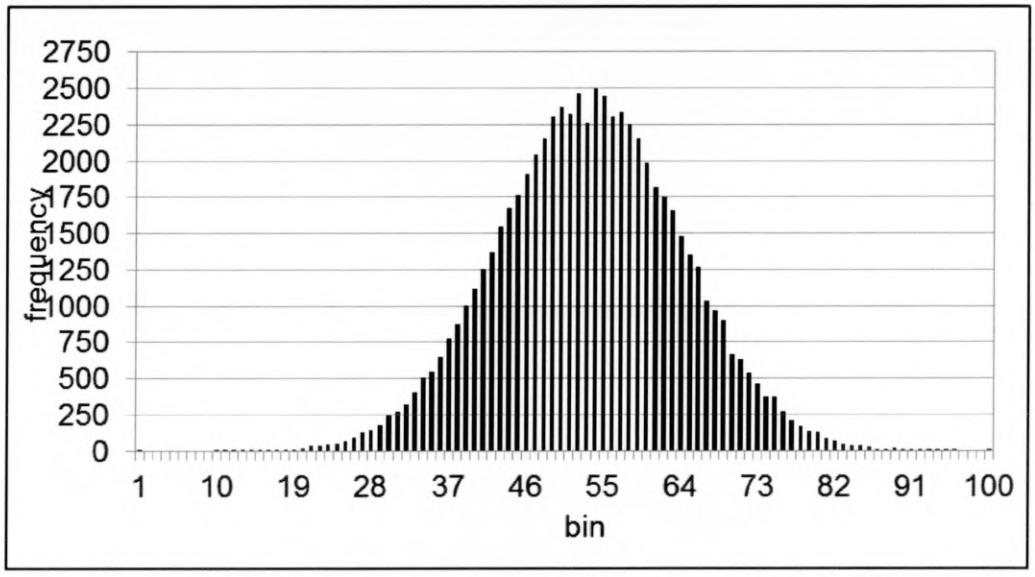

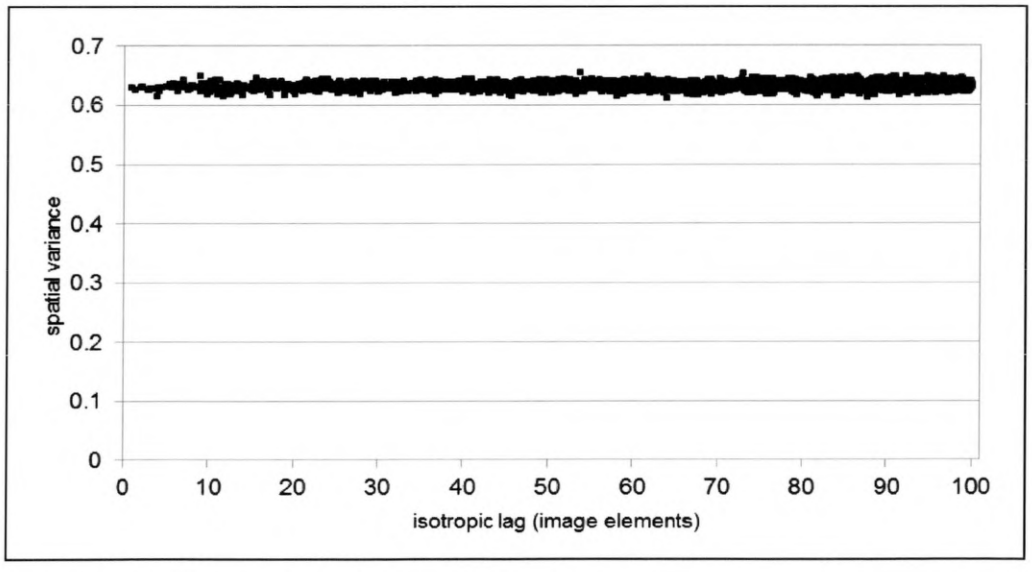

Figure 2.12 Uncorrelated Gaussian noise image.
Noise image (top) generated using ziggurat algorithm (Marsaglia & Tsang, 2000).
Histogram (middle) shows typical Gaussian distribution (with slight irregularity due to limited population size).
Semivariogram (bottom) is "pure nugget" indicating absence of spatial correlation.

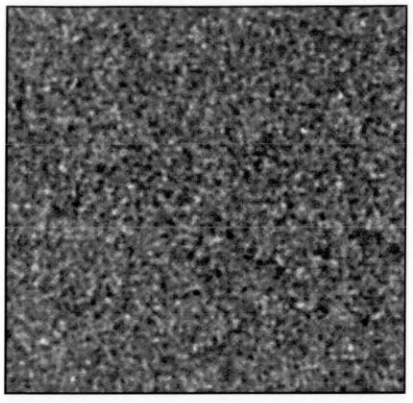

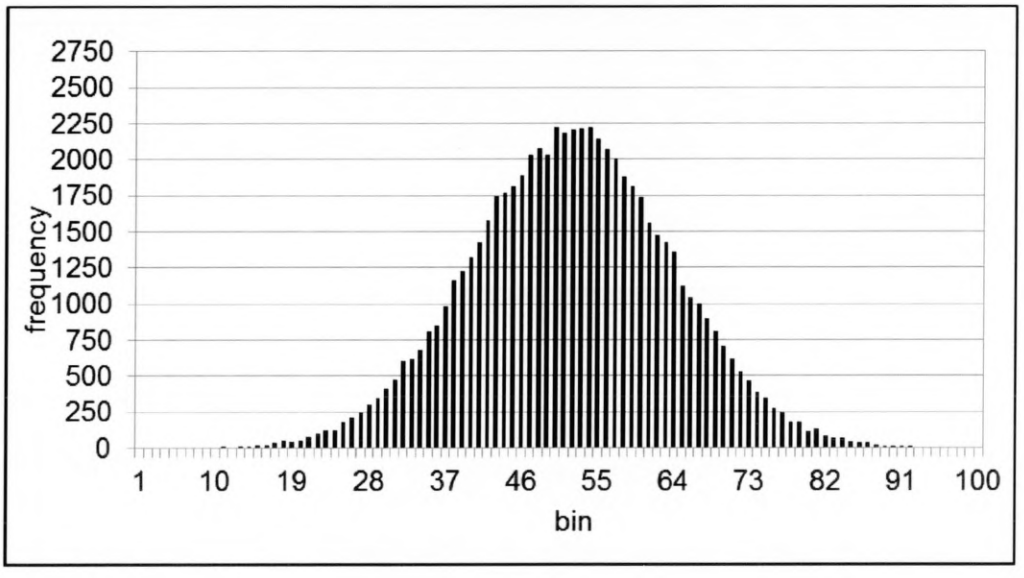

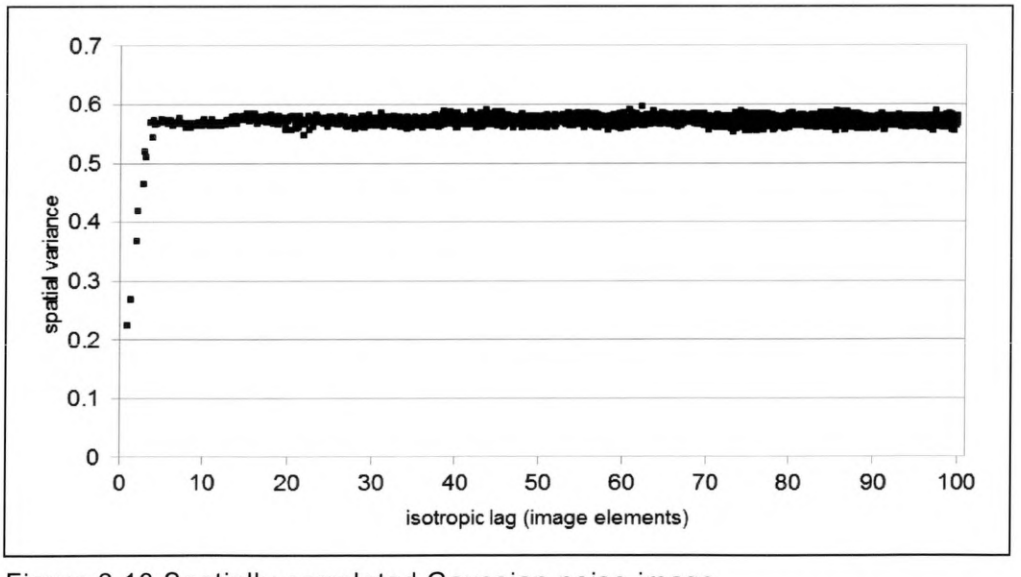

Figure 2.13 Spatially correlated Gaussian noise image.
Noise image (top) generated using ziggurat algorithm (Marsaglia & Tsang, 2000).
Histogram (middle) shows typical Gaussian distribution (irregularities resulting from limited population size).
Semivariogram (bottom) indicates spatial correlation ending at a lag distance of around four image elements.

3.0 Image Acquisition and Assessment

A recent study (Wildenschild & Sheppard, 2013) contains a thorough review of X-ray tomography techniques applied to geo-materials, covering developments in laboratory or "bench" based tomography systems and also synchrotron beamlines. The former type of system is more commonly available due to its far lower cost and is the subject of the work presented here. Due to the area of application (the analysis of soil pore structure) the focus is on *micro-tomography* i.e. systems capable of resolving features measured in microns.

3.1 X-ray Imaging: Transmission to Tomography

Computed tomography is carried out in a number of distinct steps, each of which involves significant complexity. In modern "turnkey" systems, much of this complexity can be hidden from the operator provided that a suitable "scanning profile" (i.e. a complete set of image acquisition settings) is available for the sample in question. However, for the investigation of a natural material such as soil, which is highly variable in composition, such a simplistic strategy may not be successful. It is necessary instead to tune parameters to a sample (or more usually for a set of replicates) and this requires a reasonably detailed understanding of the overall process so that informed choices can be made.

The basic principles of X-ray imaging (in a historical and technological context) are summarised first, after which some comments are made on practical issues. Following this, the process of 3D reconstruction is considered along with

aspects of the accuracy, flexibility and costs involved. Finally some issues associated with the format of 3D reconstructed image data are addressed.

3.1.1 X-ray Image Capture

The fundamental principle of X-ray imaging is the penetration of a sample with electromagnetic energy and recording of the transmitted signal with a suitable detector. The basic form of "shadow" or transmission image produced is a consequence of higher intensity radiation where the X-ray photons have passed relatively unimpeded through the sample, versus low intensity areas where the radiation has been more strongly attenuated by interacting with dense regions of the sample. This particular form of image acquisition is specifically referred to as *attenuation contrast* X-ray imaging and is the only method applied in this work. The alternative technique of *phase contrast* image acquisition (Beckmann et al. 1997) offers superior discrimination of structure but is generally only applicable in a synchrotron facility.

3.1.1.1 X-ray Generation

In its fundamental form, the generation of X-rays has not changed since Rontgen's experiments with vacuum tubes in 1895. When sufficiently fast moving electrons undergo a rapid change in momentum, X-rays are produced. In fact, any moving charged particle radiates electromagnetic energy when it's momentum is altered, but electrons are more easily manipulated than protons or heavier ions. Precise control of X-ray generation is steadily improving: at the cutting edge of technology are the free electron laser (Madey, 1971) and the more widely available synchrotron (Veksler, 1944; McMillan, 1945). These devices can trace their roots back to the betatron (Kerst, 1940) and cyclotron (Lawrence, 1934) which still find application niches. Although the free electron laser has the potential to be miniaturised, it is presently, like the synchrotron a large, expensive and power hungry item of equipment requiring careful handling and regular maintenance. Access to such equipment is necessarily limited by the costs involved, hence the growing availability of less sophisticated, but much lower cost, "bench" systems that can be installed in existing laboratories.

Cost-sensitive applications for which controllability outweighs the need for raw power continue to make use of the X-ray tube (essentially a glass capsule holding anode and target within a vacuum) and devices that are refinements of it. Medical imaging uses "soft" X-rays (these have limited penetrating power and are considered less hazardous to health) produced by a tube; scanners built in this way may be able to resolve features as small as 0.1mm in size. Contrastingly, scientific applications require a wider range of X-rays and may

require an image resolution finer than 1μm. The earliest equipment that could achieve this resolution was also based on the X-ray tube but required that the X-rays pass through a microscopic aperture, limiting beam power and significantly reducing performance. This problem was resolved by introducing the "triode electron gun" which produces a collimated beam of electrons that can be focussed accurately to a point, and also by very precise manufacturing of the entire X-ray generating "head" assembly. This combination of equipment effectively creates an extremely precise X-ray tube. The underlying problem of high resolution X-ray imaging is that the creation of a sharply defined image relies on a point-source of X-rays. In practice this means that the size of the X-ray origin should be no larger than the desired image resolution. This means that electrons must be very accurately focussed to a point or "spot" on the metal "target" from which the X-rays originate, and the spatial location of this point must be extremely stable throughout the scanning process. This latter issue is made difficult by the strong heating effect of the incident electron beam. It is therefore necessary to limit the power of the beam and to provide some method of heat dissipation, thereby limiting thermal expansion. The use of fluid coolant provides a solution, but inevitably complicates the design of the head assembly and requires an external pump and heat exchanger. A recently devised solution to this problem is the use of a jet of liquid metal (Larsson et al. 2012) as the electron beam target, permitting higher power density (i.e. a smaller or more intense focal spot) and therefore improved image quality. Unfortunately the jet composition presently available means that only soft X-rays can be generated, hence the application of such equipment is limited.

In a commercial bench CT system the X-rays are, for safety reasons, contained within a chamber in which they pass through the sample and then reach the detector, forming an image. Ideally, air would be removed from the imaging chamber so as to prevent any attenuation of X-rays except by the sample itself. Apart from the complexity (and hence cost) this would add, there is the risk that subjecting a sample to vacuum might alter its structure. For this reason air within the chamber is instead conditioned to reduce its moisture content, as water is a significant cause of interference. The interaction mechanism between electrons and electromagnetic radiation is, at the level of individual particles and quanta, non-deterministic, being a quantum mechanical phenomenon. At the macroscopic scale, particular laws have been formulated based on observation under carefully controlled conditions. Hence we distinguish between reflection, refraction and diffraction – phenomena that are perhaps most familiar in the context of geometrical optics. For visible wavelengths of light passing through reasonably homogeneous materials, these laws of optics provide a good model of interaction. For the far more energetic radiation quanta of X-rays passing through heterogeneous materials, the situation is very different. The phenomenon of X-ray scattering is a significant component of the interaction, while the simplistic model of absorption, on which the principle of attenuation contrast imaging is based, is only true to a limited degree. In fact, interactions between X-rays and atomic electrons are sufficiently complex that they are usually placed into one of three categories: absorption, Rayleigh (elastic) scattering, or Compton (inelastic) scattering. A useful introduction to these phenomena is provided in (Seibert & Boone, 2005). The main issue to be

considered is that *any* interaction between electrons and X-rays tends to result in X-rays changing direction. Such changes are governed by quantum mechanics meaning that each specific event is described by an individual and typically complex 3D distribution function, hence predicting the outcome of a sequence of events is generally impractical. Furthermore, "absorption" events can lead to the emission of secondary X-rays also known as *characteristic X-rays* (these can be used to identify the elemental composition of a sample in the process known as X-ray fluorescence imaging). These secondary rays typically travel in a direction different to that of the primary X-ray and may either interact further with the sample or may be detected at the sensor. Therefore what typically arrives at each element of a sensor is some mixture of primary and secondary X-rays whose direction has been perturbed to a variable degree within the sample (and also to a lesser extent by air within the imaging chamber). The distribution of directions of the X-ray quanta arriving at a sensor element is then a very complex function of the energy of the primary X-rays in conjunction with the sample composition and thickness. Other factors such as the size of the focal spot and the distance between the spot and the sample and also between the sample and the detector are also important. Given a sufficient density of information at the detector (i.e. quantised events are not individually discernible) and a reasonably uniform spatial distribution of elements within the sample, the perceived effect within the projected image is one of a general defocus or blurring. This is a fundamental limitation of the imaging system and cannot be corrected except by improving the design of components. Adjusting the available parameters (e.g. beam energy, magnification and exposure time)

may reduce the effect, but this is dependant on the properties of each sample individually. Furthermore, when a high degree of heterogeneity is present within a sample, as in the case of many soil types, it is to be expected that the defocusing effect will be correspondingly variable across the image and moreover will change with sample orientation relative to the X-ray beam. The final aspect of this problem is the limited illumination available within a bench type micro-tomography system, and the consequent reduction of information available at the sensor. Rather than smooth blurring, a more noisy effect becomes apparent as the number of X-ray quanta detected at each sensor element is reduced. The appropriate remedy for this problem is increasing the exposure time (i.e. the duration of image capture). The reduction in throughput of the imaging system this implies may be problematic in itself, however.

3.1.1.2. X-ray Detection

The image sensor (X-ray detector) is a key part of the imaging system and one for which recent advances in electronics may partly address some of the problems discussed previously. The earliest form of solid-state image sensor element is the photo-diode which (as part of an appropriate circuit) produces an electrical pulse in response to a suitably energetic photon. In the first generation of digital X-ray imaging systems discrete photo-diode components were used: first singly, then in lines, so that a step by step traversal was required to build up a complete raster image. Mechanical complexity, spatio-temporal accuracy and overall time requirement are obvious problems with such an approach. The development of two dimensional array CCD sensors resolved these problems

by allowing the capture of a full 2D image in a simultaneous fashion. However this type of sensor is relatively small and so a method of forming an appropriately sized image is required. This is typically achieved using a scintillation screen that converts X-rays to visible light which is then focussed onto the sensor using a lens or mirror. This approach is common in the case of synchrotron beamlines because electronic equipment in the path of the beam can malfunction owing to the intensity of radiation (the scintillation image is reflected into a shielded enclosure in this case). With the development of amorphous semiconductor manufacturing at the close of the 20th century it became possible to create large "flat panel" X-ray detectors containing high definition arrays of sensor elements. This approach offers high spatial and temporal accuracy but the sensor tends to accumulate defects through long term radiation exposure and is expensive to replace (high quality CCD sensors are comparatively inexpensive, being used in a much wider range of applications). On the technological horizon is the hybrid CMOS sensor which can categorise incident radiation from the shape of the electrical pulse generated; this has the potential to discriminate between primary and secondary (characteristic) X-rays and so provide clearer attenuation contrast images. If this technology can be sufficiently refined then bench systems may become routinely capable of advanced imaging techniques such as phase contrast tomography and also multi-spectral fluorescence image capture.

3.1.1.3 Practicalities of X-Ray Image Capture

Obtaining a good X-ray image is a matter of adjusting various parameters of the imaging system in an attempt to clearly define some features of interest. The range and precision over which individual parameters can be adjusted is in some cases quite large while others take only a few discrete values and may be highly nonlinear in their effect. Much like optical photography, an understanding of the principles involved is helpful in guiding the search for a good image, but it is necessary to find a compromise between many factors that interact in complex ways. This is then a search problem, but one that is severely hampered by the time required to capture an image (typically more than an hour) and the limited repeatability of image capture as a consequence of mechanical limitations and also the need for recalibration. The inherent variability of a natural material such as soil leads to further complications, as the presence of materials not accounted for in the selection of parameters may lead to problematic artifacts in the image. Consequently it is necessary to rely significantly on heuristic methods and strategies based on the accumulation of knowledge and experience.

Perhaps the most basic adjustments in the X-ray imaging process are the beam energy and flux, often quoted in units of keV and μA respectively. This measure of energy relates to the momentum of a single electron accelerated from rest through an electrostatic field of the quoted potential e.g. a field of 10kV results in 10keV electrons. In an X-ray tube or similar generation system, the kinetic energy of electrons is converted to electromagnetic radiation when the electron

is subsequently brought to rest by striking the metal target. It is thus common practice to describe X-rays in terms of the energy of the electrons used to generate them (e.g. "10keV X-rays") rather than wavelength, the numerical values being more convenient. Such a description can be misleading however as it ignores the complexity of interaction between electron and target; in reality a distribution of electromagnetic energy is produced resulting in a *polychromatic* beam. The flux is simply the flow rate of electrons: the primary unit of electron flow, the Ampere is equal to one Coulomb (a mole i.e. Avogadro's number of electrons) per second. Multiplying the two quantities together gives the electron beam power measured in Watts, e.g. 10kV @ 100μA = $10^4 * 10^{-4}$ = 1W. This gives the upper bound for the polychromatic radiation flux leaving the electron beam target whereas the actual flux at the target energy (10keV in this example) is somewhat less.

The beam energy is adjusted to achieve a controlled and balanced penetration of the sample: too low an energy results in a silhouette, too high and the sample appears insubstantial against the background. Between these extremes, the internal structure of the sample is seen with differing thickness and density of material being visible as light versus dark areas. The flux is adjusted so as to maximise the brightness of transmitting areas without saturating any part of the image. Saturation occurs as a consequence of limited numerical precision within the detector: associated with each sensor element is a count of the number of detected photons. The maximum allowable count is determined by the detector design in accordance with cost restrictions and a balance between

speed and precision. Typically 16bit precision sensors are employed (implying a maximum count of 64K photons) and so either flux or exposure time are limited to accommodate this restriction. Taking multiple exposures and summing these into a higher precision representation can be used to circumvent this limitation, although it increases the duration and temporary storage costs associated with image capture.

Once an appropriate beam energy and flux have been established for a sample, the system must be calibrated using at least black and white reference levels for these settings (additional reference levels may be used to define a non-linear transfer function). In other words the sample is removed from the beam, then images are captured with the X-ray beam active to provide a white level or "zero attenuation" reference. This also serves to assess the stability of the X-ray source and to identify any defective sensor elements in the detector. The black reference level is obtained with the X-ray beam inactive and allows background noise to be assessed. Periodic calibration (between scanning of physical samples) is therefore important to ensure the X-ray source and detector and functioning correctly

Except for the free electron laser, all methods of generating X-rays produce a *polychromatic* beam, in other words a distribution of wavelengths (quantum energies). For high power sources such as a synchrotron it is possible to refine the beam characteristics (to obtain putative monochromatic, collimated and polarised radiation) by discarding perhaps 99% of beam energy and still obtain

sufficient output flux to be useful. The limited power output of a bench microtomography system however means that only a very limited degree of refinement is practical, as reducing beam power leads to either longer exposure time or an increased level of noise. The most obvious effect of a polychromatic beam on image quality is the phenomenon of "beam hardening", where the softest (lowest energy) X-rays are attenuated more rapidly with distance than are the harder X-rays (more energetic and hence more penetrating by definition). This leads to an exaggerated darkening of the image where the sample thickness is greatest (Wildenschild & Sheppard, 2013). Applying a filter (i.e. a thin layer of metal) to uniformly "pre-harden" the beam allows the appearance of this effect to be reduced in the captured image. The beam attenuation introduced by this filtering must be taken into consideration when the exposure settings are defined.

3.1.2 Computed Tomography

Conventional X-ray imaging, i.e. without tomography, is inevitably limited in it's application. As more complex internal structure is studied, it becomes very difficult for humans to interpret transmission images directly. In the case of natural porous media such as soil, the complex mixture of materials and their tangled spatial structure means that only thin sections of material are directly comprehensible as transmission images. Yet thin sections are costly to prepare and may introduce errors through limitations in physical handling procedures. This is where tomographic imaging comes into play: by capturing a significant number of transmission images acquired at different angles, it is possible to *reconstruct* an estimate of the 3D volume containing the object. This is possible because each transmission image (commonly referred to as a "projection" in this context) contains information about the entire volume. In effect, each pixel of a transmission image is the "right hand side" of an equation describing the total attenuation of the X-ray beam over a linear path from source to detector. The "left hand side" of this equation is a series of terms describing the incremental attenuation of the X-ray beam along the part of this path which intersects the *reconstruction volume* i.e. the region of space that is subject to tomographic reconstruction.

By combining information from a sufficient number of projection images it is possible to determine a consistent solution for all "left hand side" terms, i.e. a very large set of simultaneous equations is solved. The accuracy of the solution is determined by the number of projection images and their definition in relation

to the definition of the reconstructed image. In other words a high definition reconstruction requires a large number of high definition input images. The angular separation of successive projection images is a key factor in determining the usable region of the reconstructed image. This can be understood by analogy: imagine the set of 2D projection images, oriented as they were captured relative to the sample, superimposed over the reconstructed volume images of the sample. In order for a reconstructed volume image element to be known reliably, it should have at least one 2D projection image element in close proximity to it, where close means lying within the separation between reconstructed image elements. Those reconstructed elements which do not meet this condition are defined via interpolation and hence they provide information with reduced spatial resolution.

The basic equation used in modelling X-ray attenuation is the Beer-Lambert law, an exponential decay model in which an initial intensity I_0 is reduced to I after travelling a distance x through a material having *attenuation coefficient* α:

$$I = I_0 e^{-\alpha x} \qquad \text{(equation 3.1)}$$

It is the attenuation coefficient that is determined by solving the system of equations described previously, the initial intensity and distance being known parameters of the imaging setup and the final intensity being measured by the X-ray detector. For certain materials in their pure form, attenuation coefficient values are well known. In fact for elemental material, the attenuation coefficient is related to the atomic number Z of that element (as this determines the

electron density). Given a homogeneous sample of known size, it is not difficult to determine the attenuation coefficient experimentally. When a sample consists of more than one material arranged in some structure however, it is necessary to subdivide space into discrete intervals along the path of the beam and then determine a value for the attenuation coefficient per interval. This is perhaps most clearly illustrated and understood when parallel projection of X-rays is employed (as is typically the case for a synchrotron X-ray source). In this case the reconstruction space corresponds directly to the 3D volume enclosing the sample and hence to the Cartesian grid of the reconstructed image. Each reconstructed image element then relates to a uniform interval along the beam for which the attenuation coefficient is estimated by the reconstruction algorithm. In this situation, the above equation decomposes into a product of terms corresponding to the image elements along a path:

$$I = I_0 \prod_{i=1,N} e^{-\alpha_i x_i} \Rightarrow I = I_0 e^{-\sum_{i=1,N} \alpha_i x_i} \qquad \text{(equation 3.2)}$$

The reconstruction volume may be interpreted as a sequence of slices, with each slice being divided into a lattice of points for which an attenuation coefficient is to be estimated. It is usual for the slice thickness and lattice spacing to be constant and equal over all slices i.e. a uniform subdivision is applied to the reconstruction space. Each slice of the reconstruction volume can therefore be treated as a separate 2D image, each such image being consistent with interpretation as a matrix of attenuation coefficients. Applying the above

equation to this matrix model, it can be seen that the projection image is formed as the *Hadamard* or element-wise product (Horn, 1994) of attenuation terms and equivalently as the element-wise sum of exponents. This leads directly to the mathematical form of the Radon transform (Johann Radon, 1917) and so each projection image captured on an X-ray detector is actually the Radon transform of the desired information. Consequently the process of tomographic reconstruction is concerned with finding the inverse Radon transform of the set of projection images. Unfortunately, this is a rather ill-conditioned problem when based on discretely sampled data which exhibits frequent large local variation (Berenstein, 1998). Consequently a robust practical implementation is more difficult to achieve in the case of geo-materials than in the case of a medical application, for example. A thorough treatment, from an engineering perspective, of the Radon transform and inverse methods is found occupying several chapters of the comprehensive work on tomography (Kak and Slaney, 1987).

In his development of commercial X-ray computed tomography, Godfrey Hounsfield (circa. 1971) devised a reconstruction method based on direct algebraic manipulation of the attenuation terms. This was a reinvention of earlier work (Kaczmarz, 1939) and this oversight was also made by (Oldendorf, 1961) in his experiments on computed tomography. Hounsfield was also unaware of work by (Cormack, 1963, 1964) who in turn had unwittingly reinvented much of the original 1917 work by Radon. It was this early work by Cormack (which went almost unnoticed for a decade), in conjunction with

Hounsfield's development of equipment, that led to the success of computed tomography.

3.1.2.1.Tomographic Reconstruction

The contribution of Cormack (1963, 1964) to computed tomography is noteworthy as this was the origin of the *filtered back-projection* reconstruction algorithm, a direct application of the inverse Radon transform in the spatial frequency domain or "inverse space". This distinguishes filtered back-projection (henceforth FBP) from the algebraic reconstruction technique (of Kaczmarz, Oldendorf and Hounsfield lineage) but the two ultimately achieve the same objective. By carrying out core computations in the frequency domain (i.e. using a spectral representation of images) FBP generally achieves better efficiency than the equivalent algebraic computation in the spatial domain. An additional computational cost of FBP (relative to algebraic methods) is in the need to apply the *discrete Fourier transform* to the projection images in order to obtain their spectral representation, and to apply the inverse transform following FBP so as to obtain the reconstructed spatial image. The cost of these transformations is high, but made tolerable by a family of efficient algorithms that have generically become known as the "Fast Fourier Transform" (henceforth FFT) originally devised by (Cooley & Tukey, 1965). The FFT is widely used in science and engineering, consequently very efficient versions have been developed to take advantage of both general purpose microprocessor hardware and more specialised devices such as the vector unit (VU), digital signal processor (DSP) and graphics processing unit (GPU). This latter form of device in particular has

made FBP practical for high definition images, using a relatively simple "brute force" algorithm.

The original FBP method of (Cormack, 1963) is limited to reconstructing images formed by parallel projection and this is still used when a parallel X-ray beam is practical to generate (e.g. in a synchrotron facility). The extension of FBP to a conical X-ray beam is due to (Feldkamp, 1984) and this, in conjunction with the flat panel detectors described previously, is the main factor in the wide availability of lab microtomography systems. Intermediate between parallel and cone beams is the fan beam which requires only a linear (rather than flat panel) detector. Although fan beam reconstruction can be exact (whereas Feldkamp FBP involves some approximation) the need for lateral as well as angular scanning of the sample tends to increase the duration of image capture while reducing accuracy, making the fan beam less practical for high definition microtomography.

Commercially oriented research and development has resulted in proprietary reconstruction algorithms that achieve very high performance. At the time of writing, the "state of the art" in FBP software is marketed by *Bronnikov Algorithms*, who claim better than two orders of magnitude performance improvement over widely used "brute force" FBP implementations. This is achieved via algebraic reformulation of the FBP problem (Bronnikov, 1999). Similarly, *Instarecon Inc.* have developed superior methods (Xia et al. 2004) and claim a performance improvement of one to two orders of magnitude.

Academic research into improved reconstruction methods is also on-going, for example the recently proposed hybrid algebraic/FBP method (Batenburg, 2012).

A problem specific to using FBP reconstruction is the presence of *ring artifacts* which as the name suggests, appear as annular distortions centred on the axis of tomographic reconstruction. Each such artifact stems from a defective element in the X-ray detector i.e. a "missing pixel" in the X-ray projection image. Data for these missing pixels must be provided (e.g. by interpolation) for the FBP algorithm and this leads to a small inconsistency over the series of angular projections. The same detector pixel is missing in each case but the beam trajectory through that pixel and it's neighbours sample is unique for each projected image, and so the interpolation varies. It is the interpretation of this inconsistent information within the frequency domain that leads to the presence of ring artifacts in the reconstructed image. The appearance of such artifacts can be reduced by re-projection of the spectral representation of the image, but this involves significant computational cost. This is one reason for renewed interest in algebraic reconstruction techniques, which, through operating in the spatial domain, permit a good deal of flexibility in accommodating problems of missing information.

3.1.2.2 Computed Tomography at the SIMBIOS Research Centre

The "CTPro" reconstruction software for Microsoft Windows used within SIMBIOS is provided by the manufacturer of the scanners used (XTek Systems Ltd.) and is of the GPU-accelerated "brute force" FBP type. This permits a smooth scan-and-reconstruct workflow as the data files containing scan settings integrate seamlessly with the reconstruction software. Making use of an alternate reconstruction application would likely require simple re-formatting of these data files but perhaps also more complex processing depending on the form of information required. For example the operator selects a noise reduction level which defines a window function for Fourier transformation and thus controls attenuation of information at higher spatial frequencies within the reconstructed image. This type of setting relates to proprietary equipment designs and software implementations, hence there is no guarantee of finding equivalent settings in alternative software.

The result of image reconstruction using CTPro is a pair of files, one is a binary data file having the file extension ".vol" containing the volume of attenuation coefficient estimates, the other has a ".vgi" file extension and contains an ASCII text description of the binary data. The data is organised as a single large array and the sample format (i.e. the binary encoding of numerical values for the per-voxel attenuation coefficient estimates) is IEEE-754 single precision floating point in little-endian byte order. Given a high definition image, the binary ".vol" data file tends to be extremely large and can readily exceed the maximum file size permitted by older (Windows-95 era) computer systems. This is a potential

hazard as many portable storage devices are factory formatted with the "FAT-32" file system, due to it being universally supported. This file system has a maximum file size of 2GBytes which in ".vol" file terms means that the maximum cubic image definition is 812 elements per axis (4 bytes per sample * 812^3 = 1.99GBytes). The reconstruction software unfortunately does not check for a compliant file system before writing huge files and this can lead to the storage device failing, with the loss of all data. It is therefore advisable to ensure that all storage devices are formatted with the "NTFS" file system which has been standard across the Microsoft product line since "Windows 2000". Support for this file system is available on a wide range of operating systems including Linux and Macintosh although extended features (e.g. file system level compression and encryption) are best avoided. The ".vol"/".vgi" file pair seems to be a simple data import method that is particular to the proprietary 3D image analysis package VGStudio (produced by Volume Graphics GmbH). It is undocumented but the ".vgi" file has a simple declarative form that is easy to interpret (basically a list of primitive symbol-value associations). However, using VGStudio to export data from a ".vol" file to a typical graphics file format requires a *transfer function* to be defined manually, leading to poor repeatability (Baveye et al. 2010) and doubtful consistency over a series of replicate samples. Consequently a robust automatic method was required to determine a suitable interval of attenuation coefficient values for mapping to the representation used within a graphics file. Once the interval limits have been determined, values within the interval are linearly mapped from floating point

representation to the target format e.g. unsigned 8 bit (which defines the whole numbers 0 to 255 inclusive).

3.2 Image File Extraction

At the outset of the project, a decision was made to develop software in C/C++ for the 32bit version of Windows XP (using Microsoft Visual Studio). This combination was widely supported and offered a reasonable balance of performance and flexibility at the expense of portability (for which Java might have been a better choice). The choice of a 32bit operating system restricts the memory available to a user *process* (i.e. an executing program) to less than 2GBytes. In practice, for 32bit Windows versions, a maximum of 1.7GBytes of data can be held in memory by each user process assuming sufficient physical RAM installed (the Microsoft implementation of virtual memory is of no benefit for this problem). Comparing this with the 9GByte size of a high definition reconstructed image, a file-based processing approach was obviously required for a 32bit program.

The software developed does not place any restrictions upon the target data representation but the file format does. In order to maximise portability between software applications the Windows "BMP" file format (version 4 or earlier) was chosen. The BMP file format does not directly support grey-scale images, but provides a colour-palette mode hence each file representing a grey-scale image is required to declare internally a linear grey-scale colour look-up table. This limits the intensity range to being represented by unsigned 8bit numbers which

have the advantage that they are compact and correspond directly to the display precision of computer graphics hardware (i.e. images can be displayed without a transfer function). Despite the author's misgivings about sacrificing half of the available information (the X-ray detector provides 16bit precision projection images) the visually apparent noise in a reconstructed image after mapping to 8bit precision suggests that the information contained in the discarded bits is of questionable value.

To avoid complicating subsequent interpretation and processing, a linear mapping is required for precision reduction. This mapping is defined by the selection of a domain interval (i.e. lower and upper attenuation coefficient values) while the range is obviously determined by the target format (0 to 255 inclusive for unsigned 8bit). The actual minimum and maximum attenuation coefficient values are not generally appropriate for mapping to a limited precision format owing to the very long "tails" that tend to occur in the distribution of reconstructed attenuation coefficient values. These extreme values are a consequence of noise and hence can be treated as statistical outliers. The outlier rejection procedure described in (Zar, 1984) is widely used in statistics and has been successfully applied to determine the domain for mapping. The information required for this procedure is the quartiles of the distribution in addition to an outlier scale parameter:

$$t_{\min} = q_1 - s(q_3 - q_1)$$
$$t_{\max} = q_3 + s(q_3 - q_1) \qquad \text{(equation3.3)}$$

The scale parameter ***s*** relates to particular scan and reconstruction settings and preferably a single value should be used throughout a given study. However, in cases where samples require individual acquisition settings, a single value might not be appropriate. The selection of an appropriate value for this parameter is discussed in some detail in chapter 6, where several values were assessed as part of a particular study. In general, a scale parameter value of 3 seems to produce reasonable results, but it may be advantageous to adjust this on the order of ±1 in individual cases.

The estimation of quartiles is complicated by the quantity of data (typically billions of image elements) meaning that a direct approach based on sorting is inappropriate. Instead it is necessary to estimate the quartiles from a histogram and this introduces another mapping problem relating to the definition of the histogram. Given that the reconstructed image is represented using floating point, it is not clear how to select an appropriate number of histogram bins, other than a sensible lower limit being 256 assuming an 8bit image is to be obtained. Varying the number of bins up to around 4000 alters the quartiles slightly but the resulting variant images are not easily distinguished from each other. As the number of bins is increased further the distribution of attenuation coefficient values tends to become "noisy" as depicted in figure 3.1 overleaf. This suggests that the reliable information content delivered by the imaging system is on the order of 12bits (i.e. 4096 grey levels).

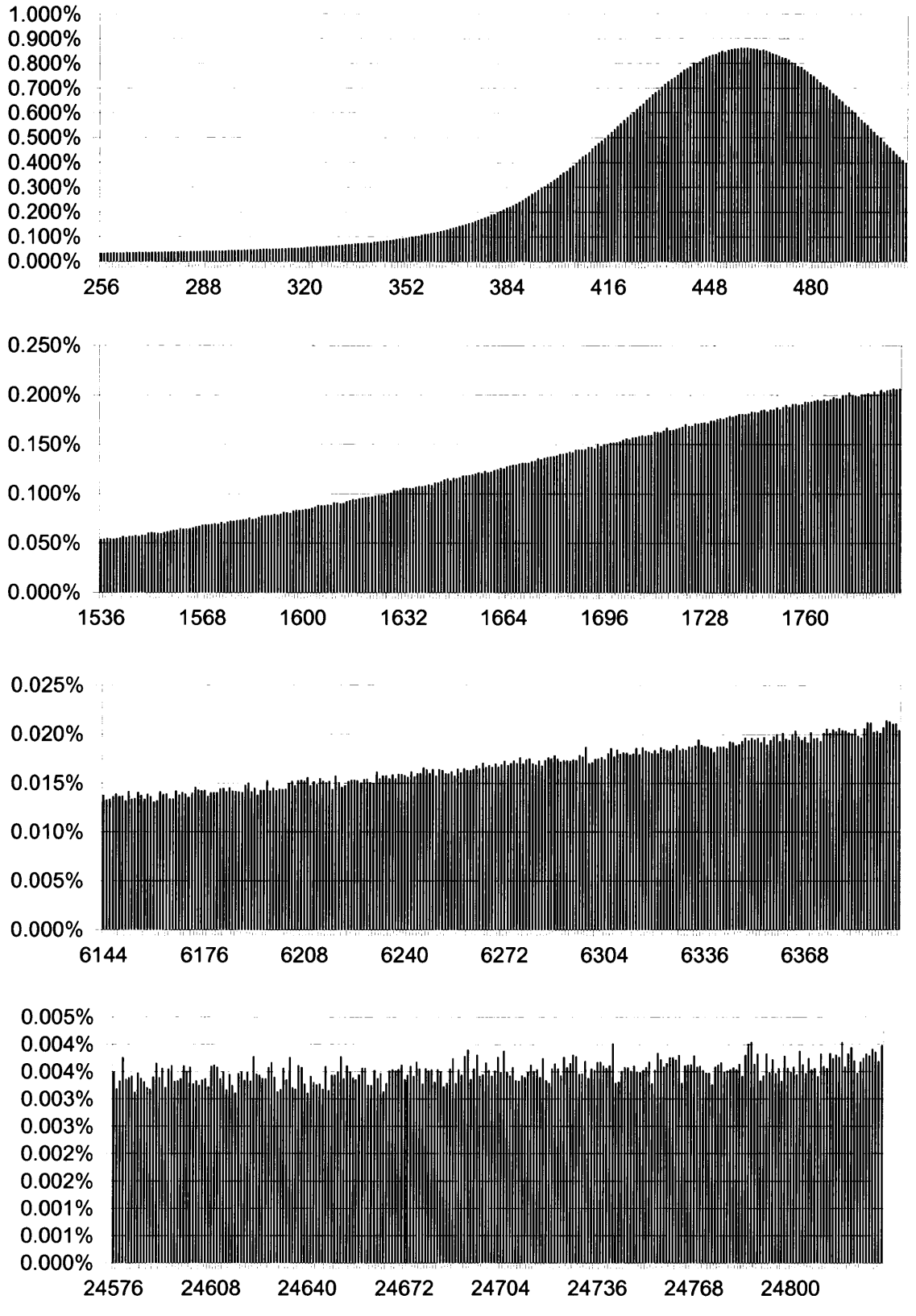

Figure 3.1 Increasing bin count for intensity histogram (PMF) of CT-image. (A subset of each histogram, 255 bins wide, is shown in each case for practical reasons.) Top is shown a subset of 1024 total bins, below this 4096 and 16384 then finally 65536 total bins in the lowest histogram.
From 4096 bins onwards a noisy character is increasingly apparent in the distribution, presumably a consequence of limited accuracy in the image acquisition process.

3.3 Image Quality Assessment

Following image acquisition, the next step is the assessment of image quality, with the objective of either accepting or rejecting the image for subsequent analysis. For a 2D image it may be immediately apparent to an observer that the image is defective in some way: the presence of anomalies, excessive noise or insufficiently distinct structure. This is more difficult in the case of a 3D image, as a 2D slice by slice inspection is extremely laborious, especially when repeated for each of the principal axes. Assessment based on some set of measures is therefore desirable and can help to reduce inconsistency resulting from a human operator (although a human operator is still required to identify large scale anomalies such as foreign bodies or ring artifacts).

Originating from analogue photography the terms *contrast*, *noise* and *sharpness* refer to image properties that are important with respect to human visual perception and cognition. Research on human visual perception has not yet progressed to the point where a comprehensive and robust model is available, hence there is no general agreement on the best way to compute such measures. For this project, readily available techniques in the area of image quality research were adapted to derive measures that facilitate relative (rather than absolute) assessment of soil image quality. That is, the measures allow comparison of the effect of processing options for a single physical sample, but cannot be used to compare different soil samples due to the lack of an absolute reference point within the measure formulation.

Examples of the application of image quality assessment measures to actual soil data are presented in chapter 7. In this chapter synthetic test images are used to demonstrate the relevance and effectiveness of each measure. The background theory and formulation for each is measure is first presented, followed by a description of the test data and finally results are presented then discussed.

3.3.1 Contrast

A measure of contrast describes the capacity for discrimination between objects of interest versus the background of the image. A series of mathematical formulations have been proposed to quantify image contrast based on ratios between differences in image intensity; based on the average, minimum and maximum of the grey-scale intensities (Peli, 1990). Due to their heterogeneous physical and chemical structure, the grey-scale intensities of soil images span a very wide range; typically the entire allowable range when unsigned 8-bit representation is selected. Therefore contrast measures based on the difference between the maximum and minimum of the grey-scale values are not appropriate, as one or two spatial locations that are extremely bright or dark can determine the contrast of the whole image. To overcome this problem, an alternative measure based on the standard deviation of the image is used. This measure is the Root Mean Square (RMS) contrast, and is simply defined as the standard deviation of the intensity distribution standardised according to the intensity range of this distribution. The RMS contrast measure has been used

previously in photographic imaging to compare between image samples of the same object (Peli, 1990).

$$C_{RMS} = \frac{\sigma_{image}}{\max(image) - \min(image)} \qquad \text{(equation 3.4)}$$

3.3.2 Noise

A noise measure describes the presence of unwanted information versus some desired signal. A precise identification of noise content therefore requires knowledge of the signal free from all noise i.e. a ground truth image. This is impossible in the case of X-ray CT images of soil due to the complex interaction between radiation and the heterogeneous distribution of elements. The unique structure of each soil sample yields a unique pattern of scattering noise with the consequence that the two (structure and noise) cannot be "untangled" by any method presently known. Discrimination between signal and noise must therefore be achieved by using the specific degree of spatial correlation within each image. A geostatistical measure such as the semivariogram has been argued in the past as being useful in addressing this problem (Atkinson et al. 2007).

An approach using the empirical semivariogram (as described in section 2.3) is adopted in this study to assess the noise content of soil images. The isotropic empirical semivariogram of the grey-scale image is computed using Matheron's estimator (Webster and Oliver, 2007). Comparison of the semivariogram value at a small lag distance with that at a large lag distance reflects the difference

between short and long range variability. Short-range variability includes noise induced during the image acquisition process as well as the variability inherent in the structure of the sample being imaged. At a range beyond the correlation length of induced noise, the significance of noise diminishes relative to true structural variability. In practice, the semivariogram is extremely computationally expensive to estimate at long range due to the large number of pairs of image elements that must be processed. To mitigate this problem, a lag distance cut-off is applied along with random sub-sampling of image elements which together can significantly reducing semivariogram computation time. These values are parameterised in the software implementation, with default values of 8 image elements as cutoff distance and a 5% rate for sub-sampling. These default values were determined through an assessment of soil images in which it was found that a distance of 8 image elements was significantly greater than the correlation length of unwanted noise. The sub-sampling ratio of 5% represents the smallest practical value before the accuracy of estimation starts to become an issue. This was determined by measuring asymmetry in the anisotropic semivariogram, at 1% sub-sampling for example the spatial variance for a lag vector and its opposite can differ significantly. The proposed measure for noise level quantification is as follows:

$$N_\gamma = \sqrt{\gamma(1) / \gamma(h_{cutoff})} \qquad \text{(equation 3.5)}$$

where $\gamma(h)$ is the value of the isotropic empirical semivariogram at lag distance h. The empirical semivariogram of a grey-scale image is based on a very large number of data pairs, hence the measure is statistically reliable.

3.3.3 Sharpness

The sharpness of an image is dictated by both the capture resolution, and by the focus quality of the imaging system as described by a Point Spread Function (PSF) which may vary spatially throughout an image. As a PSF is rather difficult to assess in the case of cone-beam tomographic reconstruction, an approach based on the analysis of spatial derivatives (Rudnaya and Ochshorn, 2011) was selected for sharpness measure estimation. Specifically, the gradient magnitude image is used to derive a measure of edge contrast amplitude. The gradient image is obtained by convolving the image of attenuation coefficient estimates with a 3D Sobel operator (Duda and Stork, 1973) defined on a 3^3 neighbourhood. The use of a Sobel operator is preferred over other gradient estimation operators, as it incorporates a degree of smoothing which helps to combat both noise and orientation sensitivity (Scharr, 2000). The weights used in the Sobel operator were obtained from the Euclidean distance between the estimation point and each of the data points used in the operator. The gradient itself is a vector quantity and its Euclidean magnitude is a scalar-valued image that can be visualised in the same fashion as the original intensity image: this is a simple form of edge detection. A sharpness measure can then be calculated as the mean value of the gradient magnitude image (Jarvis, 1976; Rudnaya and Ochshorn, 2011). However, this

measure is affected by the amplitude of image intensities, in the sense that a wide range of intensities will tend to give a larger value as compared to a narrow range. Therefore, to allow comparison over images that may differ with respect to intensity range, a standardising factor is introduced. The standard deviation of the original grey-scale image, being a measure of the dispersion in image intensity, is well suited to this purpose. The sharpness measure is therefore defined as:

$$S_G = \frac{mean(|grad(image)|)}{\sigma_{image}} \qquad \text{(equation 3.6)}$$

3.3.4 Materials and Methods

The construction of 2D test images begins as described in section 2.4 (a black circle occupying 25% of the image area against a white background). The image definition is 256^2 elements and the image elements are represented using floating point numbers, with the value zero assigned to black and one to white. A square Gaussian filter of radius 2 and standard deviation 0.75 image elements is applied to this image, softening the edges in a fashion that is consistent with the point spread function of an imaging system. This is the reference image shown along with its histogram and semivariogram in figure 3.1 following.

To the reference image of figure 3.1 are added two types of noise, each at two levels of intensity. Noise images were generated according to the methods described in section 2.4, i.e. uncorrelated noise in the first instance and spatially

correlated noise in the second. The measured statistical properties of the noise images are shown in table 3.1 overleaf.

The next step in generating test data was forming linear combinations of the base image with each of the noise images yielding two levels of each type of noise (20% and 40% additive noise in each case, relative to the base image at 100% weighting). Finally, the additive noise images were smoothed and blurred by applying a Gaussian filter (square, r=2, σ=0.75) to produce an additional four test images. The data in total was then 11 images: the reference, the two forms of noise alone, the four additive noise images and the four smoothed additive noise images. Following synthesis in floating point representation, the images were converted to unsigned 8bit format for use in assessing the quality measures.

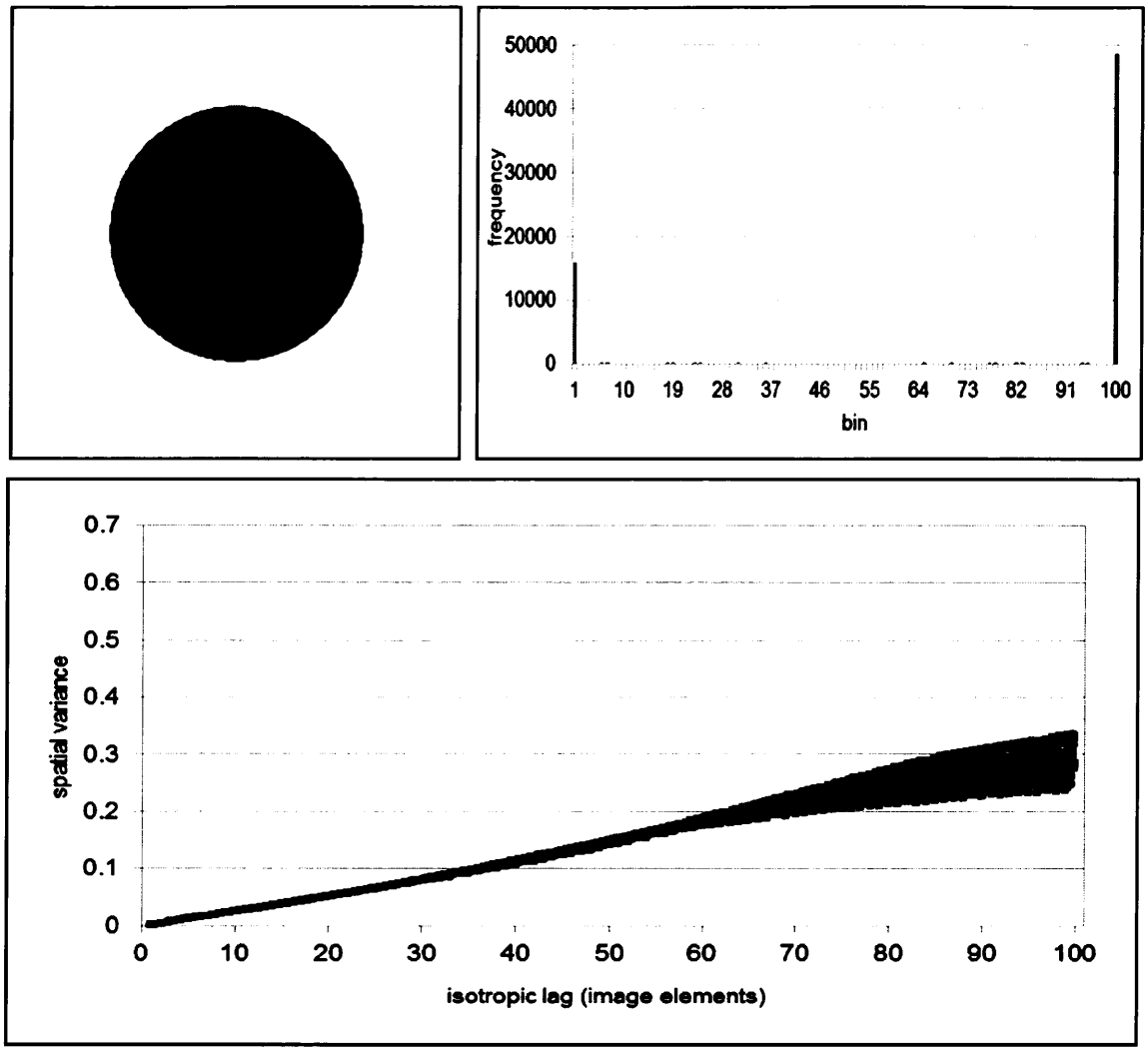

Figure 3.2 Test image A.
Reference image to which a Gaussian (r=2, σ=0.75) filter has been applied, simulating a Point Spread Function.

Noise	Min	Max	Mean	StDev
uncorrelated	-3.932	3.506	0	0.799
correlated	-3.249	3.08	0.002	0.757

Table 3.1 Noise image measured statistical properties.

The test images are labelled *A* through *K* respectively in figures and tables. Figures 3.2 to 3.9 on the pages following, show images *D* through *K* along with their histograms and semivariograms. The histograms depict the object and background populations or *modes* in the distribution of image element intensities. The degree of separation between these modes underlies the ability to discriminate between object and background in the images.

Semivariograms show the progression of disorder (i.e. decreasing correlation) with lag distance. The "nugget" of a semivariogram, which is the imagined intercept infinitesimally close to (but not on) the vertical axis of the semivariogram, indicates the lack of correlation at the smallest spatial scale. The smallest scale actually *measured* however is at a lag distance of one image element. Deducing a "nugget" requires a formal modelling approach followed by extrapolation and careful interpretation (Goovaerts, 1997).

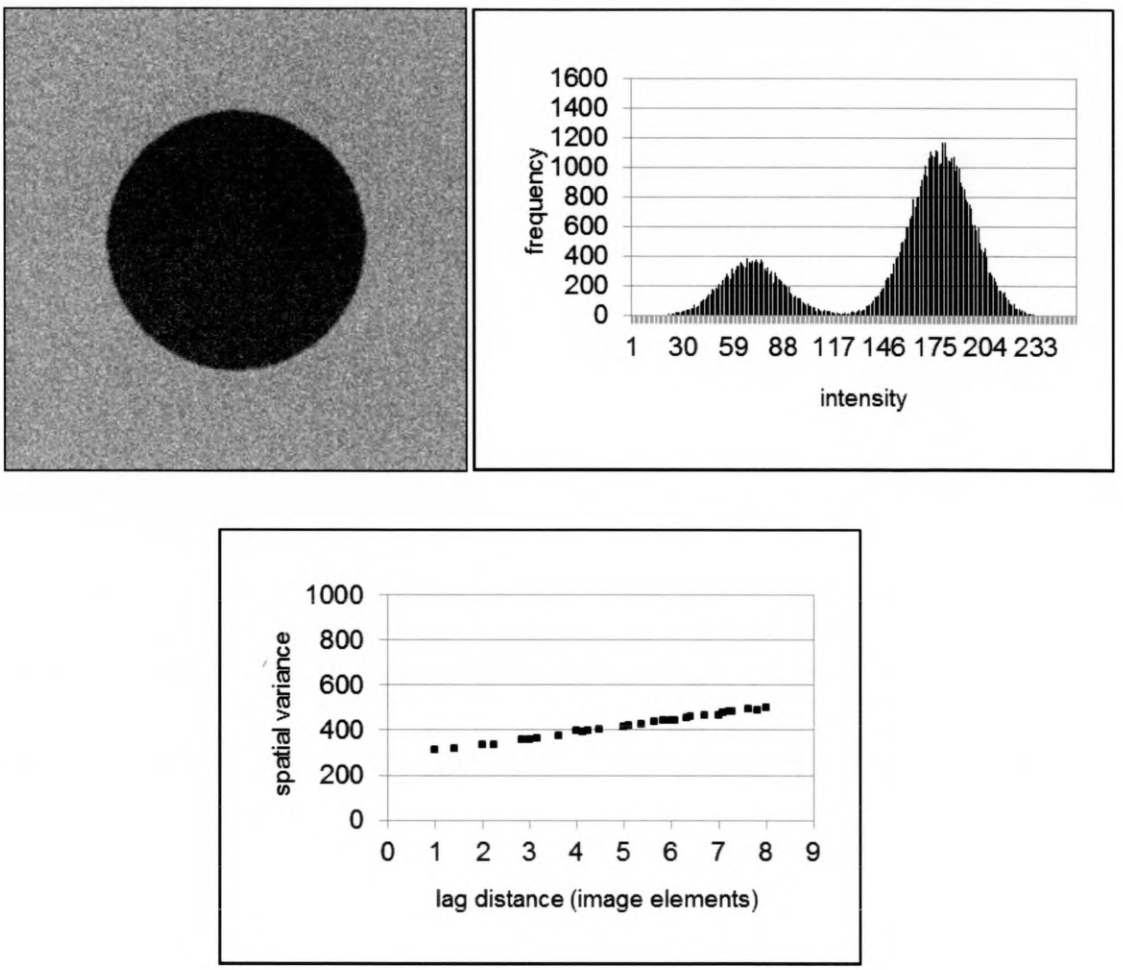

Figure 3.3 Test image D.
Contains 20% uncorrelated noise. Edges clearly visible but not especially sharp. Histogram mode separation suggests adequate contrast. Semivariogram shows gradual increase following significant "nugget" effect: there is limited correlation at minimum lag.

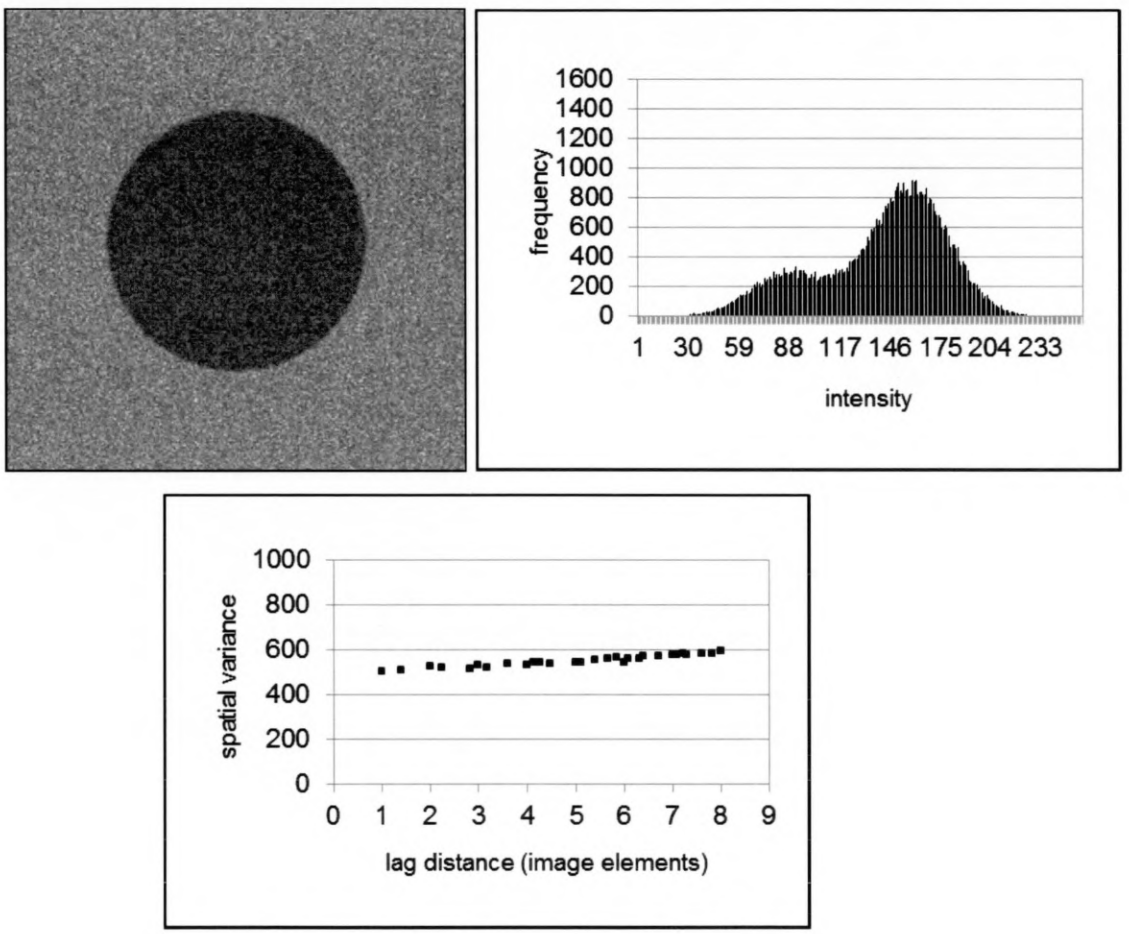

Figure 3.4 Test image E.
Contains 40% uncorrelated noise. Both edge definition and contrast very limited. Semivariogram shows little increase following large "nugget" effect: correlation at minimum lag is poor.

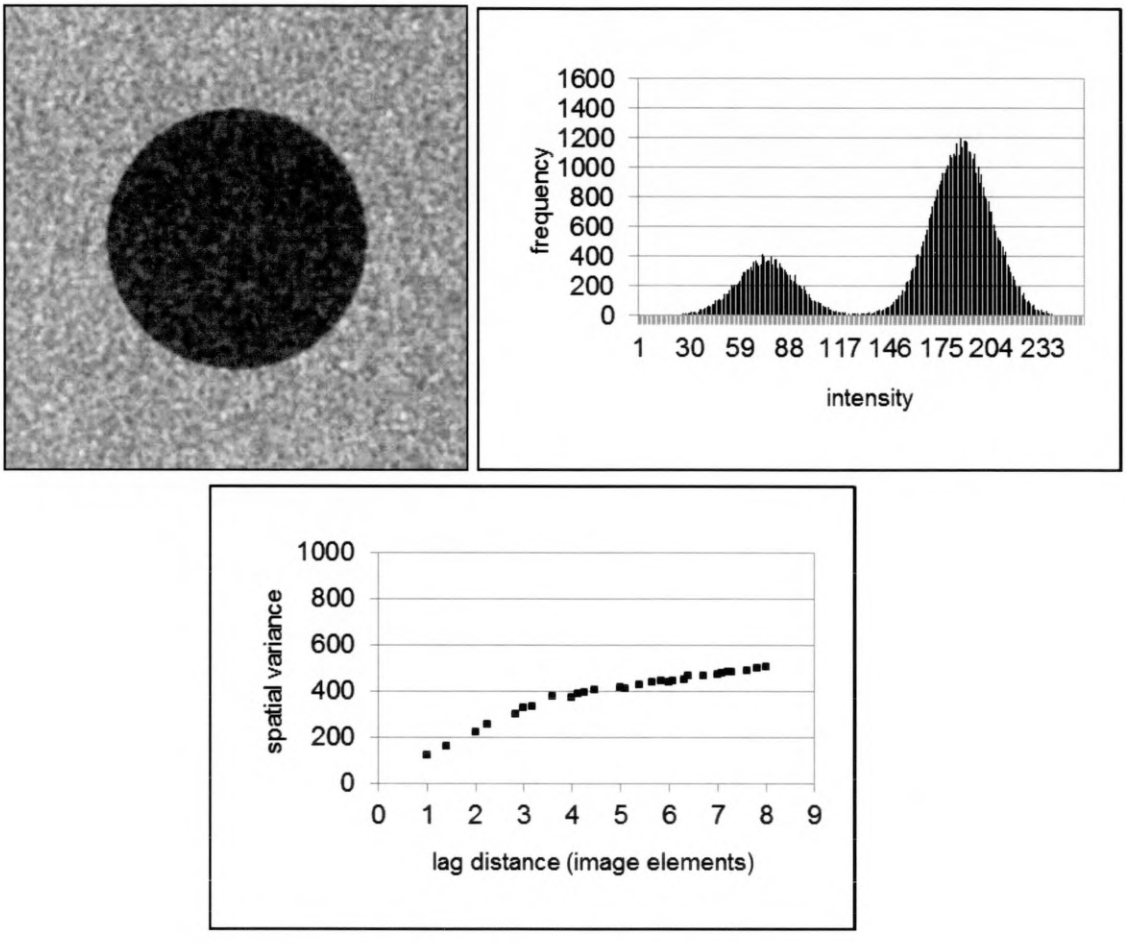

Figure 3.5 Test image F.
Contains 20% correlated noise. Histogram suggests adequate contrast. Edges disrupted in places. Semivariogram shows slight transition around lag 3.0, small "nugget" effect suggests good correlation at minimum lag.

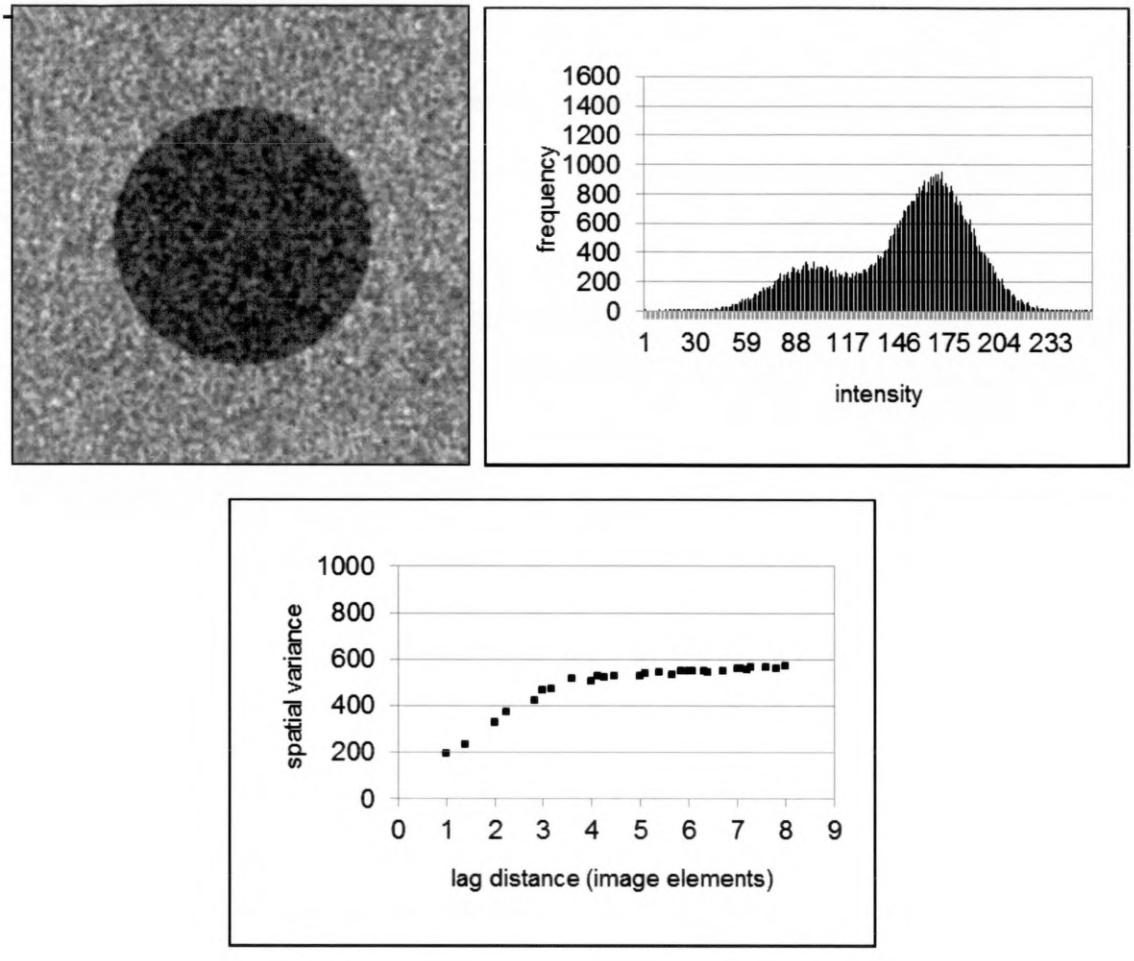

Figure 3.6 Test image G.
Contains 40% correlated noise. Contrast and edge definition notably impaired. Semivariogram shows significant transition beyond lag 3.0, moderate "nugget" effect suggests reasonably good correlation at minimum lag.

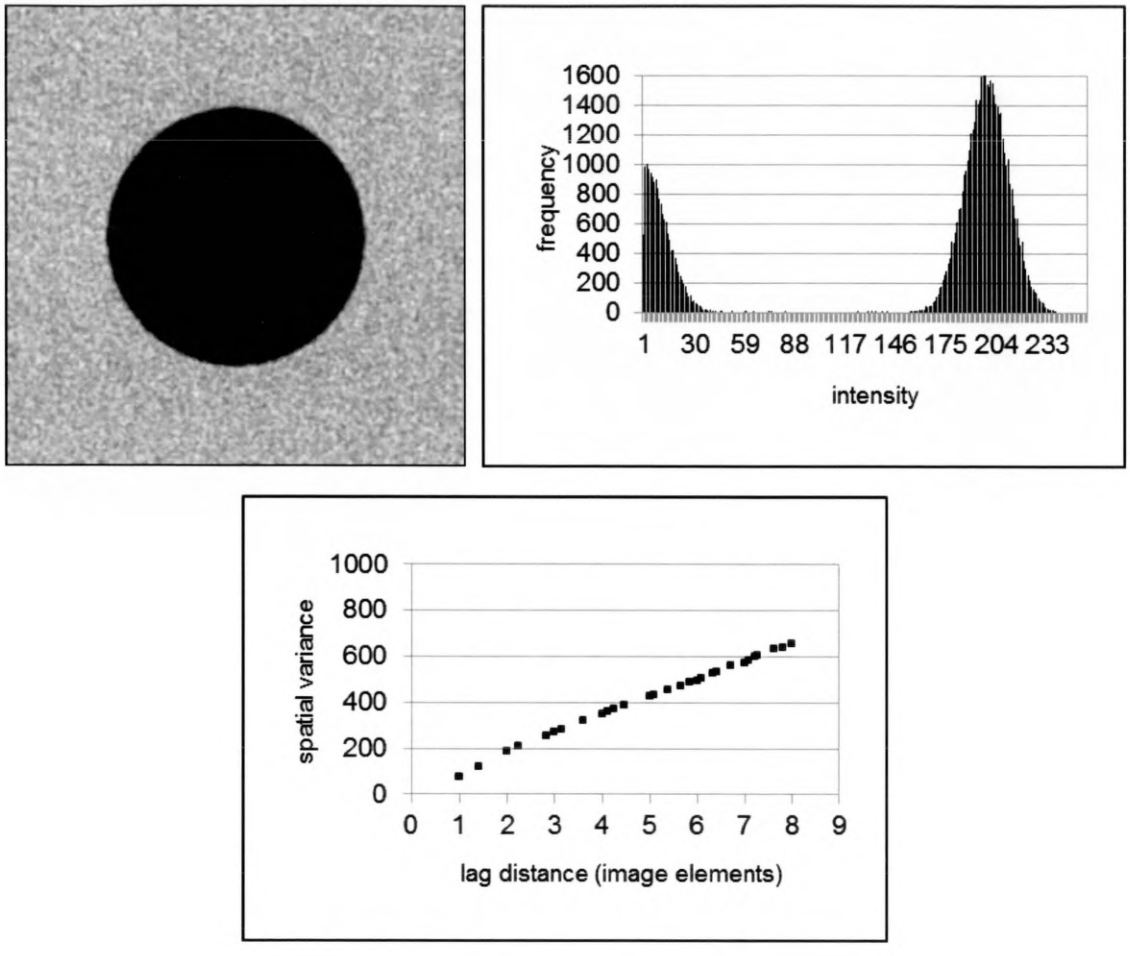

Figure 3.7 Test image H.
Gaussian filtered 20% uncorrelated noise. Mode separation on histogram suggests good contrast. Edge definition poor in image . Semivariogram shows very small "nugget" suggesting the image is well correlated at minimum lag.

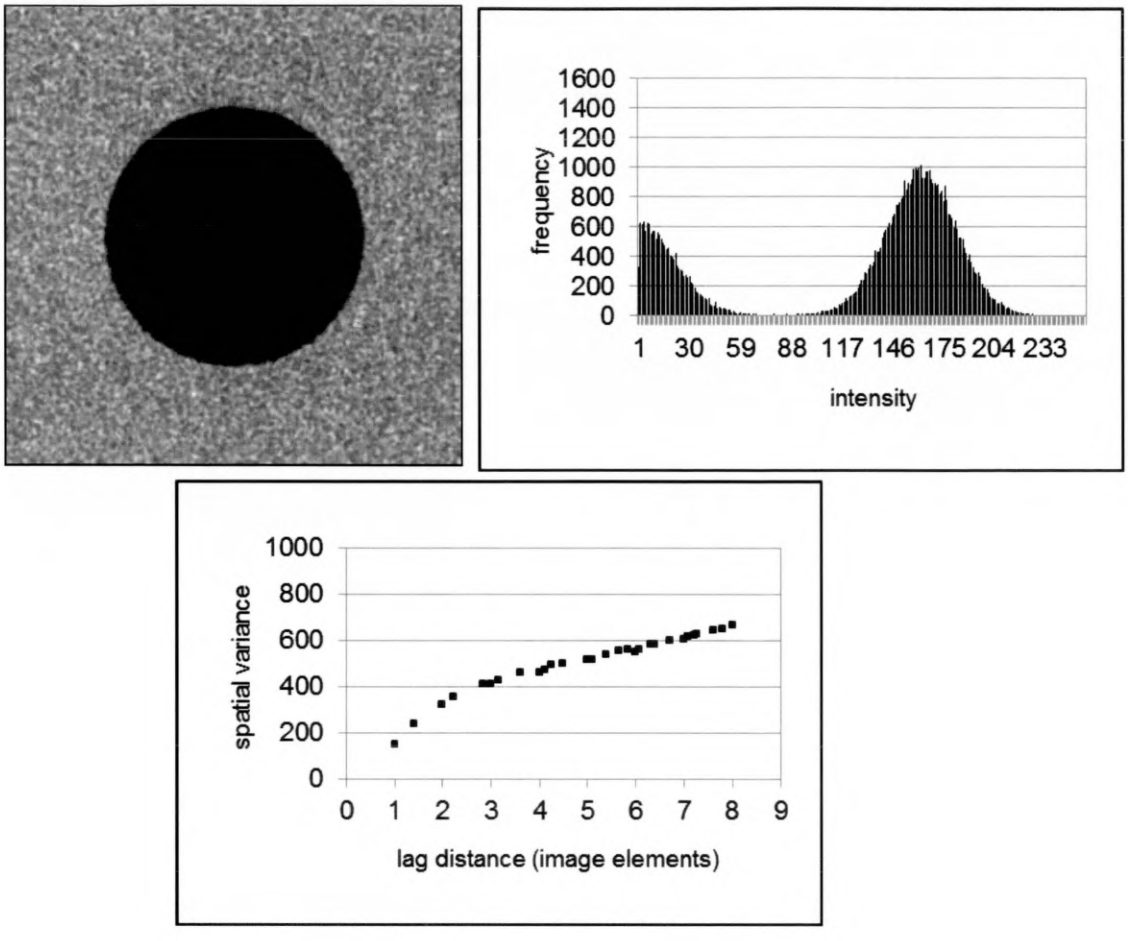

Figure 3.8 Test image I.
Gaussian filtered 40% uncorrelated noise. Contrast good but edge definition poor. Semivariogram shows noticeable transition beyond lag 2.0: limited "nugget" effect suggests significant correlation at minimum lag.

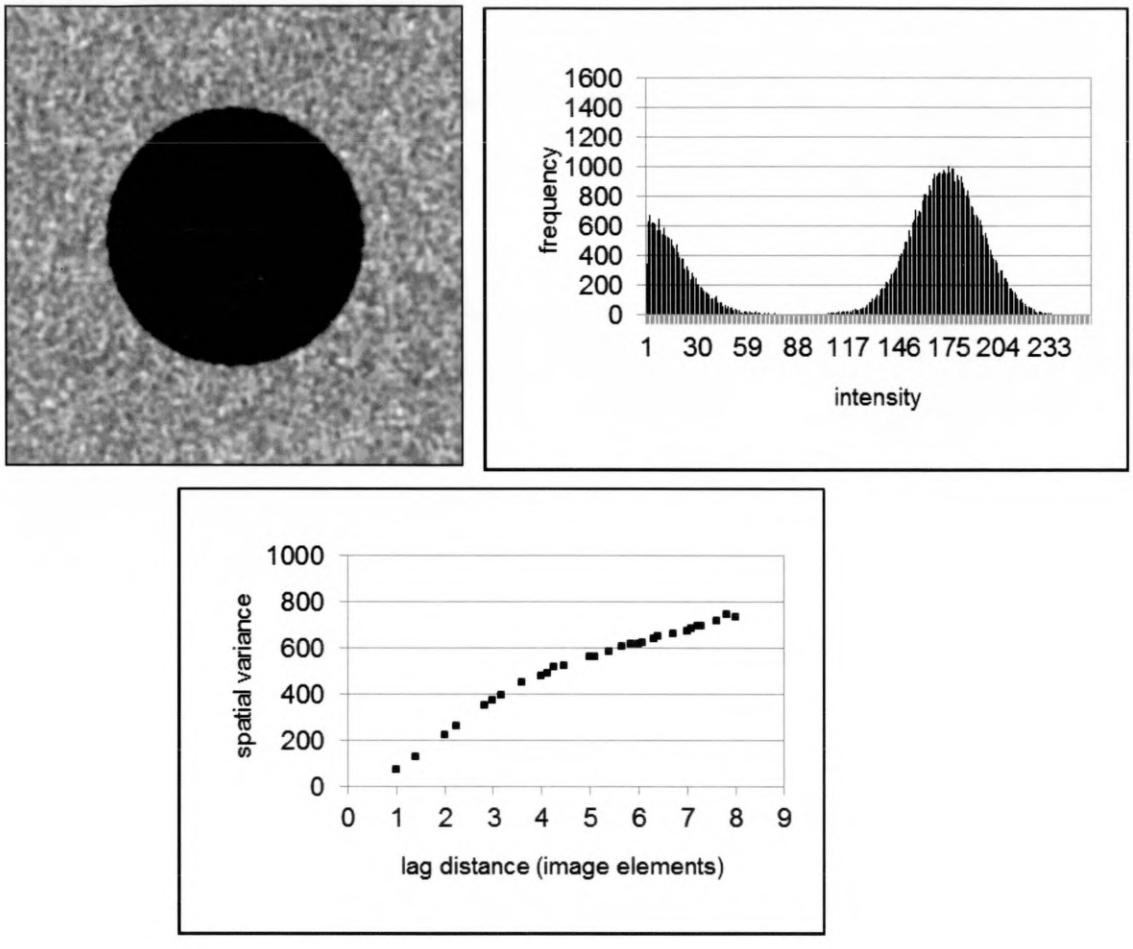

Figure 3.9 Test image J.
Gaussian filtered 20% correlated noise. Contrast good (histogram mode separation) but edges show poor definition. Semivariogram shows noticeable transition around lag 3.0, small "nugget" effect suggests good correlation at minimum lag.

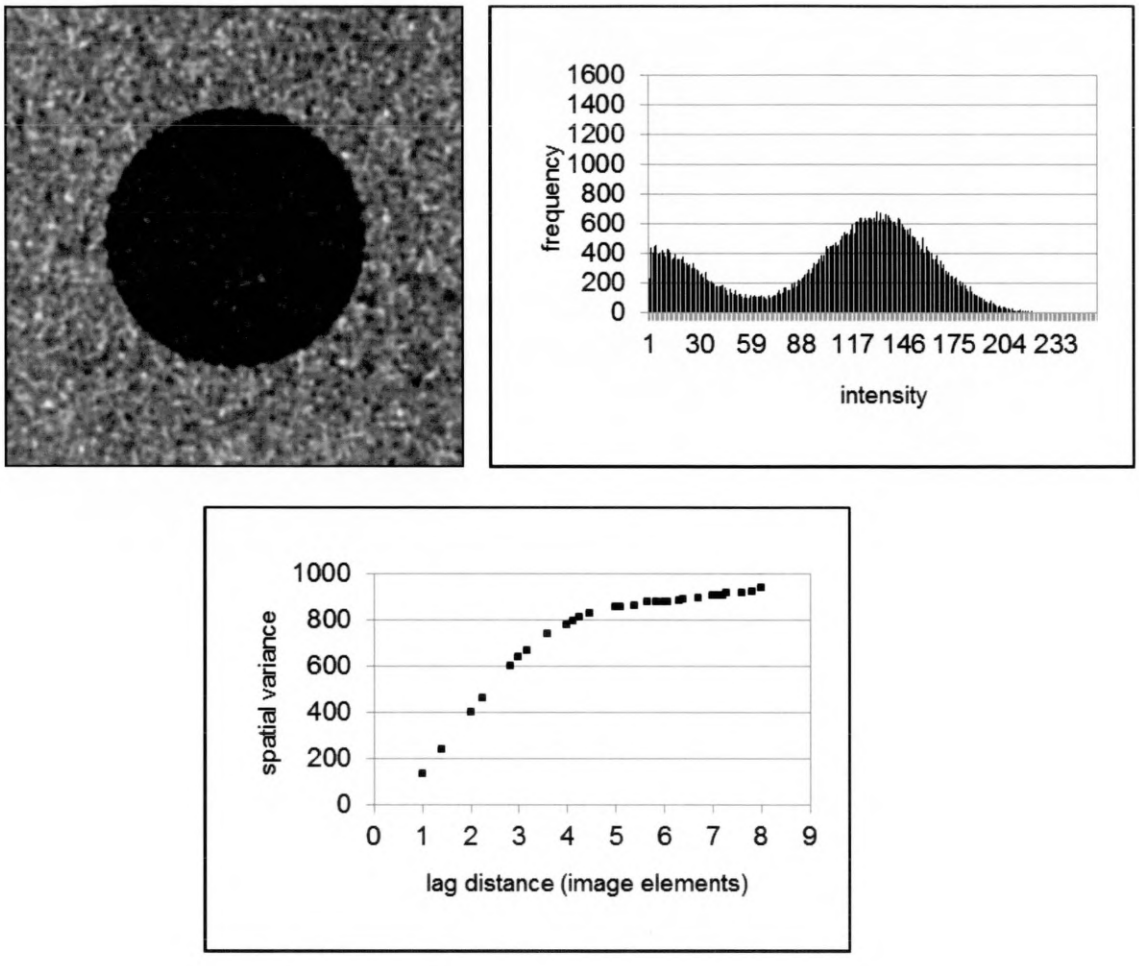

Figure 3.10 Test image K.
Gaussian filtered 40% correlated noise. Contrast limited. Edges disrupted. Semivariogram shows significant transition between lags 3.0 and 4.0, absence of "nugget" effect suggests perfect correlation at minimum lag.

3.3.5 Results and Discussion

For the unfiltered test images, the histograms shows that object and background are distinct at 20% noise content, but much more difficult to discriminate at 40% noise. Gaussian filtering significantly improves the ability to discriminate, such that all except 40% correlated noise (image *K*) exhibit very well separated histogram modes.

The semivariograms in the case of unfiltered and uncorrelated noise (images *D* and *E*) both exhibit simple linear patterns with the spatial variance at lag one being a good indicator of noise content. For correlated and unfiltered noise (images *F* and *G*) the semivariogram shows two consecutive linear patterns with the transition occurring between lag distances three and four. The first linear pattern identifies the correlation length of the noise, the second the object structure. Again, comparing the spatial variance at lag one gives a good indication of noise content when images *F* and *G* are considered alone. It is not however possible to compare between uncorrelated and correlated noise in this fashion due to the fundamental difference in variogram patterns between these two groups.

For the filtered images *H* through *K*, a degree of curvature becomes apparent in the semivariograms. This is only a faint suggestion for image *H*, but noticeable in image I and increasingly obvious in images *J* and *K*. This corresponds to the smooth spreading of noise induced by the Gaussian filter which softens the previously more abrupt changes in correlation structure. Despite this change in

pattern, consistency is however maintained in the interpretation of spatial variance at lag one. Comparing the semivariograms for the image series *D* through *G* versus the series *H* through *K*, it is seen that the relative ordering within each series is constant.

The image quality measures computed for images *A* through *K* are presented in table 3.2, below. The characteristics of each measure are discussed with reference to this table in the paragraphs following.

Image	Added Noise			Measures		
	Type	Level	Smoothing	Contrast	Noise	Sharpness
A				0.430	0.212	0.560
B	uncorrelated	100%	none	0.107	1.004	1.354
C	correlated	100%	none	0.120	0.617	1.058
D	uncorrelated	20%	none	0.197	0.791	0.706
E	uncorrelated	40%	none	0.147	0.919	0.895
F	correlated	20%	none	0.202	0.496	0.717
G	correlated	40%	none	0.150	0.578	0.918
H	uncorrelated	20%	Gaussian	0.320	0.336	0.631
I	uncorrelated	40%	Gaussian	0.256	0.471	0.589
J	correlated	20%	Gaussian	0.275	0.311	0.750
K	correlated	40%	Gaussian	0.211	0.378	0.556

Table 3.2 Results of quality assessment applied to test images.
Row A is the reference image, B and C are noise images, D through K are combined images.

The noise measure clearly indicates the relative content of a particular type of noise, but as previously stated, is not suitable for comparison between types of noise. The measure is lowest for the clean image *A* and greatest for image *B* (100% uncorrelated noise). Correlated noise consistently yields a smaller measure than uncorrelated noise due to the definition of the measure which

considers only the first and last spatial variance values. In order to correct for this it is necessary to either know in advance the correlation length of the noise or to deduce it from the semivariogram. If the measure were reformulated to consider the empirical spatial variance value at the correlation length rather than lag one, then a better measure would be obtained. This would however take advantage of prior knowledge regarding the correlation structure in the image. Without this knowledge, deducing the required information from a semivariogram such as that of test image *K* is difficult. Real CT images generally exhibit smoothly curving semivariograms and so detecting transitions in correlation length is impractical. For this reason the formulation of the noise measure (based on spatial variance at lag one) is appropriate as a measure of uncorrelated noise, but does not provide comprehensive information when correlated noise is present.

The sharpness measure performs adequately in yielding larger values for image series *D* through *G* versus the corresponding Gaussian blurred images *H* through *K*. It is however sensitive to the presence of noise as images *B* and *C* are assigned the largest values overall.

The contrast measure follows the interpretation of histogram mode separation discussed previously. Contrast is greatest for the almost perfectly bimodal image A and worst for the unimodal pure noise images *A* and *B*. Between these extremes contrast falls with increasing noise level but is regained to some

extent by filtering. The proposed measure is therefore an adequate measure of image contrast.

3.3.6 Conclusions

The presented quality assessment measures have been shown to provide appropriate information within certain constraints. The contrast measure is sensitive to the balance of light and dark populations in the image, e.g. test image *A* produces a value of 0.43 whereas if the populations were equal the maximum value of 0.5 would result. The noise measure is useful in the case of uncorrelated noise, but does not properly assess correlated noise and depends on the choice of cutoff lag for the semivariogram (which in practice is dictated by available computational capacity versus image size). The sharpness measure is significantly affected by the presence of noise and hence must be considered in conjunction with the noise measure.

These limitations, such as inter-dependance and sensitivity to population size, mean that the measures can only be used to compare images of the same physical sample. As the measures were designed to assist in determining appropriate image acquisition and reconstruction parameters for a given sample, these limitations do not restrict the intended use of the measures.

3.4 Summary

Acquisition of X-ray CT images involves tremendous underlying complexity, not all of which can be hidden from the operator. Obtaining images of good quality depends on an appreciation of many factors that influence the selection of imaging parameters. The use of objective measures for image quality assessment is important to reduce operator induced bias, but such measures can provide conflicting information that has to be interpreted appropriately. Image quality critically determines the useful information content that can be obtained in the subsequent analysis of structure. When an image of acceptable quality has been acquired, the next step is to classify each element of the image in the process generally known as image *segmentation*, the topic of the next chapter.

4.0 Image Segmentation

Segmentation is the process of classifying the elements of an image, in order to separate features of interest from background information. A set of adjacent image elements of the same class are considered to form an *object* (or a *segment* of a hierarchical object) within the image. Many forms of analysis subsequently rely on objects being defined in this fashion hence segmentation is an important step in the overall process of image analysis. By reducing a grey-scale image to an image containing few classes, the complexity of subsequent analysis is reduced, both in terms of the difficulty of implementation and also in the interpretation of results. Carrying out segmentation as a distinct step also has the advantage of allowing grey-scale and segmented images to be visually compared, hence problems may be detected which are difficult to identify by other means.

Although methods for the direct measurement of properties from a grey-scale image have been proposed, e.g. the tortuosity measure of (Gommes et al. 2009), such methods may be difficult to realise in practice. This is because forming a measure from a grey-scale image requires meaning to be deduced from grey levels and this implies that image contrast, noise content, and so on have been standardised in some manner. As concluded in section 3.4.4, it is difficult to achieve standardisation over a series of different samples and this fundamentally limits the relevance of grey-scale analysis.

Only grey-scale images are considered in the present context; this is not an intrinsic property of the problem domain but an artifact of the available image acquisition technology (as described in chapter 3). When the segmentation of a grey-scale image targets only two classes, then the process is called *dichotomization* or binary segmentation (e.g. pore versus solid). The dichotomisation of an image can be achieved using a vast repertoire of mathematical tools, used alone or in combination, and therefore selecting an appropriate method needs to be directed by the information content of the grey-scale image and also by a consideration of the type of analysis to be applied. Some segmentation algorithms are parameterised, allowing the operator to "fine-tune" their performance for a particular application. This however implies that the operator has either a sufficient (if not deep) understanding of the algorithm, so that reasoned choices can be made, or a willingness to engage in a manually-driven search process that may yield "surprising" results.

In the geo-sciences the term *thresholding* is frequently used in place of segmentation, whether from a desire for simple terminology or perhaps for historical reasons is unclear. In image analysis literature however the term thresholding carries with it an implication of simplistic approaches (Davies, 2005) that are of limited value when dealing with geo-materials.

During the course of this project, a number of image segmentation methods have been implemented in software and evaluated for use on soil images. Although many of the methods are well known (some are already included

within packages such as *ImageJ*) implementing them from first principles is instructive. The insight gained in this fashion allowed dramatic improvements in quality and efficiency to be made in at least one case (Houston et al, 2013). The segmentation methods are first described and then applied to a series of test images. The problems apparent in many of these images are discussed in relation to the segmentation algorithms. Finally recommendations are made regarding which methods might be useful for tomographic images.

4.1 Global Threshold Methods

Thresholding almost always refers to partitioning the image histogram into an upper and lower interval of intensity values, each interval denoting membership of a class. In other words, each image element is assigned class according to the result of a comparison with an intensity threshold value. The threshold is determined based on the entire image (typically the histogram alone is analysed) and it is applied over the entire image, thus the name global. In some cases a thresholding algorithm is more conveniently formulated in terms of the *Probability Mass Function* (henceforth PMF) rather than the histogram per se. The PMF is derived from the histogram by standardising each frequency relative to the sum of all frequencies; for this reason the PMF is sometimes also referred to as a “relative histogram”.

The application of a single threshold may be referred to in literature as "bi-level thresholding" (Zou et al. 2012), the term "level" in this case being used to mean class. This conflicts with the earlier definition in the context of image processing

(Stork and Duda, 1973) where *level* is used as a synonym of *threshold*. This original usage remains prevalent in the broader context of *level set* methods which are closely related to some image segmentation strategies (Beucher and Meyer, 1993). In order to avoid potential confusion, the term dichotomisation is preferred within this work.

A number of the thresholding methods described following make use of descriptive statistics defined on the image PMF. Shown below are probabilities p, means μ, and standard deviations σ defined in relation to a threshold t on a PMF. The PMF has n bins, each of which corresponds to a particular value of image intensity i. These statistical measures are used in several of the image thresholding methods presented in following sections.

$$p_0(t) = \sum_{i=0,t-1} PMF_i \qquad p_1(t) = \sum_{i=t,n-1} PMF_i$$

(equations 4.1(a) –(b)

$$\mu_0(t) = \sum_{i=0,t-1} i \cdot PMF_i \qquad \mu_1(t) = \sum_{i=t,n-1} i \cdot PMF_i$$

(equations 4.1(c) –(d))

$$\sigma_0(t) = \sqrt{\sum_{i=0,t-1} PMF_i (i - \mu_0(t))^2} \qquad \sigma_1(t) = \sqrt{\sum_{i=0,t-1} PMF_i (i - \mu_0(t))^2}$$

(equations 4.1(e) –(f))

4.1.1 Iterative Selection or Balanced Histogram (Ridler and Calvard)

Possibly the simplest method of determining an intensity threshold is due to (Ridler and Calvard, 1978). This finds the threshold which balances two assumed populations against each other, such that the average of their means lies exactly at the centre of the intensity domain. This is achieved very efficiently using a binary search and does not require the population distributions to have any particular shape. It does, however assume that the two populations do actually exist in a "well balanced" fashion such as might be expected in a typical photographic composition .

4.1.2 Minimum Intra-Class Variance (Otsu)

This method for computing an intensity threshold (Otsu, 1979) remains widely used due to it's relative simplicity. All possible global thresholds are evaluated using a discriminant function, a procedure that can be implemented very efficiently on the intensity histogram of an image. The discriminant function measures the inter-class variance of the two populations formed under each possible threshold. Maximising the inter-class variance is equivalent to minimising the intra-class variance of the two populations (but the former is more efficiently implemented). It therefore gives an optimal result in the sense of maximally separating the two populations, but does not account for overlap in their distributions. When the two populations have unequal variances or probability overlap, the model is biased, leading to a sub-optimal threshold.

$$f_{Otsu}(t) = p_0(t) \cdot p_1(t) \cdot \left(\mu_0(t) - \mu_1(t)\right)^2$$

$$t_{Otsu} = \arg\max_t \left(f_{Otsu}(t)\right) \qquad \text{(equations 4.2(a),(b))}$$

4.1.3 Entropy (Kapur, Sahoo and Wong)

The use of an entropy function to determine a threshold was first proposed by (Pun, 1980) and subsequently reformulated in (Kapur et al. 1985). This method evaluates all possible threshold values on the PMF of an image, choosing the maximum of the objective function. This function is based on the measure of information entropy defined by (Shannon, 1948) and so the PMF bins are interpreted as symbols comprising a message. The total entropy ***H*** of a sequence of image histogram bins is determined from the probability of occurrence of each:

$$H = -\sum_{i=1,n-1}\left(pmf_i \cdot \log(pmf_i)\right) \qquad \text{(equation 4.3)}$$

Given a threshold on the histogram, the entropy is calculated for both upper and lower partitions:

$$H_o(t) = -\sum_{i=1,t-1}\left(pmf_i \cdot \log(pmf_i)\right)$$

$$H_1(t) = -\sum_{i=t,n-1}\left(pmf_i \cdot \log(pmf_i)\right)$$

(equations 4.4(a),(b))

This information is used to form the objective function:

$$f_{KSW} = \log\left(p_0(t)\right) + \frac{H_0(t)}{p_0(t)} + \log\left(p_1(t)\right) + \frac{H_1(t)}{p_1(t)}$$

$$t_{KSW} = \arg\max_t\left(f_{KSW}(t)\right) \qquad \text{(equations 4.5(a),(b))}$$

4.1.4 Gaussian Mixture Model

In (Kittler and Illingworth, 1986) the computation of a minimum error threshold from a histogram that exhibits two normally distributed populations (i.e. a Gaussian mixture) is described. These authors also show that a criterion function can be defined to identify the optimal threshold without the need to model the shape of the histogram:

$$f_{KI}(t) = 1 + 2 \cdot \begin{pmatrix} p_0(t) \cdot \left(\log\left(\sigma_0(t)\right) - \log\left(p_0(t)\right)\right) + \\ p_1(t) \cdot \left(\log\left(\sigma_1(t)\right) - \log\left(p_1(t)\right)\right) \end{pmatrix}$$

$$t_{KI} = \arg\min_t \left(f_{KI}(t)\right) \qquad \text{(equations 4.6(a),(b))}$$

The Kittler & Illingworth criterion function is however approximate in that the component populations of the mixture are treated as being non-overlapping. An improvement of the method was proposed by (Cho et al. 1989), in which correcting for the biased variance estimates allows a threshold to be determined more robustly for overlapping populations. Despite the apparent simplicity of the theoretical approach, a properly robust implementation is made more difficult by the possibility that, dependant on histogram shape, the global minimum criterion value may not identify the optimal threshold. The minimum may occur at the limit of the histogram as part of a gradual "roll-off" and therefore more sophisticated analysis is required to detect the appropriate local minimum interior to the histogram. In cases where an internal minimum is absent, this indicates that the histogram is unimodal and therefore not suited to segmentation by this method.

Although the method is extensible to a histogram exhibiting more than two populations, the computational cost of identifying the optimal threshold between each adjacent pair rises combinatorially. Therefore simple linear search becomes less practical and the identification of appropriate local minima also becomes more complex.

4.1.5 Alternative Approaches to Gaussian Mixture Modelling

Preceding the use of a criterion function, (Chow and Kaneko, 1972) and (Nagawa and Rosenfeld ,1979) both describe the use of histogram shape modelling to determine the parameters of a two population Gaussian mixture model. The disadvantage of model fitting is of course the algorithmic complexity involved and depending on the method chosen and the context in which it is applied, computational cost might also be an issue. Both (Chow and Kaneko, 1972) and (Nagawa and Rosenfeld, 1979) methods were based on proprietary numerical algorithms encoded as firmware (i.e. microcode) of the IBM mainframe computers (e.g. S/360 series) that were used. Presumably these algorithms were variants of Newton's method and may have performed very well owing to their "industrial strength" implementation. To this day IBM continues to develop proprietary numerical algorithms in conjunction with Numerical Algorithms Group (NAG Ltd.) as a commercial enterprise. Such methods have not been replicated for this project due to the perceived difficulty of achieving a robust implementation and because simpler alternatives are available, as described next.

An alternative to the numerical analytic approach of estimating model parameters is the Expectation Maximisation (henceforth EM) algorithm proposed by (Dempster et al. 1977). This has proven to be a generally very attractive approach to fitting Gaussian mixtures as it can cope with complex problems i.e. any number of component populations in a space of multiple dimensions. Being a maximum likelihood search method, it is also to some extent robust with respect to noisy or incomplete data (Duda et al. 2001) and does not require any form of algorithm "tuning parameter". The result produced by EM is *unbiased maximum likelihood estimate* of model parameters, but, because EM is an iterative convergence approach, it is vulnerable to becoming trapped in local minima of the likelihood surface. Such local minima result from incomplete or conflicting information in the input data, which for the application considered here, means that the histogram does not match the expected pattern sufficiently well. This can occur when more than two populations are poorly separated on the histogram , or where one or more populations have a strongly skewed distribution. Preliminary pattern analysis of the histogram is required to address the first problem; by detecting the number of distinct modes present in the histogram, the correct number of mixture components and a suitable starting estimate can be chosen. The second problem requires a more sophisticated model formulation and this may lead in turn to the requirement for a parameter search method such as the Stochastic EM algorithm (Diebolt and Ip, 1994) in order to perform well.

4.1.6 Efficient Implementation of Objective Function Thresholds

Three of the methods described above (namely Otsu, Entropy and Kittler-Illingworth) operate by maximising or minimising an objective function calculated on the histogram. Naive implementations of these algorithms require $O(n^2)$ computations in the number of possible thresholds (i.e. histogram bins). This can be improved greatly by calculating the objective function for each successive bin using an incremental approach. In other words the descriptive statistics (or other numerical data) for each candidate threshold are adjusted by transferring the intensity and frequency information relating to a single histogram bin from the descriptive statistics of one class to the other. In this case the algorithm is O(n) and therefore can be easily applied to a histogram having a very large number of bins. This optimisation was previously "well known" in the form of an example algorithm for Otsu's method formerly available through *Wikipedia* (Wikimedia Foundation Inc). However no explanation or reference was presented, the technique merely existed within a fragment of C-language source code.

4.2 Local Segmentation Methods

The use of the term "local" in reference to an image segmentation method simply means that some form of information varying locally across the image has been taken into account. The extent to which this localises classification decisions can only be appreciated by understanding the details of the algorithm used. In general, global information is used in addition to local information to determine "local" classification criteria (such as intensity threshold values). This is typically beneficial as it ensures some level of consistency throughout the image whereas a "purely local" method is more vulnerable to irregularity or anomalous features within the image.

The previously discussed global thresholding methods can be localised by applying them to sub-regions of the image data so that many thresholds are computed throughout the image. In the case of a 2D image, this can be readily understood as producing a threshold surface which is subsequently applied to the image data. Each element of the image is then classified according to where its intensity lies in relation to the corresponding spatial location on the threshold surface. Extending this concept to 3D images results in a *threshold hyper-surface* (i.e. a volume of threshold data), which is applied in exactly the same spatial point-wise manner as for 2D images. If thresholds have been computed sparsely throughout the image then it is necessary to construct the continuous threshold surface from the sparse data by using some form of interpolation. On the other hand, if the data is dense then it may be desirable to apply some form of smoothing and so obtain a threshold surface having some degree of

continuity across the image. The main difficulty in this overall approach to localised thresholding lies firstly in deciding on appropriate parameter values such as the shape, size and spacing of sub-regions and secondly in choosing functions and parameters that achieve suitable interpolation and/or smoothing. These choices may strongly affect the computational cost and hence the applicability of such a method. The fundamental problem with this approach is the difficulty of deducing appropriate parameter values from the outset hence the user is faced with either accepting a "best guess" or conducting a parameter search (implying numerous trial segmentations) that may be extremely time consuming.

The problem of determining parameters can be neatly addressed by the "divide and conquer" strategy of *a-priori* classification. Even for images with very complex structure it is usually apparent to a human observer that within an image there exist regions representing a single class of object. If such regions can be classified by some relatively simple (perhaps global) method then two advantages are realised. Firstly, the workload has been reduced (perhaps significantly) at little computational cost; secondly, evidence is made available regarding at least part of the spatial structure of objects within the image and also how object structure relates to patterns of grey-scale intensity. The evidence gained in this fashion can then be used to construct a model, from which parameters are deduced so that the remainder of the image can be classified in a fashion consistent with this evidence. This approach, of course, trades one problem for another: the a-priori classification step influences

subsequent processing at a fundamental level hence inaccuracy in the preliminary stages may be disastrous. Manual labelling of exemplars is an obvious method of a-priori classification that remains at the core of some quite sophisticated methods (Berthod et al.1996) but the inevitable variability in human decision making means that segmentation results may not be reproducible. Perhaps the simplest objective method for obtaining an a-priori classification is to extend an existing thresholding method so as to obtain both an upper and a lower intensity threshold. This defines three intervals on the domain of image element intensities, a procedure often referred to as *hysteresis thresholding*. Any image element whose intensity lies within the hysteresis interval bounded by the two thresholds are labelled as unclassified whereas all other image elements are classified as object or background as appropriate. This approach is used in two of the local image segmentation methods described following; these differ mainly in their method of achieving a complete segmentation following a-priori classification but also incorporate some distinct methods of determining hysteresis thresholds.

4.2.1 Localised Otsu (Hapca et al.)

The method (Hapca et al. 2013) divides the image into a set of regularly spaced, uniformly sized and partly overlapping cubes. A histogram is computed for each cube and then Otsu's method is applied to each histogram, yielding a set of thresholds that each correspond spatially to the centre of their respective cube. These thresholds are smoothly interpolated to obtain a threshold hyper-surface which is then applied to the image yielding a candidate segmented image. A series of candidates is obtained by varying the size and spacing of cubes and each image is then assessed for accuracy of segmentation. The assessment is based on computing the intra-class variance of the grey scale image according to the classification of the segmented image. The segmented image yielding the minimum intra-class variance is selected as the result. This is inevitably a computationally intensive process as a large number of thresholds must be computed and then smoothly interpolated over the space of the image, this process being repeated a number of times. The use of Otsu's method guarantees that a threshold will be computed but this may be inappropriate within a local image region which has a unimodal distribution of intensity. Suppression of such "erroneous" local thresholds depends upon sufficient global smoothness of the interpolation function which therefore is formulated in terms of all thresholds within the image.

4.2.2 Gradient Masks (Schleuter, Weller and Vogel)

This method is described in (Schleuter et al. 2010) as being specifically designed for soil and extends earlier work (Vogel and Kretzschmar, 1996). In the earlier work a hysteresis threshold interval was defined manually by an operator, the deficiencies inherent in this approach are addressed in the 2010 work which proposes an automatic method. Both original and extended methods make use of a region growing approach to complete segmentation following a-priori classification. Region growing is an iterative strategy that relies on convergence towards a solution in which each image element is classified exactly once, with class being determined as a function of prior classifications in the local neighbourhood. The region growing procedure is discussed in more detail following the explanation of the method for determining the hysteresis threshold. As a step preliminary to the segmentation algorithm proper, (Schleuter et al. 2010) suggests that a filter such as the pseudo-median should be applied in order to suppress impulse noise within the image, without distorting edges. The resulting smoothed intensity image is used within all subsequent steps of segmentation, the unfiltered image is not used further. The details of the pseudo-median filter have been discussed in section 2.2.1.

In (Schleuter et al. 2010) the first step is the identification of image elements that belong to the solid-pore interface (henceforth referred to as boundary elements). This is achieved by first computing estimates of both first and second order non-directional local spatial derivatives over the grey-scale intensity image. This results in two discrete scalar fields (henceforth referred to

as *derivative images*) each of whose elements has a one-to-one correspondence with the elements of the intensity image. For each derivative image, the distribution of derivative values is analysed to deduce a threshold on that image. Each derivative threshold, applied to the corresponding derivative image, identifies those spatial locations where changes in intensity are significant. This is the origin of the term "gradient mask" used in the title of the work: a Boolean valued mask image is computed by thresholding a spatial derivative image. Such a mask image is also known as an *edge map* in cases where spatial derivatives are used for edge detection (Weska et al. 1974). Derivative estimates of both first and second order are used to obtain a sufficiently broad identification of boundary elements: within a boundary region either the first spatial derivative (the gradient magnitude) or the second (the absolute Laplacian) may have a comparatively large magnitude, but not both simultaneously. For an image consisting of exactly two distinct material phases (and each phase being internally homogenous) the procedure described so far is sufficient to identify the interface between these two phases. For CT images of soil, on the other hand, the solid phase is typically heterogeneous (mineral grains versus soil aggregates, for example) and so many interfaces can be detected within what is ultimately interpreted as solid material. In order to restrict boundary identification to the pore-solid interface, Schleuter et al. take the grey-scale intensity of image elements into account, rejecting boundary membership for any element whose intensity lies above that of the dominant mode of the intensity histogram. Having identified solid-pore boundaries within the image, the upper hysteresis threshold is then computed from the grey-scale

intensity of boundary elements. In (Schleuter et al. 2010) the upper hystersis threshold is obtained by computing the mean intensity separately for the first and second derivative mask images and then taking a simple (unweighted) average of the two. The lower hysteresis threshold is calculated using the upper threshold and the intensity mode as reference points, extrapolating to lower intensity using a ratio for which a value of 1.85 is suggested .

4.2.2.1 Gradient Masks Implementation

This segmentation method was implemented in the first instance from the description within the publication (Schleuter et al. 2010). Some issues were resolved by contacting the original author who provided additional information and helped verify the accuracy of results.

4.2.2.2 Computation and Analysis of Spatial Derivatives

A Sobel operator was used to estimate the first derivative (vector gradient) from which the Euclidean magnitude of the gradient was calculated. A Laplacian of Gaussian operator was used to estimate the second derivative. These operators are commonly implemented in the form of 3^3 element convolution kernels i.e. one can imagine forming around the estimation point a cube that touches each of the 26 nearest neighbours in 3D. Each neighbour can then be classed as a face, edge or vertex accordingly. The weights used for these operators, as recommended by Schleuter (personal communication, 2012) are as shown in the table 4.1 overleaf.

In the implementation presented here, the derivatives are stored in unsigned 8bit representation. This was selected as it is both more compact and simplifies subsequent handling compared to floating point representation. The actual computation is carried out using double precision floating point numbers which simplifies implementation (versus a fixed-point algorithm) at the expense of some computational performance. A scaling factor is applied to the computed derivatives based on the domain values of the grey-scale image so as to achieve a well defined shape in the distribution of the derivatives in 8bit representation. In the case where the input domain matches the derivative range (0 to 255 inclusive) the scaling factor is unity. The output from a filtering operation is always explicitly constrained to the target range to avoid the possibility of overflow causing values to "wrap around" between the limits of the numerical representation.

Filter	Centre	Face	Edge	Vertex
Sobel		1.732	1.225	1
Laplacian	-1	0.05234	0.03702	0.03021

Table 4.1 Filter coefficients for 3D spatial derivatives.

Once a derivative image has been estimated its histogram is calculated (a trivial operation for derivatives represented in unsigned 8bit form) and then subjected to shape analysis. The objective is to locate the high valued “knee” of the derivative distribution which marks a transition from the low-moderate derivative values typical of the majority of image elements to high values that hopefully

identify material interfaces. The "unimodal thresholding" method of (Rosin, 2001) is used for this purpose; this is essentially a triangulation between the mode of a distribution, it's upper continuous limit and the "knee" or "corner" formed between the two. The derivative value at the "knee" is then used as a threshold on the derivative image which identifies interface elements within the intensity image. This is a pragmatic approach to finding the threshold which works well in many cases but is potentially vulnerable to irregularity in the shape of the distribution. More recent work by (Coudray & Buessler, 2010) aims to achieve a robust estimate of the transition point through fitting a model to the histogram shape and therefore reducing sensitivity to phenomena such as outlying peaks. Only the (Rosin, 2001) method is implemented at present and has so far worked satisfactorily, perhaps due to the combination of noise reduction filtering and smoothed derivative estimates. However the possibility that some derivative images with "anomalously" shaped distributions might cause the method to fail cannot be ruled out.

4.2.2.3 Region Growing

In the case of the algorithm actually implemented, the classification rule is based on previously classified image elements, with only the pore versus solid labelling being taken into consideration, i.e. grey-scale information is ignored. A threshold on the proportion of pore versus solid elements is used, this information being determined for the local neighbourhood of each unclassified image element. A threshold value of 50% on the pore-solid proportion is obviously an unbiased choice but leads to a "stalemate" in cases where the

local evidence for both classes is equal. A biased threshold can resolve this problem but leads to a segmented image in which the bias can be obvious both visually and in terms of measures obtained subsequently. For this reason a "tiered" classification rule was implemented such that unbiased decisions are sought initially but, if classification cannot be completed under these conditions then progressively less strict conditions are applied. Parameterisation of these classification tiers using ID numbers is convenient in allowing the effect of different strategies to be studied. The transition between rule tiers occurs only following an image traversal in which no classifications were made and is not reversible (i.e. progress is monotonic from strict to lax criteria). The tiers were implemented as described in table 4.2 (overleaf).

As suggested previously, including $ID=1$ is essential to allow full classification in all cases. Including $ID \geq 2$ increases computational cost somewhat but this is judged to be a good compromise in order to obtain more rigorous evidence.

ID	name	pore condition	solid condition
4	strict majority	pore > (solid + unclassified)	solid > (pore + unclassified)
3	weak majority	pore > solid	solid > pore
2	default pore majority	pore >= solid	solid > pore
1	any pore connection	pore > 0	pore <= 0
0	all pore	always	never

Table 4.2 Internal parameters of region growing.

With any iteratively applied state dependant image modification, a mechanism such as image double buffering is required to ensure that decisions are not affected by image traversal order. All decisions are made based on the contents of the source image buffer, while results are written to a destination buffer; at the end of a traversal (pass or iteration) the roles of source and destination are swapped. This technique temporarily doubles the image storage requirement, which for high definition images can be problematic. Furthermore the processing cost is also high as many traversals of the entire image (both buffers) may be required (the number of passes is also likely to increase with image definition). A significant improvement can be realised by taking advantage of the fact that a smaller and smaller proportion of the image is updated within each subsequent iteration (i.e. as the image converges toward the final solution). Thus it becomes increasingly attractive to maintain a list of unclassified point coordinates so that only those parts of the image that require

update are visited in each traversal. By storing the results of classification decisions also in the list, only a single image buffer, updated with new classifications at the end of each traversal, is required. In the form currently implemented, the list processing mechanism is applied from the first pass onward with the ability to revert to buffer based processing should list storage be inadequate (the cost per element of list storage being eight times the storage cost of an image element). This results in somewhat slower progress over the first few iterations (memory access being the limiting factor on performance) but soon yields substantial performance benefits to the extent that the last few iterations are almost instantaneous from a human operators perspective.

4.2.3 Indicator Kriging (Oh and Lindquist)

Image thresholding by indicator kriging as described in (Oh and Lindquist, 1999) is a *geostatistical* method for estimating class membership of image elements in a minimum spatial variance fashion. The method relies on *a-Priori* classification of the image via a hysteresis threshold. The resulting partially classified image is subjected to majority filtering as a non-linear form of noise reduction. From this filtered image a set of indicator data points is obtained i.e. one per a-priori classified image element. The spatial variance in this indicator data is then captured in the form of an indicator semivariogram which is used as a model in resolving the remainder of image element classifications by ordinary indicator kriging. Ordinary kriging allows a variable to be interpolated within a field that may have a non-stationary mean, and hence is appropriate for images of heterogeneous materials. Following classification by kriging, another pass of majority filtering is applied to rectify any isolated misclassification of image elements.

4.2.3.1 Indicator Kriging Implementation

This segmentation method is implemented from an interpretation of the original publication (Oh and Lindquist, 1999) only. As of 2011, the *3DMA* analysis package (Lindquist et al. 2005) which contained the original implementation of the indicator kriging method was placed under the control of a commercial organisation. The previous (freely available) software was withdrawn along with all support at that point in time. The original publication presents a geostatistical approach to image segmentation, but does not comprehensively address the

implementation issues. The three principal stages of processing are briefly summarised in the following sub-sections, with more detail provided in cases where the original publication was unclear.

4.2.3.2 A-Priori Classification

The objective of a-priori classification is to obtain a representative sample of the spatial distribution of the two classes of image elements; this information therefore influences the overall segmentation result at a fundamental level. In (Oh and Lindquist, 1999) two suggestions are given for automatically determining the hysteresis interval from the intensity histogram of an image. The first is based on the Kapur entropy function which has here been described previously (in section 4.1.3). An operator defined ratio is then used to select thresholds either side of the maximum entropy. The second method involves fitting a bi-normal model using the Expectation Maximization algorithm (as described in section 4.1.4) in which case thresholds are obtained relative to the means of the two populations. It is the EM approach that is applied in the evaluation of methods presented section 4.3, following. Applying the hysteresis threshold to the image results in a partially classified image which then undergoes a majority filter (described in section 2.2.1) using a 60% majority parameter to remove isolated misclassifications (assumed to be noise). This particular instance of the filter is asymmetric in permitting a-priori classifications to be reversed i.e. an element classified as pore or solid may become unclassified, but forbids any change to unclassified elements.

4.2.3.3 Spatial Variance Model

Spatial variability is described in (Oh and Lindquist, 1999) in terms of covariance but a more common approach in geostatistics uses the semivariogram as described in section 2.3. More correctly this is referred to in

the present context as an *empirical indicator semivariogram* as it is determined by experiment from indicator data points. A generally accepted convention in geostatistics is that an *authorised model semivariogram* should be derived from the empirical semivariogram (Goovaerts, 1997) so as to ensure reliable mathematical properties. This is not discussed by (Oh and Lindquist, 1999) and it is not clear whether these authors implemented a modelling approach in their own software. Rather than risk problems arising from a defective description of spatial variance, only authorised model semivariograms are applied in the work presented here. The simulated annealing approach of (Lark and Papritz, 2003) is used to search the parameter space for each candidate model type. This approach is selected over other numerical methods because it is independent of algebraic form (i.e. no knowledge of model properties or "patterns" is required) and facilitates the constraint of parameter values e.g. ensuring a positive "nugget". The types of authorised indicator semivariogram model presently supported are the isotropic forms of spherical, exponential and Gaussian models as defined in (Goovaerts, 1997). In order to ensure a good model fit at short lag distances, the iterative refinement approach of (Webster and Oliver, 2009) is applied, which requires a weighting for each empirical datum to be defined based on modelled as well as empirical data. This means that an initial estimate of the model is first obtained using only the standard weighting (the number of observation pairs contributing to each datum). Simulated annealing is then repeated following the refinement of weights until model parameter estimates converge.

4.2.3.4 Ordinary Indicator Kriging

Based on a set of indicator data points in the vicinity of an unclassified image element (the estimation point), the spatial variance relationships between data points and estimation point are represented using a system of constrained linear equations known as the *ordinary kriging system*. The ordinary kriging system describes the local spatial correlation structure of pore versus solid elements and its solution yields a minimum variance estimate of class membership probability. Hence the previously unclassified image element is assigned membership of the most probable class. Formulated in terms of the semivariogram, the ordinary kriging system of equations including a Lagrangian constraint is explicitly stated as follows:

$$\begin{vmatrix} 0 & \gamma_{2,1} & \cdots & \gamma_{1,n} & 1 \\ \gamma_{1,2} & 0 & \cdots & \gamma_{2,n} & 1 \\ \vdots & \vdots & \ddots & \vdots & \vdots \\ \gamma_{n,1} & \gamma_{n,2} & \cdots & 0 & 1 \\ 1 & 1 & \cdots & 1 & 1 \end{vmatrix} \cdot \begin{vmatrix} \lambda_1 \\ \lambda_2 \\ \vdots \\ \lambda_n \\ \mu \end{vmatrix} = \begin{vmatrix} \gamma_{0,1} \\ \gamma_{0,2} \\ \vdots \\ \gamma_{0,n} \\ 1 \end{vmatrix}$$

(equation 4.7)

Where for known data points ***a*** and ***b*** the spatial variance between the two is given as $\gamma_{a,b}$ (and symmetrically $\gamma_{b,a}$) within the matrix. The spatial variance between the estimation point (index ***0***) and the ***n*** known data points are given by the right hand side vector. In the (unknown) left hand side vector, the λ are the desired interpolation weights and μ is the variance in the estimate.

Writing the kriging system (equation 4.7) in a more compact notation, the role of the ordinary kriging matrix $\boldsymbol{M_{OK}}$ in conjunction with the two vector quantities is perhaps more clearly seen:

$$M_{OK} \cdot \underline{\lambda} = \underline{\gamma_0}$$

$$\underline{\lambda} = M_{OK}^{-1} \cdot \underline{\gamma_0} \qquad \text{(equation 4.8)}$$

In other words, the solution of a kriging system is achieved via matrix inversion, for which a linear algebraic procedure such as *Gauss-Jordan* may be employed. Once defined, the vector of interpolation weights $\boldsymbol{\lambda}$ are summed according to the indicator class of their respective data points, yielding an estimate of the *degree* of class membership. Because an ordinary kriging system is constrained such that the sum of all weights is one, the total weight per class is consistent with the notion of class membership probability. This is slightly complicated by the fact that *negative weights* may occur in the solution as a consequence of clustering in the spatial arrangement of data points (Stein, 2002). As they do not have a valid physical meaning, all such negative weights must be removed from the solution using a correction procedure. As recommended by (Oh and Lindquist, 1999), the procedure described by (Deutsch, 1995) is used to resolve this problem in an unbiased fashion.

Oh and Lindquist propose using a spherical kriging window to determine the set of indicator data points for each unclassified data point. They suggest the radius of this window should be comparable to the correlation length over all indicator

data. Hence a kriging window of constant radius is applied throughout an image and all indicator data points (a-priori classified image elements) lying within this window are used to form a kriging system. The number of data points within any particular instance of a kriging window depends upon the local a-priori classifications surrounding an estimation point. Depending upon local conditions at the corresponding locations of the unclassified image with respect to the hysteresis threshold, there may be many or few data points available. Provided some sufficient number of data points is obtained (between four and twenty according to Webster and Oliver, 2007) then a kriged solution is based on sufficient evidence. It is therefore necessary to select an adequately large kriging window radius to obtain sufficient evidence over the entire image. The choice of window radius must however be tempered by the processing cost involved due to the use of matrix inversion in the solution of the kriging system. Matrix inversion involves a typical $O(N^3)$ cost in terms of matrix rank (in the case of kriging this is equal to the number of data points plus one for the Lagrangian constraint) and so over an image containing millions of unclassified elements, the total cost can be very large. This introduces a difficult choice for the operator who must consider the robustness of the method in relation to the practicality of obtaining an answer within a reasonable time. A consideration of patterns in the indicator semivariogram may allow correlation lengths may be deduced (as described in section 2.1.2) which addresses the issue of robustness. The practicality of a fixed size kriging window is inherently limited by the available processing capacity, however.

4.3 Assessment of Segmentation Methods

The segmentation (thresholding) methods described in the preceding sections are next compared with each other to give some impression of their relative capabilities and limitations. This introduces the need to select test data that can be assessed objectively. The most effective method of assessment is the use of a ground truth image (as described in section 2.4) such that all segment images are compared with an exact reference point. To this reference image are added noise and other distortions that will test the capability of segmentation methods.

For soil however, no true reference image exists. Methods have been proposed for sythesising soil-like images based on fractal models (Perrier et al. 1999) and also by composition using previously segmented images of soil (Wang et al. 2012). In the case of fractal synthesis the images tend to exhibit rectilinear artifacts (see figure 2.10) that may interact with a segmentation algorithm in ways that are not relevant to soil. In the case of segmented soil composites, the prior use of a segmentation method might also introduce features that subsequent algorithms are sensitive to. Because it is impossible to guarantee an unbiased test, it is preferable to use a test image which has a simple regular structure to facilitate the visual identification of problems. The visual complexity of synthetic soil-like images is judged to be a disadvantage in this respect. For this reason the 2D disk test images (used previously in quality assessment testing) are used again for segmentation testing.

4.3.1 Materials and Methods

Assessment of the thresholding methods is based on the test images introduced in section 3.4.1, specifically those labelled Fig 3.1 - 3.5 (the ground truth image and images D through G). In summary there is a ground truth image (3.1) and images with 20% and 40% uncorrelated and correlated noise (Figures 3.2 – 3.5). These are reproduced below for completeness.

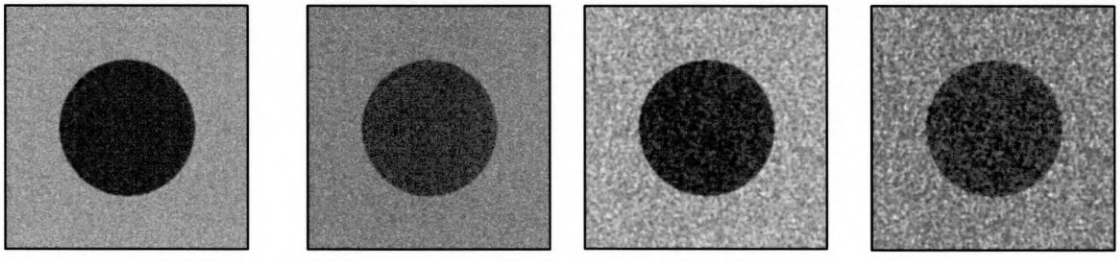

Figure 4.1 Segmentation assessment images.
Shown previously in chapter 3 (Fig 3.2 – 3.5 respectively)

Visual inspection is important for an appreciation of the severity of the problem faced by a thresholding approach, however a more scientific basis for comparison is the use of functional measures. The *Minkowski functionals* (hence forth MF) will be properly introduced in the chapter following this, but here they are applied to assess the segmentation procedure and a brief explanation is provided. Objects within a 2D image may be characterised by three fundamental measures, namely the *area*, *perimeter* and *total curvature*. Typically, each of the integral measures is presented as a sum over the entire contents of an image, that is multiple disjoint objects are treated as being one for the purpose of assessment. While area and perimeter (or boundary length) are no doubt familiar to the reader, total curvature is perhaps less so, being

closely associated with *topological* analysis. In fact the total curvature is related to the *Euler characteristic* χ by a scaling factor that depends upon the dimension of the containing the object (in 2D this factor is 2π). Under the assumption of topological convexity, χ provides a count of the number of disjoint objects. In the more general case (where concavity may be present) χ may be said to describe *connectivity* (Vogel and Kretzschmar, 1996) but interpretation in this sense can be challenging.

4.3.2 Results and Discussion

Firstly, the MF measures summarizing the segemented images are presented in table 4.4 overleaf beginning with *ground truth* information calculated from the original image of a black circle against a white background (Fig 3.1). The MF measures per segmentation method are then compared via a standardisation approach before the actual result images are presented along with ancillary information.

Inspecting table 4.3 it is obvious that total curvature is the most sensitive discriminator of structure. This is a consequence of its topological meaning, in that it counts distinct objects. An isolated misclassified image element therefore makes the same contribution to this measure as a larger cluster of misclassified elements. The least sensitive measure is area, with perimeter being intermediate in discriminating power.

There are two cases in table 4.3 that clearly stand out: for both types of noise at the 20% level (images *D* and *F*), the gradient masks method of Schleuter et al. (2010) manages to recover image information with exceptional accuracy. In fact this method is superior to the others for all except test image *G* where the indicator kriging method of (Oh and Lindquist, 1999) performs best. These two methods are also distinguished from the others by incorporating local spatial correlation information in their classification decisions.

In order to facilitate overall comparison of the relative effectiveness of thresholding methods in terms of the functional measures, it is necessary to standardise the information in some fashion. The chosen method of standardisation is to first calculate the relative error for each numerical value individually with respect to the corresponding ground truth measure value. Then, *Z-scores* of relative error are calculated for each type of functional measure (i.e. standardisation is relative to the standard deviation in the relative error for each measure type). It is then feasible to take an absolute sum over any set of measures yielding the "Sum of Absolute Standardised Relative Error" which is interpreted as an index of error. This is the information presented in table 4.4 below, where clear rankings of the thresholding methods are seen in terms of each measure individually and also collectively.

Image	Threshold Method	Area	Perimeter	Total Curvature
Truth		**0.2520**	**1.804**	**6.3825**
D (20% uncorr. noise)	R&C	0.1574	22.725	-5891.1
	Otsu	0.2527	2.178	248.9
	Entropy	0.2778	10.288	8590.9
	GMM-K&I	0.2517	2.112	3.2
	GMM-EM	0.2519	2.092	41.5
	Hapca	0.2512	1.892	-25.5
	SWV	0.2520	1.810	6.4
	O&L	0.2580	2.302	379.8
E (40% uncorr. noise)	R&C	0.0534	16.104	9727.0
	Otsu	0.2998	26.291	14676.6
	Entropy	0.2722	21.681	7451.6
	GMM-K&I	0.2095	19.648	-6085.7
	GMM-EM	0.2392	18.663	-915.9
	Hapca	0.2095	12.556	-2387.1
	SWV	0.2497	1.935	-73.4
	O&L	0.2554	2.373	497.8
F (20% corr. noise)	R&C	0.1541	18.680	-1503.1
	Otsu	0.2523	2.012	105.3
	Entropy	0.2824	10.930	4885.8
	GMM-K&I	0.2518	1.980	-25.5
	GMM-EM	0.2519	1.992	12.8
	Hapca	0.1865	13.678	-1024.4
	SWV	0.2539	1.823	6.4
	O&L	0.2584	2.104	86.2
G (40% corr. noise)	R&C	0.0437	11.431	3153.0
	Otsu	0.2944	20.404	5476.2
	Entropy	0.2787	17.752	4190.1
	GMM-K&I	0.2213	14.351	-1011.6
	GMM-EM	0.2440	14.177	769.1
	Hapca	0.1598	16.918	-315.9
	SWV	0.2448	4.338	-223.4
	O&L	0.2658	2.512	185.1

Table 4.3 Minkowski functionals of segmentation test result images.

Threshold Method	Error Index (Sum of Absolute Standardised Relative Error)			
	Area	Perimeter	Total Curvature	Sum
R&C	9.989	7.626	4.804	22.419
Otsu	1.518	5.395	4.854	11.766
Entropy	1.716	6.601	5.946	14.264
GMM-K&I	1.231	3.814	1.693	6.738
GMM-EM	0.353	3.670	0.409	4.433
Hapca	3.353	4.673	0.895	8.922
SWV	0.192	0.332	0.073	0.598
O&L	0.491	0.256	0.266	1.014

Table 4.4 Comparison of standardised relative errors.

The obvious "outlier" in table 4.5 is the approach of Ridler and Calvard which is by far the worst performer in terms of area and perimeter measures. The entropy method Kapur is the next poorest performer overall, followed by Otsu's method. For these three methods the error ranking of individual measures is consistent over all cases.

The localised Otsu method of (Hapca et al. 2012) performs poorly in terms of area and perimeter but somewhat better in terms of total curvature. This is explained by the highly connected mass of misclassified image elements in which many concavities as well as objects are present. These two features tend to balance out to some extent, making the numerical values less extreme than might otherwise be expected.

The Gaussian mixture modelling approach clearly out-performs the other global thresholding methods tested, with the EM algorithm noticeably superior in terms of both area and total curvature. This is perhaps surprising given the small difference in model parameter estimates between the two methods.

The best segmentation method overall, as already suggested, is the gradient masks method of (Schleuter et al. 2010) which manages an impressively small level of error in all measures. The indicator kriging method of (Oh and Lindquist, 2009) is then ranked a relatively close second overall.

The results of applying each thresholding method to each test image are shown in figures 4.1 to 4.20 on the pages following. Where appropriate, additional information such as distributions of criterion function evaluations displayed adjacent to each result image. Comments are made on the suitability of each method, prior to the images and graphs being presented.

4.3.2.1 Iterative Selection or Balanced Histogram (Ridler and Calvard)

As can be seen in the test images below, this method does not perform well for images with a soil-like intensity distribution. The dominance of solid phase material leads to a very low threshold resulting in the majority of pore space being misclassified. This distortion of the proportions of phases is so severe that no useful information can be obtained hence the method cannot be considered appropriate for the type of images tested.

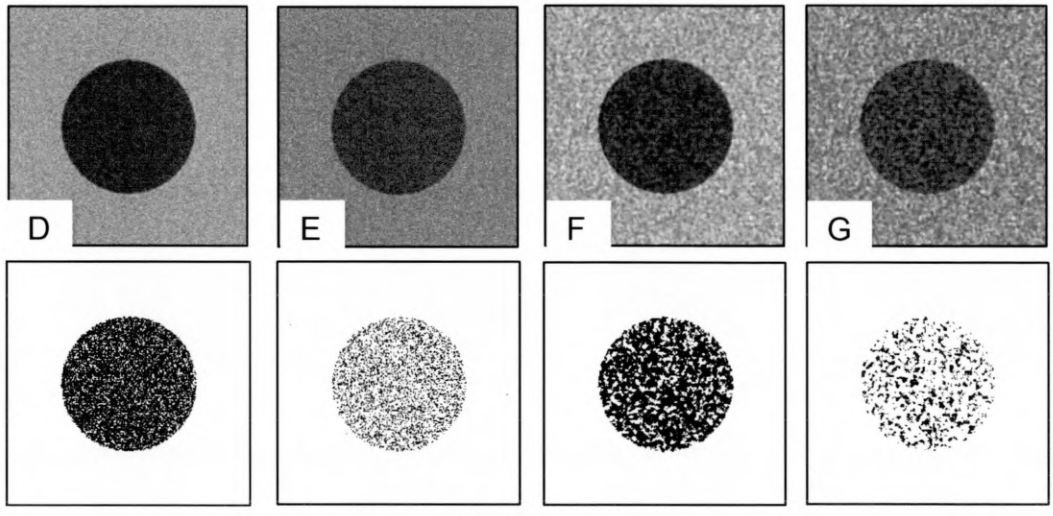

Figure 4.2 Ridler and Calvard method results.
Original images on top row, segmented result on bottom row.

4.3.2.2 Minimum Intra-Class Variance (Otsu)

The effect of the bias is clearly seen in the test images where misclassification is more common in the solid phase (which has the larger population). Despite this misclassification, useful information could be recovered from images D and F by applying a majority filter to the segmented images. This is because the misclassified image elements are sparse and hence are easily identifiable as noise. For test image E the application of filtering is of questionable value due to the disruption of the interface between object and background. In the case of test image G containing 40% correlated noise, however, it is not possible to remove the larger clusters of misclassified image elements without badly distorting the interface. Overall this method performs surprisingly well given its known limitations, but is clearly not suited to very noisy images .

(Otsu)

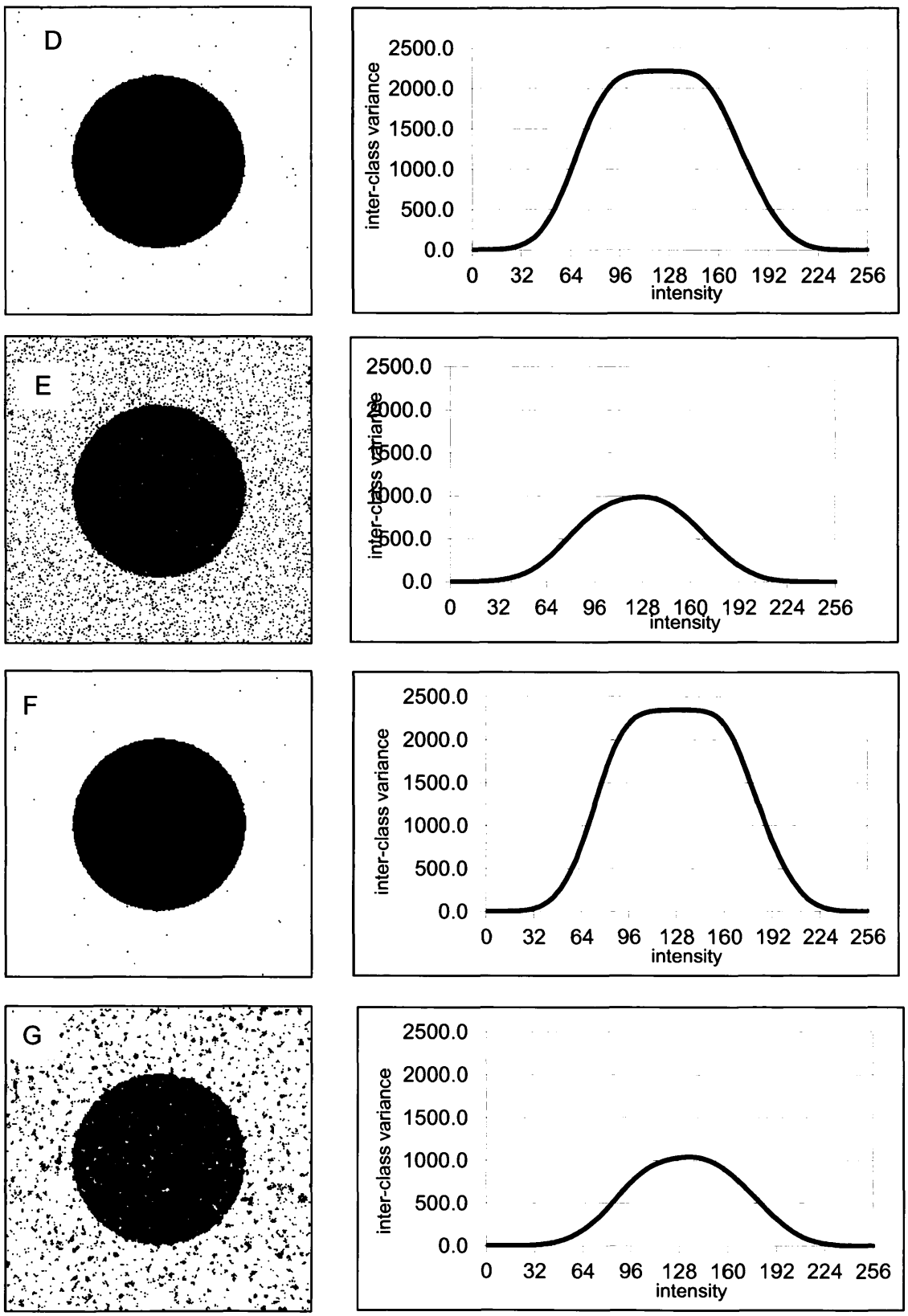

Figure 4.3 Otsu's method results.
The plots of inter-class variance are shown to the right of each image..

4.3.2.3 Entropy (Kapur, Sahoo and Wong)

This method results in extensive misclassification of the solid phase and also of the pore phase at the higher level of noise. For image *D* (20% uncorrelated noise) some useful information might be recovered by majority filtering, but even at this modest level of noise, the boundary between classes appears slightly "ragged". This method is poorly suited to dichotomising the type of images tested in this study.

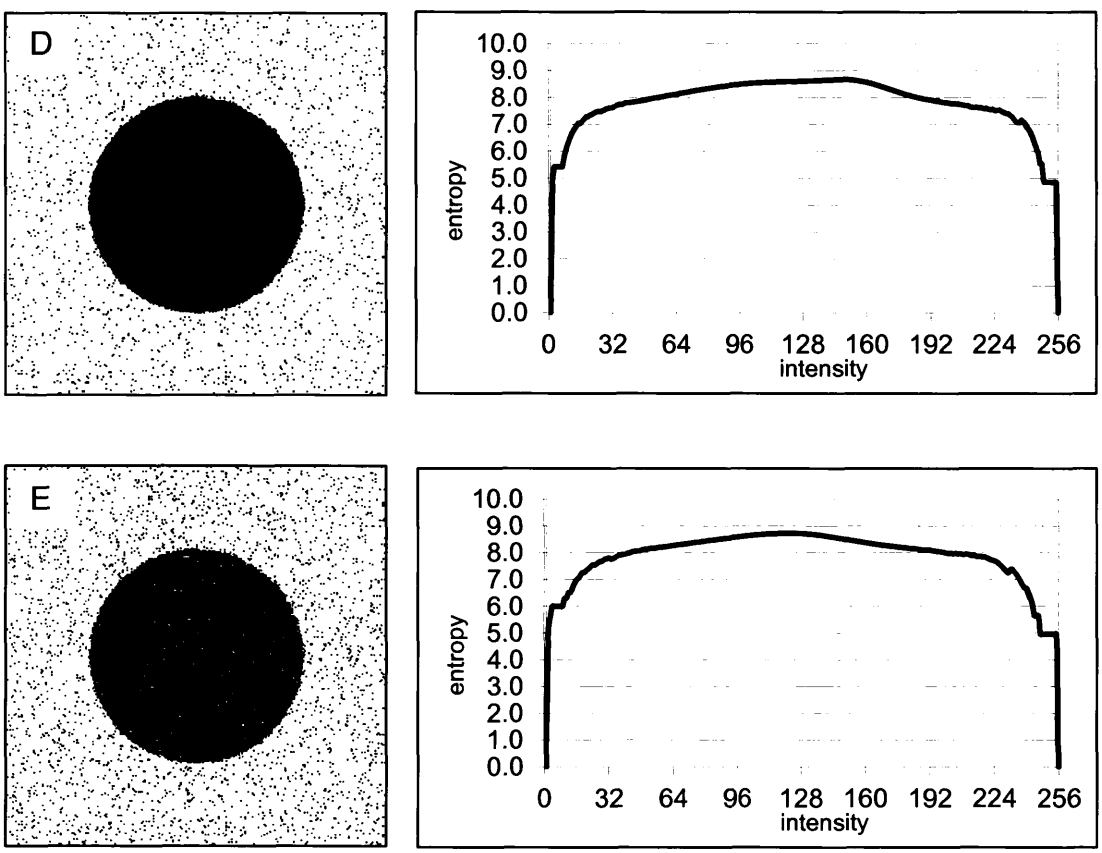

(continued overleaf.)

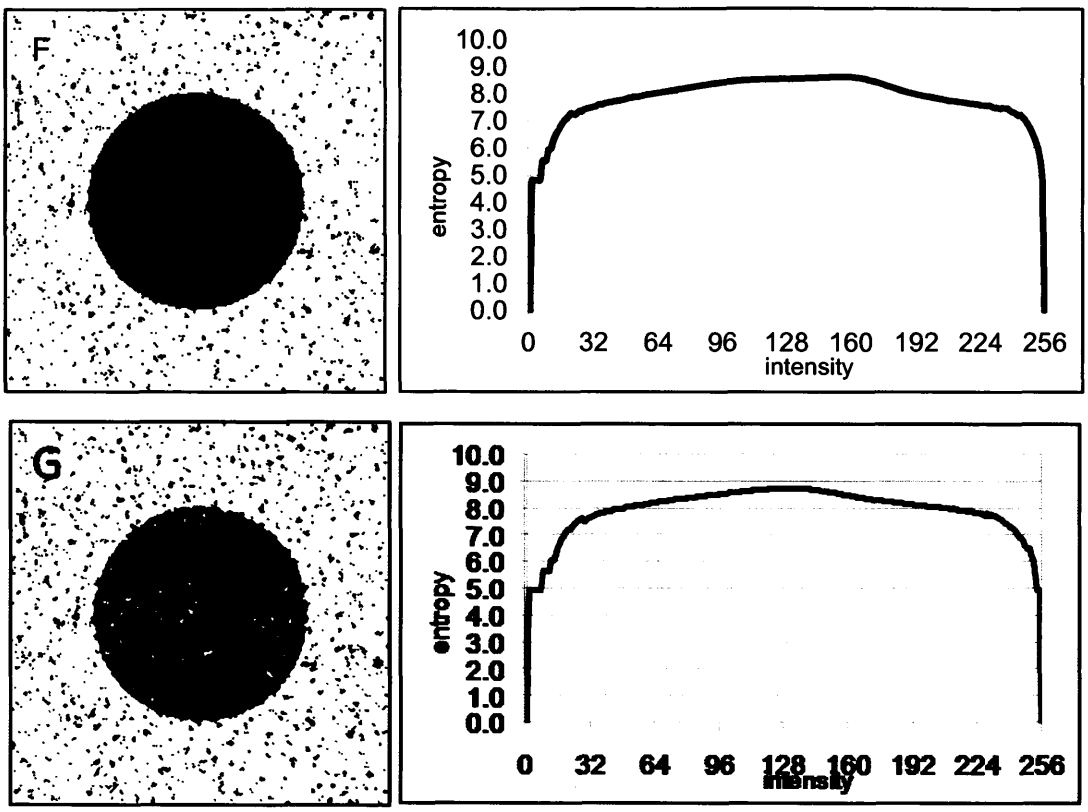

Figure 4.4 Entropy method results.
The Entropy function is shown to the right of each image.

4.3.2.4 Gaussian Mixture Models

The results of both methods (Kittler and Illingworth and also Expectation Maximisation) evaluated against the test data, are shown in figures 4.5 through 4.6 respectively. In each case alongside the segmented image, the mixture model is shown plotted. In the Kittler & Illingworth case the model is biased as described previously but this is only apparent to a limited degree. The model (and hence threshold) resulting from the Expectation Maximisation model fitting approach does appear to be slightly superior to Ridler and Calvard in terms of the population probabilities. Both of these methods provide a *balanced* result in the sense that errors in both the object and background are equally apparent in each image. However neither performs well at the higher noise level.

(Kittler and Illingworth)

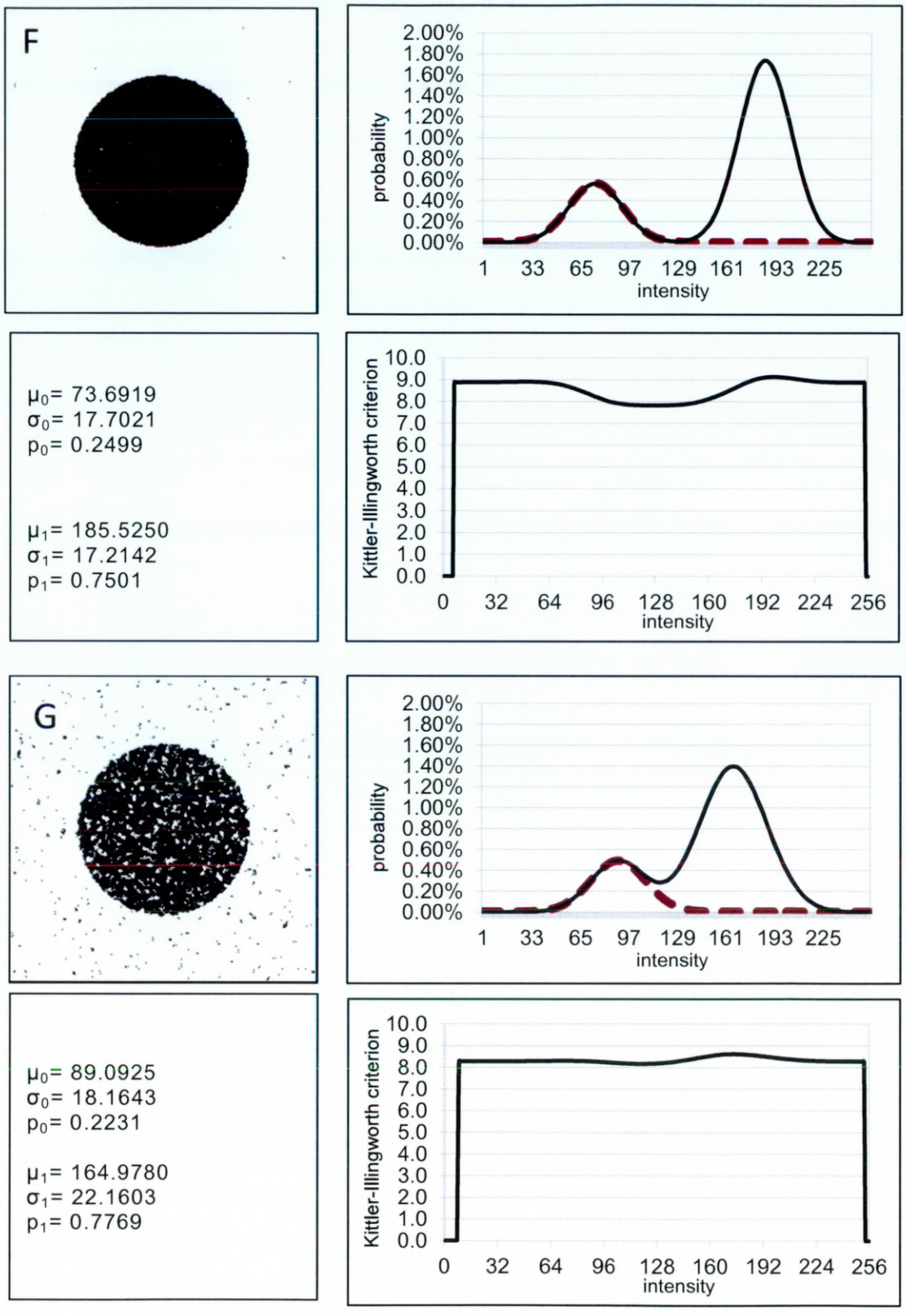

Figure 4.5 Kittler and Illingworth method results.
Mixture model to right of each image, discriminant function and parameters below.

(Expectation Maximisation)

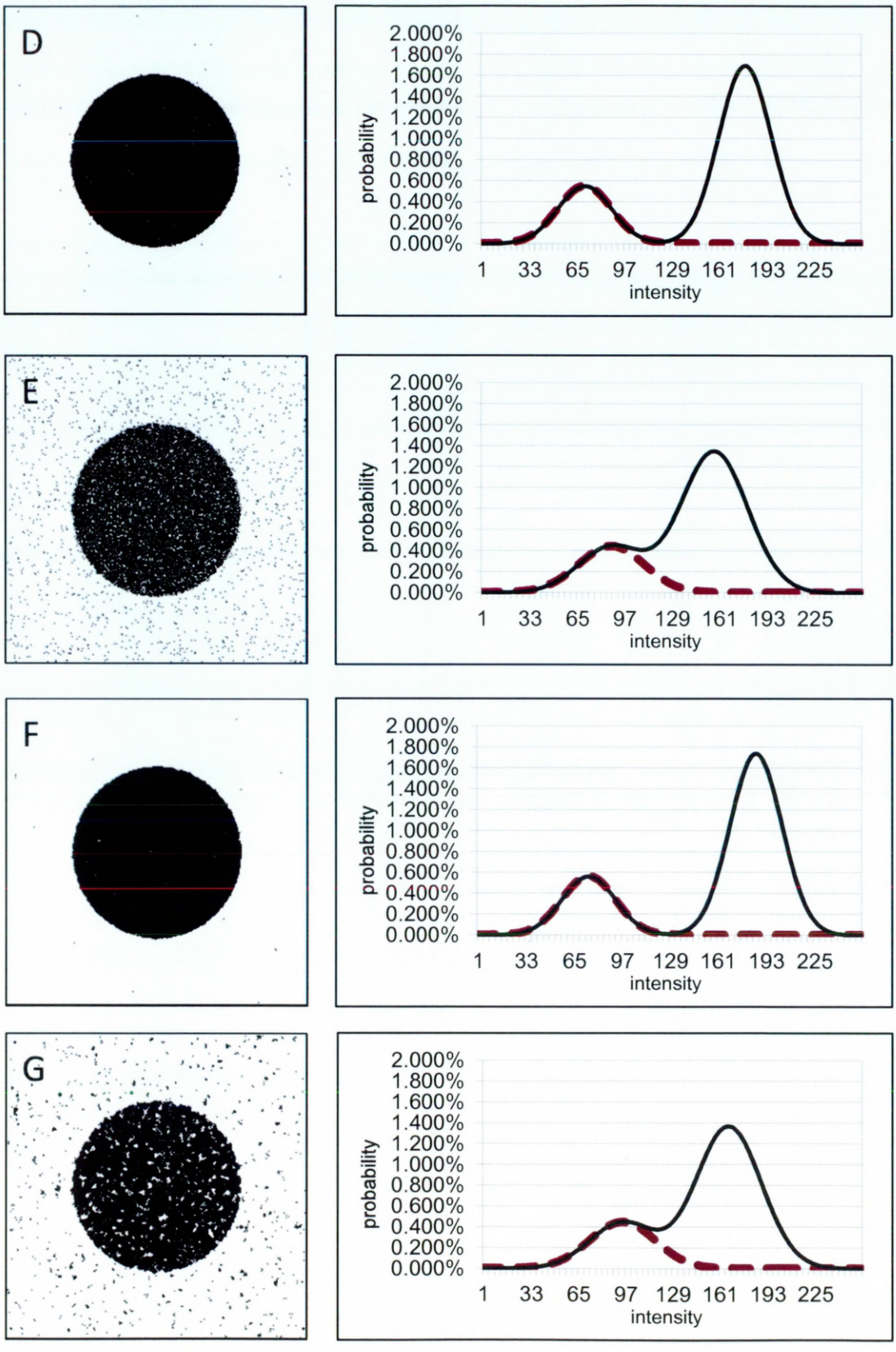

Figure 4.6 Expectation Maximisation.
Segmented image on left, mixture and model on right.

4.3.2.5 Localised Otsu (Hapca et al.)

This method is particularly sensitive to noise, with a systematic increase in classification error versus both the level and type of noise. Only test image *D* (20% uncorrelated noise) has been segmented acceptably, but would benefit from a post-processing "cleanup" operation to remove isolated fragments in the pore phase.

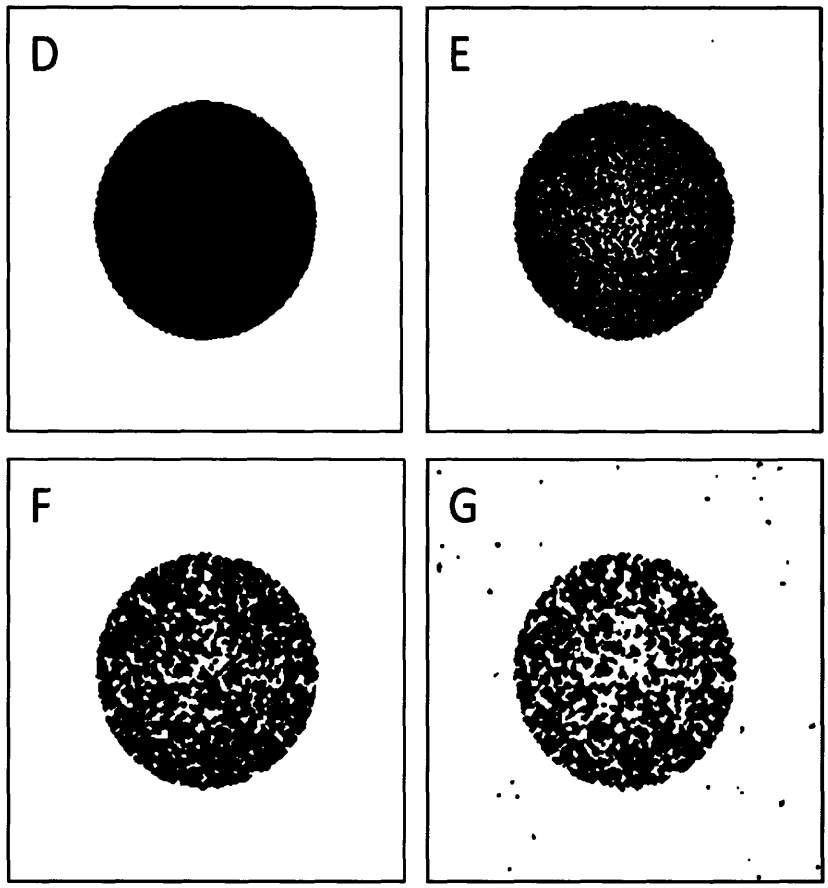

Figure 4.7 Localised Otsu (Hapca et al.) method results.

4.3.2.6 Gradient Masks (Schleuter, Weller and Vogel)

This method seems robust against noise at low levels but suffers when levels are as high as 40%. For test image *E* (40% uncorrelated noise) the misclassifications are relatively minor and could be rectified by post-processing. Test image *G* (40% correlated noise) however exhibits significant problems in the pore phase for which no simple remedy is available.

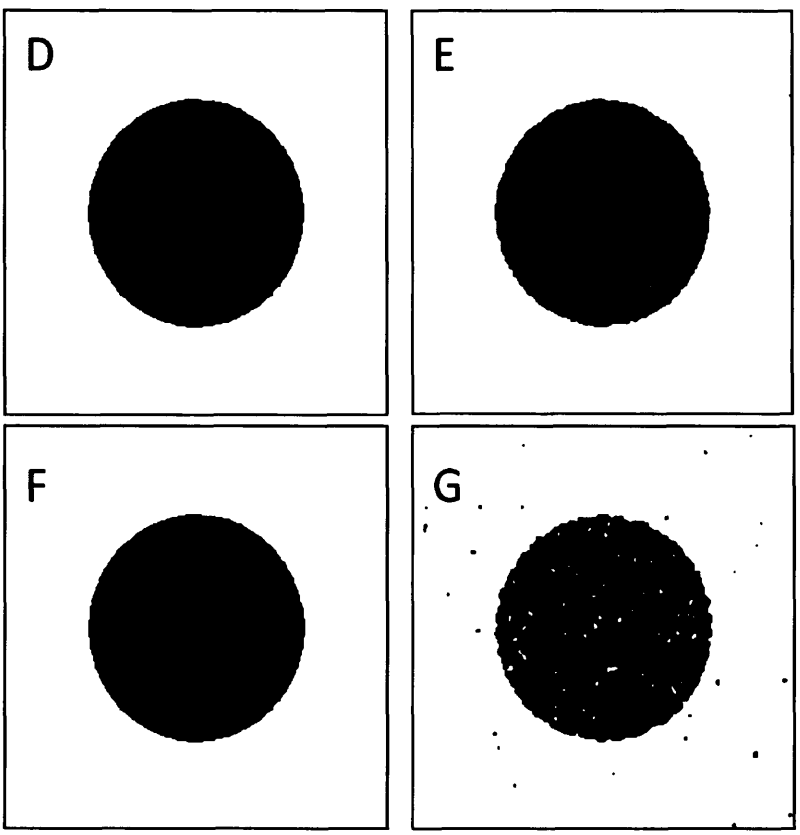

Figure 4.8 Gradient masks (Schleuter et al.) method results.

4.3.2.7 Indicator Kriging (Oh and Lindquist)

This method provides perhaps the most consistent results across types and levels of noise, including misclassifications seen in the vicinity of the pore-solid interface in every case. Some of these misclassifications might be remedied by post-processing, particularly in the case of uncorrelated noise (test images *D* and *E*). The 60% majority filter included within the method seems to have been ineffective, perhaps due to the reduced neighbourhood size within a 2D image (8 neighbours versus 26 for a 3D image).

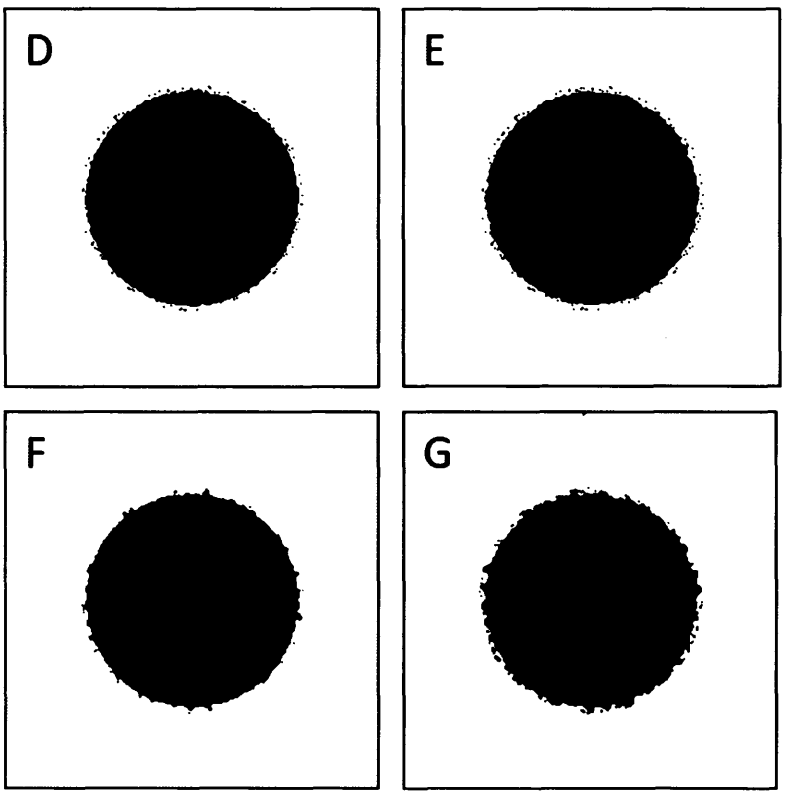

Figure 4.9 Indicator Kriging (Oh and Lindquist) method results.

4.4.Conclusions

For images with a significant noise content, global thresholding methods result in extensive misclassification and are best avoided. Similarly, the localised application of a threshold method such as Otsu does not address the problem of noise.

The use of spatial correlation information is a powerful approach to improving segmentation accuracy but relies on good a-priori classification. This is evidently a weakness in the histogram modelling approach of Oh and Lindquist, for which the test data seems ideally suited. Despite the accuracy of modelling achieved by the EM algorithm, the hysteresis thresholds derived in this fashion do not yield superior results compared with those obtained by the gradient masks method. This suggests that the use of local evidence (i.e. spatial information such as derivative magnitude) within the a-priori classification stage is important for overall robustness. The topological approach to spatial correlation, in the form of region growing, is notable for achieving good quality spatial correlation at a relatively low computational cost. Indicator kriging is potentially more flexible than region growing in terms of how it weighs evidence but this come at significant computational cost.

5.0 Image Analysis

This chapter focuses on some important functional measures that are useful for describing and comparing the spatial properties of both objects and entire images (including the assessment of image segmentation methods, as shown in the preceding chapter). These measures are concise and can be computed efficiently and with good accuracy (limited by the image representation). They are therefore a convenient means of illustrating both variability and trends occurring within all manner of image data. They also have an exact meaning in terms of physical properties but in some cases this might be difficult to relate directly to data from physical experiments. Although interpretation of the measures in physically relevant terms can be challenging, this does not diminish their discriminating power.

In addition to functional measures, evaluating both connectivity and size distributions of objects within digital images are useful in reaching an understanding of pore structure (Vogel, 2000). It is however challenging to be both complete and accurate when evaluating such properties, as problems of computational cost tend to arise.

The contents of this chapter firstly describes the underlying principles of the selected analysis measures, then summarises implementation mechanisms and finally discuss issues of accuracy and robustness that arise.

5.1 Minkowski Functionals

The term "Minkowski functionals" is attributed to Georges Matheron and Jean Serra whose collaboration during the late 20th century led to significant advancement in the practice of spatial data analysis (for digital images in particular). They chose the name to honour the physicist Herman Minkowski who initiated the study of the *geometry of numbers* as this subject area underpins functional analysis in general. Another very important figure is Hugo Hadwiger whose theorem published in 1957 illustrates that an N dimensional space has N+1 fundamental functional measures and these form a basis for all possible linear measures of the space. As such, the "Minkowski functionals", as they have subsequently become known, form a very efficient description that facilitates analysis and comparison of spatial structure.

The 3D Minkowski functionals (henceforth MF's) relate to familiar concepts such as volume and area and also to measures of curvature in both a geometric and topological sense. Being relatively new (on the time-scale at which mathematical theory is disseminated into practice) there are some issues regarding the dimensional scaling and standardisation of individual MF measures. This may cause confusion when comparing published work as not all authors are rigorous in their use of terminology; some give "raw" measures of volume etc. with attached physical units while others report standardised measures such as volume fraction. A holistic perspective is given in (Ohser and Mucklich, 2000) where physical measures are related in a consistent fashion to the results of Hadwigers Theorem. Properly comprehending this material does

however require some familiarity with integral and differential geometry. A thorough treatment of the latter topic is provided in (Spivak, 1999) together with a historical perspective that was found to be helpful.

In the sub-sections following, the 2D and 3D MF's are described very briefly with respect to practice in physical science before some of the essential mathematical concepts are explained in a non-technical fashion. (The proper interpretation of MF measures requires that *all* the measures be considered together, hence a thorough explanation of curvature is warranted.) Following this is a discussion of how the estimation of MF measures may be achieved in the case of digital images (i.e. discrete scalar fields) with consideration given to the accuracy of estimation. Towards the end of this section, test images are used to experimentally verify the implemented MF measures and reveal some systematic error behaviour. Examples of the application of MF measures to assess segmentation methods is provided in chapter 4 and application to real data is discussed in chapter 7.

5.1.1 An Overview of Two and Three Dimensional Minkowski Functionals

In two dimensional space the quantities of interest are *area*, *perimeter* and *total curvature.* Consider a *thin section* image containing a number of objects of interest; the area of objects in relation to background represents the relative abundance of the interesting form of matter, whereas the perimeter describes the potential for physical interaction between objects and background. In the

sense of some bio-chemical process these measures together indicate the limiting rate at which the objects can interact with their environment. The total curvature is determined by summing the local curvature at each point on the perimeter of every object and has a simple interpretation provided that a restricted form of object is considered. Provided that objects are solid (meaning each has only a single continuous perimeter i.e. no internal cavities) then the total curvature is simply the number of objects multiplied by 2π. This can be seen as a generalisation of the fact that the internal angles of a triangle, or any *convex planar* figure, must sum to give 360° (2π radians). Consequently, total curvature may be used to determine an object population count *provided that only objects without concavities are considered*. In order to put the 2D MF measures into a physical context is useful to consider that area, perimeter and total curvature have measure dimension two, one and zero respectively. Hence given a space measured in terms of a length unit l then the quantities will have units l^2, l^1 and l^0 respectively. In other words total curvature is a dimensionless quantity which is consistent with the topological meaning of this measure.

In three dimensional space the quantities of interest are *volume*, *surface area*, *integral mean curvature* and *total curvature* (having units l^3, l^2, l^1 and l^0 respectively). The volume and surface area of objects within a 3D image are directly analogous to area and perimeter within a sectional 2D image; it is easy to see how these can be interpreted in terms of the mass of reactive (or catalytic) material and contact area. Mean curvature (also known as Germain's curvature) is a local average measure of surface curvature which can be either

positive or negative according to whether the surface is locally convex or concave. When integrated over a globally convex (or concave) surface, this measure resembles an intuitive notion of curvature i.e. "the overall degree of curvedness" of a surface. In the general case, when both convexity and concavity are present, the integral mean curvature loses this simple interpretation. In this case curvature information must be considered carefully in conjunction with other measures and in the context of a particular problem or question. The total curvature (which may also be referred to as Gaussian curvature) in three or more dimensions conveys the same meaning as two dimensional total curvature. Again it is stressed that both mean and total curvature are signed quantities hence integral curvature measures have a simple interpretation only in the case of strictly *convex* objects.

5.1.2 Understanding Curvature

To be absolutely specific, the term curvature in the context of the work presented here refers to the *extrinsic curvature* of objects embedded within a Euclidean space (as opposed to the *intrinsic curvature* of a *Riemann manifold*). Extrinsic curvature is defined only in relation to the interface between an object and the image background i.e. on the perimeter or surface of an object. This means that the dimensionality of curvature information is at most one less than that of the space being analysed i.e. a 3D volume image leads to 2D curvature information and a 2D image yields only 1D information.

A straight line or flat surface is by definition not curved, in other words it has zero curvature at all points of its spatial extent. In contrast, a circle or sphere has constant curvature i.e. for any specific instance of an object the measured value of curvature must be the same at every point. This latter fact leads to a convenient definition for curvature in terms of the radius of a circle; the local curvature κ at each point on an object is defined as the reciprocal of the radius r of an *osculating* circle (i.e. one that exactly fits the local curvature, see Figure 5.1 below).

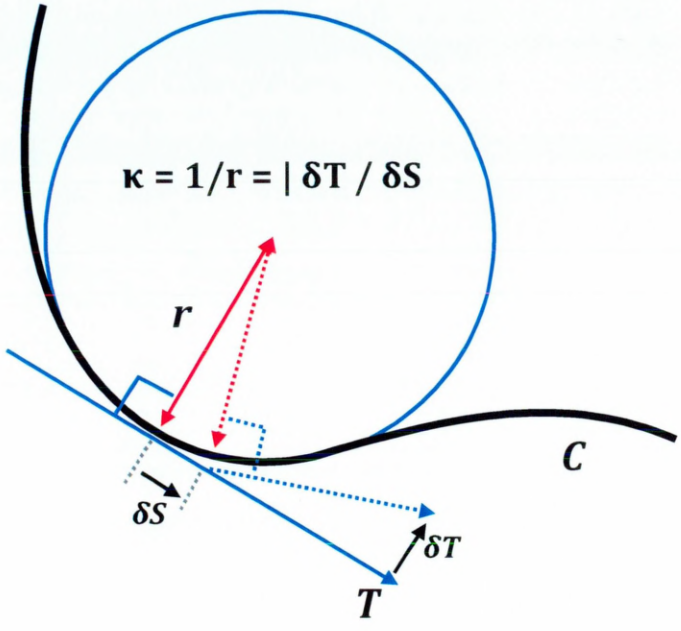

Figure 5.1 Curvature in 2D.
Local measurement of 2D curvature via an osculating circle. Curvature is measured by the reciprocal radius of the circle, and is equal to the local rate of change of orientation.

Although this two dimensional definition in terms of a circular radius is elegantly simple, it does not lead directly to an efficient approach for curvature measurement in practice. Rather, through consideration of curvature as the rate of change of orientation a more practicable formulation for 2D curvature is achieved via differential calculus; the generalisation of this notion leads to the Frenet-Serret formulae (Serret, 1851; Frenet, 1852; as presented in Spivak, 1999) which describe any curved path through space. At this point it is reiterated that curvature is a *signed* quantity and the sign describes whether the curve is convex or concave with respect to some frame of reference.

The curvature sign convention used in this work is that when an osculating circle is matched against the interior of an object the curvature is positive (meaning the object surface is locally convex from an external observers perspective) whereas matched against the exterior of an object the curvature is negative hence the surface is locally concave from an external perspective.

In the case of a space of three or more dimensions, a point on the surface of an object is not limited to a single value of curvature. At any given point on such a surface there are actually an infinite number of planes in which curvature can be measured. Any plane perpendicular to the tangent plane of the surface at the point of interest (see figure 5.2 following) can be used to measure the local curvature of the surface, and each may lead to a value distinct from the others. Only in the case where a surface is locally spherical is the curvature constant for all possible measurement planes.

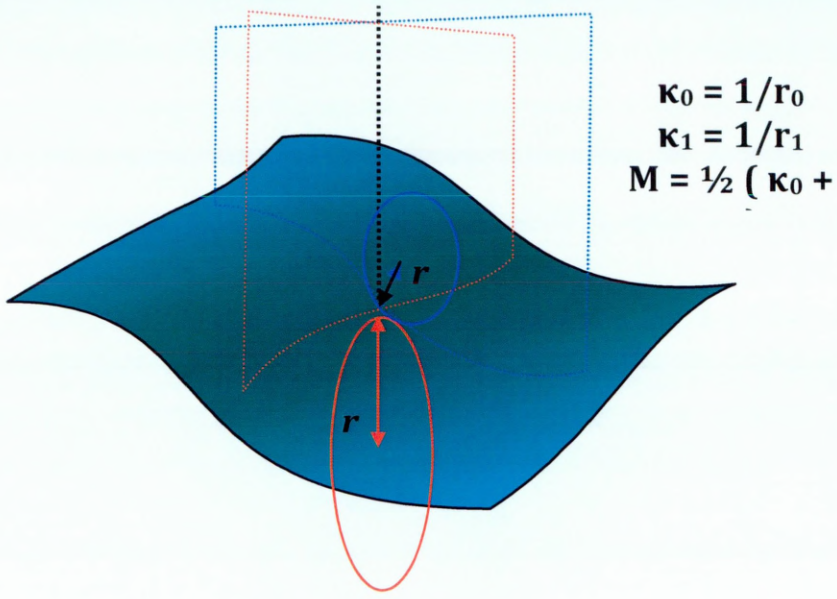

Figure 5.2 Principal curvatures in 3D.
Local measurement of 3D curvature via two orthogonal osculating circles. The two principal curvatures are determined as the maximum and minimum of local curvature measures. The principal curvatures are combined to form the mean curvature M and also the total curvature K

In the more general case of a non-spherical surface, curvature changes continuously with the orientation of measurement planes. The solution to this problem is provided by the two *principal curvatures* κ_0 and κ_1 measured orthogonal to each other at any given point on a 3D surface (Euler, 1760; as presented in Spivak, 1999).

The principal curvatures at a point are simply the minimum and maximum over all curvature values for that point (bearing in mind that the frame of reference must be consistent over all measures). The total curvature at a point on a surface in 3D space is calculated as the product of these principal curvatures; in the 2D case the single curvature value κ is in fact the total curvature. An

alternative measure in 3D space is the *mean curvature* which is the arithmetic average of the principal curvatures; there is no 2D equivalent measure. Although related by their definition, the total and mean curvatures have distinctly different meaning, except in the case of a planar surface (when all curvature measures are zero). This can be appreciated by considering that if only one of the principal curvatures is zero (such as on a cylinder) the total curvature alone is zero, whereas if the principal curvatures are of equal magnitude but opposite sign (a symmetric "saddle" point) the mean curvature alone is zero.

While locally determined curvature measures are useful in the detailed analysis of selected surfaces in 3D space, the total quantity of curvature information in a volume image is typically far too great to be meaningfully interpreted. Instead, some measures that succinctly capture the essential properties of objects within an image are required. For this reason the local curvature measures are each integrated over the surface of an objects within an image yielding the measures of *integral total curvature* and *integral mean curvature*. These two integral measures are fundamentally important descriptions of spatial structure (Hadwiger, 1957) and are closely related to measures obtained by quite different routes. The total curvature is closely related to the topological measure known as the *Euler characteristic* χ (which can be reached by graph-theoretic analysis) while the integral mean curvature is equal to the stereological measure *mean-breadth* (known to microscopists as the mean calliper diameter). The significance of these facts is briefly discussed in the sub-sections following.

5.1.3 Total Curvature and Topology

The total curvature is equal to the Euler characteristic χ scaled by 2π. hence for a two dimensional topologically convex (i.e. "solid") object, $K=+2\pi$ as $\chi=+1$. The significance of a topological concavity (i.e. a "hole") within an object is that the value of χ changes by an amount -1 per cavity, becoming zero or negative where two or more cavities exist. In an image containing many objects in which cavities are present it is therefore impossible to deduce the object count from χ.

In the case of 3D images, the relationship between χ and total curvature needs to be approached very carefully. Owing to a lengthy historical development and the propagation of partial information, some confusion can exist between the calculation of χ and it's interpretation. The classical formula determines χ from the number of uniquely counted vertices (v), edges (e) and faces (f) in an object represented as a spatial graph (see table 5.1 below).

Description	Formula	Square					Cube				
		v	e	f	c	chi	v	e	f	c	chi
Euler (classical)	v – e + f	4	4	1	-	+1	8	12	6	-	+2
Euler-Poincare	v – e + f – c	4	4	1	0	+1	8	12	6	1	+1

Table 5.1 Formulation of topological measure.

In three dimensions the classical Euler characteristic of a solid object has the value +2 and so an image containing n solid objects will have a total curvature measure of $4\pi n$.

For each convex (i.e. "solid") object the result of this classical formula is ***+1*** in two dimensions, but ***+2*** in three dimensions. This classical formula was further developed by Lhuilier (as noted in Naveira, 2005) and finally resolved by (Poincare, 1895) who each added terms describing topological invariant properties of the object under study. The resulting generalised formula for the Euler-Poincare characteristic provides dimensional consistency i.e. a convex object yields the value ***+1*** irrespective of spatial dimensionality. The broader mathematical consequence of this addition is a more rigorous formalisation of the relationship between the extrinsic curvature of objects versus the intrinsic curvature of the embedding manifold.

Some sources (Ohser and Mucklich, 2000) do not explicitly state which form of measure is used and this may lead to incorrect interpretation. This can however be resolved by examining the equation relating χ to total curvature in three dimensions, if such is presented. The presence or absence of an extra factor of ***2*** reveals which form of measure has been applied e.g. in (Ohser and Mucklich, 2000) the total curvature is specified as $4\pi\chi$, meaning that χ has been estimated in the form of the Euler-Poincare characteristic rather than the classical Euler characteristic.

In the work presented here the Euler-Poincare characteristic is preferred, therefore the relationship between the topological measure χ and total curvature in three and two dimensions respectively is stated here as:

$$\mathrm{K} = \sum \kappa_0 \cdot \kappa_1 = 4\pi\chi$$

$$C = \sum \kappa = 2\pi\chi \qquad \text{(equations 5.1(a),(b))}$$

As a reminder of these equations, it is useful to recall that in 2D the exterior angles of a convex polygon must sum to 2π radians while in 3D the *angular defect* of a convex polyhedron is 4π radians.

5.1.4 Mean Curvature and Breadth

The *mean breadth* of an object is a concept originating in the methods of analysing physical samples. Traditionally, a pair of callipers might be used to measure the maximum separation between opposing exterior surfaces of a sample (or perhaps a photographic image). Similarly the minimum separation between opposing surfaces might be measured. These two separations are the principal measures of the breadth of an object and taking their mean gives a crude measure of mean breadth. Better accuracy is achieved by measuring the breadth over a rose of directions and then take the mean over all these measurements. This measure is only defined in the case of a strictly convex body which excludes any body having a negative measure of curvature (as defined previously) at any point on its surface. This can be used to classify the

shape of spherical to ellipsoidal or capsule-shaped micro-organisms, for example. The integral mean curvature of a convex body is equal to it's mean breadth hence shape classification of an isolated convex object is possible via integral mean curvature.

5.1.5 Estimation of Minkowski Functionals

The widely known "point count method" (Thompson, 1930) is a simple and obvious method for estimating the volume of an object within a 3D image (or area within a 2D image). Traditionally, this was a manual procedure carried out on thin sections (Gazzi, 1966; Dickson, 1970) upon which a sampling grid was overlaid and the number of object versus background points counted. This approach is trivially simple to implement as an algorithm operating on a segmented digital image. Each image element is a sample point belonging either to the object or to the background and by counting the total in each class the volume fraction is estimated by a simple ratio:

$$\frac{V_{object}}{V_{image}} = \frac{N_{object}}{N_{object} + N_{background}} \qquad \text{(equation 5.2)}$$

An example of this calculation is shown overleaf in figure 5.3, here 14 object elements versus 35 background elements are shown on a rectangular 2D image lattice, 7^2 elements in size.

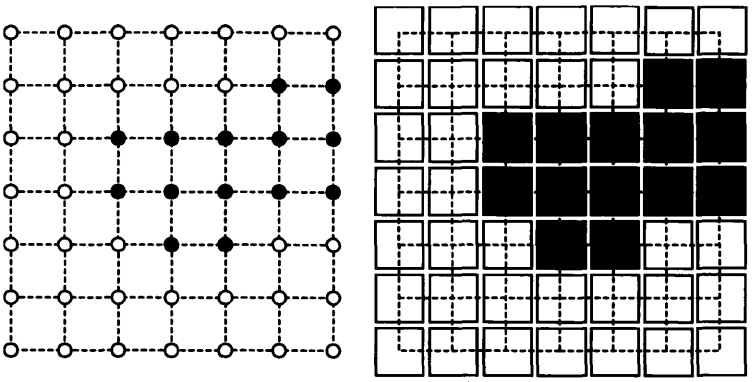

Figure 5.3 Rectangular lattice of a 2D image.
Point lattice (left) and (right) the geometric model implied by point counting. Object elements shown in black, background in white. The object fraction in this figure, estimated by point counting, is: 14 / (35 + 14) = 0.2857.. or 28.6%.

Although it may not be immediately obvious, the point count method does apply a geometric model to the image elements. In effect, the rectangular lattice of point samples in the image has been interpreted as an array of tiny rectangles and the elementary area of each attributed to either object or background. This form of model has a clear advantage of simplicity but is not particularly accurate except when objects are large compared to the image resolution, or when all object edges are aligned to the principal axes of the image. For irregularly shaped objects with structural features covering a wide range of size scales, these conditions are not met and consequently there are some naturally occurring structures for which a point-counting estimation method is not appropriate. Geo-materials are an extreme example of this problem as they frequently exhibit spatially complex structure on scales from nanometres to metres and beyond.

Although it might appear to be an obvious solution, improving the resolution of images does not address this problem in practice. This is due to the need for a representative sample volume i.e. an image including macroscopic features (typically on the order of centimetres in size) that is also able to resolve the smallest features (typically on the order of tens of nanometres in size). Decades into the future it is conceivable that images might be acquired with a resolution and definition that eliminates concern over the accuracy of point counting. Estimation of other Minkowski functional measures (surface area, perimeter and curvature) however is far more sensitive to the model applied to the image lattice. This is explained in the sub-section following, where a flawed implementation of Minkowski functionals on images is described.

5.1.6 Minkowski Functionals: Initial Implementation Attempt

During the early stages of development and following the example of (Michielsen and DeRaedt, 2000), an estimation method based on the model of rectangular image elements was implemented. When tested on images containing simple parametrically generated objects (cubes or spheres), the expected value of total curvature (topological measure) was obtained in all cases. The estimate of volume is also quite accurate in the case of such test images, being limited mainly by discretisation error; increasing the lattice resolution allows this error to be made arbitrarily small. The error in estimating surface area is however significant in the case of an object with non axially aligned surfaces and in this case the error is difficult to conquer via increased image resolution. This is because modelling image elements with rectangular

geometry simply cannot accurately represent smooth changes in orientation. This problem is more significant in the case of mean curvature as only changes in orientation of ±90° can be represented by a rectangular geometric model. For a smoothly changing surface orientation this leads to a rounding error as large as ±45° for every image element on the object interface. The measures of surface area and mean curvature cannot be estimated reliably by such a model unless object geometry is known to be both rectilinear and aligned to the image axes. This form of estimator is therefore of little use for a material such as soil.

5.1.7 Accurate Implementation: The Image Cell

The problem of measuring spatially complex structure is addressed by applying a better model to the image elements. In fact it is actually the spatial relationship *between* image elements that is important rather than any notion of shape applied to elements themselves. This line of thinking goes back to the fundamental principle that image elements, whether 2D pixels or 3D voxels, are point samples and therefore cannot be treated as having area or volume. Any measure involving some notion of spatial distance (length, area, curvature etc.) can therefore be defined only in terms of two or more image elements. The obvious step is then to define some grouping of image elements as the building block for analysis. For an image represented using a 2D rectangular lattice an obvious choice is the rectangle formed by four adjacent image elements. In other words, given some location within an image, the four elements nearest that point form the *image cell* enclosing that point. Therefore an image of dimensions Nx by Ny image elements consists of Nx-1 by Ny-1 image cells,

each of which has an identical area measure as shown in figure 5.4. Similarly, for a 3D rectangular lattice an image cell can be formed by interpreting 8 adjacent image elements as the vertices of a cuboid. Being a cuboid, the volume of a cell is easily computed as the product of edge lengths and these lengths are equal to the spatial resolution of the image (this is the usual interpretation of resolution information within a graphics file format).

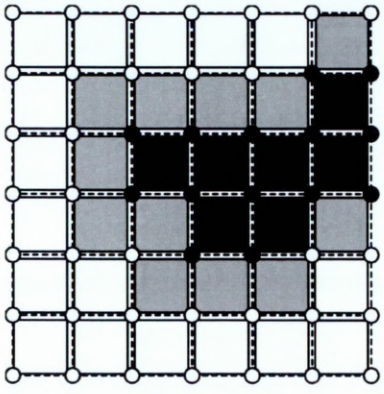

Figure 5.4 A 2D rectangular point lattice with cells superimposed. Object cells are shown dark grey interface cells light grey

If all vertices of a cell belong to the same class (either object or background) then the measure (e.g. area in the 2D case or volume in 3D) contributes to that class only; summing by class over all such cells then yields an incomplete estimate of the measure per class. The estimate is incomplete because many cells consist of more than one class of vertex; these are interface cells and so the contribution of the cell must be divided between object and background classes (figure 5.4). A naive approach of apportioning the measure in proportion to the number of vertices per class does not take account of spatial relationships; this is merely a subversive reintroduction of the point counting method. The interpretation of interface cells is the key issue for accurate

estimation of object volume within a 3D image (or area in 2D). For the functional measures of lower dimensionality, surface area and curvatures in 3D or perimeter and total curvature in 2D, the interface cells are in fact the entire issue; these measures can be defined only in relation to an interface. It should then be clear that a model allowing the internal geometry of an interface cell to be interpreted in an unbiased fashion is critically important for the accuracy of estimation. The design of such models from a solid theoretical foundation was achieved by Matheron and Serra as part of their long-running collaboration on Mathematical Morphology. The two major milestones of their effort are (Matheron, 1975) and (Serra, 1982) with the length of the time interval perhaps a good indicator of the depth and breadth of mathematical knowledge required to interpret this body of work. For the present author (who is interested mainly in practical application) it remains a longer term objective to develop a thorough understanding of the underlying theory.

5.1.8 The Cell Pattern Histogram

As explained previously, the *image cell* is the basic unit of analysis (either a cuboid in 3D or a rectangle in 2D) and each of it's vertices is an image element that belongs to either the object or the background class. The fact that each vertex exists in one of two states is particularly useful for computer implementation; the vertex information can be represented using exactly one bit (binary digit) of information. Any 3D cell can therefore be completely described using 8 bits (an *octet* or, more commonly, a *byte*) of information as shown in figure 5.5 (below), in this case the total number of possible states of a cell is 2^8

= 256. Each distinct possible cell state has a unique pattern of bits which is naturally interpreted as a number and can therefore be used as an index.

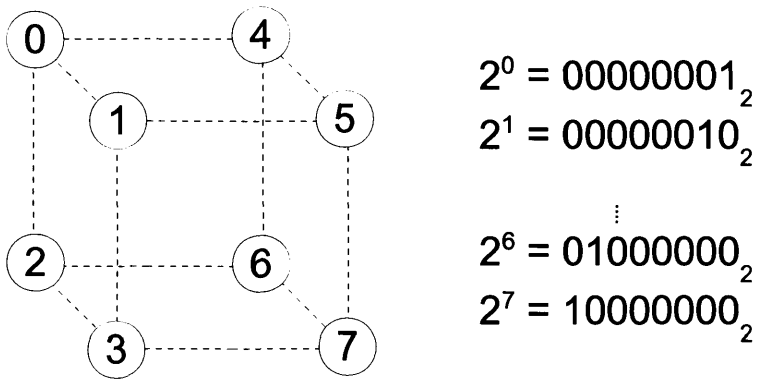

Figure 5.5 The 3D image cell definition.
Image elements numbered consecutively from zero. The corresponding powers of two are shown with their binary representation on the right.

Some sources (Serra, 1982; Ohser and Mucklich, 2000) refer to this representation of a spatial pattern within a single element as a "grey scale" value. This term is however more commonly used to refer to continuous tone (i.e. unsegmented) images, a convention that is followed in the present work. Rather, the term *bit-set* will be used in reference to the binary patterns of cell states as this is felt to be less ambiguous and immediately understood to mean a collection of bits, each denoting set membership.

By interpreting each cell bit-set as an integer value and applying this as an array index, it becomes possible to describe a dichotomised 3D image of arbitrary size using a 256 bin histogram, see figure 5.6. Each bin gives the frequency of occurrence of one of the possible spatial patterns of the elements

within the cells of the image. This compact representation is used to simplify computation: geometric properties need to be evaluated only once for each of the possible spatial patterns and the results scaled according to histogram frequency (i.e. the number of instances of the pattern within the image). Any such cell pattern histogram then represents an ensemble of image realisations, each possible realisation having an identical population of cell patterns, but each with a unique spatial organisation constrained by object-background interface continuity. Excepting relatively few trivial cases, synthesising images according to such a histogram is difficult because of the combinatorial nature of the spatial constraint. Hence calculation of a cell pattern histogram is in practice a one-way information reduction process.

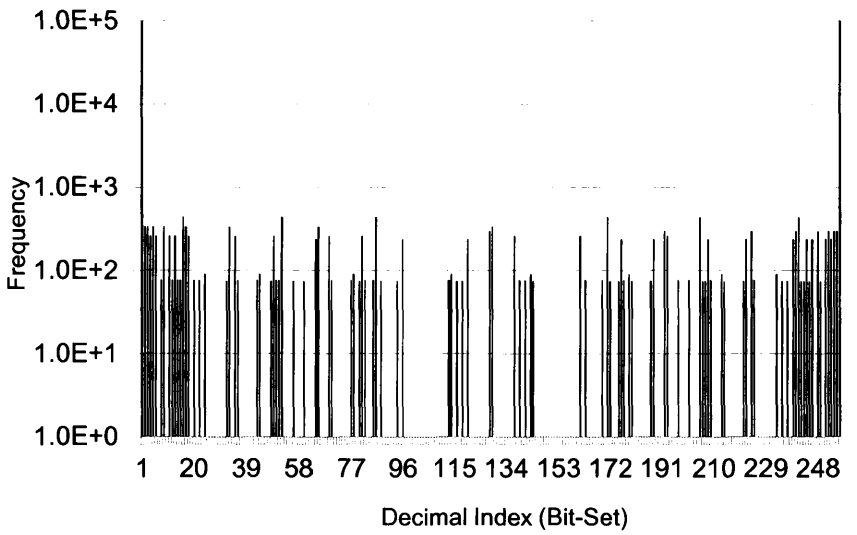

Figure 5.6 Cell pattern histogram of sphere.
Sphere radius 31 elements, within image definition of 64^3 elements.

The algorithm generating the cell pattern histogram has been rewritten in several forms during the course of this project, each providing a different balance between flexibility and computational performance. An abstraction of the image representation, support for image sub-regions and a parameterised image element comparison operator have all been found useful under particular circumstances. Development in this respect is set to continue as there are specialised application areas (e.g. porous objects with irregular boundaries) for which the present implementation is unsatisfactory. Another longer term objective is parallel computation of the histogram, this becomes desirable when more complex comparison operators are applied to high definition images.

5.1.9 Cell Interface Model

As previously noted, interface cells require a model describing their internal geometry so that measures can be defined. (Cells entirely of a single class are already fully described by the cell geometry, hence there are always two trivial cases for any dichotomised image, irrespective of the lattice employed.) In the case where a 3D interface is aligned with the principal planes of a rectangular image lattice, creating four object vertices on one side and four on the other, bisection of the cell by a plane is the only unbiased assumption as figure 5.6 illustrates. Similarly, when a single vertex belongs to one class and all others do not, it is easy to imagine a plane dividing the cell into a tetrahedral corner fragment versus a complementary shape (an irregular heptahedron) as in figure 5.7 (below).

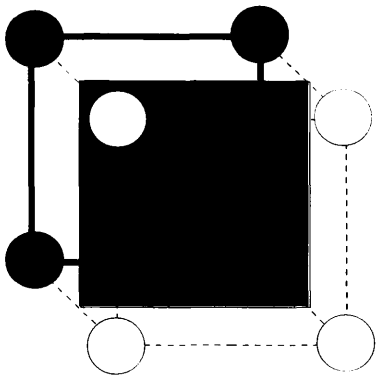

$2^0 + 2^2 + 2^4 + 2^6$
$= 01010101_2$

Figure 5.7 Image cell in 3D – axially aligned interface.
Pore object elements in black, solid background in white.
Object surface shown in grey.
Corresponding bit set on right (one for object, zero for background).

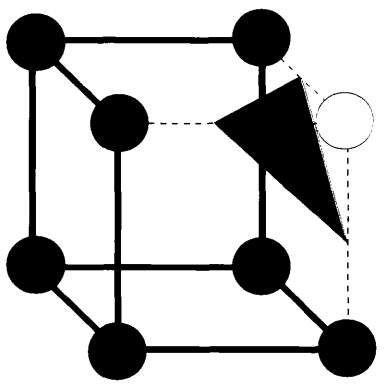

$2^0 + 2^1 + 2^2 + 2^3$
$+ 2^4 + 2^6 + 2^7$
$= 11011111_2$

Figure 5.8 Image cell in 3D - corner interface.
Pore object elements in black, solid background in white.
Object surface shown in grey, bit set on right.

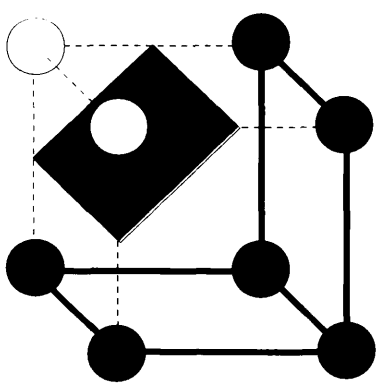

$2^2 + 2^3 + 2^4$
$+ 2^5 + 2^6 + 2^7$
$= 11111100_2$

Figure 5.9 Image cell in 3D - edge interface.
Pore object elements in black, solid background in white.
Object surface shown in grey, bit set on right.

In the case of two vertices that are adjacent according to the lattice axes/edges (i.e. not diagonally) a plane divides the cell into a triangular prism edge fragment plus its complement see figure 5.8. These are the only really simple cases; any other arrangement having two or more vertices per class cannot be described by a single planar section. Considering these three simple patterns and the symmetry of a rectangular lattice, it can be seen that there are in total 8 corner + 12 edge + 6 cuboid = 26 simple cases in addition to the 2 trivial cases where the entire cell is a single class. Therefore there are 256 – (26 + 2) = 228 cases that may be considered complex because they require more than a single section plane. All of these more complex cases exhibit some degree of symmetry which may in principle be exploited to condense the algorithms. For geometric measures (i.e. everything except total curvature) however, the spatial resolution of the image must be considered. If the spatial resolution is allowed to differ between the principal axes of the image then general purpose algorithms are required (see Ohser & Mucklich, 2000, pp.116-137). These algorithms, based upon the stereological formulae of Crofton, are used for all practical work unless otherwise stated. In an attempt to digest the algorithms and improve comprehensibility, the source code has been partly re-factored during the course of the project. It was this subdivision and re-structuring of the "monolithic" functions of Ohser & Mucklich that was instrumental in achieving a solid understanding of the principles underlying these estimation algorithms.

In order to reinforce understanding of cell model geometry, a manual exercise comparing conceptual 2D models was undertaken. These models were conceived from purely geometric considerations i.e. without reference to any statistical method. These are presented using two simple objects as examples in figure 5.10 overleaf along with their associated area and perimeter estimates shown in table 5.2 following. In the figure, the interface between object and background that is determined under a particular model is shown as a solid line in each case. In the first column on the left is the square element model, in the middle is linear subdivision of edges and finally on the right is an edge subdivision using segments of a circle.

The table shows the variation in geometric measures resulting from the choice of model; as much as 30% relative to the smallest estimate for area and perimeter. The topological measure χ estimated from object vertices and edges (shown as solid in the figure) is in all cases equal to +1 i.e. the total curvature is 2π. Which of these models is considered more accurate depends only upon the specific details of the application; all embody some form of assumption regarding the shape characteristics of the objects to be analysed.

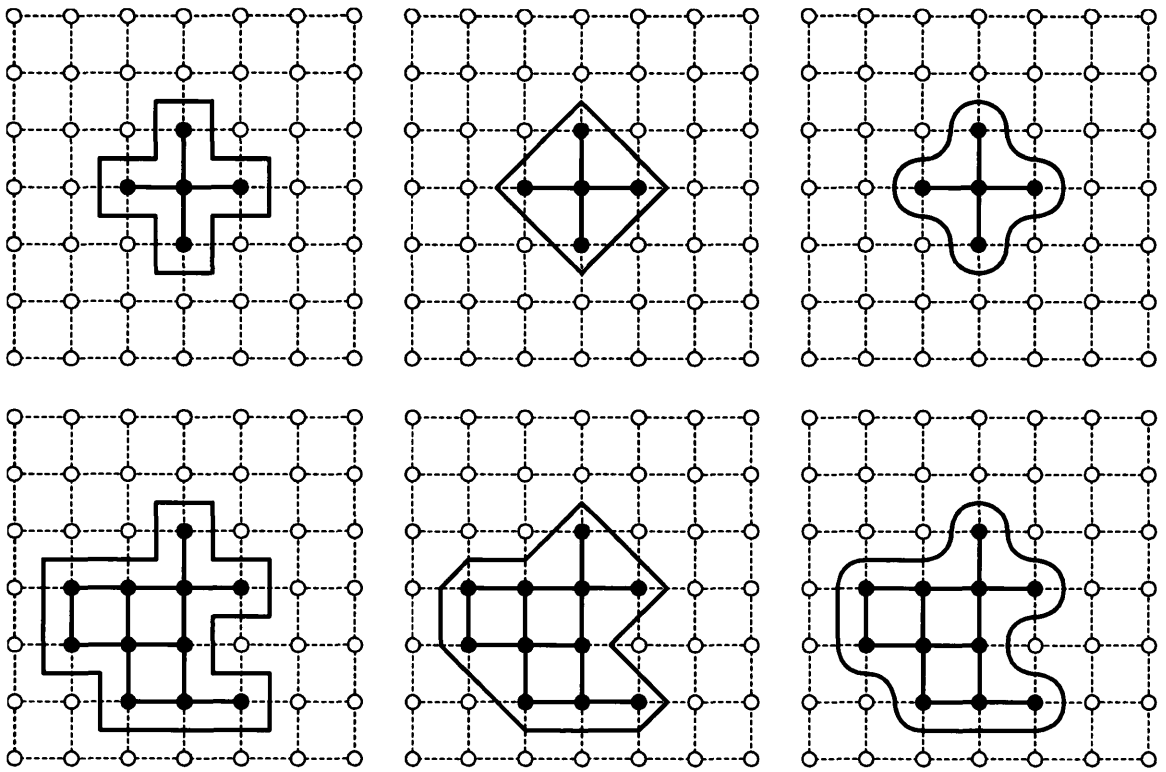

Figure 5.10 Comparison of 2D cell interface models.
Cross and irregular object with rectangular (left), linear edge bisection (middle) and circular edge bisection (right) cell interface models.
The image lattice is shown using dashed lines, with circles representing background image elements. Objects are shown using solid image elements connected by solid lines.

Shape	Measure	Cell Interface Model		
		Square	**Linear bisect.**	**Circle bisect.**
Cross	Area	*5*	*4.5*	$4+\pi/4 \approx 4.8$
	Perimeter	*11*	$2\sqrt{6} \approx 8.5$	$3\pi \approx 9.4$
Irregular	Area	*11*	*10.5*	$10+\pi \approx 13.1$
	Perimeter	*18*	$4+14/\sqrt{2} \approx 13.9$	$4+14\pi/4 \approx 15.0$

Table 5.2 Comparison of 2D cell interface measures.
(See figure 5.10 for a depiction of shapes.)

5.1.10 Image Boundaries

So far no consideration has been given to how measure estimation is affected by image boundaries. As with other spatial discretisations it is feasible to choose boundary conditions yielding periodicity, continuation or isolation, as required by the application. For the analysis of soil or other materials with a complex aperiodic structure an isolated boundary is a sensible choice; nothing is assumed about structure beyond the boundary. This is the mechanism presently implemented such that only interior image cells are processed into the cell pattern histogram, there are however consequences in this approach for objects that intersect the boundary. For measures at the dimensionality of the image (volume for a 3D image, area in the 2D case) this is a relatively minor issue in practice. Assuming the dimensions of the image are large and object elements are not concentrated on the boundary, the contribution of boundary elements is very small in relation to the whole. This is not necessarily true in the case of lower dimensional measures however, so care must be taken in their interpretation. Consider the image of figure 5.4 in which object elements (dark grey) lie on the image boundary, these are surrounded by interface elements except on the boundary i.e. no measure relating to the interface can be defined along the boundary. This leads to somewhat unnatural measures of curvature because a closed surface is not present; in the case of total curvature, the estimated measure for each object intersecting the image boundary can be no more than half of the value of the complete object (and as little as one eighth for an object intersecting at a 3D image corner).

5.1.11 Extended Estimators (Cell Interface Models)

The estimation procedure described previously is limited by the information available for a single image cell, the 8 binary classified elements of a 3D image cell lead to only 256 possible different states. This means that measures are quite crudely quantised at the cell level because an interface can only bisect an edge between two elements. In terms of orientation this means that only angles of 0° and 45° relative to a principal axis can be accounted for. Similarly, for surface area and volume, only a modest number of discrete steps in each measure is possible. (A topological measure such as χ and hence total curvature is, of course, unaffected by any such concerns, being independent of distance and direction.) By including further image elements (i.e. by considering a larger neighbourhood) in the estimation procedure for a cell, it is possible to judge that the cell is subdivided more finely then by edge bisection. In terms of numerical analysis, a *quadrature rule* of more than 8 points is applied to estimate each measure. For example, consider a 4^3 region of binary classified image elements i.e. a neighbourhood of 3^3 image cells with the cell to be estimated at the centre. Estimators based on this scheme make use of $4^3 = 64$ points (image elements) and so reduce the quantisation of measures significantly; this may be considered a smoothing mechanism. Such improvements are however costly to implement: dealing with image boundaries becomes more complex, and specialised programming techniques are required to deal a cell pattern description 64 bits in size. Apart from implementation difficulties, locality of estimation is reduced by adopting such a scheme. Whether this is a problem depends upon the nature of the image; if it consists of

objects whose most spatially detailed structures are large compared to the image definition then smoothing is generally advantageous. For an image dominated by spatial structures at the limit of image resolution (as in the case of many soil images) then an extended estimator is unlikely to offer much benefit.

5.1.12 Verification

The implementation was assessed and verified using images of objects with known properties. The obvious choices for this purpose are simple geometric objects (such as cuboids and spheroids) for which functional measures can be determined analytically. Synthesising volume images of such objects involves discretisation of a geometric model and this was implemented without great difficulty by a rejection-test method. It is important to consider objects in various orientations with respect to the image lattice as this affects the accuracy of estimation in some circumstances, hence asymmetric objects were used to achieve a more robust verification (a sphere or ball for example is not appropriate). The verification was also carried out at image definitions of 256 elements and 512 elements to assess the extent of discretisation effects. For each verification an object occupying between 15.5% and 15.9% of the image volume (without contacting the image boundary) was used. The object was synthesised then analysed at each orientation from -90° to +90° in steps of 5°. Analytically computed MF measures were used to standardise the estimated measures, expressing them in the form of a percentage which allows all the measures to be displayed together using a single scale. The resulting graphs are shown in figures 5.11 and 5.12 on the pages following; the total curvature is not displayed on any graph because the exact value of 4π is recovered in all cases (i.e. it is always 100% accurate). This exactitude is a consequence of the "fine tuning" of the topological measure according to the lattice employed for estimation (Ohser & Mucklich, 2000, pp.121-124). In the following discussions the term "error" refers exclusively to the systematic bias (continued on p.167)

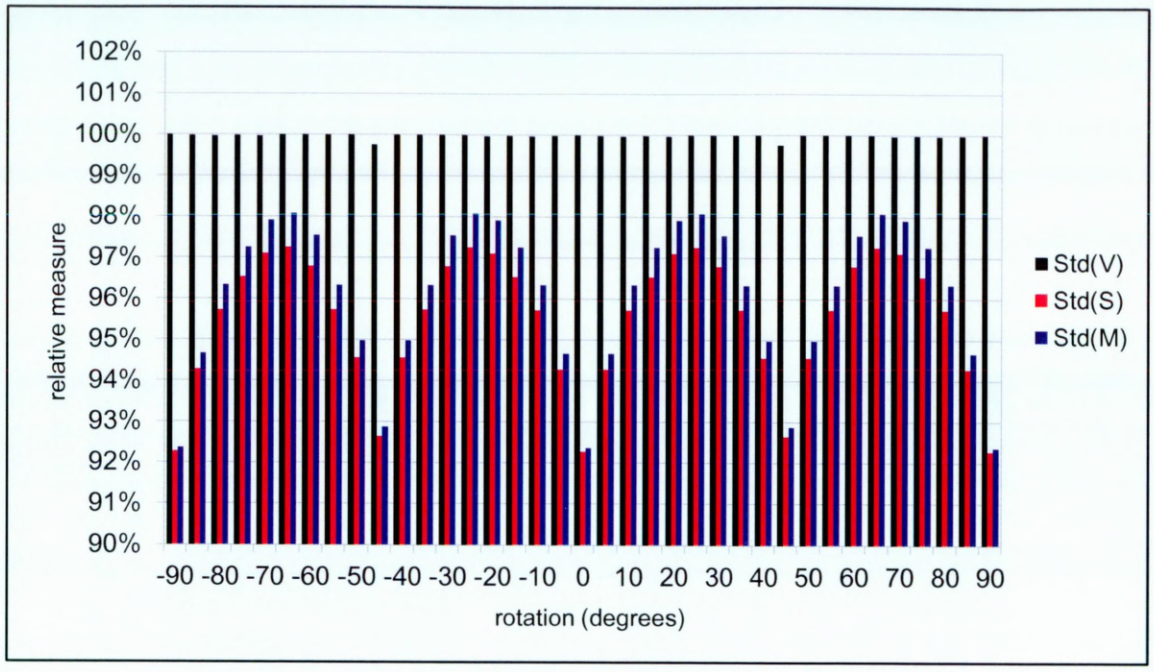

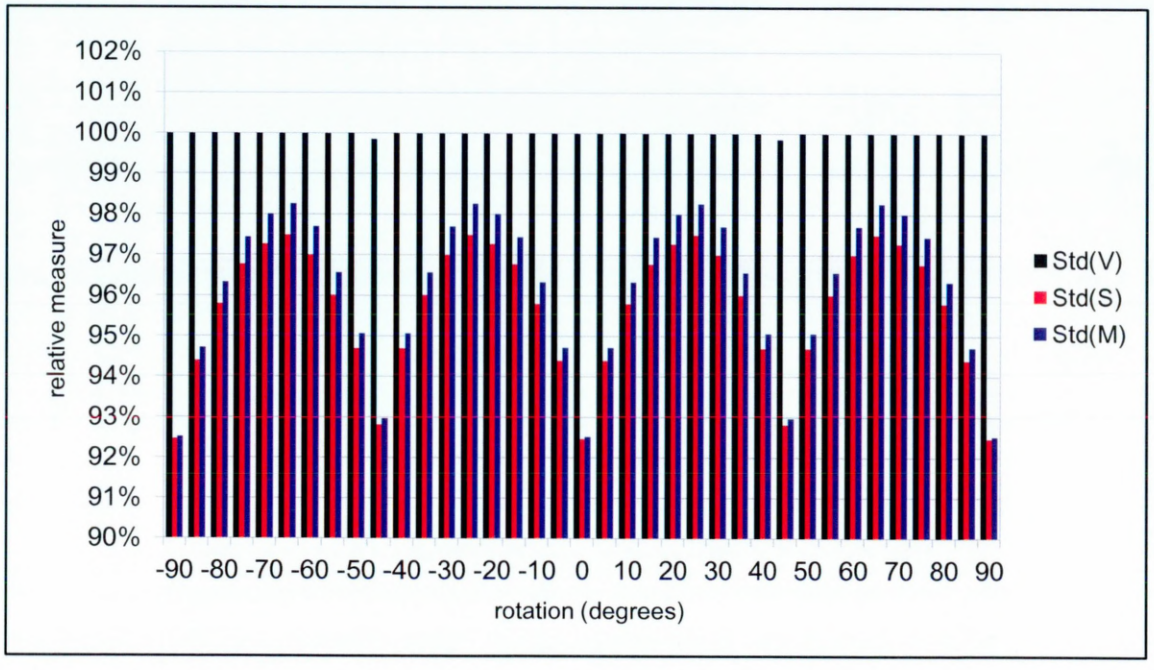

Figure 5.11 Cuboid orientation sensitivity of functional measures.
Discrete oriented cuboids at image definitions of 256^3 (uppermost) and 512^3 (lower). Volume (V), surface area (S) and integral mean curvature (M) are standardised relative to analytically determined values. Cuboid side lengths are 180, 120 and 120 image elements along the X, Y and Z axes respectively at zero rotation for the 256^3 image; double these values for 512^3 definition. The measures are computed for the cuboid rotated in increments of 5 degrees about the Z axis from -90 to +90 degrees.

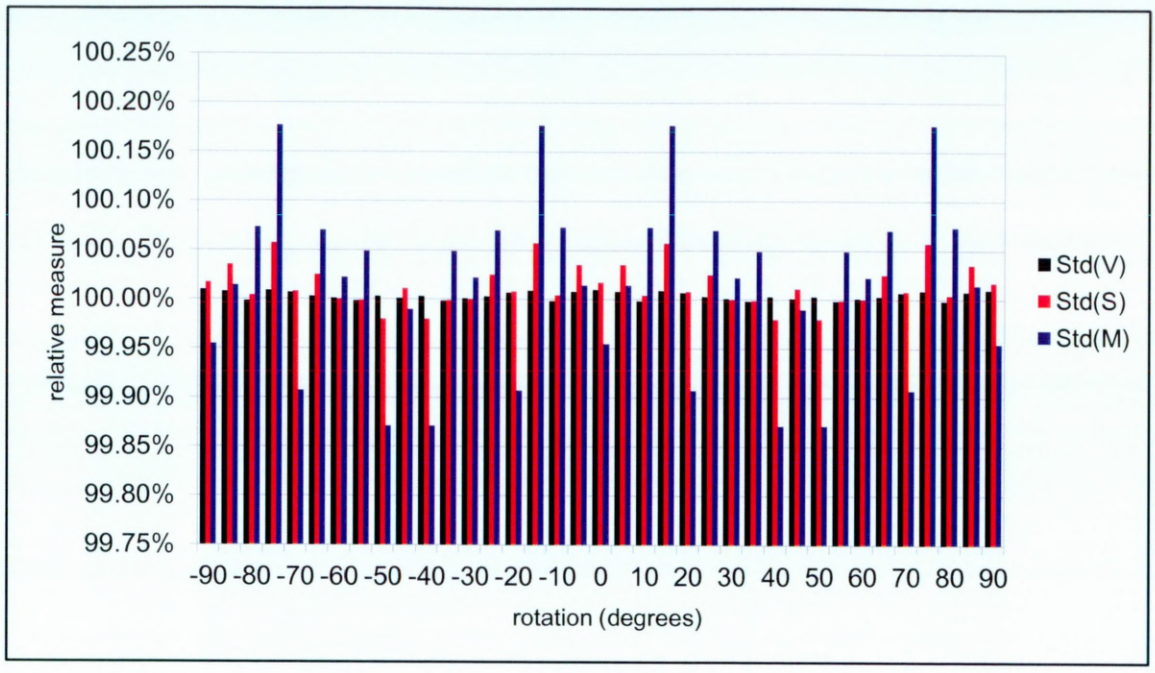

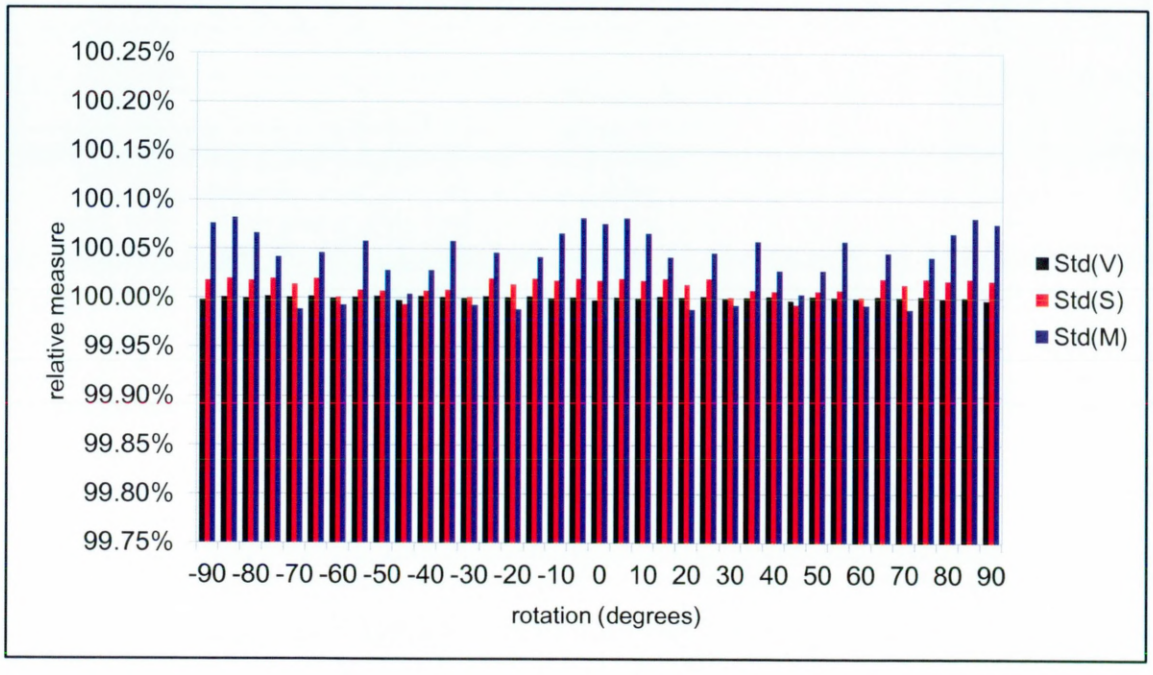

Figure 5.12 Spheroid orientation sensitivity of functional measures.
Discrete oriented spheroids at image defintions of 256^3 (uppermost) and 512^3 (lower). Volume, surface area and integral mean curvature are standardised relative to analytically determined values. Semi-major radii are 112, 75 and 75 image elements along the X, Y and Z axes respectively at zero rotation for 256^3 images; double these values for 512^3 definition. The measures are computed for the spheroid rotated in increments of 5 degrees about the Z axis from -90 to +90 degrees.

in measures resulting from the discrete represenattion of images.

It is immediately obvious that the estimate of volume for a cuboid is very accurate; there is approximately $\pm 0.25\%$ error at 45° rotation and less than ±0.03% error at other angles in the case of the 256 element image definition. At the higher definition of 512 elements these errors reduce to less than ±0.15% and ±0.005% respectively. The estimates of surface area and integral mean curvature for a cuboid both follow a rectified sinusoid pattern with the maximum error occurring at 0° and thereafter at multiples of 45°. These errors are large in magnitude, lying between -1.93% and -7.73% in the case of the 256 element definition and reducing slightly to between -1.75% and -7.54% at higher definition. In other words while the accuracy of volume estimation is dominated by image discretisation error (doubling the image definition along each axis resulted in nearly halving the error) the estimation of measures defined on the surface of a cuboid is more difficult to characterise; this is discussed at the conclusion of this section, below.

Comparing figure 5.12 to figure 5.11 it is obvious that estimates for the spheroid are much more accurate than those for the cuboid (note the different scale on the graphs). The spheroid volume estimate is accurate to within $\pm 0.01\%$ at 256 element definition and this improves to within $\pm 0.003\%$ at 512 element definition. The surface area and integral mean curvature estimates are accurate to within $\pm 0.057\%$ and $\pm 0.177\%$ respectively at lower definition and these are improved at higher definition to $\pm 0.02\%$ and $\pm 0.08\%$ respectively. It is

therefore reasonable to conclude that image definition is the dominant factor affecting the accuracy of estimates for the spheroid.

The difference in estimation accuracy between the two objects can be explained by considering their surface geometry in relation to the estimation mechanism. In the case of an oriented cuboid only six planar faces exist in the image and for every image cell of a particular face, the same local estimation error is repeated many times. There can be no cancellation of error between either parallel or orthogonal faces because the periodicity of the error is 45° (which follows from theoretical considerations outlined previously) and so for a cuboid all local errors accumulate, resulting in a large global error. For a spheroid on the other hand, surface orientation varies continuously through all directions of 3D space and so the estimation error differs slightly between adjacent image cells on the surface. The global error is therefore reduced by cancellation; over estimation can approximately balance underestimation over the surface as a whole.

The rudimentary problem in estimating surface area and integral mean curvature based on image cells stems from a lack of *angular resolution* i.e. the model applied to the lattice structure does not describe orientation with sufficient accuracy. In principle, this problem can be addressed by using an extended estimator to gain angular resolution at the cost of sacrificing spatial resolution. In (Ohser & Mucklich, 2000, pp.138-139) this problem is briefly discussed in a 2D context using a "rolled stainless steel" example image. The angular resolution problem is however compounded with one of spatial

resolution when a faceted, rather than smoothly continuous, surface is considered because changes in orientation are localised in an "all or nothing" fashion. This implies that accurately computing surface measures based on the *locally detected* surface of a faceted object requires infinite resolution in the image i.e. an approach based on a discrete image lattice is inappropriate for this form of object. As an alternative, image-global surface extraction (Li et al. 2006) could be used and measures determined from the resulting geometric description.

The relative importance of local estimation errors being cancelled raises questions regarding the accuracy of surface based measures for objects that intersect image boundaries. In figure 5.13 (following) objects identical to those of the low definition examples in figures 5.11 and 5.12 have been truncated by centering them on an image boundary (the plane y=0). From these graphs it is obvious (noting the necessarily different vertical scales) that the main effect of object truncation is to cause volume to be overestimated. In the case of the truncated spheroid, the maximum error occurs at 0° rotation and reduces smoothly towards 90°. The orientations 0° and ±90° correspond respectively to the maximum and minimum areas of intersection between object and boundary. For the truncated cuboid a decaying pattern is also discernable. The pattern in other measures (with the exception of total curvature which has the exact value 2π in the case of the halved objects) closely resembles that of the non-truncated objects.

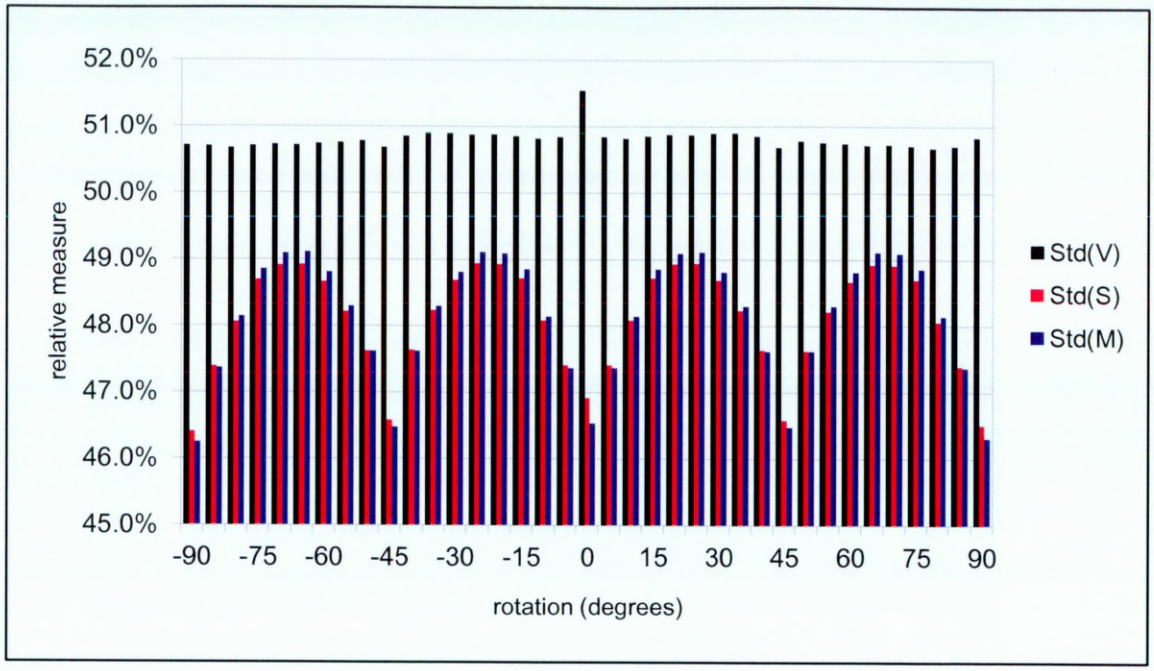

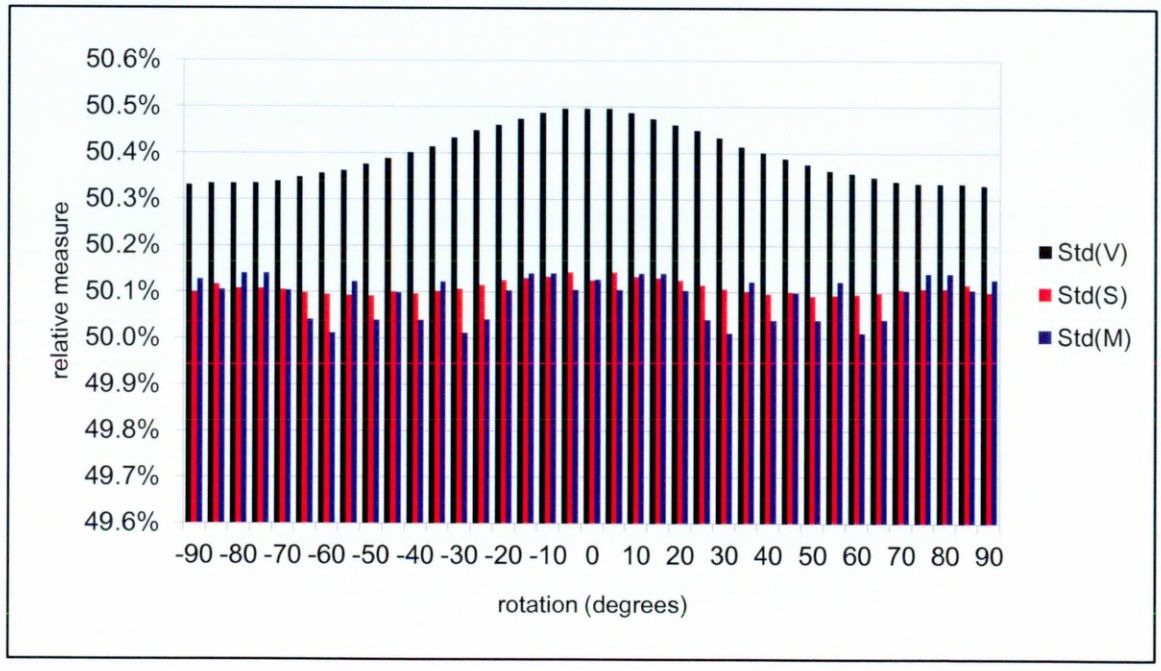

Figure 5.13 Truncated object orientation sensitivity of functional measures. Discrete oriented spheroid (uppermost) and cuboid (lower) both at 256^3 image definition. Measures are standardised relative to analytically determined values for the full object (without truncation and independent of orientation). Other parameters are the same as in the previous 256^3 definition images of figures 5.11 and 5.12.

5.1.13 Conclusions on Verification

The conclusion of this verification work is that image cell based estimators are appropriate for images in which surface orientation is significantly variable throughout the image. The degree of accuracy is related to the ability to resolve object structure (i.e. the object size relative to image definition) but is also significantly affected by the balance of local estimation errors. In general, for any naturally occurring material such as soil (containing many "randomly" oriented surfaces), these estimators are not the limiting factor on accuracy. Instead it is limited image resolution and failings of image acquisition and segmentation procedures that are likely to be the main causes of error.

In the case of materials with an apparently more angular (i.e. a less random) structure, inspection of the cell pattern histogram may help in identifying some accuracy problems. The degree of uniformity in the distribution can be used as an indicator of estimation accuracy: strongly non-uniform distributions (typical of "engineered" structures) are indicative of orientation sensitivity and hence potentially limited accuracy.

5.2 Connectivity

The general concept of connectivity has long been considered by mathematicians; the famous paper on the "Seven Bridges of Konigsberg" problem (Euler,1736) laid the foundations for modern *graph theory* and this remains the basic tool for connectivity analysis (Tanenbaum, 1981). Graph theory is also intimately related to topology (Euler, 1736) hence the Euler characteristic χ is sometimes used in describing connectivity. An example of this latter approach applied to soil is (Vogel, 2002) in which χ is used to characterise changing topological structure with respect to *seiving* of pore size classes achieved by morphological transformation of an image.

It is easy to see how graph theory can be applied e.g. in the study of traffic flow along physical road networks; road junctions are the *nodes* or *vertices* of the graph and these are connected by *links* or *edges* which are unbroken sections of road, see figure 5.14. In this example the edges are shown as straight lines rather than following the geometry of the roads; the reduction of detail is taken further in the right hand section of the figure where a topological representation of the road network is shown. This is a convenient abstraction rather than a requirement of graph representation; arbitrarily complex information can be associated with any node or edge.

There are numerous ways in which a graph can be represented (Bondy and Murty, 1976) of which three commonly used schemes are shown in figure 5.15. Of these the *incidence list* (also known as the *edge list*) is the most compact

scheme for a sparse graph (i.e. one in which the number of edges is much less than the theoretical maximum). The graphs considered here are undirected i.e. edges do not carry directional information and so the cost of traversing an edge from node A to node B is equal to that of traversing from B to A. An undirected graph having ***n*** nodes has at most ***n(n-1)*** edges; the road network example graph may fairly be considered sparse because 8 edges is significantly less than 6*5=30. Each node of a graph can be characterised by the number of edges linking it to other nodes, this is referred to as the *degree* of the node; for the adjacency list representation shown in figure 5.14 (overleaf) the degree of each node is the number of indices in each tuple.

For a graph having many nodes, a useful summary description is its *degree distribution* i.e. a histogram of node degree. Using the characteristics of this distribution a graph may be compared to one of a number of distinct models such as (Barabasi and Albert, 2002) versus (Watts and Strogatz, 1998) or (Erdos and Renyi, 1960).

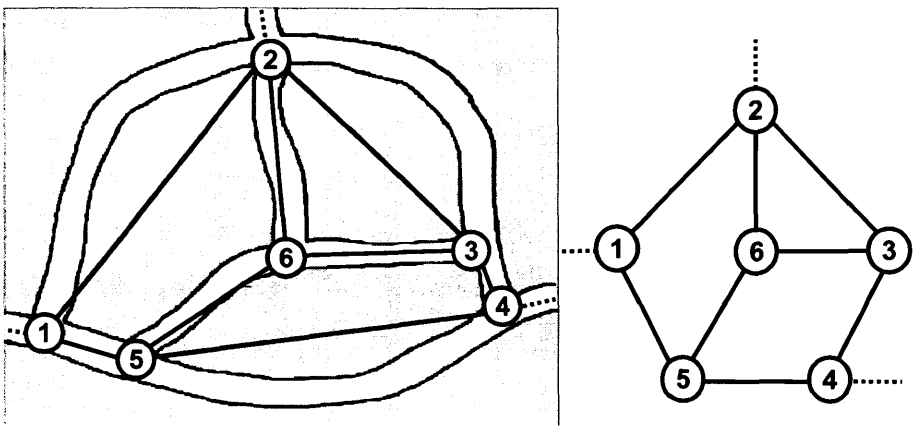

Figure 5.14 Road network graph.
Sketch of road network with graph superimposed (left).
Nodes (numbered circles) placed at road junctions are connected by edges (heavy black lines).
Uniform node spacing (right) helps reveal structure; the two graphs are *topologically* identical.

Adjacency Matrix:

-	1	2	3	4	5	6
1	-	1	0	0	1	0
2	1	-	1	0	0	1
3	0	1	-	1	0	1
4	0	0	1	-	1	0
5	1	0	0	1	-	1
6	0	1	1	0	1	-

Adjacency list:

```
1:(2,5),
2:(1,3,6),
3:(2,4,6),
4:(3,5),
5:(1,4,6),
6:(2,3,5).
```

Incidence list:

```
(1,2),
(2,3),
(3,4),
(4,5),
(5,1),
(5,6),
(6,2),
(6,3).
```

Figure 5.15 Graph data representation schemes.
Relates to images of figure 5.14.
Matrix representation (left) is useful in revealing structure.
A sparse graph may be more efficiently described using one of the possible forms of list (middle and right).

There are, broadly speaking, two ways to approach the measurement of connectivity in digital images, each having its advantages and disadvantages. The first, which may be considered a reductionist approach, seeks to abstract the spatial complexity of each object into a minimal form such as that represented visually in figure 5.15. This is achieved via a morphological thinning operation (Serra, 1982) that reduces the set of image elements making up an object to a minimal set known as the *skeleton* (Pfaltz and Rosenfeld, 1967). Subsequent analysis of the skeleton image allows a compact graph to be extracted from it.

The principal stages of graph extraction for the road network example are illustrated in figure 5.16 (overleaf) and this example demonstrates that an apparently simple 2D image can generate more nodes and edges than expected. The procedure used in this case was that implemented in the "Skeletonize3D" plug-in module of the image analysis package known as FIJI, a software distribution of ImageJ, as described in (Schindelin et al. 2012). It appears that this implementation is sensitive to fine detail in the vicinity of junctions as node ***3*** in figure 5.15 is so close to node ***2*** that the two are difficult to discriminate without magnification. The edge connecting the two is superfluous with respect to the intended meaning of the original sketch image and represents a significant relative increase in nodes and edges (+17% and +14% respectively). This means that a connectivity measure determined from the graph may not accurately reflect the structure of the original image.

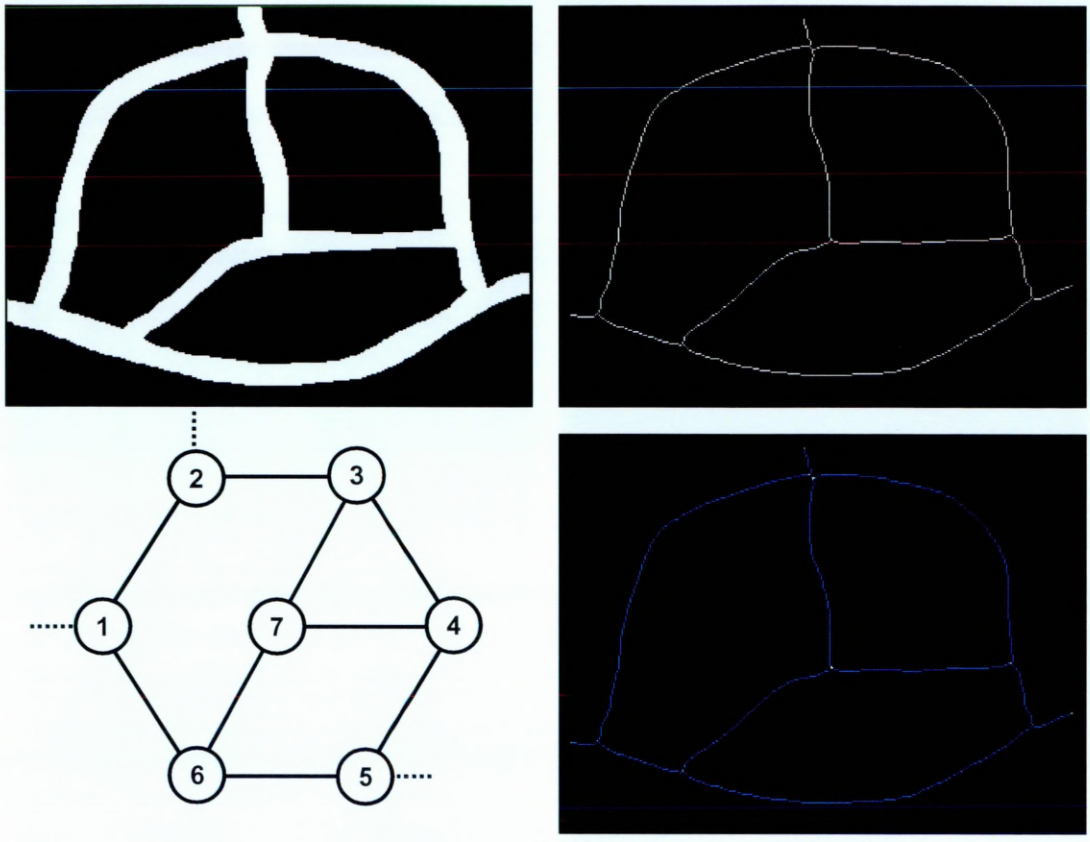

Figure 5.16 Stages in the extraction of a graph from an image.
Clockwise from upper left: segmented image object in white, object skeleton, analysed skeleton with colour coded features, extracted graph with uniform node spacing. The *Skeletonize (2D/3D)* plug-in module for *FIJI* was used to produce the second and third images.

Additional problems may occur in 3D images, where morphological thinning can produce a 2D surface (rather than a 1D edge) embedded in 3D. This occurs where a hollow object envelops some background obstacle creating a "shell" of possible paths (Lindquist et al. 2000). In the case of soil images this is not uncommon as isolated fragments of solid phase material (which is the background with respect to a pore connectivity analysis) may appear to "float" close to a larger mass of solid material. In reality such a fragment is presumably in contact via a "bridge" of solid material, but this bridging structure has not been sufficiently resolved by the imaging system and hence has not survived the segmentation procedure. One can also imagine that organic matter, acting as a form of "glue", might play a role in this phenomenon; the limited X-ray attenuation of organic matter means it is typically classified as pore under a two-phase segmentation model. Whatever the cause may be, the result is a 3D shell of skeleton elements, often with an approximately spherical form. Representing this shell structure using nodes and edges leads to a highly interconnected sub-graph; the spatial extent of the structure is typically small leading to a high spatial density of graph nodes. Such spatially dense sub-graphs are usually not representative of the overall structure within an image yet may strongly affect a connectivity measure, yielding misleading analysis results (personal communication of "Paco" Perez-Reche within SIMBIOS) and also implied in (Lindquist et al. 2000).

In practice, developing a reliable skeletonisation procedure involves some difficult decisions regarding the acceptable trade-off between algorithmic

simplicity and robustness. For example, reducing dense sub-graphs via an iterative "edge-collapse" procedure controlled by a Euclidean distance criterion is quite easy to implement, but automatically determining the appropriate criterion value (which may vary locally through the image) is challenging. In summary, analysis of connectivity via a skeletonisation procedure has significant value, but is difficult to implement with a level of robustness sufficient for a material as spatially complex as soil.

The second approach to analysing connectivity in digital images may be considered a "brute force" technique as it interprets every image element belonging to an object as a node of the objects graph; this is exactly the concept seen previously in figure 5.10. The seminal work on this approach is (Rosenfeld, 1970), notwithstanding prior art by Matheron and Serra (circa 1966) that remained obscure until the publication of (Serra, 1982). For the simple example objects shown in the figure, any graph representation (e.g. an adjacency list) can be used without concern about storage or processing costs. In practical cases, however, objects exceeding 10^6 image elements (and hence nodes) are commonplace within volume images and so graph representation is a matter of concern. In this case an adjacency list, for example, may have a storage cost greatly exceeding that of the image from which it is derived and this also tends to result in very large processing costs. Such problems can be avoided by using the classified image to represent the graph implicitly; nodes are simply image elements while edges are determined dynamically as required using a neighbourhood defined on the image lattice.

The basic neighbourhood in 3D space is shown in figure 5.11, this particular pattern is known by various names such as "6-connected neighbourhood" or "7-stencil" (Rosenfeld and Kak, 1982). In this work a neighbourhood will be identified by edge count (rather than node count) so terms such as "6-connected neighbourhood", abbreviated as 6CN, are used henceforth. Applying a neighbourhood recursively over an image in conjunction with a membership condition (that discriminates object elements from the background) allows a cluster of elements to be detected. Figure 5.17 shows a 3D neighbourhood of object elements (solid black circles) and the connections between them (heavy black lines) according to the 6CN. An example of 3D clusters formed by the 6CN is shown in figure 5.18. Choosing other neighbouring lattice points allows 8CN (the vertices of a cuboid) and 12CN (midpoints of the edges of a cuboid) to be defined; conventionally, a neighbourhood should be symmetric to the extent possible for a given lattice. Although the edges of the 6CN, 8CN and 12CN represent different steps in Euclidean distance between lattice points, this is not significant for topological analysis. The 6CN, 8CN and 12CN can therefore easily be treated as building blocks and used in combination to define 6+8=14, 6+12=18, 8+12=20 or 6+8+12=26 connections between a lattice point and its neighbours. The 6CN, unless otherwise specified, is used for all subsequent examples of cluster extraction from images.

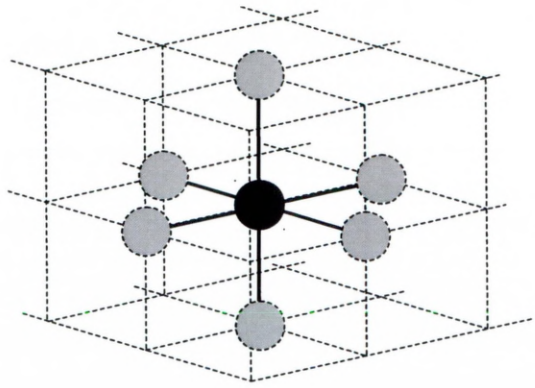

Figure 5.17 The 6-connected 3D neighbourhood.
The central element is shown in black, neighbours in grey.

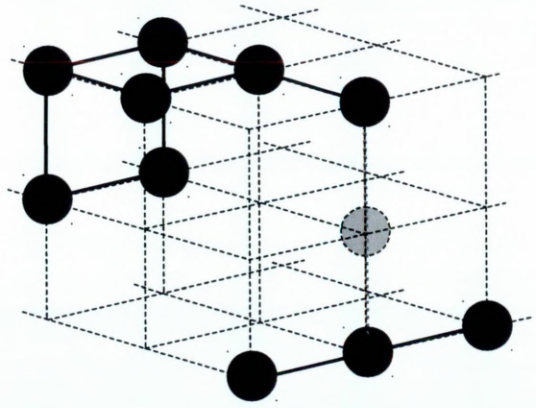

Figure 5.18 Clusters in the 6-connected 3D neighbourhood.
Two objects (in black) are defined via the 6-connected neighbourhood.
Adding a further object element (shown in grey) would join the two,
forming a single cluster.

5.2.1 Implemented Forms of Analysis

Once the graph structures within an image have been identified, they can be analysed. Only certain forms of analysis are likely to be useful in relation to certain forms of graph, however (DaCosta et al. 2007). This is particularly relevant when considering the difference between graphs obtained by skeletonisation versus those implicitly represented on an image lattice. The importance of this distinction can be readily understood by considering the degree distribution; in the latter case (an image lattice graph) the node degree is constrained by the neighbourhood applied to the image lattice. A graph obtained using the 6CN, for example, has a degree distribution that consists of only six histogram bins. Given such a limited quantity of information it is difficult to extract a meaningful characterisation from an image lattice graph (whereas a skeletal graph typically has a wide range of node degrees in its distribution and hence can be compared to some reference model). This problem resulting from the implicit definition of a graph on an image lattice means that measures of connectivity based on the degree distribution have poor relevance. Similarly measures based on the notion of *clustering* (Watts and Strogatz, 1998) are of little use in the case of the 6CN. The recursive expansions of a neighbourhood so as to consider neighbours of neighbours, and so on, is of questionable value on the regular lattice structure of an image. Discrimination over shorter ranges remains poor, but analysing longer range structure is hampered by the combinatoric explosion of paths through locally dense sub-graphs. It may be that this problem can be conquered by an efficient algorithm, but this is not a problem addressed within the present work.

There is however useful information to be gained by identifying connected clusters on an image lattice when measures such as the Minkowski functionals can be determined selectively rather than for the image as a whole. This permits pore objects to be ranked according to a measure (volume or surface area for example) or summarised according to how they fill or connect regions of space. With respect to the latter criterion, it is useful to consider how the pore space within a region of interest connects to the space outside (i.e. the image boundary in the default case where the entire image is analysed).

A simple measure of bulk connectivity within an image region can be obtained by computing the relative fraction of pore volume that connects with the region surface:

$$C_E = \frac{V_{surface}}{V_{region}} \qquad \text{(equation 5.3)}$$

This can be interpreted as a region "escape probability" i.e. it is the probability that a connected path exists between a randomly chosen pore element and the surface. This measure contains no directional information but does implicitly define a range of distances beginning at zero (for elements on the region boundary) and continuing up to the dimensions of the region of interest. It is a simple measure and thus has the virtue of being easy to communicate. This measure can of course be extended to provide some directional information; by summarising the clusters that connect to each region surface (e.g. each of the six planes of a cubic region) an escape probability can be computed for each.

Comparing the directional probabilities then permits a crude assessment of the degree of pore anisotropy.

A stronger assessment of soil pore connectivity can be obtained by considering *percolation* behaviour i.e. the ability to support transport over some distance (Grimmett, 1999). A simple Boolean measure is the existence of a connected path between two locations separated by some distance. In principle this simple measure can be extended to a comprehensive description over an entire object in the form of a co-occurrence distribution (i.e. a distribution of probability versus distance) or, if direction also is considered, a co-occurrence matrix. In practice however such a computation is difficult because of the need to consider all pairs of locations. The combinatoric growth of pairs with cluster size means that a naïve implementation becomes impractical at around 10^8 elements ($5*10^{15}$ pairs processed at 10^9 per second means more than five days processing time). As a cluster size of 10^9 elements may readily be found within an image of dimensions 512^3, so techniques of parallel computation and sub-sampling would be necessary to make such an approach practical in the general case.

Another potentially useful method of describing spatial structure is the *correlogram* whose close (complementary) relative the semivariogram was explained in chapter 2. The computational challenge in this case is even more extreme as processing cannot be restricted to some local neighbourhood of a particular cluster; the pattern of mid to long range spatial correlation is equally, if

not more, interesting than at short range. Additionally, there is the difficulty of interpreting and comparing distributions or matrices of data; such detailed information tends to create new analysis problems.

It is perhaps better then to consider how to pose a question that directly yields a "simple" result (i.e. a scalar or 3D vector value) as this helps to reduce the burden of technical knowledge associated with interpretation of measures. This can be achieved by considering two regions within an image separated by some distance and to calculate some average measure of the connectivity between the two. A relatively simple way to define such regions is by using the boundary planes of a cubic region of interest; the three pairs of opposing planes allow a measure to be computed for each of the principal axis directions. A simple method of obtaining a measure for each direction is then to determine the *spanning volume* for each pair of opposing planes (i.e. the total pore volume within the region of interest that connects both planes) and divide by the total pore volume in the region of interest:

$$C_S = \frac{V_{spanning}}{V_{region}} \qquad \text{(equation 5.4)}$$

This "axis spanning probability" is very similar to the escape probability measure described previously, except that a minimum separation condition has been imposed with respect to each principle axis. This has an important application in terms of studying transport processes through the soil structure. If C_S is zero for any axis, then transport is not supported in that direction.

5.2.2 Implementation of Cluster Detection

The cluster detection algorithm described following is based on a *breadth first* search (Knuth, 2011) through the image; see figure 5.19 for a pseudo-code description. Breadth first search (henceforth BFS) is used because it can be implemented such that peak memory consumption is reduced compared to depth first search (whereas DFS is more easily implemented).

```
set queue to empty
for each location in image
   if location is unlabelled-object
      set location to labelled-object
      add location to end of queue
     while queue is not empty
         remove search-location from head of queue
         (process search-location if required by
                                          application)
         for each visit-location in neighbourhood of
                                          search-location
            if visit-location is unlabelled-object
               set visit-location to labelled-object
               add visit-location to end of queue
            end-if
         end-for
      end-while
```

Figure 5.19 Breadth-first connectivity pseudo-code.
The entire image is traversed and for each unlabelled object (pore cluster) a breadth first search is initiated. Breadth first search uses a neighbourhood definition (typically the 6CN) in conjunction with a queue (FIFO list) to systematically process connected image elements. Changing the labelled-object value per cluster allows clusters to be individually identified.

The storage requirement for this algorithm can be divided into three parts: the segmented image, the label information used to prevent repeated visiting of an element, and the queue of elements being processed. In the form implemented, the segmented image and label information are merged to form a *connectivity map* in which sufficient bits are allocated for each map element such that three or more classes can be identified (background, unlabelled-object and labelled-object) with additional class identifiers being used to uniquely label individual clusters at the users option. The basic storage requirement that can be calculated in advance is therefore dictated by the image dimensions and the maximum number of clusters to be uniquely identified in the connectivity map.

The additional storage requirement for the breadth-first queue depends upon the spatial organisation of pore elements and hence is unknown in advance, but an upper bound is easily determined from the total number of pore elements. For a high definition image with significant porosity, the BFS queue is typically the dominant storage cost as each entry must store a 3D image coordinate. Also the peak queue size tends to become a significant fraction of the total number of pore elements with increasing connectivity and this is dependant in part upon total porosity. In order to manage this cost, the 3D coordinate information is packed into 32bits by allocating 10bits for each of the X, Y and Z indices (the remaining two bits are presently unused). This strategy does limit the dimensions of a region of interest to 1024^3 elements but this size is not far from the practical limit that can be handled easily, due mainly to the difficulty of segmenting such large images.

Another memory saving is realised by implementing the BFS queue using a linear table without link information (e.g. pointers or indices) so that queue order is implicitly given by table order. This table is managed in a lazy fashion i.e. BFS queue entries are not deleted for reuse until absolutely necessary. Rather, when table capacity is running low, the remaining active portion of the BFS queue is relocated to the base address of the table, overwriting the dead entries. As a consequence of these strategies, the software is able to extract detailed information from a high definition image, with the entire image as region of interest, using less than 1.2 Gigabytes of memory in total. A high definition region does require 5 to 10 minutes to process on contemporary hardware whereas a small region such as 256^3 can be analysed in a matter of seconds.

Parallel computation of connectivity has been addressed in (Rosenfeld, 1970) but only in an image-global sense; accelerating the detection of local cluster connectivity remains challenging. Although it is conceivable that the BFS based cluster detection algorithm presented here could operate by subdividing the image region of interest into blocks and processing many in parallel, the results of all sub-tasks must be merged together. This merging is in itself is a costly process i.e. it may be a limiting factor on performance. In part this is due to the current implementation using the minimum number of bits per connectivity map element. If instead, all cluster fragments are allowed globally unique identifiers, then the merging process is simplified. This however requires up to 32bits per

connectivity map element (there might be millions of cluster fragments in a high definition image) leading to very large memory requirements and reduced processing rate as a consequence. In short, efficient parallelisation of this type of algorithm is difficult and may not yield a clear benefit over the much simpler serial algorithm. Problems of this nature have been considered previously by (Rosenfeld and Pfaltz, 1966) who similarly conclude that parallelisation is not always practical.

Another consequence of the memory conservative approach adopted is the need to record information on each cluster as it is found. This information takes the form of a root point plus an axis aligned bounding box and these together permit a detailed analysis to be obtained with reasonable efficiency. A high definition image may contain a great many pore clusters of just a few elements in size yet these contribute little useful information compared with the few large clusters that may span a region. For this reason a threshold is implemented so that only clusters with a significant number of elements are recorded (those not individually recorded are still labelled and analysed "en masse"). The actual threshold number is parameterised within the software, with a value of one hundred being used by default (corresponding to a 3D cluster of 5 by 5 by 4 elements). This allows the storage requirement for cluster recording to be reduced, typically by several orders of magnitude, and eliminates the risk of software failure in the case of "rogue" images with 10^7 or more pore clusters. For clusters that are recorded, a distinction is made between those that connect to a region boundary versus those that are isolated. These distinct classes are

stored in separate lists with priority given to the connected list: in the unlikely event that storage capacity is exhausted, isolated clusters are replaced as necessary with new connected clusters.

Following cluster extraction, Minkowski functionals are computed for the region of interest as a whole and then for individual recorded clusters. The recorded cluster information is sorted into descending order of connectivity rank and then element count so that the individual labelling of clusters (if required by the user) produces a consistently organised connectivity map. Connectivity rank is determined firstly by the number of pairs of opposing region planes that a cluster contacts and secondly by the number of planes considered individually. The first (highest ranked) cluster is assigned the identifier zero, the next one and so on. All isolated clusters, irrespective of size, are assigned a special identifier that is one less than the background (solid phase) value. In other words, for an 8bit connectivity map image there can be at most 254 individually labelled connected clusters (using values zero to 253 inclusive) in addition to an arbitrary number of isolated clusters (all of which are assigned the value 254) against a background value of 255.

5.2.4 A Brief Example of Connectivity Analysis

A 3D colour rendering of a segmented soil image and its 6CN map image are shown in figure 5.20 (overleaf) with a summary of functional measures given in table 5.8 (the region of interest in this case is the entire image as shown). The immediate impression obtained from this table is that the majority of segmented pore space is interconnected. More detailed information is given in table 5.9 from which it can be judged that the image (region) is dominated by a large spanning pore cluster that connects along all three principal axes. Further, the fraction of pore space connected to each of the region planes is quite similar, suggesting that the spatial distribution of pores is reasonably uniform. The ultimate level of detail is obtained by examining the properties of individual pore clusters, table 5.10 shows selected information for the most and least significant of the surface connected pore clusters that were recorded. This clearly shows the extent to which the image is dominated by a single cluster and provides the means to identify specific clusters for further processing; the identifier is given in the form of a hexadecimal number e.g. $31_{16} = 49_{10}$ hence a total of 50 surface connected clusters were identified.

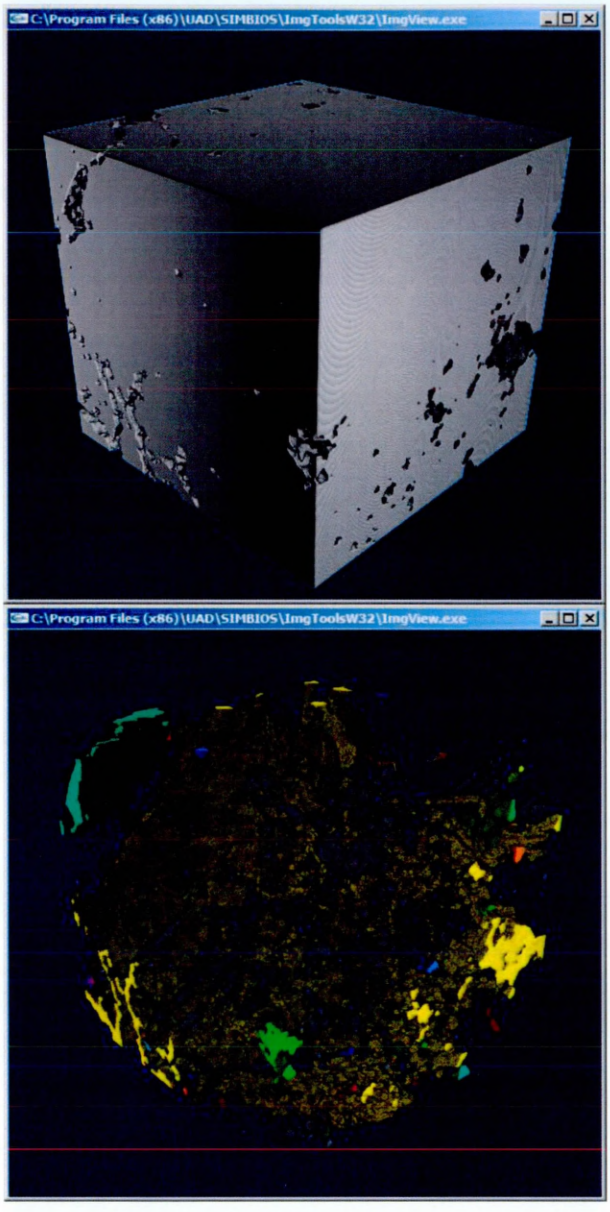

Figure 5.20 Soil connectivity map.
Above is a segmented image of soil rendered with solid phase opaque and pore transparent. Below is the corresponding connectivity map extracted using the 6CN; here the solid phase is transparent. A total of 3901 pore objects were identified of which 49 (shown in bright colours) are surface connected, representing ~9.5% of the image volume. The isolated pores (shown in grey) represent ~0.6% of the image volume.

Object Class	Vol. Conn. Ratio	Minkowski Functionals			
		V	S	M	K
Region	1	0.1013	11.899	381.2	37540
Surface	0.940	0.0952	10.112	167.1	-9498.0
Spanning	0.867	0.0878	9.339	147.1	-9042.9

Table 5.3 Functional measures by axial/planar connectivity class.

Category	Minkowski Functionals				MF Ratios			
	V	S	M	K	V	S	M	K
Region	0.101	11.899	381.2	37540	1	1	1	1
Principal Axis Spanning (Percolating)								
X axis	0.088	9.339	147.1	-9042.9	0.867	0.785	0.386	-0.241
Y axis	0.088	9.339	147.1	-9042.9	0.867	0.785	0.386	-0.241
Z axis	0.088	9.339	147.1	-9042.9	0.867	0.785	0.386	-0.241
Union	0.088	9.339	147.1	-9042.9	0.867	0.785	0.386	-0.241
Surface Connected								
X=0	0.089	9.492	153.1	-9236.2	0.876	0.798	0.402	-0.246
X=255	0.093	9.794	152.8	-9444.4	0.921	0.823	0.401	-0.252
Y=0	0.093	9.742	150.7	-9383.0	0.918	0.819	0.395	-0.250
Y=255	0.088	9.419	150.3	-9048.2	0.872	0.792	0.394	-0.241
Z=0	0.088	9.445	151.6	-9043.9	0.874	0.794	0.398	-0.241
Z=255	0.093	9.769	152.1	-9366.0	0.919	0.821	0.399	-0.249
Union	0.095	10.112	167.1	-9498.0	0.940	0.850	0.438	-0.253

Table 5.4 Surface connected pore clusters.
3D Minkowski functionals of pore element clusters that reach the surface of the region of interest.

Cluster		Minkowski Functionals				MF Ratios (relative to region)			
ID	# Elem.	V	S	M	K	V	S	M	K
0x0000	1474520	0.088	9.339	147.1	-9042.9	0.867	0.785	0.386	-0.241
0x0001	88499	0.005	0.394	3.1	-365.6	0.051	0.033	0.008	-0.010
0x0002	3775	0.000	0.023	0.5	-34.4	0.002	0.002	0.001	-0.001
0x0003	2962	0.000	0.024	0.6	-14.8	0.002	0.002	0.002	0.000
0x0004	1079	0.000	0.007	0.2	3.2	0.000	0.001	0.001	0.000
0x0005	754	0.000	0.005	0.2	0.5	0.000	0.000	0.000	0.000
0x0006	570	0.000	0.007	0.4	-32.8	0.000	0.001	0.001	-0.001
...			...				...		
0x0031	103	0.000	0.001	0.1	6.4	0.000	0.000	0.000	0.000

Table 5.5 Functional measures of spanning clusters.
3D Minkowski functionals of pore element clusters that span the principal axes of the image.

5.3 Pore Size Distribution

The pore size distribution (henceforth PSD) has been used to characterise porous media including soil since the early 20th century but despite a lengthy development, PSD estimation methods suffer from numerous issues as described in (Nimmo, 2004). Intrusion porosimetry using mercury or some other fluid is constrained by the pore *throat* or *neck* size (Nimmo, 2004) in relation to fluid properties, while image based techniques are limited by finite resolution effects. PSD has historically been estimated manually from serial sections but judgement of local pore size can be challenging and the work-load involved in applying this approach to high definition volume images is prohibitive. The ability to automatically determine PSD from a digital image is therefore attractive; the errors, assumptions and variability introduced by physical experiment and manual analysis can be avoided. This is not to say that automatic methods of PSD estimation from digital images are straightforward, in fact there are difficulties of algorithmic complexity as well as the more obvious problems of finite resolution and accurate image segmentation (Peth et al. 2008).

There seem to be two distinct approaches to estimating PSD from digital data: the "brute-force" stochastic sampling procedure described by (Battacharya and Gubbins, 2006) versus the determinism of the morphological analysis based method described by (Lindquist et al. 2000). The former method is notionally simpler to implement but consumes almost limitless processing power in its naive form; (Battacharya and Gubbins, 2006) are largely concerned with rather

complex enhancements which, in addition to parallelisation of the algorithm, help to deliver acceptable accuracy (according to a statistical convergence criterion) in reasonable time. The latter method, described in some detail by (Lindquist et al. 2000) is based on reducing the pore space to its discrete skeleton (a set of image elements as described previously) using a sequence of morphological erosions under topology preserving constraints (Lee et al. 1994). In (Lindquist et al. 2000) the term *medial axis* is also used to refer to the pore space skeleton, this is however somewhat imprecise. The medial axis can be precisely defined in a way that is particularly relevant to the estimation of a PSD:

"The set of centres of maximal spheres inscribed within an object."

which leads to a measure such as the diameter of inscribed spheres being used to form the size distribution. Note that in the 2D case, illustrated in figure 5.21 below, the above definition could be phrased:

"The set of centres of circles which touch the surface at two or more points."

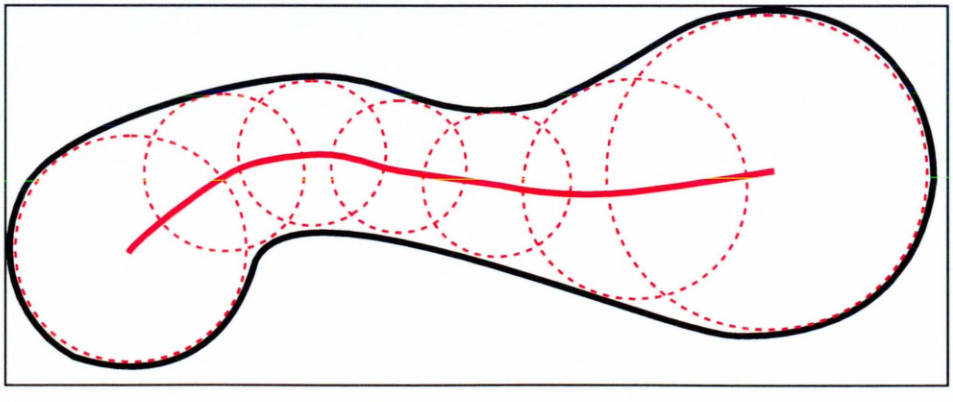

Figure 5.21 - Medial axis definition.
The boundary of a 2D shape (solid black) and its medial axis (solid red). The centre of any maximal inscribed circle (dashed red) must lie on the medial axis.

Many authors use the terms *skeleton* and *medial axis* interchangeably but in the context of the present work *skeleton* will be used in reference to a discrete image-based representation (i.e. a set of voxels in 3D) whereas *medial axis* will be used for the broader meaning, implying a greater degree of spatial continuity, in accordance with the original proposal by (Blum, 1967). Of course this distinction is open to criticism in that any medial axis obtained from a tomographic image is based on a discrete representation, yet an algorithm can approximate the original continuous function from the discrete form (and perhaps make use of additional evidence, such as the unsegmented grey-scale image, in doing so). Discrimination between a voxel-based skeleton and a continuous form is also supported by the fact that the medial axis is determined as the boundary between the Voronoi regions (Siddiqi and Pizer, 2008) of an enclosing granular material phase (i.e. soil particles enclosing the pore). Defined in such a way, it is clear that the medial axis consists of geometric entities (both line segments and polygons) that have real-valued coordinates.

Unfortunately such precision enhancements, although interesting and potentially valuable, could not be achieved within the present body of work owing to their relatively high complexity and the limited development time remaining. However, the importance of the medial axis as an efficient description of complex shape (and hence as a tool for investigating the transport properties of porous media) quickly became clear. For this reason it was decided to develop a PSD estimator based on readily available tools i.e. the "Skeletonize3D" plug-in module (Arganda-Carreras et al. 2010) available for

FIJI/ImageJ, with a view to implementing more robust and accurate medial axis extraction when possible.

The skeletonisation plug-in module of (Arganda-Carreras et al. 2010) requires an input image with 8bit elements consisting only of the states zero (displayed as black representing the background) or 255 (displayed as white representing the object) and generates an output image of the skeleton in the same format; figure 5.22 (overleaf) shows an example. Once a pore space skeleton image has been obtained, it is necessary to calculate some form of local size measure for each skeleton element, from which a distribution can be formed. Unfortunately a naive approach to determining a measure such as sphere diameter (e.g. finding the minimum Euclidean distance using a blind search outward from each skeleton element) is rather costly to compute. Lindquist et al. (2000) do not specify any particular algorithm for this task but they do make the following point:

> "Note there is no uniformity of definition of pore size distribution, and care must be taken to note the exact distribution being discussed/measured..."

Later it is discussed how measures of diameter, perimeter, cross sectional area or volume may be employed (but not how they may be efficiently determined). As well as explaining some different possible notions of pore size, (Lindquist et al. 2000) discriminate between distributions calculated for throats (i.e. paths of the medial axis) versus those of pores which they consider to be located

specifically at junctions of paths. While such detailed information may be important to the accuracy of some studies (e.g. Ngom et al. 2011) it exceeds the more basic requirement considered here.

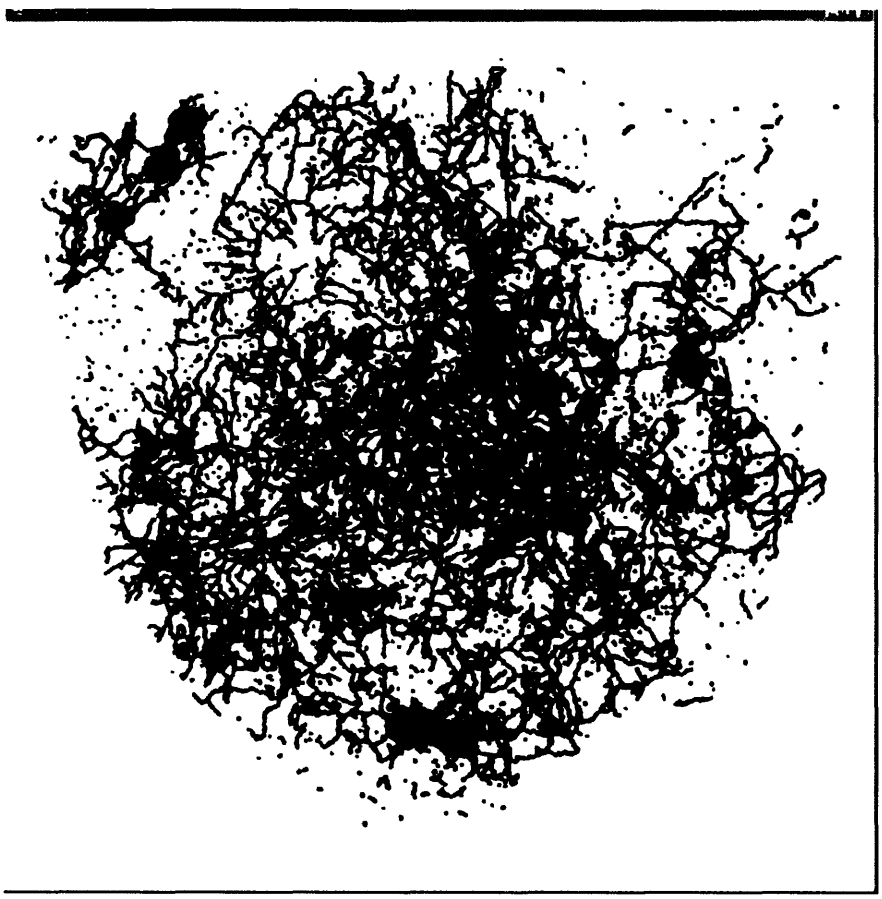

Figure 5.22 Discrete skeleton of pore space.
Image generated by the "Skeletonize3D" plug-in module of FIJI (ImageJ). The soil sample used to produce figure 5.20 was also used to produce this figure.

In order to achieve a working implementation within the limited time available, a more general PSD calculated irrespective of local topological features was required. Presented in the form of a probability mass function, this can be used to determine the probability that a randomly chosen pore element belongs to a local feature of a given size while the overall shape of the distribution can be

used to make inferences about the extent of pore space at resolutions beyond those present in the image.

A local size measure can be obtained very efficiently by computing a *distance transform* image (Rosenfeld & Pfaltz, 1968) from the pore space image. This stores, for every image element, the distance to the nearest solid element i.e. it is zero for all solid elements, one for all pore elements adjacent to a solid element and increases monotonically according to the distance measure used. This is particularly easy to compute if a *Manhattan distance* measure (aka. city-block distance) is employed; figure 5.23 (overleaf) shows a pseudo-code description of the algorithm, often referred to as a "burning" or "grass fire" algorithm (due to the conceptual similarity with the progression of a combustion front). Distance measures obtained in this way are sometimes referred to as "burn numbers" to distinguish them from other (more accurate) measures. In (Lindquist et al. 1996) burn numbers are referred to as the "discrete analog of the pore-size".

Figure 5.24 shows a single slice of the image resulting from the algorithm of figure 5.23 alongside the corresponding skeleton slice. As noted in the pseudo-code, the distance transform is implemented based on iterative application of the 6CN until all pore elements are assigned a distance. It is the use of the 6CN which causes Manhattan distances to "emerge" as successive layers of pore elements are assigned; there is no explicit calculation of distance (using coordinates, for example).

```
set pore-list to empty
for each location in image
   location-distance= 0
   if location is pore
      if any 6CN neighbour is solid
         location-distance= 1
      else
         add location to pore-list
      end-if
   end-if
end-for

while pore-list not empty
   for each location in pore-list
      get next image-location from pore-list
      get minimum-distance for 6CN neighbours of
                                              image-location
      if minimum-distance > 0
          location-distance= minimum-distance + 1
          delete location from pore-list
      end-if
   end-for
end-while
```

Figure 5.23 Manhattan distance (burn number) transform pseudo-code.

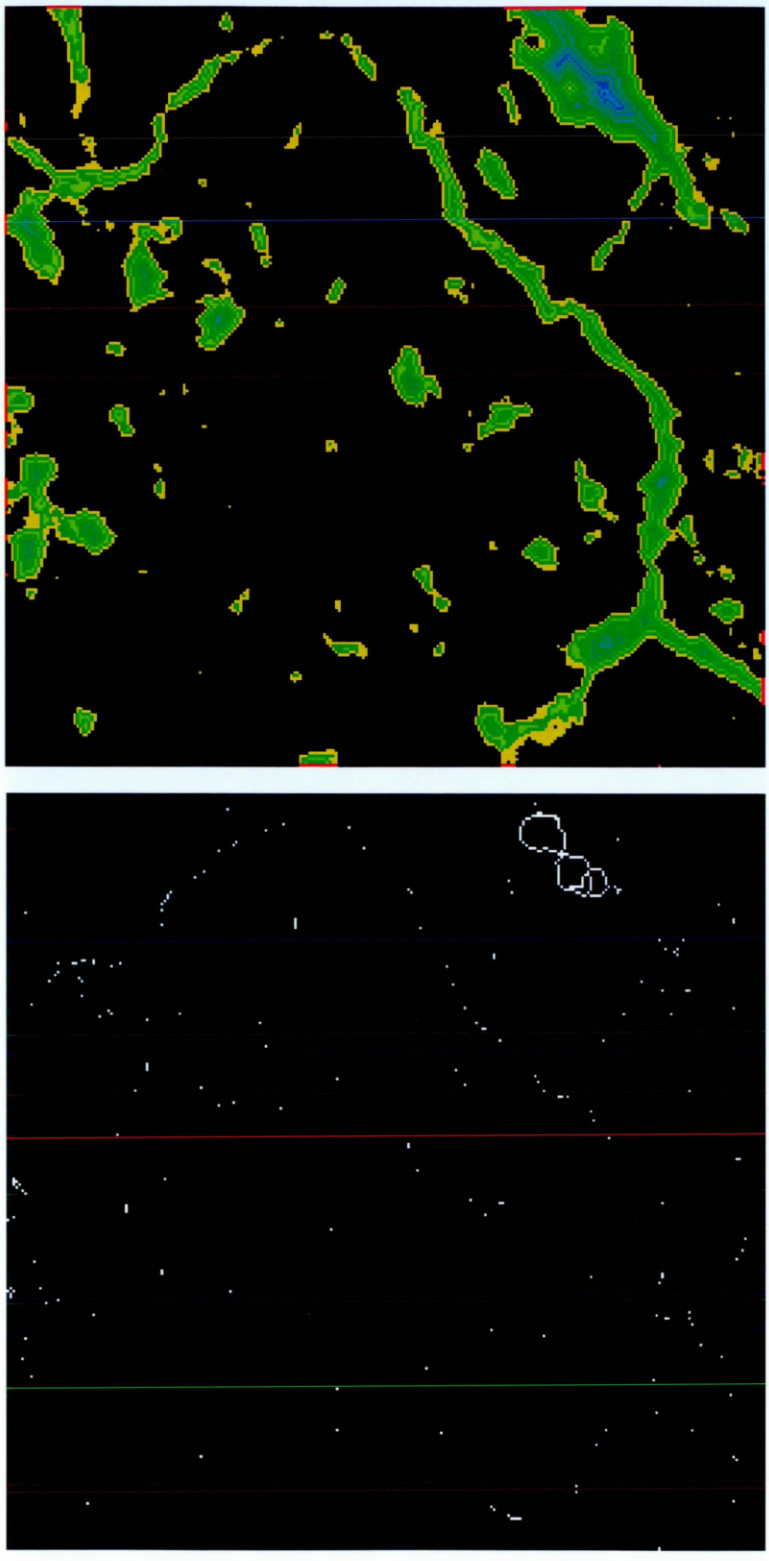

Figure 5.24 Manhattan distance transform and discrete skeleton. Slice from a distance transform image (above) and the corresponding slice from the skeleton image (below). The distance classes have been colour coded in an alternating scheme to give an effect resembling contour lines. Apart from the looped structure at the upper right, the 3D skeleton appears fragmented within a single slice image.

An alternative method of obtaining the Manhattan distance map is through applying a progressive sequence of *morphological erosion* operations (Serra, 1982). Labelling each eroded image element with the iteration number in which it was removed produces identical results to the burning algorithm, but typically at much greater computational cost.

By choosing another neighbourhood such as the 26CN and setting the distance increments appropriately (1, $\sqrt{2}$, $\sqrt{3}$) it is possible to obtain a distance measure that better approximates the Euclidean distance. In (Rosenfeld and Pfaltz, 1968) this is demonstrated for 2D image examples by comparing square, hexagonal and octagonal neighbourhoods. Accuracy is particularly important to achieving rotation stability of distance measures (Borgefors,1996).

Determining the exact Euclidean distance transform (henceforth EDT) is possible but requires a substantially more complex algorithm (Huang and Mitchell, 1994) assuming the high computational cost of a brute-force approach is to be avoided. A potential problem with the widespread definition and implementation of the "exact" EDT is the use of a biased measure of distance (as found in ImageJ plug-in modules for 2D and 3D "Exact EDT"). The use of *one* as the smallest distance is often carried over from the non-exact forms such as the Manhattan distance transform (yielding in effect a *categorical* measure based on a local neighbourhood interpretation).The Minkowski functionals on the other hand interpret the space between horizontally or vertically adjacent object and background elements as being *bisected* by the

interface (illustrated in figure 5.7). A distance measure of 0.5 is clearly appropriate in that case while for diagonal adjacency, figures 5.8 and 5.9 depict the situation. Consequently, in the case of geometry having diagonal interfaces, a simple "correction factor" approach (subtracting 0.5) is not appropriate. Obtaining a consistently unbiased distance measure then requires the exact EDT to be implemented from first principles, based on an appropriate cell interface model. This would allow measures of PSD to be related to Minkowski functionals in a consistent fashion.

Combining distance transform and skeleton images yields an approximate *Medial Axis Function* (Blum, 1967) this being a description consisting of distance values at all points on the medial axis. This information can be used directly to construct a form of PSD: if a Euclidean distance measure were employed then a pore radius distribution would be obtained. The Manhattan distance distribution is perhaps the most basic form of PSD; an example is shown in figure 5.25 below.

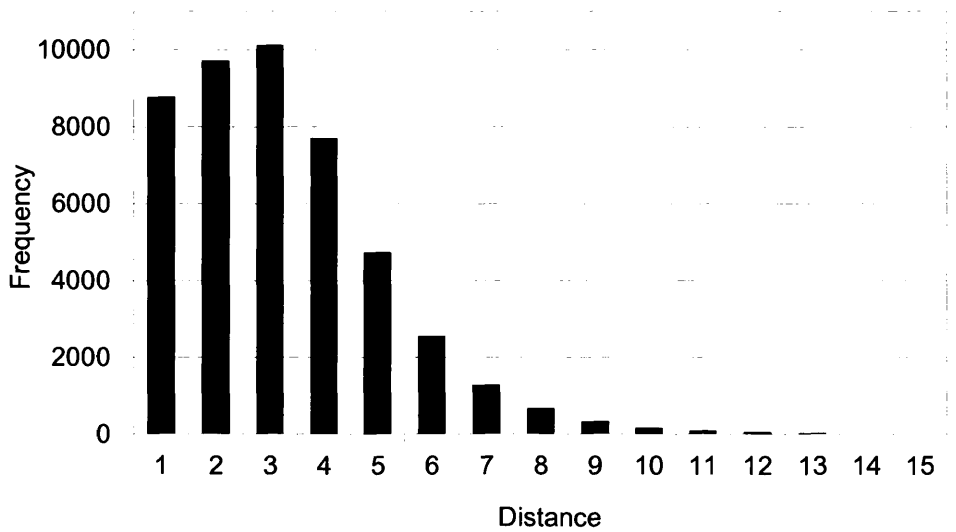

Figure 5.25 Manhattan Pore Size Distribution.
Estimated from Manhattan distance (burn number) on discrete skeleton.

5.4 Conclusion

Functional measures relevant to segmented volume images have been implemented in software with consideration given to both flexibility and efficiency. Volume, surface area, integral mean curvature and total curvature (also measures of connectivity derived from volume measures) can be determined per object and also summarised over entire images by classes of connectivity. Accuracy with respect to spatial orientation and discretisation has been assessed for these measures, yielding an improved understanding of their limitations. Early stage work on measuring the pore size distribution has also been presented and the means of progressing this work has been made clear. In this chapter the focus has been upon the theoretical background and technical implementation details of measures for the analysis of images. In subsequent chapters these measures are applied to practical problems, both in soil and other systems exhibiting complex spatial structure.

6.0 Adaptive Window Indicator Kriging

In this chapter the topic of image segmentation is revisited. The method of (Oh and Lindquist, 1999) is significantly revised in order to address its major weakness: the fixed size kriging window. This work has previously been published in the article (Houston et al. 2013).

The indicator kriging method of (Oh and Lindquist, 1999) was introduced in section 4.2.3 where it was applied, along with other image segmentation methods, to simple 2D test images. In the comparison of results it was seen that indicator kriging is robust against forms and levels of noise that are problematic for many other segmentation methods. However it was also noted that the kriging window size must be large enough to admit sufficient data points (a-priori classified image elements) that a valid solution can be obtained. When a kriging window of fixed size is applied to a 3D image, the number of data points within each specific instance (of the window) is expected to be proportional to the cube of the window radius. Given that the cost of solving a kriging system is typically $O(N^3)$ in the number of data points, a processing cost as great as the *sixth power of the window radius* is to be expected. In other words the radius of a fixed size kriging window is severely limited by practical considerations.

In cases where a-priori classified image elements occur with reasonable regularity throughout an image, then it is not too difficult to select a kriging window size that will provide an acceptable balance of estimation accuracy versus processing cost. Contrastingly, when the spatial distribution of a-priori

classifications is heterogeneous then choosing a window size becomes problematic. The window must be large enough to cope with regions where evidence is sparse, but this can lead to very large kriging systems in regions where evidence is dense. This problem is significant in the case of geo-materials (in particular soils) that are not well characterised by a single correlation length. The computational cost of classifying a soil image using a fixed size kriging window may thus be so great that the method is impractical. This problem can be addressed very efficiently, and without sacrificing any accuracy, by allowing the kriging window size to adapt to local conditions throughout the image.

6.1 The Adaptive Window Principle

The adaptive window strategy was devised as part of a "low-level" optimisation of spherical window processing, used to accelerate filtering operations as well as kriging. A naive method of selecting information within a spherical window is based on applying a rejection test to each point within a minimal cube enclosing the sphere (a cube being trivially simple to traverse algorithmically). Approximately 48% of all elements are rejected however, and the test itself involves a non-trivial computational cost. If instead the sphere is described using a table of 3D window vectors from the central point, then both the cube traversal and spherical rejection test can be eliminated. This introduces an issue with image boundaries however, as it then becomes necessary to test each candidate sphere point (i.e. the central point plus each window vector in turn) against the extent of the image. Contrastingly, in the case of a cube

traversal with rejection test, it is reasonably easy to "clip" the cube extent to that of the rectangular image. For a table of window vectors, the boundary testing overhead can be greatly reduced by storing the window vectors sorted by length. With the addition of an indexing mechanism, all vectors of a specific length can be easily accessed, hence it is possible to partition the vector table very easily by distance. This description of a spherical window based on vectors along with indexing information is henceforth referred to as an *ordered spherical window*. When a point within an image is processed using an ordered spherical window, the first operation is to determine the minimum of the six axial distances (from the window centre) to the image boundary. This minimum distance partitions the window vector table such that all vectors of lesser length are applied without bounds checking, whereas all others are individually checked. As image definition increases in relation to window size, the elimination of redundant boundary checking afforded by an ordered spherical window provides a modest but welcome performance improvement. The value of this mechanism to a kriging window soon becomes obvious: in addition to the distance partition for image boundary checking, additional tests can be applied per distance class. These tests assess the collected evidence, allowing the evidence gathering procedure to be halted or suspended as required: this is the essence of the adaptive window.

There are potentially many ways in which the evidence within an adaptive kriging window might be assessed and choosing a good strategy depends partly upon the application. The method described following has been found to work

well for soil images. In addition to very efficiently exploiting the coherent lattice structure of the image via the ordered spherical window (see Figure 6.1a for a 2D example) the acquisition of indicator data points by equidistant groups allows the size of kriging systems to be controlled in an effective, if imprecise, manner. In order to obtain good quality evidence, neither the window radius nor the number of data points can be constrained; instead lower and upper *target* numbers of points *per class* of indicator datum are used to guide the evidence acquisition procedure. When suitable combined targets are achieved then classification by kriging proceeds. Finally, recognising the possibility of classification failure, multiple attempts per estimation point are supported. Each additional classification attempt includes further data points in the kriging system i.e. the evidence gathering procedure is resumed as necessary.

The criteria for satisfactory evidence are that either both indicator classes must meet the lower target number of points, or the upper target must be met for at least one class. For example, setting lower and upper targets to 4 and 16 respectively means that search cannot end until at least 8 data points (4 or more per class) have been found. If only 3 points of one class are found then search continues until at least 16 points of the other class are found giving a total of at least 19 points. Bearing in mind that data points are found in groups by lag distance, the number of points per class may exceed the target, hence the size of kriging system is theoretically unlimited. In practice, targets are significantly exceeded only when an estimation point has few data points

nearby; greater lag distances tend to include many data points. Where data points of all indicator classes are abundant, it follows that low targets should be met quickly, resulting in a kriging system of modest size. Contrastingly, where a single class of indicator datum dominates, the upper target is more relevant hence kriging systems are typically larger. An example of the adaptive window mechanism as applied to a 2D problem is shown in Figure 6.1 and Table 6.1.

By applying adaptive window mechanism to the 2D problem illustrated in Fig 6.1, there is progressive growth in the number of data points with increasing window size (radius). A fixed window of radius 3 would use the cumulative information in the right-most column of table 6.1 irrespective of local conditions. An adaptive window advances column by columns checking the cumulative total per class, it ends when enough evidence has been determined.

Class	**Tally**	**Radius** (image elements)					
		1	√2	2	√5	2√2	3
Pore	additional	+3	+3	+2	+2	+2	+0
	cumulative	3	6	8	10	12	12
Solid	additional	+0	+0	+1	+1	+2	+2
	cumulative	0	0	1	2	4	6
Unclassified	additional	+1	+1	+1	+5	+0	+2
	cumulative	1	2	3	8	8	10
Total	additional	+4	+4	+4	+8	+4	+4
	cumulative	4	8	12	20	24	28

Table 6.1 2D adaptive window processing.
A fixed window of radius 3 would use the cumulative information in the right-most column irrespective of local conditions. An adaptive window advances column by column checking the cumulative total per class against targets. If the lower and upper targets per class were 4 and 8 respectively then evidence collection would end at radius 2 because the upper target is met for the pore class. If the upper target were raised to 16 then evidence collection would extend to radius 2√2 where

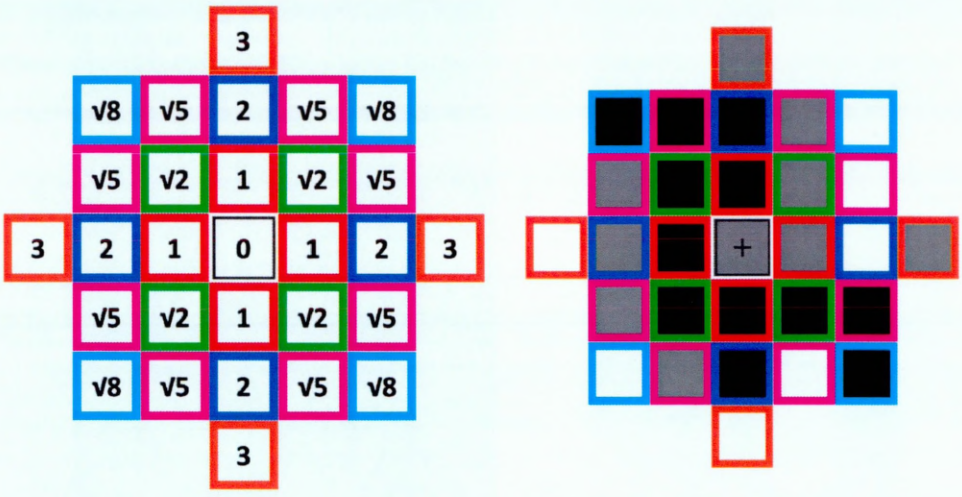

Figure 6.1 2D adaptive window pattern.
On the left is Illustrated a 2D circular window pattern of radius 3. Elements are labelled with their Euclidean distance from the central estimation point. on the right is an Example of a partly classified image region with elements assigned coloured borders (According to left hand image). Pre-classified image elements (i.e. data points for kriging) are shown in black for pore and white for solid. Unclassified elements are shown in grey and the estimation point (the centre of the window) is marked with a cross. border colour is assigned according to this distance.

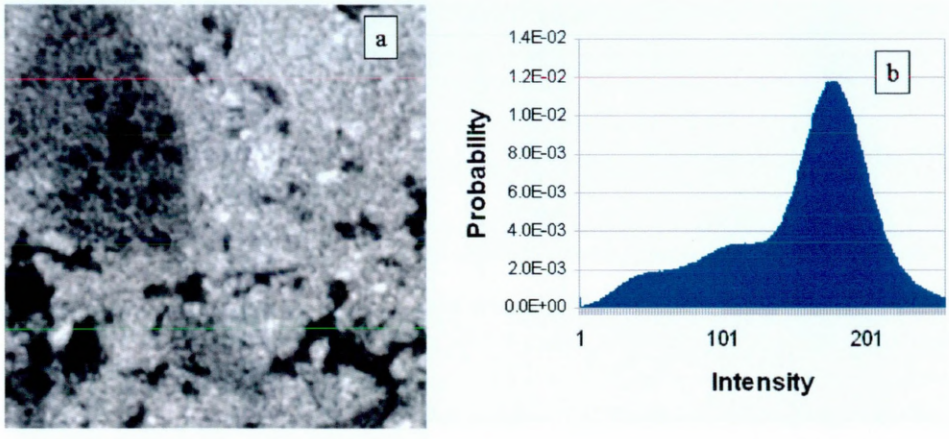

Figure 6.2 Example soil image and histogram.
(a) Grey scale (unclassified) image slice mapped from tomographic reconstruction of X-ray attenuation coefficients.
(b) Intensity histogram of the entire volume image.

6.2 Materials

Five soil samples are used to demonstrate the effectiveness of the method. Images of each sample were acquired using an X-Tek HMX CT scanner and then tomographic reconstruction was achieved using CTPro version 1.2 (Nikon Metrology X-Tek Systems Ltd, Tring, UK). The image acquisition settings that were used are stated in Table 2. Noise reduction was achieved as part of the filtered back-projection reconstruction algorithm; the proprietary CTPro setting "NR2" was used throughout. This was judged to suppress impulse noise to an acceptable degree without excessive distortion of the image intensity distribution and while preserving edge information. Non linear filtering is applied as part of the segmentation method, but follows pre-classification and does not affect grey-scale images. A single region of interest, 256^3 voxels in size, was selected from each reconstructed image. The 32-bit floating-point representation of the tomographic reconstruction was mapped to unsigned 8-bit representation using the method described in section 3.2.

Sample	***Energy-flux set***		***Filter***		***Proj.***	***Res.***
	kV	*uA*	*element*	*mm*	*#*	*mm*
Image 1	*110*	*93*	*Al*	*0.25*	*3010*	*0.032*
Image 2	*110*	*93*	*Al*	*0.25*	*3010*	*0.032*
Image 3	*150*	*50*	*Al*	*2*	*1200*	*0.035*
Image 4	*150*	*50*	*Al*	*2*	*1200*	*0.035*
Image 5	*150*	*47*	*Al*	*2*	*1200*	*0.035*

Table 6.2 Image acquisition settings.
Parameters used in CT scanning and reconstruction of images.

6.3 Method Implementation

The overall segmentation procedure is the same as that described in section 4.2.3: a-priori classification (including majority filtering), followed by spatial variance modelling and finally classification by kriging with an additional majority filtering step.

6.3.1 A-Priori Classification

The a-priori classification strategies proposed by (Oh and Lindquist, 1999) have already been introduced in section 4.2.3 but neither of these methods works satisfactorily in the general case of soil CT images (Prodanovic, 2006; Iassonov, 2009). The image intensity histogram of a soil sample frequently exhibits a skewed unimodal character (Figure 6.2) hence the automatic identification of two distinct modes is typically unstable and sometimes impossible. An attempt was made to resolve this problem by removing boundary image elements (identified by gradient magnitude) from the image histogram before pattern analysis. Unfortunately the histogram shape was not significantly improved and automatic determination of thresholds remains unreliable.

The thresholds actually used were based on a number of attempts at Gaussian mixture modelling of the intensity histogram of each sample image. None of the automatically fitted models was entirely satisfactory, hence the selection of upper and lower intensity threshold values was based on operator judgement.

6.3.2 Spatial Variance Modelling

The general approach to spatial variance modelling based on the empirical indicator semivariogram is described in section 4.2.3. To constrain computational cost for the 3D images, the lag distance is limited to 12 image elements. This value was found to be sufficient in the case of all sample images presented here.

The collection of 3D empirical semivariogram data is achieved using the classical estimator proposed by Matheron (equation 2.2) however the details of implementation are less obvious. The indicator data is represented as an image with each indicator data point having either value one (representing solid class) or zero (representing pore) while a third value represents the absence of indicator data (i.e. an unclassified image element). Indicator semivariogram calculation then makes use of the ordered spherical window to locate all indicator data within the cut-off lag distance. However it is not necessary to sum the squared differences, as the nature of indicator data dictates that the squared difference is either zero or one, according to whether a pair of indicators belong to the same or different classes. Thus it is necessary only to

count the number of instances of each possible pattern per lag. The indicator semivariance at each lag is then easily generated from this information:

$$\gamma = \frac{n_{0-1} + n_{1-0}}{n_{0-0} + n_{1-1} + n_{0-1} + n_{1-0}} = \frac{n_{different}}{n_{same} + n_{different}} \qquad \text{(equation 6.1)}$$

Computational performance was enhanced by using multiple threads of execution for semivariogram estimation. The image is divided into blocks and worker threads process these blocks in parallel, each worker thread accumulating partial image results in it's private data area. Thread synchronisation therefore occurs only when an image block is claimed by a worker thread, hence image blocks should be sufficiently large to reduce the incidence of thread blocking (an example of *coarse-grained parallelism*). Once all blocks have been processed, each worker thread submits its partial result to be merged (a serial operation) and then exits. For multi-core processors this strategy greatly improves overall throughput, and provides the maximum benefit when the number of workers equals the number of execution units.

6.3.3 Classification by Kriging

In the fixed size kriging window implementation (with which the adaptive window is compared) there is no way to resolve a classification failure within a single pass through the image. In their original manuscript, (Oh and Lindquist, 1999) do not give any indication of how this problem should be addressed. In the case of results presented here, complete classification under a fixed-window was achieved by applying indicator kriging iteratively in a number of passes over the

image. The indicator semivariogram model, as well as all previous classifications remain unchanged during each subsequent pass. This is therefore an approximation that feeds back the classification results of previous kriging systems into new systems and is consequently vulnerable to numerical error. In the event of a classification failure under an adaptive window, it is relatively easy to collect further indicator data points by resuming the search within the ordered spherical window. This allows another (larger) kriging system to be formulated, perhaps yielding a valid solution. Applied iteratively, this *progressive solution* strategy leads to an incremental "search and solve" algorithm, extending the basic adaptive window strategy described previously. The consequence is that progressively larger window sizes are employed until either a valid solution is obtained or some practical limitation of data storage or processing requirements is encountered.

6.4 Evaluation of Segmentation Performance

Segmented images are evaluated using both the 3D Minkowski functionals as defined previously (section 5.1). The 3D Minkowski functionals have been successfully used in the past for the physical characterisation of soil structure (Vogel et al. 2010; Falconer et al. 2012). Also used is the connectivity measure described in section 5.2, which for the present application is determined solely from the *six-connected* neighbourhood, i.e. only face-face voxel connections are considered. Finally, classification error is estimated based on the *intra-class variance* calculated on the original greyscale image with respect to the segmented image (Otsu, 1979; Zhang et al. 2008; Hapca et al. 2013).

6.5. Results and Discussion

6.5.1 Accuracy of Semivariogram Models

For each image an empirical indicator semivariogram was calculated and modelled using the approach described previously. As illustrated in Figure 6.3, all of the images in this study are in general well represented by the Gaussian mode l of form:

$$\gamma_h = \beta_{nugget} + \beta_{sill-nugget}\left(1 - e^{-\left(\frac{h^2}{\beta_{range}}\right)}\right) \quad \text{(equation 6.1)}$$

The sill of an indicator variogram must not exceed 0.25 as this is the upper bound for the variance of a Bernoulli random variable (Papritz, 2009). In addition, when a Gaussian model is fitted to the indicator variogram, a positive nugget constraint is implemented, for the model to be consistent with the triangular inequality requirement as indicated by (Matheron, 1989). Although the Gaussian model proved to provide the best fit, some limitations in the accuracy of fit at small lag distances are apparent, relating to the extremely small values of the empirical indicator semivariogram at these lag distances. It therefore seems that a nested model formulation (which is not presently implemented) might be suited to accurately model both short and long range behaviour.

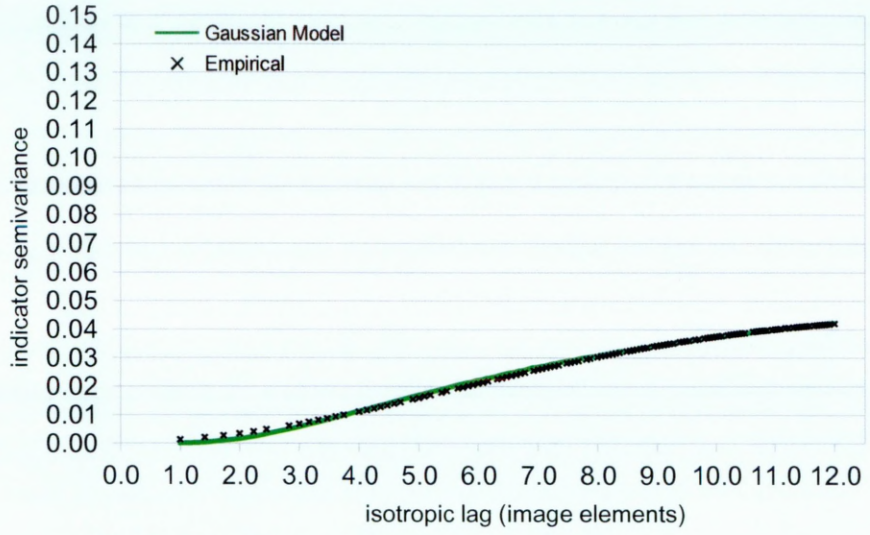

Semivariogram model for sample image 1.

$$\gamma_h = 0.0006987 + 0.0456724\left(1 - e^{-\left(\frac{h^2}{7.78126^2}\right)}\right)$$

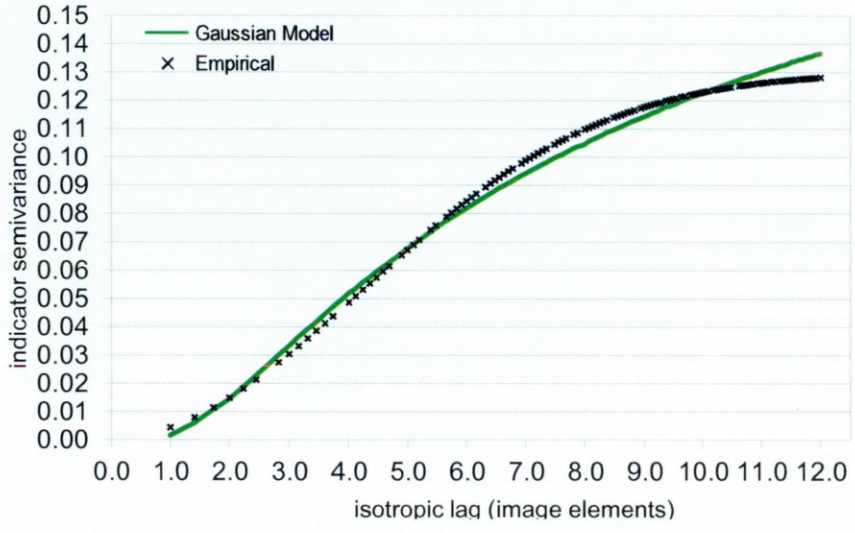

Semivariogram model for sample image 2.

$$\gamma_h = 0.000694804 + 0.129463\left(1 - e^{-\left(\frac{h^2}{5.88193^2}\right)}\right)$$

Figure 6.3 Semivariogram models.
Gaussian authorised models are shown fitted against empirical data for each sample image (continued on following pages). In each case these models have been selected as providing a better fit than others (exponential or spherical). Near the origin, the fit is limited by the requirement for a positive "nugget" (y-axis intercept) value. The fitted model is also shown for each sample image.

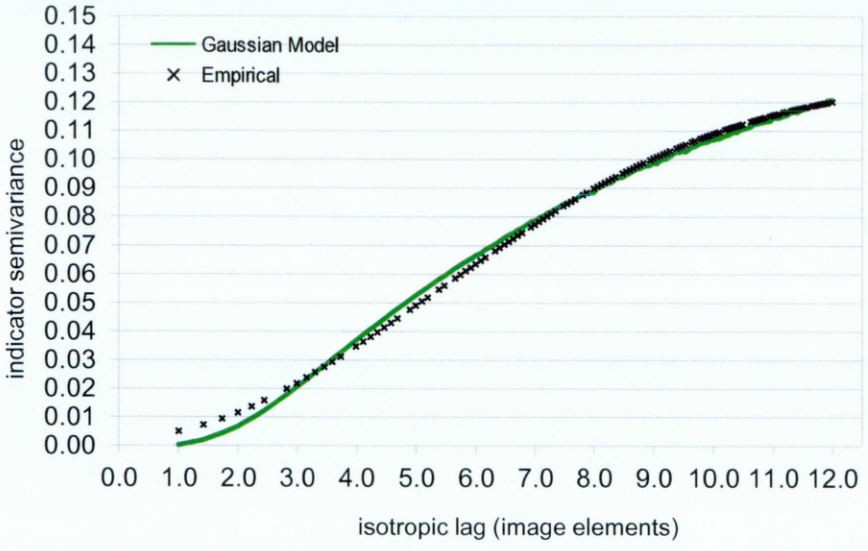

Semivariogram model for sample image 3.

$$\gamma_h = 0.0028506 + 0.126698\left(1 - e^{-\left(\frac{h^2}{7.419^2}\right)}\right)$$

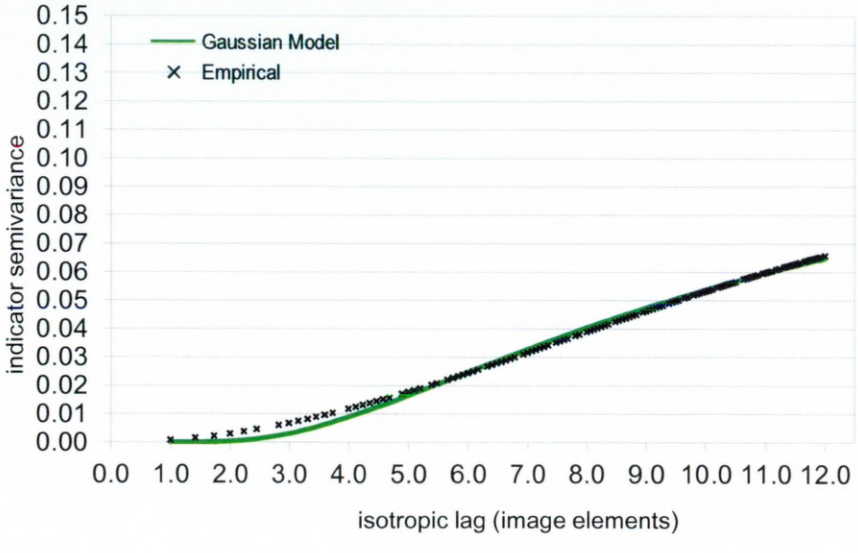

Semivariogram model for sample image 4

$$\gamma_h = 3.34195\text{E-}5 + 0.0937941\left(1 - e^{-\left(\frac{h^2}{10.899^2}\right)}\right)$$

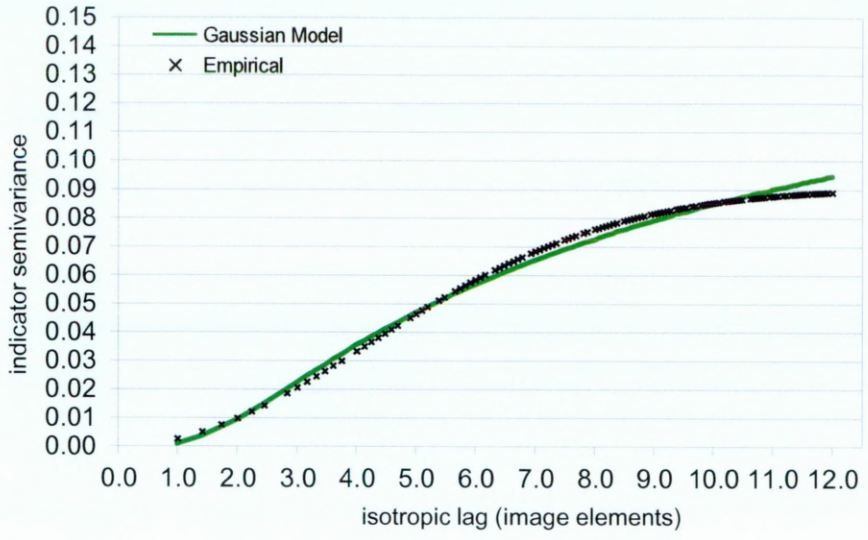

Semivariogram model for sample image 5.

$$\gamma_h = 6.3259\text{E-}7 + 0.090482\left(1 - e^{-\left(\frac{h^2}{5.89842^2}\right)}\right)$$

6.5.2 Robustness of Kriging Systems

For an adaptive window, the size of kriging systems is influenced by the lower and upper target number of indicator data points (i.e. pre-classified image elements) per class of indicator datum. A parameter range from 1 to 10 inclusive was evaluated for the lower target, with upper targets remaining constant at 16. For each sample image, the 10 segmentations show the expected progression of kriging matrix rank and other statistics as seen in table 6.13. For comparison, fixed window results are also shown in table 6.13. Due to limited processing capacity, only two fixed size kriging window segmentations per sample image are evaluated. These segmentations are based on fixed size kriging windows of radii of three and four respectively.

Image Sample	Window Parameter		Effective Window Size			Kriging Matrix Rank			Elapsed time	Mean Rate
	Adaptive low target	Fixed radius	Mean	StDev	Max	Mean	StDev	Max	All kriging attempts (seconds)	(classifications per second)
Image 1	1	-	2.01	0.58	5.92	10.31	6.42	36	1.98	2.5E+06
	2	-	2.21	0.56	6.16	14.63	6.64	40	2.54	1.9E+06
	3	-	2.32	0.54	6.16	17.17	6.29	40	2.84	1.7E+06
	⋮	-	⋮	⋮	⋮	⋮	⋮	⋮	⋮	⋮
	10	-	2.62	0.50	6.40	26.31	4.86	47	5.30	9.3E+05
	-	3	2.99	0.11	3.00	47.08	20.14	123	32.00	1.5E+05
	-	4	3.92	0.20	4.00	106.76	41.09	240	352.24	1.4E+04
Image 2	1	-	1.72	0.50	5.20	9.48	6.39	38	3.09	1.7E+06
	2	-	1.94	0.47	5.39	14.25	6.79	40	4.45	1.2E+06
	3	-	2.06	0.46	5.39	16.98	6.51	41	5.79	9.3E+05
	⋮	-	⋮	⋮	⋮	⋮	⋮	⋮	⋮	⋮
	10	-	2.39	0.37	5.83	27.14	5.40	49	12.71	4.3E+05
	-	3	2.97	0.17	3.00	56.84	20.00	123	116.69	4.6E+04
	-	4	3.91	0.26	4.00	129.09	38.41	257	1269.64	4.3E+03
Image 3	1	-	1.96	0.57	6.00	10.03	6.31	37	3.12	2.0E+06
	2	-	2.16	0.55	6.08	14.35	6.52	38	4.51	1.4E+06
	3	-	2.27	0.53	6.08	16.90	6.21	39	5.59	1.1E+06
	⋮	-	⋮	⋮	⋮	⋮	⋮	⋮	⋮	⋮
	10	-	2.59	0.47	6.40	26.50	5.02	48	11.69	5.3E+05
	-	3	2.99	0.10	3.00	47.78	20.60	123	75.29	8.2E+04
	-	4	3.93	0.18	4.00	107.77	40.84	257	815.54	7.5E+03
Image 4	1	-	2.56	0.96	11.87	10.81	6.34	35	3.07	2.2E+06
	2	-	2.75	0.95	12.04	14.79	6.38	37	4.04	1.7E+06
	3	-	2.85	0.95	12.04	17.15	5.83	39	4.56	1.5E+06
	⋮	-	⋮	⋮	⋮	⋮	⋮	⋮	⋮	⋮
	10	-	3.12	0.98	12.12	25.17	4.28	48	7.52	9.2E+05
	-	3	3.00	0.06	3.00	40.33	18.91	123	35.90	1.9E+05
	-	4	3.93	0.15	4.00	88.03	40.03	257	351.53	2.0E+04
Image 5	1	-	1.78	0.56	5.10	9.64	6.39	38	2.55	2.1E+06
	2	-	2.01	0.52	5.48	14.34	6.71	39	3.69	1.4E+06
	3	-	2.13	0.50	5.48	17.01	6.37	40	4.71	1.1E+06
	⋮	-	⋮	⋮	⋮	⋮	⋮	⋮	⋮	⋮
	10	-	2.46	0.42	5.92	26.78	5.35	49	9.95	5.3E+05
	-	3	2.97	0.18	3.00	53.45	21.33	123	83.30	6.3E+04
	-	4	3.90	0.29	4.00	120.88	41.47	257	898.45	5.9E+03

Table 6.3 Statistical properties of kriging systems.
Kriging window and matrix performance is shown for both fixed and adaptive window parameter ranges. The effective window size is determined per kriging system as the farthest lag distance incorporated into the system. All of the values presented in this table are calculated over all kriging systems formed within a particular sample image and parameter combination. Note that for a fixed window, the small variability seen in lag distance is caused by a local absence of data points in some cases. Adapted from (Houston et al. 2013).

For all sample images evaluated, both mean and maximum radii (measured over all indicator data points) increase very slowly versus increments in the adaptive window parameter, while the standard deviation decreases slightly. This indicates that the quantity of evidence collected through using an adaptive window is on average relatively stable across the image as a whole. This is further supported by the statistics on kriging matrix rank which exhibit very similar patterns.

An assessment of kriging system solutions, in terms of the occurrence of negative weights, is presented in table 6.4. The mean fraction of negative weights measured over all kriging systems is seen to increase steadily with matrix rank. Although the fractions for adaptive versus fixed window processing overlap, the larger matrix rank of fixed windows means that a greater absolute number of negative weights occur in fixed window processing. This suggests that an adaptive window avoids processing redundant information, and so is intrinsically more efficient.

Window Parameter		Image Sample									
		Image 1		Image 2		Image 3		Image 4		Image 5	
Adaptive low target	Fixed radius	Single pass failures	Negative weights mean proportion	Single pass failures	Negative weights mean proportion	Single pass failures	Negative weights mean proportion	Single pass failures	Negative weights mean proportion	Single pass failures	Negative weights mean proportion
1	-	0	29.0%	0	33.1%	0	28.0%	0	39.2%	0	44.0%
2	-	0	30.6%	0	35.2%	0	29.0%	0	42.3%	0	47.1%
3	-	0	31.7%	0	37.9%	0	30.0%	0	44.2%	0	48.3%
...											
10	-	0	38.4%	0	45.5%	0	36.6%	0	46.9%	0	49.5%
-	3	8595	37.7%	376	44.9%	8365	37.1%	373941	42.6%	1680	49.1%
-	4	436	45.8%	7	56.7%	251	45.5%	154163	51.1%	16	50.0%

Table 6.4 Classification failures and negative weight proportion.
The number of classification failures following the first kriging pass are shown for both fixed and adaptive window parameter ranges. Also shown is the mean proportion of negative weights over all kriging systems. Adapted from (Houston et al. 2013).

6.5.3 Adaptive Window: Effect on Functional Measures

Changing the adaptive sampling parameter (i.e. the lower target per class of indicator datum) so as to increase the effective kriging window size (henceforth EKWS) has the effect, on average, of increasing both matrix rank and spatial extent of kriging systems. As illustrated in Table 6.5, this increase causes both surface area and mean curvature to decrease monotonically, in other words the structure of the pore-solid interface becomes somewhat smooth (at the finest length scales) as the average size of the kriging system grows. This is entirely consistent with the interpretation of kriging as an interpolation method. This interpretation is also supported by the fact that, for the soil samples used in this study, the porosity generally tends to decrease with larger values of EKWS as the dominant solid phase begins to mask the relatively sparse evidence of pore phase (Figure 6.4 and 6.5).

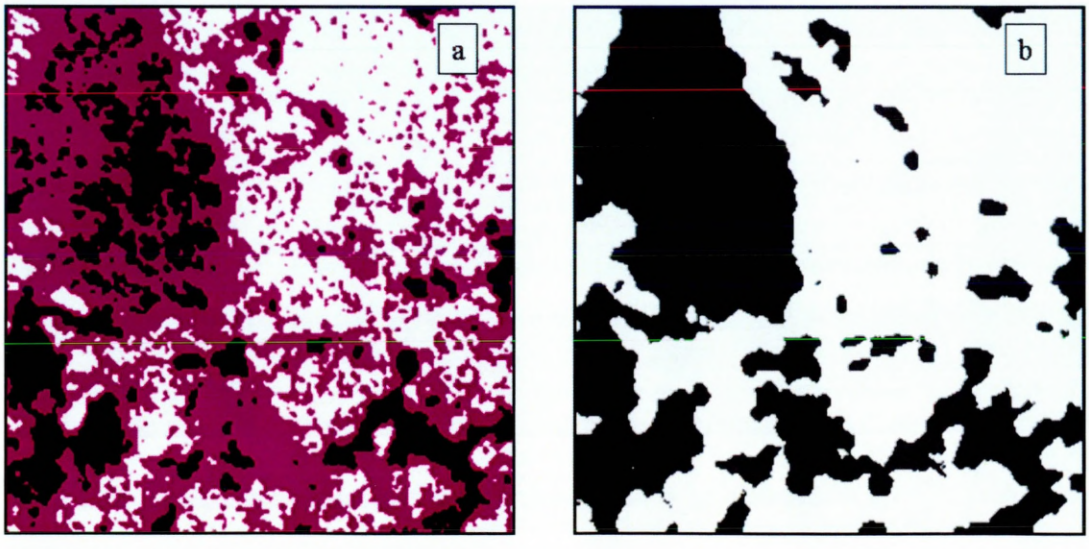

Figure 6.4 A-priori classification.
(a) Pre-classified image slice obtained by applying a hysteresis threshold to the grey scale image slice shown in figure 2. Pore elements are shown in black, solid elements in white and unclassified elements in purple.
(b) Complete classification by adaptive-window indicator kriging of the image slice shown in (a). Adapted from (Houston et al. 2013).

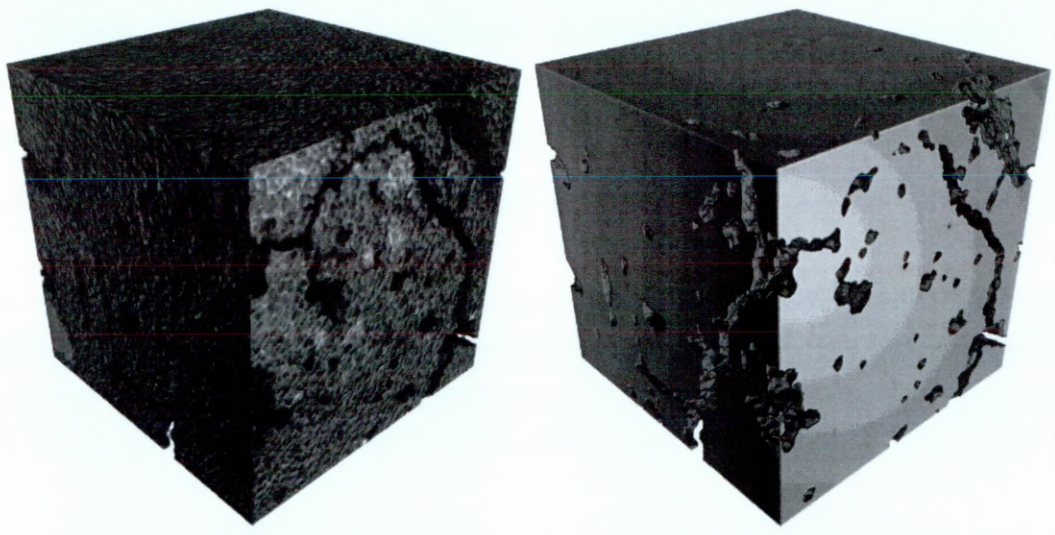

Figure 6.5 Segmented volume image comparison.
Rendering of 3D sample image 1 before and after segmentation. On the left is the grey-scale image, on the right is the binary image segmented using adaptive window indicator kriging (parameters used were lower and upper targets of 4 and 16 respectively). Adapted from (Houston et al. 2013).

Given that pre-classified pore elements are relatively rare and clustered together, it can be argued that extending the radius tends to favour solid elements. Over smaller ranges of EKWS there is no simple pattern of porosity change, which is judged to be a consequence of the different correlation structures of the images. The total curvature shows obvious change with EKWS in every case, indicating that the number and topology of individual pore clusters is changing. In two cases the total curvature changes sign, a positive to negative transition indicating that the connection of previously isolated pore clusters contains "bridges" of solid material penetrating through the pore space. A negative to positive transition indicates that previously existing solid "bridges" have been removed leaving a more simply connected pore space.

The connectivity measure appears to be stable with respect to changes in the EKWS, with less than 1% fluctuations. This suggests that, despite the expected dominance of solid phase over longer ranges, the evidence from a-priori classification is sufficient to define long-range connectivity of pore clusters. Moreover this evidence is interpreted in a consistent and stable fashion through kriging systems of various sizes, suggesting that the adaptive window is highly robust.

Finally, in all the tested images, an increase in the EKWS produced an increase in the intra-class variance measure (Table 6.5), which is explained by the increased degree of spatial averaging that tends to occur in larger kriging systems. If ICV is interpreted as a measure of classification error, the smallest EKWS therefore produces better segmentation results.

Image Sample	Window param.		Minkowski Functionals				Connectivity	Intra Class Variance
	Adaptive low target	Fixed radius	Volume	Surface	IMC	ITC		
Image 1	1	-	0.0981	10.02	202.70	3205.19	87.97%	1142.8
	2	-	0.0977	9.83	192.40	2635.14	87.35%	1146.47
	3	-	0.0974	9.68	183.01	1835.17	87.52%	1149.14
	...							
	10	-	0.0969	9.30	168.72	2791.43	87.72%	1158.62
	-	3	0.0972	9.22	175.08	2801.49	88.68%	1164.16
	-	4	0.0949	8.54	150.45	2137.67	82.29%	1185.83
Image 2	1	-	0.2897	27.40	422.38	17578.70	97.92%	1194.13
	2	-	0.2891	27.01	387.71	3472.20	97.96%	1197.26
	3	-	0.2892	26.66	361.98	-4790.83	98.06%	1201.02
	...							
	10	-	0.2877	24.91	304.09	-6423.09	98.21%	1218.80
	-	3	0.2852	23.49	278.08	-11685.40	98.44%	1239.81
	-	4	0.2823	22.41	244.75	-12427.10	98.55%	1248.32
Image 3	1	-	0.2771	24.39	357.11	-13097.30	97.14%	1344.56
	2	-	0.2763	23.95	343.51	-12936.20	97.25%	1348.99
	3	-	0.2758	23.55	327.67	-14213.00	97.22%	1352.75
	...							
	10	-	0.2749	22.63	302.68	-10820.30	97.12%	1367.09
	-	3	0.2750	22.18	305.04	-11754.30	97.49%	1382.18
	-	4	0.2711	20.53	265.20	-9318.88	97.44%	1412.70
Image 4	1	-	0.2732	13.85	181.95	-1314.92	96.29%	883.96
	2	-	0.2731	13.85	181.41	-1215.32	96.31%	886.40
	3	-	0.2732	13.76	177.95	-1270.42	96.35%	888.62
	...							
	10	-	0.2724	13.17	166.85	1078.11	96.46%	897.15
	-	3	0.2731	13.26	178.24	-529.78	96.45%	895.48
	-	4	0.2701	12.41	161.35	638.92	96.67%	917.08
Image 5	1	-	0.2516	20.89	380.71	37767.70	95.23%	1839.43
	2	-	0.2483	20.30	334.97	21451.40	95.53%	1846.57
	3	-	0.2475	19.96	308.12	12862.10	95.65%	1856.52
	...							
	10	-	0.2454	18.74	254.88	14673.90	95.56%	1885.74
	-	3	0.2452	18.26	251.17	12057.90	95.79%	1899.21
	-	4	0.2413	17.06	193.76	5979.13	95.91%	1918.66

Table 6.5 Measures on segmented images.
Both fixed (radius 3 and 4) and adaptive (low target 1 to 10) window parameter ranges are shown. Adapted from Houston et al. (2013).

6.5.4 Fixed versus Adaptive Kriging Window: Evaluation of Performance

The adaptive window produces a substantial reduction in average matrix rank compared to a fixed window, greatly improving computational performance. The processing time for indicator kriging using an adaptive window ranged between 2 to 13 seconds (Table 6.3), while for a fixed window the time lies between 32 seconds and 22 minutes. In the fixed window case at least two kriging passes were required to completely classify each image. Table 4 shows the number of classification failures at the end of the first kriging pass, for sample image 4 this amounts to more than 2% of the image for a fixed window of radius 3, falling to less than 1% at radius 4. In order to avoid such problems (Iassonov et al. 2009) implemented indicator kriging with a fixed window of radius 5. The samples used in this study however require a window radius exceeding 5, in particular sample 4 requires a window of size 12 to achieve complete classification in one pass. Such a large window size implies a basic processing cost approaching 27 times (12^3 / 4^3) that of a radius 4 fixed window, with matrix inversion representing a further potential 27^3 cost factor. This was judged to be impractical due to its very inefficient use of computing resources.

In general, the two methods produced very similar results in terms of functional measures with a difference in the estimated pore volume of less than 0.1% and a difference in connectivity measure of less than 1%. Compared to an adaptive window, a fixed size kriging window has the tendency to reduce the pore volume, pore surface and the IMC measures, while the ITC and connectivity

measures have larger values (Table 5), a trend that is consistent throughout the five samples. As the EKWS increases, adaptive window results appear to converge with fixed size window results, this trend confirming the robustness of the adaptive window. Additionally, for all samples the ICV measure is consistently smaller under the adaptive window approach, again this favours the newly developed method.

6.6 Conclusion

The adaptive window mechanism has been developed specifically for indicator kriging of digital images and seems very well suited for that purpose. It is an extremely efficient approach to obtaining local spatial evidence by exploiting the coherent lattice structure of a raster image. Moreover it is robust against extreme variations in the local density of evidence (i.e. the spatial heterogeneity of image content). The high density of information in a CT image of soil is essential to accurately locating the solid-pore interface so that valid estimates of soil characteristics such as surface area, curvature and connectivity can be obtained. Adaptive window indicator kriging meets this need through well-localised minimum variance interpolation, making good use of evidence that may be relatively sparse but is also relatively more reliable.

7.0 Selected Applications of Image Analysis

The main body of work in this project has been investigating the theoretical aspects of image analysis, developing algorithms that extend the capability within the local research group and evaluating performance and correctness to some degree. This chapter reviews the application of the image analysis tools, particularly the Minkowski Functional tools, developed herein to soils and other application areas. The investigations described following have led to publication in peer reviewed journals. Descriptions of work not executed by the present author are clearly identified as such; in all other cases full credit is claimed for original methods and strategies conceived and developed as part of the study. All references to software applications refer to the software tools developed herein and described in Chapter 5.

7.1 Simulated Soil, Water and Fungi

The investigation (Falconer et al. 2012) is an advanced modelling study involving a number of analysis problems that were resolved in part through the application of software tools described previously within this work. The methods of applying these tools and approach to interpreting results are considered innovative within the subject area.

7.1.1 Project Background

Following the segmentation of soil CT images of and extracting a region of interest 128^3 voxels in size from each, Falconer produced simulated water distributions in the pore networks of each region of interest. This data was obtained by Falconer via a two-phase segregation problem (starting from a conceptual water versus air random mixture) using *Palabos*, an open source package for lattice-Boltzmann computational fluid dynamics (henceforth LBCFD). The resulting data was a scalar field (in floating point number format) representing the spatial density of fluid. This however included the virtual water density on solid interfaces that Palabos uses to achieve *wetting* i.e. the adhesion of water to the interface. These virtual densities must be removed which was achieved using the segmented pore region as a mask, such that only pore elements could possess a non-zero density. The next analysis task requires classifying all pore elements as either wet or dry according to the density in each location of the simulated water-air interface. This is a difficult thresholding problem as the water density obtained from LBCFD simulation exhibits a very gradual spatial transition: very different from the clearly defined air-water interface that is found at the macroscopic scale in a physical experiment. This poorly defined interface is a consequence of stability requirements in the numerical simulation which constrain the water/air density ratio to a value several orders of magnitude less than that expected in reality. This greatly reduces the intra-phase cohesion force responsible for segregation, allowing the simple (Eulerian) integration regime, necessary within the Lattice Boltzmann method, to be applied.

7.1.2 Analysis Methods

In order to better understand the spatial distribution of water density, a range of thresholds, each creating an iso-surface, were assessed using the 3D visualisation software known as *ImgView* (Houston, unpublished) and used to present figures in this thesis, e.g. Fig 6.5, 5.20, 5.22 & 5.24. As visualisation failed to identify an obviously correct threshold value, analysis proceeded by the calculation of Minkowski functionals (henceforth MF's) over the range of possible thresholds. In other words, MF's were used to evaluate the *threshold parameter space*, an approach suggested by (Michielsen & DeRaedt, 2000). This capability of exploring a parameter space was incorporated into the MF analysis software such that measures are presented neatly tabulated in physical measure form (i.e. having physical units) and also in standardised form. Standardisation maps from the domain of each measure, as determined over the evaluated parameter space, to the interval (0,1) in the case of volume and area while for curvature measures, the interval (-1,1) is used. This permits all information to be presented overlaid onto a single graph so that overall trends and patterns can be revealed more succinctly. This type of standardisation can of course be realised by other means (e.g. using spreadsheet formulae) but any level of automation is welcome where numerous experimental replicates are concerned.

More than a hundred threshold parameter values per minute are evaluated at 128^3 image definition, making this form of automation valuable for studies involving many replicates. Given that floating point data is used in the water

distribution images, it is necessary to restrict the search of parameter space in some way. Although a search method that could adapt automatically to a high precision data set is appealing, it was judged to be impractical to develop an appropriately robust search algorithm within the time constraint of the project. Instead, parameters specifying the threshold interval (i.e. the minimum and maximum) and step-size were incorporated into the interface of the application software, making the user responsible for a simple linear search.

7.1.3 Results

Examining the resulting graphs it was clear that a rapid transition in all measures occurs at a threshold parameter value slightly greater than the water density value chosen for simulation. (Happily, this confirms that, despite the constrained density ratio, the simulated behaviour is physically plausible.) In other words a form of "tipping point" in object morphology occurs with respect to a particular density threshold. This is seen clearly in figure 7.1 (overleaf) where the functional measures are presented on separate graphs for clarity.

Consensus was reached among the investigating team that an appropriate wet/dry threshold value was one density unit greater than the simulated water density used in each case (values of 150 and 200 were evaluated for each pore network). In order to evaluate the reliability of this threshold, standard descriptive statistics were calculated for each of the two populations formed under this threshold. Comparing means and standard deviations revealed that the populations were distinct in the case of all pore networks but one.

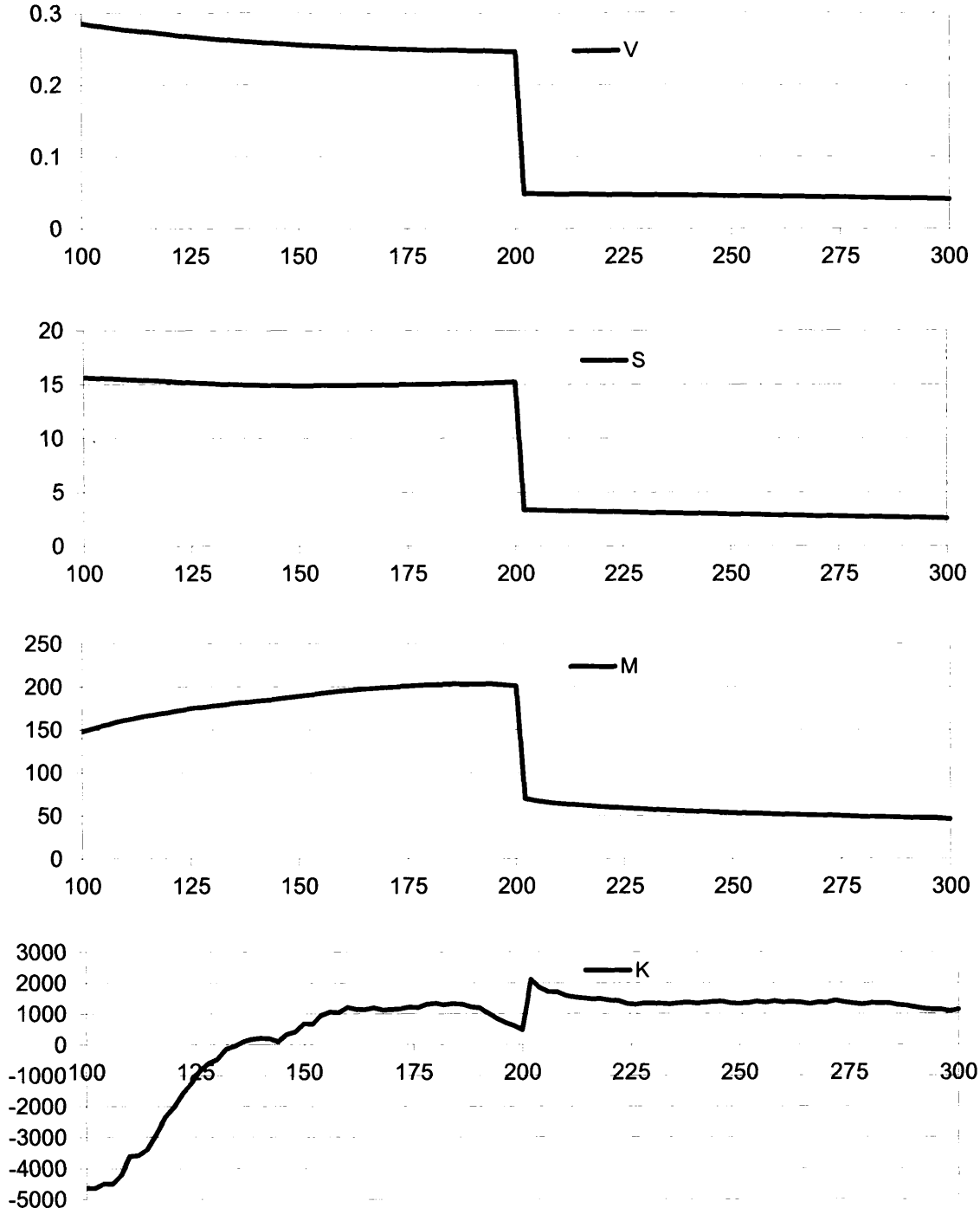

Figure 7.1 Water versus air threshold determination using Minkowski functionals. A range of thresholds are applied to the density field of simulated fluid (LBCFD simulation of phase separation within a soil pore network.) Minkowski functionals (from top to bottom: volume, surface area, mean curvature and total curvature) are computed at each threshold, revealing a rapid transition in structure beginning at fluid density 200. This suggests the liquid-vapour interface can be defined by constructing an iso-surface within the transitional range.

The image "N3" (see figure 7.3) exhibits a noticeable overlap in high versus low water density populations and this is attributed to the abundance of narrow pore channels, yielding a much greater surface area per unit volume of pore space compared to the more "open" pore organisation in other images. This meant that phases were unable to separate clearly due to limited spatial resolution and the density ratio constraint (which places a limit on the local density gradient).

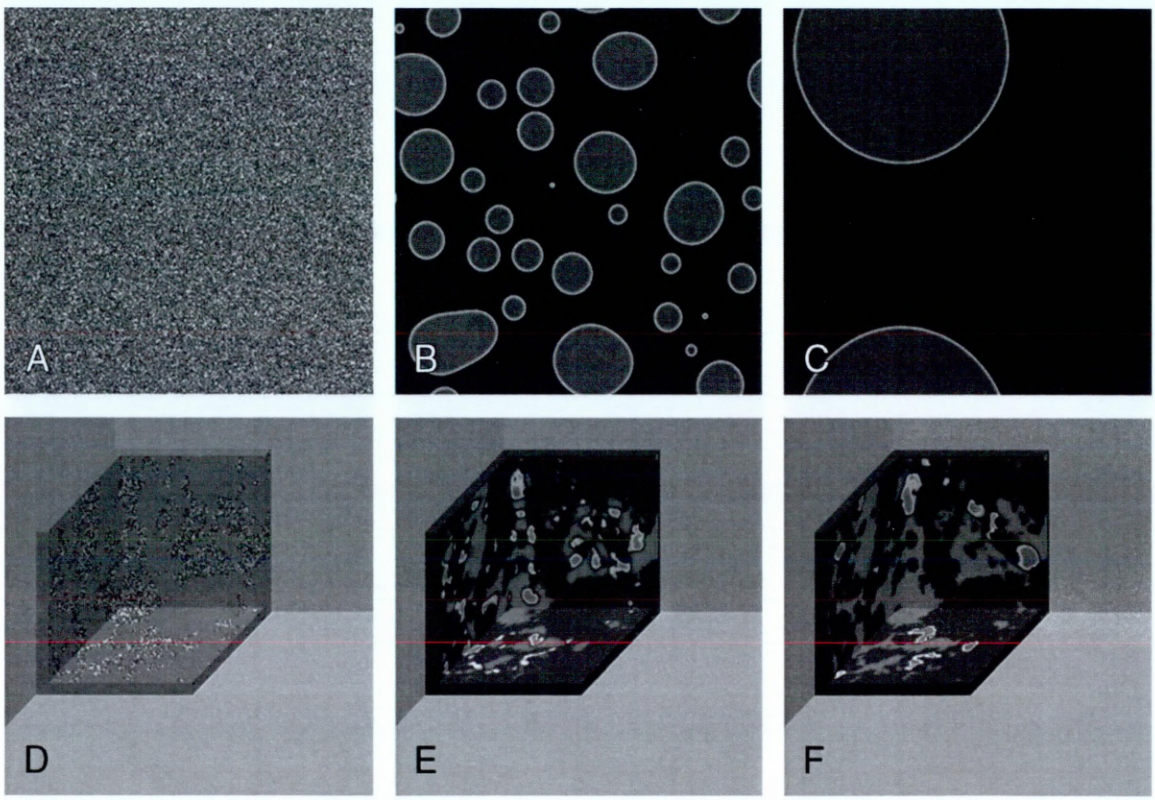

Figure 7.2 Fluid phase separation.
Progressive separation is shown within, firstly, a two-dimensional unstructured environment, at time points (A) t = 0, (B) t = 300, and (C) t = 1,000 iterations, and secondly, within a porous medium at (D) t = 0, (E) t = 300, and (F) t = 50,000. Adapted from (Falconer et al. 2012).

Ideally, such a structure would be simulated at a multiple of the image definition actually used (128^3) but technical limitations in the hardware-software configuration available for LBCFD made this impractical. Despite this issue, the

phenomenon of narrower pore channels being more obstructed by water droplets was demonstrated as expected (figure 7.2).

Having obtained a satisfactory wet/dry labelling of the pore network for each image, the second stage of the project proceeded. This involved simulating the growth of fungi through the wet/dry pore network, where the presence of water acted as a local growth inhibitor; this work was carried out by Falconer. The fungal growth simulation developed by (Falconer et al. 2008) is a discretised reaction-diffusion system, usually implemented on a rectangular lattice. The output from the simulation process is a time series of volume data representing spatial distributions of fungal biomass. These are encoded as a sequence of 3D images (i.e. scalar fields) having elements that are double precision floating point numbers. The first stage in analysing this data was again visual assessment using *ImgView*. In this case it was necessary to apply a logarithmic mapping to the biomass data, such that an intensity range suitable for display was obtained. This is a common requirement when visualising diffusion processes: the exponential decline in concentration with distance produces values over many orders of magnitude. The mapping function necessarily ignores any value less than or equal to zero and is expressed as follows:

$$i = i_{\min} + (i_{\max} - i_{\min}) \times \frac{\left(\log(C_{biomass}) - \log(C_{\min})\right)}{\left(\log(C_{\max}) - \log(C_{\min})\right)} \qquad \text{(equation 7.1)}$$

where (C_{min}, C_{max}) is the concentration interval to be mapped and (i_{min}, i_{max}) is the required intensity interval (e.g. 1 through 255 when unsigned 8bit precision

is used). This transformation was incorporated into *ImgView* and, when enabled by the user, is applied to the data when it is loaded. The interval (C_{min}, C_{max}) is determined from the entire scalar field subject to the stated constraints, while the interval (i_{min}, i_{max}) is determined by graphics hardware capabilities. Having reviewed the images, it was decided by Falconer that the presence of any biomass (i.e. any value greater than zero) was sufficient evidence to label that image element (simulation lattice site) as being "fungal". MF measures were then calculated on this basis of this simple thresholding decision. The MF measures were used as the basis for determining the effect of simulated water distribution on fungal growth: simulation results were analysed in the described manner both with and without the presence of water (two water density values, 150 and 200 were evaluated).

At the final analysis stage of the project, the data to be analysed consisted of three soil structures and for each of these two water distributions and three biomass distributions. MF's were calculated for each structure and then used to standardise the corresponding water and biomass MF's in terms of volume fraction. This novel presentation of information in terms of "structural capacity" (e.g. the fraction of available volume occupied by fungal biomass) allows efficient and effective comparison across a series of individual structures.

Another novel and very powerful investigative technique was creating a scatter-plot from pairs of functional measures. Given the four MF measures there are six pair-wise combinations of measures that can be plotted in this way. These

plots revealed clustering and trends that were otherwise difficult to spot. Most importantly they provided a clear discrimination between simulated behaviour of fungi in respect of soil pore networks having different structural properties, these properties affecting the spatial distribution of water within the pore network.

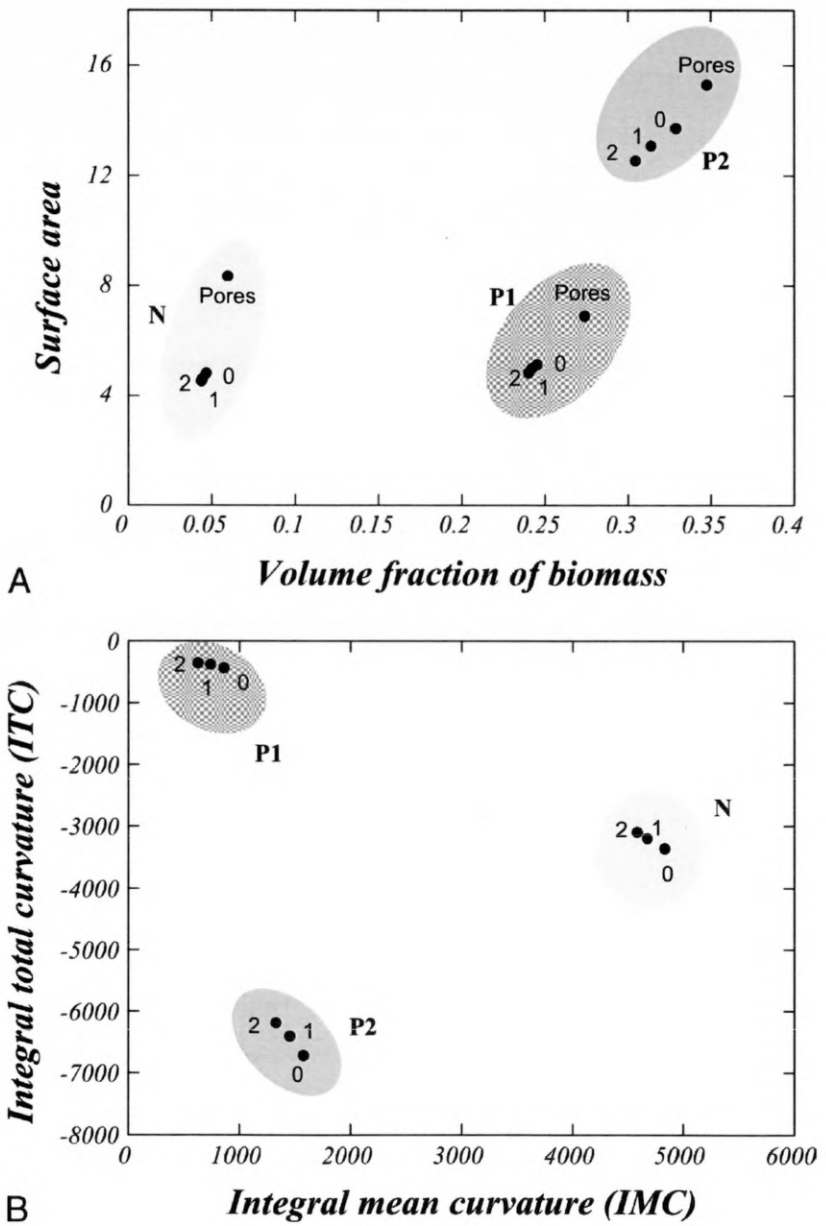

Figure 7.3 Discrimination of fungal growth patterns.
Plots of the surface area versus volume fraction (A) and IMC versus ITC measures for the biomass (B) at the 3 moisture contents. In the graphs, P1_Pores, P2_Pores, and N_Pores represent the functional measures of pore space. Adapted from (Falconer et al. 2012).

7.2 Morphology of In-Vitro Tumours

This project was handled mainly in the style of a consultancy: advising and training those specialised in biology and cytology in the use of image processing software and analysis techniques. Much of the practical work was carried out by Savage, first author of the resulting publication (Savage et al. 2012).

7.2.1 Project Background

The objective was to find a means of discriminating between sets of human cancer cell cultures grown in vitro. These cultures had been treated with antibody markers (to detect specific biological features) and then imaged by optical tomography. All of this practical work had been carried out at facilities of Edinburgh University prior to the involvement of investigators at Abertay; the images were delivered without the possibility of revision. The limited quality of information within these images represented a major challenge for this work as the antibody labelling was erratic giving a very disjoint and "speckled" appearance. At the time this work was underway (early 2011), development of adaptive window indicator Kriging segmentation was still at an early stage and not appropriate for use in a study. This was unfortunate, as the spatial characteristics of these images might have been ideally suited to AWIK segmentation, which might have saved much effort.

7.2.2 Analysis Methods

A sequence of image processing operations (noise reduction, Otsu segmentation and morphological dilation) was applied to each of the sample images. These were judged to yield a satisfactory segmented image of tumour structure. Minkowski functionals were then calculated for these segmented images and the resulting information was assessed to find patterns that might discriminate between samples.

7.2.3 Results

The novel method of scatter-plotting pairs of MF measures (developed as part of the previous investigation - Falconer et al. 2012) was also decisive in discriminating between treatments of tumour cells (figure 7.3), this discrimination was statistically significant. Of particular interest were plots of surface area versus curvature that can be used to infer a degree of "ruggedness" or irregularity on the surface of an object. This is an important characteristic with respect to tumour development as the degree of departure from a smooth shape is a strong indicator of the developmental stage and "aggressiveness" of a tumour (i.e. formation of metastases).

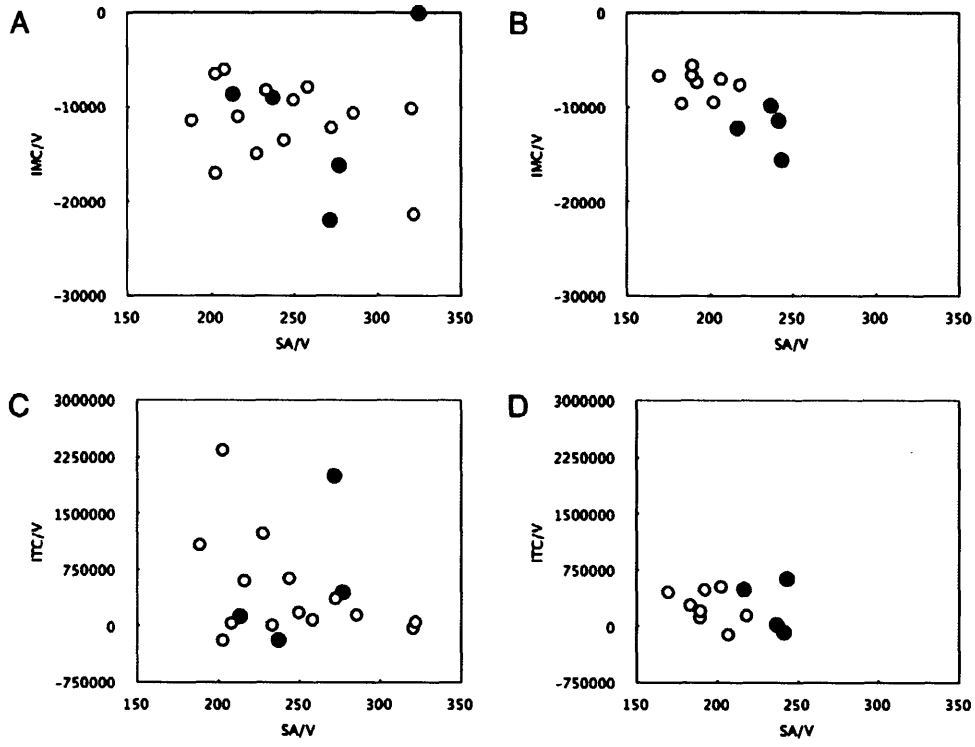

Figure 7.4 Discrimination of tumour treatment via rational functional measures. Plots of geometric (IMC) and topological (ITC) measures of curvature standardised by volume, versus surface area (SA) standardised by volume. Both plots A and C relate to untreated tumours while both B and D relate to tamoxifen-treated tumours. Adapted from (Savage et al. 2012).

7.3 CT Imaging Parameters for Soil Samples

This was a significant project within the broader scope of evaluating image acquisition and subsequent handling procedures within the SIMBIOS research centre. As such, it relates closely to much of the work presented previously in chapters three through six. The overall scope of practical work was substantial, with tasks being divided between Houston, Schmidt and Hapca. The results of this investigation are the subject of a recent paper (Houston et al. in press).

7.3.1 Project Background

The primary objective was the assessment various parameters of the X-ray CT image production process (including parameters of tomographic reconstruction, and mapping of attenuation coefficient estimates to a low precision form that is typically used within graphics file formats). Image series produced using the various parameter combinations were assessed in terms of the image quality measures described previously (section 3.3). Additionally, the relative stability of image segmentation methods over these image series was evaluated using Minkowski functional and connectivity measures (as described in chapter five) on the segmented images.

7.3.2 Analysis Methods

Five soil samples were CT scanned by Schmidt, each using two physical resolutions of projection images. Both resolutions were tomographically reconstructed and aligned by Schmidt and then compared by Hapca. From the

higher resolution projection image series alone, a 256^3 region of interest centred within the physical sample was selected. This region was, for each sample, tomographically reconstructed using four noise reduction settings provided by *CTPro* software (XTek Systems Ltd.). The resulting images series were then mapped from floating point to unsigned 8bit representation using six parameter values for outlier rejection (according to the procedure described in section 3.1.3). Image quality measures were then calculated for each image variant (noise reduction and mapping) and visual inspection verified that differences in the appearance of the image variants were consistent with changes in the value of each measure. Following this initial investigation it became apparent that the response to noise reduction was quite simple. Noise reduction setting "NR2" appeared to be optimal on the image series. Weaker values yield erratic variation while stronger values lead to excessive smoothing and loss of detail. Subsequent analysis (of segmented images) was then restricted to the "NR2" series, reducing the number of variant images from 120 to 30.

All variant images were then segmented using the methods of (Otsu, 1979), (Schleuter et al. 2010), (Houston et al. 2013) and (Hapca et al. 2013). The method of (Houston et al. 2013) was applied using the hysteresis threshold parameters computed via the method of (Schleuter et al. 2010) which were found to be suitable in all cases. The 3D Minkowski functionals and the connectivity measure (both as described in chapter five) were then determined

for all segmented images, resulting in five measures for each of the four segmentations of 30 image variants.

7.3.3 Image Quality Results

Examining table 7.1 (overleaf) it is clear that all image quality measures behave in a consistent fashion with respect to the noise reduction (NR) level parameter specified for tomographic reconstruction. For increased NR, both noise and sharpness measures decrease while contrast increases. The reduction in noise measure is consistent with the smoothing effect of the NR level while the reduction in sharpness is consistent with the blurring of edges that accompanies this form of smoothing ("optimal" filtering applied in the frequency domain as part of the FBP reconstruction algorithm). The increase in contrast measure is a consequence of the image representation in conjunction with the ratio via which contrast has been defined. Filtering has broadened the dispersion of the intensity distribution but the domain of values is constrained by the unsigned 8bit representation used, while the standard deviation is not.

In table 7.2 the change in contrast measure versus outlier rejection parameter is consistent over all images. As the extremes of the distribution of tomographic reconstruction attenuation coefficient estimates (in floating point representation) are less truncated by larger parameter values, the intensity distribution in the resulting image appears "compressed" i.e. the standard deviation is reduced relative to the domain. Visually this corresponds to a reduced ability to discriminate between image elements i.e. a loss of contrast. Similarly, the

difference in intensity between adjacent image elements is reduced leading to reductions in noise and sharpness measures (which are defined in terms of such differences).

Sample Nr	RMS Contrast			Noise			Sharpness		
	NR2	NR3	NR4	NR2	NR3	NR4	NR2	NR3	NR4
1	0.134	0.137	0.141	0.385	0.353	0.309	0.361	0.351	0.328
2	0.117	0.119	0.122	0.427	0.393	0.340	0.375	0.366	0.342
3	0.105	0.106	0.109	0.435	0.399	0.343	0.354	0.343	0.316
4	0.120	0.121	0.123	0.375	0.349	0.308	0.334	0.325	0.304
5	0.116	0.118	0.121	0.379	0.355	0.312	0.348	0.339	0.317

Table 7.1 Image quality measures versus noise reduction.
Noise reduction is achieved as part of the filtered back projection algorithm used for tomographic reconstruction. Adapted from (Houston et al. in press).

Sample Nr / Interfence ratio	RMS Contrast					Noise					Sharpness				
	1	2	3	4	5	1	2	3	4	5	1	2	3	4	5
IQR2	0.191	0.176	0.167	0.190	0.175	0.426	0.456	0.451	0.386	0.405	0.400	0.413	0.376	0.339	0.380
IQR3	0.161	0.142	0.131	0.145	0.145	0.395	0.437	0.438	0.379	0.380	0.371	0.388	0.357	0.333	0.350
IQR4	0.134	0.117	0.105	0.120	0.116	0.385	0.427	0.435	0.375	0.379	0.361	0.375	0.354	0.334	0.348
IQR6	0.100	0.091	0.084	0.099	0.095	0.383	0.421	0.429	0.372	0.373	0.363	0.374	0.355	0.334	0.350
IQR8	0.087	0.079	0.072	0.085	0.081	0.381	0.418	0.429	0.371	0.380	0.366	0.374	0.358	0.336	0.353
No outlier correction	0.020	0.017	0.022	0.035	0.033	0.404	0.444	0.444	0.376	0.380	0.370	0.374	0.353	0.324	0.351

Table 7.2 Image quality measures versus mapping parameter.
The mapping parameter is a scale factor applied to the inter-quartile gap to determine the limits for mapping. These limits define the domain of attenuation coefficients that are linearly mapped to intensities during image precision reduction. Adapted from (Houston et al. in press).

7.3.4 Segmentation Results

Examining the information presented in figure 7.4 it can be seen that in most cases, each of the four image segmentation methods appears intrinsically consistent or stable over the outlier rejection parameter range from 3 to 8 with respect to Minkowski functional and connectivity measures. The notable exception is the (non-local) method of (Otsu, 1979) applied to image 2 where instability is apparent (measures oscillate between small and very large values). The differences in these measures between local segmentation methods are however substantial, the minimum approaching as little as 50% of the maximum for a given parameter value in a few cases. In other words, the physical truth remains elusive, but importantly a useful picture of variability between methods has been gained.

From a consideration of the mechanisms within the tested segmentation methods it might be judged that the truth lies somewhere between the extrema of the results of the local methods. That is, the smooth continuity of both indicator kriging and region growing provides a very conservative estimate of pore space, whereas the local sensitivity of Hapca's method results in class membership being assigned more freely.

To what degree an under-estimate or an over-estimate of some measure might be considered acceptable, and whether one might be preferred over the other, depends upon the application. However, the accuracy of functional measure estimation does itself depend on the size of individual objects relative to the

image definition (as explained in section 5.1.4). This may be a relatively minor problem for the volume fraction (porosity) but is of increasing significance for measures of lower dimensionality. The size distribution of pore space within a segmented image would therefore be useful in judging the potential for error: a greater number of smaller objects implies a less reliable estimate of functional measures. This reasoning further suggests that image comparison would be more reliable if carried out using functional measures calculated by classes of object size.

For each of the local segmentation methods it can be seen that discrimination across samples is reliable with respect to the mapping from reconstructed attenuation coefficients to image intensities. This has clear application to a comparative study of soil type for example.

For a study which considers treatment response within a specific sample however the results presented here do not address: there is no consideration of the effect of sample orientation or other factors associated with the repeated scanning of samples. Information generated from segmented images is shown in the following two tables and the series of graphs in figure 7.4.

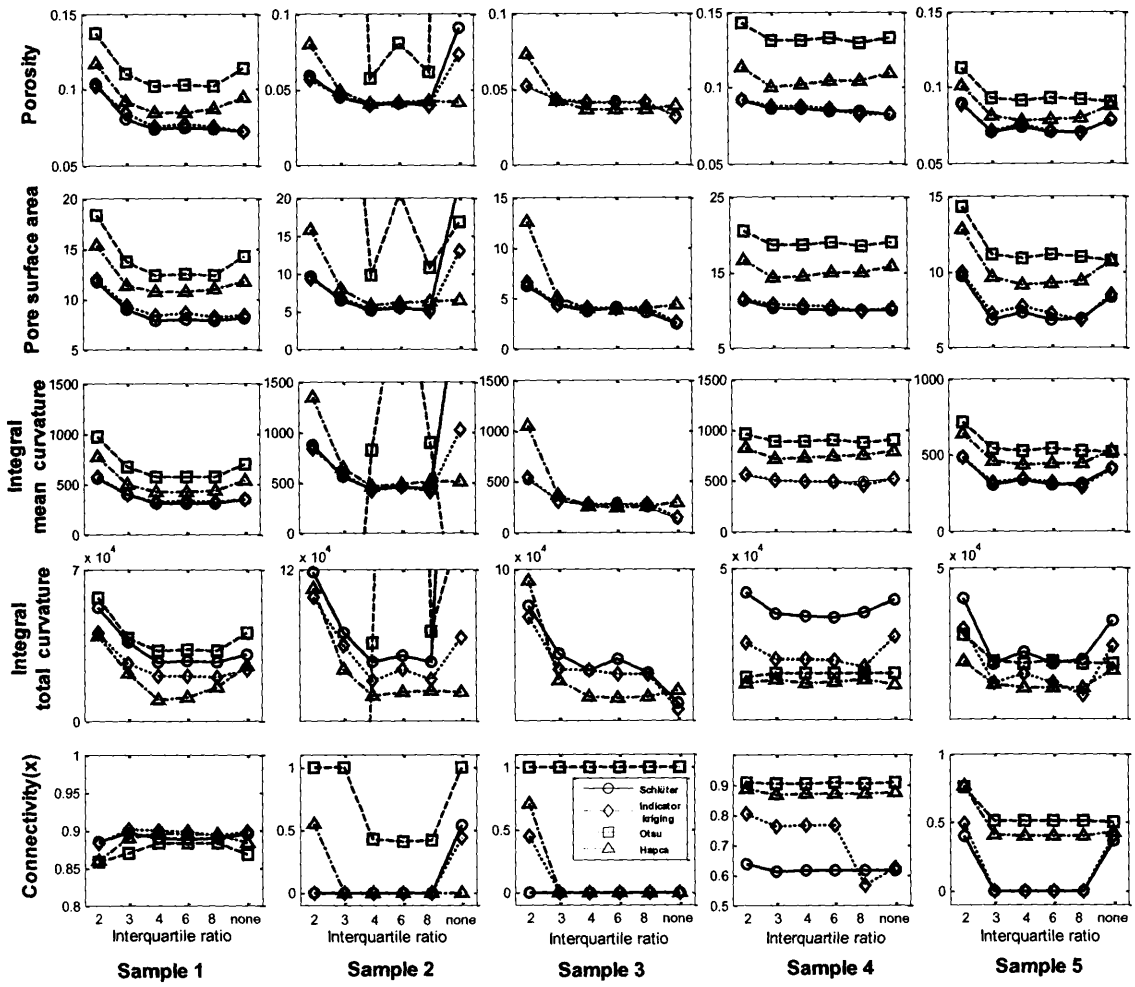

Figure 7.5 Measures on segmented images.
Adapted from Houston et al. (in press).

7.4 Conclusions

The image analysis techniques described within this thesis have been applied to a wide range of problem areas. The quantification of spatial structure is important in many contexts, whether pore networks, microbial biomass distributions or tumour growth. It has been shown that the Minkowski functionals are a powerful means of discriminating between several fundamental aspects of spatial structure. In the examples presented it has furthermore been shown that functional measures can be presented in perhaps unconventional ways; projecting measures onto spaces that may be unfamiliar in terms of physical meaning but nonetheless provide excellent discriminating power.

8.0 Conclusions and Future Work

This work has selected, innovatively developed and evaluated methods appropriate for understanding soil pore structure within digital images. The key objectives of improving the accuracy and robustness of soil image segmentation and of obtaining measures of soil pore structure have been achieved. The level of accuracy in these measures has been established as has their relevance to CT images of soil and other materials. In addition, the analysis software has been developed so as to be extremely computationally efficient, making it widely applicable without specialised computing requirements. The main points of each chapter are next briefly summarised, followed by comments on the overall accuracy of soil image analysis. Some suggestions are then made for assessing the difficult problems associated with repeatable image acquisition. Finally a number of suggestions for the future development of image analysis tools are given.

8.1 Summary of Contents

In chapter one, beginning with the importance of soil and the relevance of CT imaging in understanding soil structure, the history of digital image analysis and it's application to soil was briefly summarised. Some key developments in the application of image analysis applied to soil (and other geo-materials) were noted, and the need to develop a coherent, robust and accessible framework of analysis tools appropriate for soil images was explained.

Chapter two introduced some of the relevant ideas and terminology that are widely used in image analysis. Also introduced was the variographic analysis of

images which is a powerful tool well known within geo-science but not widely used in more general digital imaging applications. Methods for synthesising test images using noise functions were also introduced.

Chapter three reviewed the issues surrounding X-ray image acquisition and computed tomography, hopefully providing an adequate overview of what is a very large and complex subject area. It was noted that *micro*-CT imaging is a relatively new, but rapidly maturing technology being driven to a large extent by industrial requirements. The natural sciences however, may be the major beneficiaries of advanced image acquisition technology that is currently under development. Some of the problems associated with handling tomographic images were noted and practical solutions presented, including methods for assessing image quality. The value of an analysis tool such as the variogram was clearly illustrated in this context, the assessment of noise content in images of geo-materials being an important consideration in the overall analysis process.

Chapter four reviewed a range of approaches to image segmentation, revealing that simple approaches (global thresholding) are inadequate for images with significant noise content. Advanced segmentation methods developed specifically for geo-materials were shown to perform much better in this regard but their complexity raises issues of reliable and efficient implementation.

Chapter five introduced analysis techniques for assessing the structure within segmented images. The Minkowski functionals were described and methods for their estimation on images investigated. The stability of Minkowski functionals with regard to shape and orientation of objects was briefly assessed, showing that sample orientation within a reconstructed image may need to be considered as part of a robust experimental design. Importantly, this also implies that other analysis methods (including the preceding step of segmentation) might be sensitive to sample orientation. Concepts and methods of representing connected spatial structure within images were introduced. Implementation methods for some basic, but practically useful, measures of connectivity were given. The incorporation of Minkowski functionals within a connectivity analysis procedure was described and the potential enhancement of descriptive power and accuracy noted. Finally an important description of structure in porous media, the Pore Size Distribution was considered. Various definitions and methods of implementation were briefly reviewed before a simple, but limited in accuracy, method of calculation was presented.

Chapter six revisited the subject of segmentation, presenting the authors own innovation as an advancement of the state of the art in segmenting images of porous media. The stability of the method applied to a selection of soil images was demonstrated.

Finally, chapter seven briefly reviewed some image analysis projects to which an important contribution was made. The practical application of analysis tools

within the context of a published investigation is an extremely important part of the analysis method development cycle. Deficiencies in a method are far more likely to be recognised when working with something other than familiar or "well behaved" test data. Also involved is a more strategic level of problem solving, rather than the more limited perspective of algorithmic tuning and refinement.

8.2 Accuracy of Soil Image Analysis

The overall accuracy of information obtained via the CT image analysis process applied to soil samples remains unknown, as only the final step of measure calculation has been assessed using reliable test data. An appropriate and practical means of assessing the accuracy of soil image acquisition and segmentation is difficult to devise. Although segmentation can, in principle, be assessed using synthetic soil images, the construction of these images may introduce an unknown level of bias. Image acquisition is the most difficult step in the overall process to assess reliably for soil samples, due to the complex interactions between strongly heterogeneous material and radiation. The two steps of acquisition and segmentation might be assessed using a physical test sample that is constructed firstly, from a material that accurately reflects the properties of soil with respect to X-ray transmission, and secondly whose structure is known with high precision. These two requirements seem to conflict with each other but a solution might eventually be accessible via advanced manufacturing technology such as 3D printing (Otten et al. 2012). At present this technology is not compatible with a material such as soil, hence a rigorous means of assessment is not apparent. For this reason it is necessary to

carefully consider possible causes of error within the acquisition and segmentation processes with a view to addressing them via rational judgement on the results of the analysis process overall.

Perhaps the most significant issue affecting the analysis of soil images, is the dispersion and size distribution of soil particles with respect to image resolution. A well consolidated soil (e.g. with a significant clay content acting as "glue") presents relatively few problems by virtue of its more orderly structure. The accuracy of analysis is still limited by finite resolution, but it can be argued that errors are random in nature and thus cancel out to some degree at the observed scale. Contrastingly, a very friable soil, in which an abundance of small particles are found, is very difficult to analyse at any presently achievable resolution. This is most true when dispersed grains of metal-bearing minerals are present, as these can produce strong attenuation even at very small size. Thus, a strongly attenuating particle smaller than the image resolution may be detected and classified as solid, whereas a similar sized particle of weakly attenuating material (e.g. silica) is ignored. This means that the effective resolution of the imaging system varies unpredictably according to material properties within the sample.

Quantitative measures based on images containing such "rogue" features are then inevitably in error because they use an incorrect length scale. This type of error is systematic and becomes more pronounced for measures based on integration over higher derivatives i.e. surface area is more error prone than

volume. A topological measure does not directly include a measure of length, yet topological structure relies on the definition of connectivity at the element scale and hence in practice incorporates length scale dependant information. The consequence is that frequent occurrence of small isolated clusters of image elements is detrimental to the accuracy of soil image analysis. This might be remediable in the case where the distribution of particle sizes beyond the resolution of the image was known and that measures incorporating this information could be devised. At present this does not seem particularly likely and so the remaining practical course of action is the removal of isolated image elements during segmentation (as in Oh and Lindquist, 1999) with subsequent identification of "potentially unphysical" (Peth et al. 2008) clusters during connectivity analysis. As stated previously, it is important that such remediation is conducted on the basis of rational judgement: presenting analysis results in an appropriately structured fashion (e.g. by size classes of object) is therefore important.

8.3 More Reliable and Repeatable CT Imaging

A very important problem affecting many investigations is the degree of repeatability in CT imaging: given an unchanging sample, what level of variability in analysis results might be expected, and is a systematic change detectable with the age of equipment. This is a critical first step in assessing the usefulness of equipment, but has been overlooked within this project due to an initial limited understanding of the issues involved, and also due to the

perceived importance of other problems that had to be addressed. Two specific problems relating to repeatability are next briefly considered.

The first of these problems is obtaining an appropriate unchanging sample i.e. one that is robust against physical handling but which embodies the properties of soil: air filled pores resulting from the packing of irregular granular material containing various minerals. Microcosms constructed by repacking soil fractions (obtained by graded sieving of natural soil) have been studied previously at SIMBIOS, but their long-term stability with repeated handling is unknown. If the soil fractions could be bonded together permanently during (or following) repacking and without seriously altering the soil structure, then this would provide a calibration sample with long-term viability. Such a sample could also be more confidently transported to different facilities in order to assess variability between equipment. Constructing such a bonded soil is however difficult: the bonding agent must be dispersed over the grains in sufficient quantity to be effective, but without filling pores, nor should it affect the agglomeration of grains. Perhaps a resin, inert at room temperature, could be used so that following packing, the sample is heat treated to effect the bonding. The resin might be dispersed over the soil fractions prior to mixing, by spraying with either an ultra-fine powder or with the aid of a suitably volatile solvent.

The next problem in sequence is the accurate mounting of samples in the CT scanner: presently this seems to be a process of dead reckoning, encouraged by reliance on image registration software (VGStudio Max) for comparison of successive reconstructed images. Registration requires an affine transformation

(rotation, translation and possibly scaling) being applied to one or both images and consequently involves an implicit down-sampling of image resolution (i.e. transformed images consist of elements that are linear combinations of input elements). Such processing is always necessary due to the partial volume effect: a shift in position by even a tiny fraction of the image resolution is sufficient to alter the intensities of elements on a boundary. However the accuracy of the reconstruction procedure itself is affected by sample mounting, as the location of the rotation axis within the sample must be known accurately. The axis is estimated by software based on a number of reference slices through the sample hence it is important that the sample be mounted as consistently as possible across consecutive image captures. Although the equipment manufacturer provides a selection of sample mounting tables and clamps, these are manufactured from metal and so partly obscure a soil sample at lower beam energy. For this reason, X-ray transparent (or at least very low density) sample mounting equipment is desirable, provided it can be manufactured to reasonable tolerances. One method of achieving this is the rapid manufacturing processes that are being evaluated within SIMBIOS (producing mineral-free soil structures that aid in the study of microbial growth).

8.4 Analysis Tools: Specific Development Projects

The potential for improvement of the developed image analysis tools is almost limitless: detection of local texture and shape might allow tremendous improvements in classification ability (albeit at high computational cost). Estimation of interfaces, and hence functional measures, with sub-pixel

accuracy is another low-level capability (i.e. at the image element neighbourhood scale) that could benefit both accuracy and robustness. At the object (e.g. pore cluster) to image levels, more detailed information might be extracted parametrically, e.g. by classes of size, yielding structural descriptors in the form of distributions. Following are some specific suggestions for future work to improve the image analysis tools available to the soil science community. Each has been selected as being worthwhile in terms of original work i.e. there is some degree of novelty in how techniques are combined and/or applied.

8.4.1 Size Distributions

The method for obtaining an approximate pore size distribution from a discrete skeleton image in conjunction with a distance transform image was described briefly in chapter 5. This is limited in accuracy by the discrete skeleton which, being defined in terms of morphological erosion operations, describes only a subset of the true medial axis (i.e. axial surfaces are thinned to lines and points) with limited precision. An alternative approach uses the distance transform image alone, detecting *singularities* in the distance field via analysis of its spatial gradient (Siddiqi and Pizer, 2008).

Once medial axis locations have been determined, detailed information can be obtained using the *structure tensor* (Knutsson, 1989). This is actually a covariance matrix formed from weighted combinations of gradient vectors in the local neighbourhood of a point. The eigensystem of this covariance matrix reveals local anisotropy in object structure and hence can be used to infer

dimensionality (point, line or plane). This allows accurate geometric description (i.e. including surface orientation) of the medial axis to be extracted, which in turn permits size distributions to be computed more efficiently and accurately. The obvious disadvantage of this approach is computational cost: a large number of covariance matrices must be constructed and their eigensystems determined.

8.4.2 Connectivity

The connectivity measures so far implemented, the "surface connected fraction" and "spanning volume fraction" of pore volume can only be calculated in relation to the single spatial scale defined by each axis of a region of interest. If such a measure were computed for all possible regions of interest, then a distribution of connectivity versus distance could be formed. This is however not directly computable due to the combinatoric nature of the problem: there are N*(N-1)/2 intervals per axis, leading to $O(N^6)$ connectivity assessments for a complete evaluation in 3D. Fortunately there is another, much more efficient way to determine this information by using pore cluster bounding volumes. These are already determined as part of the connectivity analysis and take the form of an AABB (axis aligned bounding box - the axes in question being the principal axes of the image coordinate system). The length of each axis of an AABB therefore defines the scale over which space is connected by the axial projection of the pore cluster. A crude distribution can then be formed by adding the volume of each pore cluster to a category defined by axial length i.e. the frequency axis of the histogram is a sum of volumes. The three axes can either be used to form three distinct directional distributions, or the three might be merged to form a

single pseudo-isotropic distribution. Each category then contains a sum of pore cluster volumes relating to a specific projected interval, but fails to account for any longer intervals. In other words, from such a histogram it is possible to determine the probability that a randomly chosen element belongs to an exact distance class whereas it is generally more useful to know the (cumulative) probability of it being within a given distance. For this reason each distance class should include information from all greater distance classes. Standardising over all frequencies (so that they sum to one) gives information in the form of a PMF, but this is actually a form of size distribution rather than a connectivity distribution. This is because the measure thus far described does not account for the spatial distribution of cluster volume within the axial interval.

To obtain a connectivity distribution it is necessary, for each axis of each pore cluster AABB, to calculate the volume partitions of the pore cluster, adding each to the relevant distance class. Thus for a cluster having a projected width of 100 image elements, the entire cluster volume is added to the 100th distance class, then each partition sub-volume (e.g. at length ratios 1:99, 2:98, 3:97 ... 98:2, 99:1) is added to the distance class corresponding to the partition length. If this method is extended such that a separate connectivity distribution is computed per axial slice, then a complete description of spatial variation in connectivity by classes of distance can be obtained (with the caveat that this is based on axial projection and therefore does not properly account for directional variation). However, such information may be unmanageably large (a number of distributions equal to the image definition per axis is obtained) and would

benefit from reduction to a single distribution. This would allow both mean and variance in connectivity to be determined for every distance class throughout a region of interest: this represents a huge improvement in both accuracy and robustness compared to the current SCF measure.

8.4.3 Multi-phase Segmentation

Ideally, the physical scientist wishes to observe the spatial distribution of individual material phases. In the case of soil this means, in the general case, discriminating between pore, organic matter, aggregate, mineral and in some cases water. The ability to automatically recognise such different components of soil, distinguishing between different forms of organic matter (OM) and mineral for example, would be very useful. This is however a challenging objective that, despite advanced image acquisition technology, has proven difficult to realise (Sleutel et al. 2011; Elyeznasni et al. 2012). This is ultimately due to the limited image resolution that can be achieved with respect to a typical physical sample size, the partial volume effect then means that many image elements represent a phase mixture. When only two material phases are involved (pore and solid) and these exhibit a strongly contrasting response to X-rays, this problem is effectively addressed by considering local spatial correlation (e.g. indicator kriging). When further materials with intermediate X-ray response (such as organic matter) are considered, then discrimination becomes very difficult.

A limited solution is available in terms of using a X-ray contrast agent such as Osmium Tetroxide which binds preferentially to cell membranes, and thus can be used to identify micro-organisms (Lilje et al. 2013). A more general approach

is to obtain further evidence in the form of a multi-spectral image: typically referred to as a "dual-energy" CT image (Garnier et al. 1998). The differing contrast between energy levels per image element can provide extra evidence that allows more accurate classification. Unfortunately, this strategy is itself problematic as a rather low beam energy (20 to 30kEV) is required to discriminate between air and OM whereas a relatively high energy (>70kEV) may be required to penetrate soil samples. It is conceivable that lower energy levels may be workable in the case of smaller physical samples (improving penetration) subject to a sufficient X-ray flux being available (reducing statistical noise). This however implies the use of a synchrotron source, for which multi-spectral imaging may not be so straightforward as in the case of a "bench" system. An alternative approach is the use of phase contrast (Beckmann et al. 1997) which offers better discrimination of OM and is practical at high energy (100kEV). However being based on interferometry, this requires a monochromatic X-ray beam to be split with controlled phase separation and so requires using a relatively complex synchrotron beam line.

Whatever the mode of image acquisition, it is not certain that discrimination between multiple phases will be obvious in all cases. The partial volume effect will inevitably make a proportion of image elements difficult to classify, hence methods based on spatial correlation (e.g. indicator kriging) may be required. In this case a spatial variance model description and solution method appropriate for a multi-phase system would have to be developed.

8.4.4 Analysis of Non-Cuboid Objects

The analyses applied to CT images within this project have assumed that a cuboidal region of interest (henceforth ROI) is taken from the interior of an object. This is to some extent an adequate approach for high definition images of soil, given the process by which a physical sample is obtained and also the nature of the tomographic imaging process. Specifically, forcing a sampling ring into soil, and then twisting in order to extract a core, risks inducing structural deformation in the outer part of the sample. Subsequently, the collection of angular projection images for tomographic reconstruction means a progressive decrease in the 3D density of information with respect to distance from the rotation axis of the sample. Reconstruction of this information yields a solution that is biased in favour of the 3D space close to the rotation axis. These two factors mean that the innermost part of the physical sample is most reliably captured in the image, hence extracting a sub-volume centred on the rotation axis permits information of lower reliability to be rejected.

A sufficiently small cuboid may be judged to be adequately reliable yet the shape is inherently non-uniform with respect to the information quality within the reconstructed image. Ideally, a cylindrical ROI would be extracted from a reconstructed image, preferably based on some assessment of information reliability (rather than a perhaps arbitrary decision made by an operator). A cylindrical volume of image data is however not especially convenient to represent directly within a programming language and may introduce problems of data portability (e.g. a non-standard file format). For better generality then, it

is preferable to retain a cuboid of image data but to somehow define within this a cylindrical ROI. The storage overhead of this approach is fractionally greater than 27%, which does not seem excessive. The processing cost is more difficult to define as this depends on the details of the image traversal; an efficient approach might involve significant cost to develop.

The most general scheme for defining the spatial locations of valid image elements (ROI) is to use a binary valued *mask image* with which arbitrarily complex shapes can be described. To represent a cylinder simply requires the image of a disk (replicated an appropriate number of times) centred on the rotation axis of the sample image. If a parametric description of the cylinder is available then the appropriate volume mask image is trivially simple to generate and need not be stored. The mask image strategy then provides a good balance between the complexity of development and the flexibility of analysis. A brute force scheme based on the repeated "dumb" checking of the mask image could be implemented quite simply, then later refined if required.

The use of mask images is particularly important for the analysis of isolated porous objects having an irregular boundary e.g. soil aggregates or biochar fragments. In such cases the distinction between object interior and exterior is not entirely clear: deciding whether a surface indentation is a shallow pore or merely a surface wrinkle depends upon the scale of observation. Generating a mask image for a complex shape is commonly achieved using a *morphological closing* operator (Serra, 1982) based on spatial length scales defined by a

structuring element. Starting with a (binary) classified image of the object, the closing operation seals all gaps less than or equal to the length scale. The ideal structuring element is spherical (yielding a rotationally symmetric closing operator) but the computational cost may be extremely high, particularly in the case of 3D images. An assessment of the required level of rotational symmetry versus computational cost is advisable.

8.4.5 Improved Accuracy of Functional Measures

In principle it is possible to identify the location of surfaces (e.g. the pore-solid interface) with accuracy beyond the level of individual image elements. This requires that each classified image element has a value describing it's degree of class membership, rather than just a class index. Instead of simply bisecting the edges of interface cells (this being a cuboid formed from 8 neighbouring image elements of more than one class, as used in the algorithms presented in (Ohser and Mucklich, 2000), each cell edge may be subdivided according to the ratio of class membership degree. For example given a cell edge delimited by two image elements A and B, having membership degrees D_A, D_B then the edge ratio r_{AB} may be defined as:

$$r_{AB} = \frac{D_A}{D_A + D_B} \qquad \text{(equation 8.1)}$$

A description of the surface geometry within any cell can be deduced from all edge intersections in some local neighbourhood. In the simplest case, by considering only the twelve edges of each cell, a set of triangular surface elements is obtained. In this case, the extracted surface description is identical to that obtained from the *Marching Cubes* iso-surface extraction algorithm (Lorensen & Cline, 1987). Measures such as volume and surface area can be

computed from the local surface description within each cell and summed over all cells. Computing mean curvature requires the change in orientation at each face of a cell to be considered, hence a set of neighbouring cells is required, making the curvature calculation somewhat more complex. For a topological measure such as total curvature, the results are unaffected by the accuracy of subdivision, hence such a measure is more efficiently calculated using the original and simpler method.

Obtaining a class membership degree value for each image element is simple in the case of indicator Kriging: it is the class index (i.e. zero or one) in the case of a-priori classified elements, and the kriged membership probability otherwise. Other methods for obtaining such a value can be defined using the grey scale image in conjunction with a model of image intensity e.g. a Gaussian mixture model, in which case membership degree can be calculated from normal population "Z-scores".

The process of determining an edge ratio is actually closely related to the concept of a *watershed transform* (Beucher & Lantuejoul,1979). This transform can be defined and implemented in many ways (Roerdink & Meijster, 2001) but commonly is based on the use of spatial gradients to detect the location of interfaces between regions. A watershed transform applied to a class membership image can therefore be seen as equivalent to the edge ratio method described previously.

8.5 Concluding Remarks

At the outset of this project, the objective was to develop "novel quantitative techniques for soil CT image analysis". In the sense of providing analysis tools, the project has been successful: soil CT images can now be reliably segmented and functional measures computed quickly and accurately. These tools have also been successfully applied to the study of human cancer development and there may well be further bio-medical applications. The principal novelty in the project is the conception and development of the adaptive window indicator kriging segmentation method, with some degree of novelty in how Minkowski functional measures have been applied within general connectivity analysis and also their application to specific analysis problems. As far as quantitative techniques applied to physical experimental data are concerned, the results are not decisive and there remains a number of important unanswered questions regarding the interpretation of soil CT images. The lack of predictability in soil structure combined with unquantified sources of uncertainty in the imaging process mean that accuracy is difficult to assess. Advances in technology are however allowing strategies to be envisaged that may finally address these problems.

References

Abramoff M D, Magalhaes P J, Ram S J. (2004) Image Processing with ImageJ. Biophotonics International, Col.11:7, pp.36-42.

Albert R, Barabási A-L. (2002) Statistical mechanics of complex networks. Reviews of Modern Physics Vol.74:1, pp.47-97.

Arganda-Carreras I, Fernandez-Gonzalez R, Munoz-Barrutia A, Ortiz-De-Solorzano C. (2010) 3D reconstruction of histological sections: Application to mammary gland tissue. Microscopy Research and Technique, Vol.73:11, pp.1019–1029.

Barber C B, Dobkin D P, Huhdanpaa H T. (1996) The Quickhull algorithm for convex hulls. ACM Transactions on Mathematical Software, Vol.22:4, pp.469-483.

Baveye PC, Laba M, Otten W, Bouckaert L, Dello-Sterpaio P, Goswami RR, Grinev D, Houston AN, Hu Y, Liu J, Mooney S, Pajor R, Sleutel S, Tarquis A, Wang W, Wei Q, Sezgin M. (2010) Observer-dependent variability of the thresholding step in the quantitative analysis of soil images and X-ray microtomography data. Geoderma Vol.157:1-2, pp.51-63.

Barnes G E. (2010) Soil Mechanics: Principles and Practice (3rd edition). Palgrave Macmillan, ISBN 0230579809.

Batenburg K J. (2012) Fast Approximation of Algebraic Reconstruction Methods for Tomography. IEEE Transactions on Image Processing, Vol.21:8, pp.3648-3658.

Beckmann F, Bonse U, Busch F, Günnewig O. (1997) X-Ray Microtomography Using Phase Contrast for the Investigation of Organic Matter. Journal of Computer Assisted Tomography, Vol.21:4, pp.539-553.

Berenstein C A. (1998) Radon transforms, wavelets, and applications. (In Lecture Notes in Mathematics 1684: Integral Geometry, Radon Transforms and Complex Analysis, pp.1-33, editors: Tarabusi E C, Picardello M A, Zampieri G.) Springer-Verlag, ISBN 3540642072.

Berthod M, Kato Z, Zerubia J. (1995) DPA: A Deterministic Approach to the MAP. IEEE Transactions on Image Processing, Vol.4:9, pp.1312-1314.

Berthod M, Kato Z, Yu S, Zerubia J. (1996) Bayesian Image Classification Using Markov Random Fields. Image and Vision Computing, Vol.14:4, pp.285-295.

Besag J. (1986) On the Statistical Analysis of Dirty Pictures Journal of the Royal Stataistical Society B, Vol.48:3, pp.259-302.

Beucher S, Lantuejoul C. (1979) Use of watersheds in contour detection. International workshop on image processing, real-time edge and motion detection/estimation (Proceedings).

Beucher S, Meyer F. (1993) The morphological approach to segmentation: the watershed transformation. (In Mathematical Morphology in Image Processing, pp.433–481, editor: Dougherty E.) Kluwer, ISBN 0824787242.

Bhattacharya S, Gubbins K E. (2006) Fast Method for Computing Pore Size Distributions of Model Materials. Langmuir, Vol.22:18, pp.7726-7731.

Blair J M, Falconer R E, Milne A C, Young I M, Crawford J W. (2007) Modeling Three-Dimensional Microstructure in Heterogeneous Media. Journal of the Soil Science Society of America, Vol.71:6, pp.1807-1812.

Blum H. (1967) A transformation for extracting new descriptors of shape. Models for the perception of speech and visual form (Proceedings), pp.362-380. M.I.T. Press.

Bondy J A, Murty U S R. (1976) Graph Theory with Applications. McMillan, ISBN 0444194517.

Borgefors G. (1996) On Digital Distance Transforms in Three Dimensions. Computer Vision and Image Understanding, Vol. 64:3, pp.368-376.

Bronnikov A V. (1999) Numerical solution of the identification problem for the attenuated Radon transform. Inverse Problems (Institute of Physics), Vol.15:5, pp.1315-1324.

Bullock P, Thomasson A J. (1979) Rothamsted studies of soil structure II. Measurement and characterization of macroporosity by image analysis and comparison with data from water-retention measurements. Journal of Soil Science, Vol.30:3, pp.391–413.

Canny J. (1986) A computational approach to edge detection. IEEE Transactions on Pattern Analysis and Machine Intelligence, Vol.8:6, pp.679-698.

Chan T, Shen J. (2005) Image Processing and Analysis: Variational, PDE, Wavelet and Stochastic Methods. SIAM, ISBN 089871589X.

Cho S, Haralick R, Yi S. (1989) Improvement of Kittler and Illingworth's minimum error thresholding. Pattern Recognition, Vol.22:5, pp.609–617.

Chow C K, Kaneko T. (1972) Automatic boundary detection of the left ventricle from cineangiograms. Computer and Biomedical Research, Vol.5:4, pp.388-410.

Coleman J, Jenkinson D S. (2008) RothC-26.3; A model for the turnover of Carbon in soil. Rothamstead Research, ISBN 0951445685.

Cooley J W, Tukey J W. (1965) An algorithm for the machine calculation of complex Fourier series. Mathematics of Computation, Vol.19:90, pp.297–301.

Cormack, A M. (1963) Representation of a Function by Its Line Integrals, with Some Radiological Applications. Journal of Applied Physics. Vol.34:9, pp.2722-2727.

Cormack, A M. (1964) Representation of a Function by Its Line Integrals, with Some Radiological Applications II. Journal of Applied Physics. Vol.35:10, pp.2908-2914.

Coudray N, Buessler U. (2010). Robust threshold estimation for images with unimodal histograms. Pattern Recognition Letters, Vol.31:9, pp.1010–1019.

DaCosta L, Rodrigues F A, Travieso G, VillasBoas P R. (2007) Characterization of complex networks: A survey of measurements. Advances in Physics, Vol.56:1, pp.167-242.

Davies E R. (2005) Machine Vision (3rd edition). Morgan Kauffman (Elsevier), ISBN 0122060938.

De Gryze S, Jassogne L J, Six J, Bossuyt H, Wevers M, Merckx R. (2006) Pore structure changes during decomposition of fresh residue: X-ray tomography analyses Geoderma, Vol.134:1–2, pp.82–96.

Delerue J-F, Perrier E. (2002) DXSoil, a library for 3D image analysis in soil science. Computers and Geosciences, Vol.28:9, pp.1041–1050.

Deurer M, Grinev D, Young I, Clothier B, Müller K. (2010) The impact of orchard management on macro-pore topology and function. 19th World Congress of Soil Science.

Deutsch C V. (1996) Correcting for negative weights in ordinary kriging. Computers and Geosciences, Vol.22:7, pp.765-773.

Dickinson WR. (1970) Interpreting detrital modes of graywacke and arkose. Journal of Sedimentary Petrology, Vol. 40:2, pp.695–707.

Dobbie K E, Bruneau P M C, Towers W (eds). (2011) The State of Scotland's Soil. SEPA.

Duda R O, Hart P E. (1973) Pattern Classification and scene analysis. Wiley-Blackwell, ISBN 0471223611.

Duda R O, Hart P E, Stork D G. (2001) Pattern Classification. (2nd edition) Wiley (NY), ISBN 0471056693.

Dungait J A J, Hopkins D W, Gregory A S, Whitmore A P (2012) Soil organic matter turnover is governed by accessibility not recalcitrance. Global Change Biology, Vol.18:6, pp.1761-1796.

Elliot T, Heck R. (2007). A comparison of 2D vs 3D thresholding of CT imagery. Canadian Journal of Soil Science, Vol.87:4, pp.405-412.

Ellis S, Mellor A. (2010) Soils and Environment (2nd ed). Routledge, ISBN 0415213509.

Elyeznasnia N, Sellamib F,Pota V, Benoita P, Vieublé-Gonoda L, Young I, Peth S. (2012) Exploration of soil micromorphology to identify coarse-sized OM assemblages in X-ray CT images of undisturbed cultivated soil cores. Geoderma, Vol.179-180, pp.38-45.

Erdos P, Renyi A. (1960) On the evolution of random graphs. Mathematical Institute of the Hungarian Academy Sciences, Vol.5, pp.17-61.

Euler L. (1736) Solutio problematis ad geometriam situs pertinentis. Comment of the Academy of Sciences Petropolitana, Vol.8, pp.128-140.

Falconer R E, Bown J L, White NA, Crawford J W. (2008) Modelling Interactions in Fungi. The Royal Society Interface. Vol.5:23, pp.603–615.

Falconer R E, Houston A N, Otten W, Baveye P C. (2012) Emergent behavior of soil fungal dynamics: Influence of soil architecture and water distribution. Soil Science, Vol.177:2, pp.111-119.

Feldkamp L A, Davis L C, Kress J W. (1984) Practical cone-beam algorithm. Journal of the Optical Society of America A, Vol.1:6, pp.612-619.

Galerne B, Gousseau Y, Morel J-M. (2011) Random Phase Textures: Theory and Synthesis. IEEE Transactions on Image Processing, Vol.5:1, pp.257-267.

Garnier P, Angulo-Jaramillo R, DiCarlo D A, Bauters T W J, Darnault C J G, Steenhuis T S, Parlange J-Y, Baveye P (1998) Dual-energy synchrotron X ray measurements of rapid soil density and water content changes in swelling soils during infiltration. Water Resources Research, Vol.34:11, pp.2837-2842.

Gazzi, P. (1966) Le Arenarie del Flysch Sopracretaceo dell'Appennino Modenese: Correlazioni con il Flysch di Monghidoro. Mineralogica e Petrografica Acta, Vol.12, pp.69-97.

Geman S, Geman D. (1984) Stochastic Relaxation, Gibbs Distributions, and the Bayesian Restoration of Images. IEEE Transactions on Pattern Analysis and Machine Intelligence, Vol.6, pp.721-741.

Glasbey C A, Horgan G W. (1995) Image analysis for the biological sciences. Wiley, ISBN 0471937266.

Goovaerts P. (1997) Geostatistics for Natural Resources Evaluation. Oxford University Press, ISBN 9780195115383.

Grimmett G. (1999) Percolation (2nd edition). Springer Verlag, ISBN 3642084427.

Hall N W, Dalrymple J B. (1979) A method for making serial thin sections of soils and other unconsolidated materials. Earth Surface Processes, Vol.4:1, pp.85-88.

Harris K, Young I M, Gilligan C A, Otten W, Ritz K. (2003) Effect of bulk density on the spatial organisation of the fungus *Rhizoctonia solani* in soil. FEMS Microbial Ecology, Vol.44, pp.45-56.

Hadwiger H. (1957) Vorlesungen über Inhalt, Oberfläche und Isoperimetrie. Springer (Berlin).

Hapca SM, Wang ZX, Otten W, Wilson C, Baveye PC. (2011) Automated statistical method to align 2D chemical maps with 3D X-ray computed micro-tomographic images of soils. Geoderma Vol.164:3-4, pp.146-154.

Hapca SM, Houston AN, Otten W, Baveye PC. (in press) New objective segmentation method based on minimizing locally the intra-class variance of greyscale images. Vadose Zone Journal.

Haralick R M, Shapiro L G. (1985) Image segmentation techniques. Computer vision, graphics, and image processing, Vol.29:1, pp.100-132.

Houston A N, Otten W, Baveye P, Hapca S. (2013) Adaptive Window Indicator Kriging: A thresholding method for computed tomography images of porous media. Computers and Geosciences, Vol.54, pp.239-248.

Huang C T, Mitchell O R. (1994) A Euclidean distance transform using grayscale morphology decomposition. IEEE Transactions on Pattern Analysis and Machine Intelligence Vol. 16:4, pp.443–448.

Iassonov P, Gebrenegus T, Tuller M. (2009) Segmentation of X-ray computed tomography images of porous materials: A crucial step for characterization and quantitative analysis of pore structures. Water Resources Research, Vol.45:9, pp.139-151.

Jähne B, Scharr H, Körkel S. (1999) Principles of filter design. In: Handbook of Computer Vision and Applications (Ed. Jahne B, Geissler P, Haussecker H). Morgan Kaufmann (San Francisco), ISBN 0123797705.

Juarez, S., Nunan, N., Duday, A., Pouteau, V., Schmidt, S., Hapca, S., Falconer, R., Otten, W. and Chenu, C. (2013) Effects of different soil structures on the decomposition of native and added organic carbon. Submitted to European Journal of Soil Biology.

Kaczmarz S. (1937). Approximate solution of system of linear equations. (Translation from German. 1993) International Journal of Control. Vol.57:6, pp.1269-1271.

Kak A C, Slaney M. (1987) Principles of Computerized Tomographic Imaging. IEEE Press, ISBN 089871494.

Kapur J N, Sahoo P K, Wong A C K. (1985) A New Method for Gray-Level Picture Thresholding Using the Entropy of the Histogram. Graphical Models and Image Processing, Vol.29:3, pp.273–285.

Kato Z, Zerubia J, Berthod M. (1996) Bayesian Image Classification Using Markov Random Fields. Image and Vision Computing, Vol.14:4, pp.285–295.

Kato Z, Zerubia J, Berthod M. (1999) Unsupervised Parallel Image Classification Using Markovian Models. Pattern Recognition, Vol.32:4, pp.591-604.

Kernighan B, Ritchie D. (1978) The C Programming Language. Prentice Hall, ISBN 0131101633.

Kerst D W. (1940) Acceleration of Electrons by Magnetic Induction. Physical Review, Vol.58:9, pp.841-847.

Kittler J, Illingworth J. (1986) Minimum Error Thresholding. Pattern Recognition, Vol.19:1, pp.41–47.

Knuth D E. (1992) Lecture Notes in Computer Science 606: Axioms and hulls. Springer-Verlag, ISBN 3540556117.

Knuth D E. (2011) The Art of Computer Programming. Addison Wesley, ISBN 0321751043.

Knutsson H. (1989) Representing local structure using tensors. Linkoping University, Computer Vision Laboratory.

Kroon D. (2009) Numerical Optimization of Kernel Based Image Derivatives. University of Twente. http://www.k-zone.nl/

Lark, MR, Papritz A. (2003) Fitting a linear model of coregionalization for soil properties using simulating annealing. Geoderma Vol.115:3-4, pp.245-260.

Larsson D H, Lundström U, Westermark U, Takman P A C, Burvall A, Henriksson M A, Hertz H M. (2012) Small-animal tomography with a liquid-metal-jet x-ray source. Proceedings of SPIE, Vol.8313.

Lawrence E O. (1934) Method and apparatus for the acceleration of ions. US patent 1948384.

Lee T-C, Kashyap R, Chu C N. (1994) Building skeleton models via 3-D medial surface/axis thinning algorithms. Graphical Models and Image Processing, Vol.56:6, pp.462–478.

Li K, Wu X, Chen D, Sonka S. (2006) Optimal Surface Segmentation in Volumetric Images - A Graph-Theoretic Approach. IEEE Transactions on Pattern Analysis and Machine Intelligence Vol. 28:1, pp.119–134.

Lindquist W B, Lee S M, Coker D, Jones K, Spanne P. (1996) Medial axis analysis of void structure in three-dimensional tomographic images of porous media. Journal of Geophysical Research, Vol.101:B4, pp.8297-8310.

Lindquist W B, Venkatarangan A, Dunsmuir J, Wong T (2000) Pore and throat size distributions measured from synchrotron X-ray tomographic images of Fontainebleau sandstones. Journal of Geophysical Research, Vol.105:B9, pp.21509–21527.

Lorensen W E, Cline H E. (1987) Marching Cubes: A high resolution 3D surface construction algorithm. Computer Graphics, Vol. 21:4, pp.163-169.

Madey J. (1971) Stimulated emission of bremsstrahlung in a periodic magnetic field. Journal of Applied Physics, Vol.42:5, pp.1906-1913.

Magid E, Octavian, Soldea O, Rivlin E. (2007) A Comparison of Gaussian and Mean Curvature Estimation Methods on Triangular Meshes of Range Image Data. Computer Vision and Image Understanding, Vol.07:3, pp.139-159.

Mardia K V, Hainsworth T J. (1988) A Spatial Thresholding Method for Image Segmentation. IEEE Transactions on Pattern Analysis and Machine Intelligence, Vol.10:6, pp.919-927.

Marr D, Hildreth E. (1980) Theory of Edge Detection. Proceeding of the Royal Society B, Vol.207:1167, pp.187-217.

Marsaglia G, Tsang W W. (2000) The Ziggurat Method for Generating Random Variables. Journal of Statistical Software, Vol.5:8. http://www.jstatsoft.org/v05/i08/

Matheron G. (1963) Principles of geostatistics. Economic Geology, Vol.58, pp.1246-1266.

Matheron G. (1975) Random sets and integral geometry. John Wiley and Sons, ISBN 0471576211.

McMillan M. (1945) The Synchrotron - A Proposed High Energy Particle Accelerator. Physical Review, Vol.68:5-6, pp.143-144.

Michielsen K, DeRaedt H. (2000) Morphological image analysis. Computer Physics Communications, Vol.132, pp.94-103.

Middelton L, Sivaswamy J. (2005) Hexagonal Image Processing: A Practical Approach. Advances in Pattern Recognition, Springer-Verlag, ISBN 1852339144.

Nagawa Y, Rosenfeld A. (1979) Some experiments on variable thresholding. Pattern Recognition, Vol.11, pp.191–204.

Naveira A M. (2005) The Riemann Curvature Through History. Review of the Royal Spanish Academy of Sciences, Series A - Mathematics, Vol.99:2, pp.195–210.

Newman M E J, Strogatz S H, Watts D J. (2001) Random graphs with arbitrary degree distributions and their applications. Physical Review E, Vol.64:2, pp.401-419.

Nimmo J R. (2004) Porosity and Pore Size Distribution. Encyclopedia of Soils in the Environment (Hillel D, Editor), Vol.3, pp.295-303. Academic Press, ISBN 0123485304.

Nixon M S, Aguado A S. (2012) Feature Extraction and Image Processing (3rd edition). Academic Press, ISBN 0123965497.

Ngom N F, Garnier P, Monga O, Peth S. (2011) Extraction of three-dimensional soil pore space from microtomography images using a geometrical approach. Geoderma, Vol.163:1, pp.127-134.

Nunan N, Wu K, Young I M, Crawford J W, Ritz K. (2003) Spatial distribution of bacterial communities and their relationships with the micro-architecture of soil. FEMS Microbiology Ecology, Vol.44:2, pp.203-215.

O'Gorman L, Sammon M J, Seul M. (2008) Practical algorithms for image analysis (2nd edition). Cambridge University Press, ISBN 052188411X.

Oh W, Lindquist W B. (1999) Image Thresholding by Indicator Kriging. IEEE Transactions on Pattern Analysis and Machine Intelligence, Vol.21:7, pp.590–602.

Ohser J, Mucklich F. (2000) Statistical Analysis of Microstructures in Materials Science. Wiley, ISBN 0471974862.

Oldendorf W H. (1961) Isolated flying spot detection of radio density discontinuities - displaying the internal structural patterns of a complex object. IRE Transactions on Biomedical Electronics, Vol.8:1, pp.68-72.

Otsu, N., 1979. A threshold selection method from gray-level histograms. IEEE Transactions on Systems, Man and Cybernetics, Vol.9:1, pp.62-66.

Otten W, Pajor R, Schmidt S, Baveye P C, Hague R, Falconer R E. (2012) Combining X-ray CT and 3D printing technology to produce microcosms with replicable, complex pore geometries. Soil Biology and Biochemistry, Vol.51, pp.53-55.

Pajor R, Falconer R., Hapca S, Otten W. (2010) Modelling and quantifying the effect of heterogeneity in soil physical conditions on fungal growth. Biogeosciences, Vol.7:11, pp.3731-3740.

Parton W J, Schimel D S, Cole C V, Ojima D S. (1987) Analysis of factors controlling soil organic matter levels in Great Plains grasslands. Soil Science Society of America Journal, Vol.51:5, pp.1173-1179.

Perrier E, Bird N, Rieu M. (1999) Generalizing the fractal model of soil structure: the pore–solid fractal approach. Geoderma, Vol.88:3-4, pp.137-164.

Peth S, Horn R, Beckman F, Donath T, Fisher J, Smucker A J M. (2008) Three-Dimensional Quantification of Intra-Aggregate Pore-Space Features using Synchrotron-Radiation-Based Microtomography. Soil Science Society of America Journal, Vol.72:4, pp.897-907.

Pfaltz J L, Rosenfeld A. (1967) Computer Representation of Planar Regions by their Skeletons. Communications of the ACM, Vol.10:2, pp.119-122.

Pratt W, Cooper T, Kabir I. (1985) Pseudomedian filter. Architectures and Algorithms for Digital Image Processing II, Proc. SPIE 534, pp.34– 43.

Press W H, Teukolsky S A, Vetterling W T, Flannery B P. (2007) Numerical Recipes: The Art of Scientific Computing (3rd ed.) Cambridge University Press (NY), ISBN 0521880688.

Radon J. (1917) On the determination of functions from their integral values along certain manifolds. (Translation from German. Parks, P C. 1986) . IEEE Transactions on Medical Imaging, Vol.5:4, pp.70–176.

Rasband W S. (1997) ImageJ. U.S. National Institutes of Health, Bethesda, Maryland, USA. http://imagej.nih.gov/ij/

Rawlins D J, Shaw P J. (1991) The point-spread function of a confocal microscope: its measurement and use in deconvolution of 3-D data. Journal of Microscopy, Vol.163:2, pp.151-165.

Richter D D, Markewitz D. (1995) How deep is soil? Bioscience, Vol.45:9, pp.600-609.

Ridler T, Calvard S. (1978) Picture thresholding using an iterative selection method. IEEE Transactions on System, Man and Cybernetics, Vol.8:8, pp.630–632.

Ringrose-Voase A J, Nortcliff S. (1987) The application of stereology to the estimation of soil structural properties: A preview. Soil Micromorphology 7 (proceedings).

Ringrose-Voase A J. (1996) Measurement of soil macropore geometry by image analysis of sections through impregnated soil. Plant and Soil, Vol.183:1, pp.27-47.

Rivest J-F, Soille P, Beucher S. (1992) Morphological gradients. Centre for Mathematical Morphology, Paris School of Mines. http://cmm.ensmp.fr/~beucher/publi/morph_grad.pdf

Roerdink J B T M, Meijster A. (2001) The Watershed Transform: Definitions, Algorithms and Parallelization Strategies. Fundamenta Informaticae, Vol.41:1-2, pp.187-228.

Rosenfeld A, Pfaltz J L. (1966) Sequential Operations in Digital Picture Processing. Communications of the ACM, Vol.13:4, pp.471-494.

Rosenfeld A, Pfaltz J. (1968) Distance Functions on Digital Pictures. Pattern Recognition, Vol.1:1, pp.33 – 61.

Rosenfeld A. (1969) Picture Processing by Computer. ACM Computing Surveys, Vol.1:3, pp.147-176.

Rosenfeld A. (1970) Connectivity in Digital Pictures. Journal of the ACM, Vol.17:1, pp.146-160.

Rosenfeld A, Kak A C. (1982) Digital Picture Processing. (2nd edition) Academic Press, ISBN 0125973012.

Rosin P L. (2001) Unimodal thresholding. Pattern Recognition, Vol.34:11, pp.2083–2096.

Savage A, Katz E, Eberst A, Falconer R E, Houston A, Harrison D J, Bown J. (2012) Characterising the tumour morphological response to therapeutic intervention. Journal of Disease Models & Mechanisms, Vol.6:1, pp.252-260.

Scharr H. (2000) Optimal Operators in Digital Image Processing. University of Heidelberg (Doctoral dissertation in German). http://archiv.ub.uni-heidelberg.de/volltextserver/

Schindelin J, Arganda-Carreras I, Frise E, Kaynig V, Longair M, Pietzsch T, Preibisch S, Rueden C, Saalfeld S, Schmid B, Tinevez J-Y, White D J, Hartenstein V, Eliceiri K, Tomancak P, Cardona A. (2012) Fiji: an open-source platform for biological-image analysis. Nature Methods, Vol.9:7, pp.676-682.

Schlüter S, Weller U, Vogel H-J. (2010) Segmentation of X-ray icrotomography images of soil using gradient masks. Computers & Geosciences, Vol.36:10, pp.1246–1251.

Schneider CA, Rasband WS and Eliceiri KW. (2012) NIH Image to ImageJ: 25 years of image analysis. Nature Methods, Vol.9, pp.671-675.

Schulze M A. (1990) Mathematical properties of the pseudomedian filter. University of Texas at Austin. (Masters dissertation.)

Seibert A J, Boone J M. (2005) X-Ray Imaging Physics for Nuclear Medicine Technologists. Part 2: X-Ray Interactions and Image Formation. Journal of Nuclear Medecine Technology, Vol.33:1, pp.3-18.

Serra J. (1982) Image Analysis and Mathematical Morphology. Academic Press, ISBN 0126372403.

Shannon C. (1948) A Mathematical Theory of Communication. Bell System Technical Journal, Vol.27:3, pp.379–423.

Siddiqi K, Pizer S M (editors). (2008) Medial Representations: Mathematics, Algorithms and Applications. Springer, ISBN 1402086571.

Sijbers J, Ceulemans T, VanDyck D. (2002) Algorithm for the computation of 3D Fourier descriptors. IEEE Pattern Recognition (Proceedings), Vol.2, pp.790-793.

Sleutel S, Cnudde V, Masschaele B, Vlassenbroek J, Dierick M, Van-Hoorebeke L, Jacobs P, De Neve S. (2008) Comparison of different nano- and micro-focus X-ray computed tomography set-ups for the visualization of the soil microstructure and soil organic matter. Computers & Geosciences, Vol.34:8, pp.931–938.

Smith S W. (1997) The Scientist & Engineer's Guide to Digital Signal Processing. California Technical Publications, ISBN 0966017633.

Spivak M. (1999) A Comprehensive Introduction to Differential Geometry volume 2 (3rd edition). Publish or Die Press, ISBN 0914098713.

Stoyan H, De-Polli H, Böhm S, Robertson G P, Paul E A. (2000) Spatial heterogeneity of soil respiration and related properties at the plant scale. Plant and Soil, Vol.222:1-2, pp.203–214.

Taina I A, Heck R J, Elliot T R. (2008) Application of X-ray computed tomography to soil science: A literature review. Canadian Journal of Soil Science, Vol.88:1, pp.1-19.

Tanenbaum A S. (1976) Structured Computer Organization. Prentice-Hall, ISBN 0138545057.

Tanenbaum A S. (1981) Computer Networks. Prentice-Hall, ISBN 0133499456.

Terribile F, FitzPatrick E A. (1992) The application of multilayer digital image processing techniques to the description of soil thin sections. Geoderma, Vol.55:1-2, pp.159-174.

Thompson E. (1930) Quantitative Microscopic Analysis. Journal of Geology, Vol.38:3, pp.193-222.

Thompson ML, Singh P, Corak S, Straszheim WE. (1992) Cautionary notes for the automated analysis of soil pore-space images. Geoderma, Vol.53:3-4, pp.399–415.

Veksler I V. (1944) A New Method of the Acceleration of Relativistic Particles. Doklady Akademii Nauk SSSR 43:346. (In Russian.)

Webster R, Oliver M A. (2007) Geostatistics for environmental scientists (2nd edition). Wiley, ISBN 9780470028582.

Vogel H-J, Kretzschmar A. (1996) Topological characterization of pore space in soil sample preparation and digital image-processing. Geoderma Vol.73:1-2, pp.23–38.

Vogel H-J. (2000) A numerical experiment on pore size, pore connectivity, water retention, permeability, and solute transport using network models. European Journal of Soil Science, Vol.51:1, pp.99-105.

Vogel H-J. (2002) Topological characterization of porous media. (In Lecture Notes in Physics 600: Morphology and Condensed Matter - Physics and Geometry of Spatially Complex Systems, pp.75-92, editors: Mecke K, Stoyan D.), Springer-Verlag, ISBN 9783540442035.

Wang W, Kravchenko A N, Smucker A J M, Rivers M L. (2011) Comparison of image segmentation methods in simulated 2D and 3D microtomographic images of soil aggregates. Geoderma, Vol.162:3–4, pp.231–241.

Wang W, Kravchenko A N, Smucker A J M, Liang W, Rivers M L. (2012) Intra-aggregate pore characteristics: X-ray computed microtomography analysis. Soil Science Society of America Journal, Vol.76, pp.1159-1171.

Watts DJ, Strogatz SH. (1998) Collective dynamics of 'small-world' networks. Nature, Vol.393:6684, pp.440-442.

Webster R, Oliver M. (2007) Geostatistics for Environmental Scientists (2nd edition). Wiley, ISBN 9780470028582.

Weska JS, Nagel RN, Rosenfeld A. (1974) A threshold selection technique. IEEE Transactions on Computers, Vol.23:12, pp.1322-1326.

Wildenschild D, Sheppard AP. (2013) X-ray imaging and analysis techniques for quantifying pore-scale structure and processes in subsurface porous medium systems. Advances in Water Resources, Vol.51, pp.217–246

Xia S, Bresler Y, Munson DC. (2004) Methods and Apparatus for Fast Divergent-Beam Tomography. US Patent 6771732-B2.

Young IM, Crawford J. (2004) Interactions and Self-Organization in the Soil-Microbe Complex. Science, Vol.304:5677, pp.1634-1637.

Zar JH. (1984) Biostatistical analysis (2nd edition). Prentice-Hall, ISBN 0130779253.

Zou Y, Liu H, Song E, Huang Z. (2012) Image bilevel thresholding based on multiscale gradient multiplication. Computers and Electrical Engineering, Vol.38:4, pp.853-861.

Appendix A – Software Release Notes

ImgToolsW32B52D8 - May 2013
All programs are constrained by the 32bit process memory limit: <= 1.6GB in practice (this assumes system has >2GB RAM installed).
Contents of installer archive:

ImgStat.exe
Global image statistics plus contrast, noise and sharpness measures.

ImgKrig.exe
Segmentation by Indicator Kriging. Auto threshold determination by Schleuter-Weller-Vogel method.

ImgVogSeg.exe
Image segmentation using the method of Schleuter-Weller-Vogel with revised filtering & derivative estimation.

imgThresh.exe
Image thresholding and mapping (by various methods)

Minkowski.exe
Minkowski functional measure estimator as described by Ohser and Mucklich (2000).

ImgConn.exe
Connectivity analysis (of segmented images) using Minkowski functional measures.

ImgView.exe
Image viewing (low-medium definition RAW, BMP, TIFF or VOL/VGI format).

ImgFileOp.exe
Applies arithmetic and logic operations to image files.

vims.exe
Volume Image Merge Split.

General Windows Usage
Drag and drop an image file or folder (containing multiple slice images) onto the program icon. Output file and folder name patterns are automatically generated from the input filename pattern. An identifier (eg. "VogSeg") is injected into all output filenames to avoid accidental overwriting or confusion. Output files are grouped into a sub-folders where appropriate; output is typically generated within the input folder. Note that applying these programs to remote data (on a network share folder for example) may be very slow; copying data to a local folder first is recommended.

TIFF File Support

The Tagged Image File Format (aka Thousands of Incompatible File Formats) is supported in limited form:
* READ-ONLY = NOT WRITEABLE: specify another format for output e.g. "-fmt:u8,bmp".

* Uncompressed data only.
* 8, 16 or 32 bits per sample (other sizes might work depending on "row/strip" organisation).
* Multi-page images, as used by ImageJ/FIJI are supported (i.e. many image slices per file).
* Many tags are not supported (local origin, colour models etc.)

File Lists

(supported by Minkowski.exe, ImgConn.exe and ImgStat.exe, works with image stack folders as well as volume files).

Individual file parameters are supported within lists so that e.g. image resolution can be specified independant of the file format. Parameter id and assigned value must follow the file name with a TAB '\t' character separating the fields (see example below).

This allows a batch of samples to be processed using a list file (rather than a batch file). Because a single program invocation is used, the results over all samples are formatted within one file, avoiding tedious manual formatting. This functionality is accessed either by invoking the program with an arguement (e.g. drag & drop file onto program icon) containing the keyword ".list" e.g. "myproject.list.txt" or by using the -list flag. (This also means that sample data files should not contain the word ".list".)

A list file can be generated using the DOS shell, e.g.

```
C:\user\al\projects\test> dir /B test*.u8 > test.list.txt
```

generates a file called "test.list.txt" in the current working directory (C:\user\al\projects\test) listing all files in that directory whose name matches the pattern "test*.u8"; the switch /B generates a "bare" list i.e. date & time information is stripped from the file list. The /S switch may also be useful to apply this to all subdirectories.

A list file contains a line-break (i.e. any combination of CR-LF "\r\n" characters) separated list of file (path) names. A path declaration is optional but useful for eliminating common text, particularly when reorganising a project or when data are stored on removable media. Differing media mount points (i.e. "drive letters" on Windows) mean that the path may have to be edited when moving between systems. Presently, only one path declaration per file is permitted, it must precede all list items and is applied to all subsequent file names. File-system meta-names such as . (cwd) and .. (parent) are not presently supported. The contents of a list file look something like:-

```
PATH=J:\myproject\
treatment1\sample1      res=57E-6
treatment1\sample2      res=54E-6
treatment2\sample1      res=36E-6
treatment2\sample2      res=53E-6
etc.
```

This will generate an output file "myproject.list.mink.txt" containing a list of raw functional measures with the generating filename and parameters adjacent to each. Standardisation over the series (according to the maximum magnitude of each measure) is also provided; this allows a graph to be easily plotted for example.

ImgStat.exe

Calculates global statistics of an image (or list) and its gradient magnitude field (magnitude of first derivative estimated by a Sobel operator). The domain, mean, standard deviation, quartiles and semi-variance model are given in each case. These are used to estimate measures of contrast, noise and sharpness that may be of use in selecting tomographic reconstruction and filtering parameters. Be advised however that there is no generally accepted method of calculating such measures; they are designed to reflect attributes of human visual perception/cognition which is inherently subjective. (This is due to both variability within the human population and the lack of a comprehensive and robust model of the perception and cognition process).

ImgKrig.exe

Segmentation by indicator Kriging including semivariogram model estimation. Refer to publications [Houston et al. 2013] and [Oh & Lindquist, 1999] for technical background.
UPDATE Iterative refinement model fitting implemented, as described in [Webster & Oliver, 2007].

-thresh:swv determine thresholds by method of Schleuter-Weller-Vogel.
-thresh=90,215 pre-classify the image using intensity thresholding; pore population <= 90, solid population >= 215,
90 < unknown population < 215
-mx60 employ 60% majority filtering based on cubic radius 1 neighbourhood (nearest 26 neighbours); pre-classified image elements may be transfomed to unclassified.
-svar[=8] collect empirical semivariance information for pore-solid populations up to radius 8 (default is 12) and output to text file
[,sub=0.1] apply 10% sub-sampling in the collection of empirical semivariance

-fit fit a semi-variance model to the empirical data and output to text file
[,auth] require an authorised model.
[,ext] require an extended/experimental model.
[,spherical] require spherical model type (gaussian and exponential models also supported).

-krig classify the unknown population by indicator kriging using a semi-variance model, various options:-
[,empirical] use empirical rather than modelled semivariance data to formulate kriging systems.
[,radial=2,7] specifies min and max lag (radius) to be considered within Kriging window (defaults 1, 20).
[,adaptive=10,20] specifies min and max elements (for each of the pore and solid populations) desired within each Kriging system (defaults 2, 16).
[,ORC] employ Order Relation Correction when estimating the membership probability of each Kriged solution.

Limitations:

1) The method is critically dependant on the accuracy of the specified thresholds; the ratio of pre-classified pore versus solid has a significant constraining effect on the results of Kriging (if the

locally available evidence is 70% solid versus 30% pore then a Kriged solution inevitably reflects this).

2) Both semivariogram estimation and solution of Kriging systems are computationally expensive. For large images (where one or more axes significantly exceeds 500 elements) it is advisable in the first instance to use 10% sub-sampling, and to limit the adaptive sampling to something like the range 1,4. Once the thresholds have been verified as being more-or-less correct (i.e. segmented pore-solid interfaces match reasonably well against the evidence in the "raw" greyscale image, according to competent human judegement) then a more robust solution may be attempted.

3) Processing is most efficient when the image dimensions are multiples of 64 (this allows optimisations related to the processor cache line size) otherwise memory usage and processing cost may increase significantly.

ImgVogSeg.exe

Requires grey-scale images in either RAW or BMP format. 24bit RGB BMP images are accepted provided ALL pixels are GREY; the data is mapped to 8bit during loading so that memory usage remains acceptable. Outputs binarised images (black and white) in the same file-format as input.

-mx60 Apply 60% majority filter before region growing (i.e. after hysteresis thresholding).
-dist:trim=#[,#] Specify lo (and hi) rejection threshold for intensity histogram mode detection; allows "anomalous" modes to be rejected.

Limitations:

1) Input images must have reasonable contrast within boundary regions and have a smoothly continuous (C1) histogram.

2) Only soil-like images are approriate; the solid phase should be dominant e.g. 60% versus 40% pore.

2) The method is memory-hungry due to the use of filtering and the need to simultaneously access several scalar fields (the filtered image and it's first and second derivatives). The theoretical size limitation is 700^3 but exceeding 512^3 seems to be problematic.

imgThresh.exe

Supports Otsu, Gaussian Mixture Model and Clustering methods; the latter two offer hysteresis threshold (pre-classification) options that are designed to work with the mapping option.
Hysteresis without mapping generates "pure" classified output using a minimum number of bits, e.g. a 2bit hysteresis image uses the mappings:-

0 (0b00) -> class 0 (pore)
1 (0b01) -> class 1 (solid)
2 (0b10) -> unclassified
3 (0b11) -> classification error or outside region-of-interest

Mapping generates a "continuous" range of unclassified intensity values lying between two classes, e.g. an 8bit map image uses the mappings:-

```
      0   (0x00)  ->    class 0 (pore)

      1   (0x01)  ->    unclassified: 1/255 = 0.392% (strong likelihood
of being pore)
      ...
      127 (0x7F)  ->    unclassified: 128/255 = 49.8% (strong degree of
uncertainty)
      128 (0x80)  ->    unclassified: 128/255 = 50.2% (strong degree of
uncertainty)
      ...
      254 (0xFE)  ->    unclassified: 254/255 = 99.6% (strong
likelihood of being solid)

      255 (0xFF)  ->    class 1     (solid)
```

The unknown values may be interpreted as degrees of fuzzy membership or probabilities. Interpreting these values directly as "partial porosities" is NOT recommended; further analysis and processing (such as pattern analysis and/or Kriging) is required to generate robust partial porosity information.

```
-irc        Iterative Riddler-Calvard aka "balanced histogram"
thresholding.
-otsu       Classic two-phase Otsu i.e. minimisation of intra-class
variance.
-entropy    Entropy function threshold.
-bnm        Kittler-Illingworth bi-normal threshold.
-gmm[=#[,#]][,hyst[,map]]     Gaussian mixture model generated by EM
algorithm applied to image intensity PMF (derived from histogram);
Bayesian minimum error threshold determination. Optionally specify min
(and max) number of components required; default is 2.

-map  Used in isolation to map from wide precision images (e.g.
VGI/VOl using 32bit floating point) to a format having smaller bit-
depth. A statistical fence procedure is applied to the image histogram
in order to reject outliers (i.e. the long tails of the distribution).
This improves discrimination of intensities within the part of the
image histogram that usually contains "interesting" information (i.e.
close to the median of the distribution).

-bins=#     Histogram bin count to be used for distribution analysis.
-bits=#     Target bit depth (i.e. the output format).
-m60  Apply 60% majority filter to segmented image.
```

Otsu is simple, fast and seems to work for images reconstructed with significant noise reduction filtering (NR3 or higher) at the cost of discarding fine scale structure. It can be used as a relatively quick method for finding regions of interest given that the "core" of large pore structures will not change significantly under more sophisticated segmentation methods; the interface characteristics and fine scale connectivity may of course change substantially.

If the image has two or more distinct modes (i.e. peaks are well separated) then GMM segmentation is useful; if the model fit exceeds 95% then results can be very good. Also this is the only thresholding

method that supports three or more phase segmentation (but hysteresis is not presently supported in this case). Being based on the analytic solution of quadratic systems of equations (one system per successive pair of phases) the method has a very sound mathematical foundation. Misclassification can also be estimated analytically.

Minkowski.exe

Requires grey-scale images in either RAW, BMP or VOL/VGI format. Computes Minkowski functional measures for a volume image. Unbiased estimates (according to Ohser & Mucklich, after Matheron) are given for 2D and 3D images.

-res=# Specify image element resolution from which to calculate measures.
-object=0 Default object ID value; analyse objects comprised of elements equal to zero.
-object>0 Used for non-zero objects against a zero background

-object=1,255,1 Default threshold series beginning at one, ending at 255 (maximum intensity value of an 8-bit image) and calculating measures at intervals of one (i.e. generates table of 255 sets of results). Each row of output (functional measures) is prefixed with the relevant threshold value.
-object>-0.25,3.75,0.125 Threshold series for floating point data; starts at -0.25 and proceeds up to 3.75 in increments of 0.125 (Caveat Emptor: small increments imply many measurements i.e processing may take a long time).

ImgConn.exe

Requires binarised (i.e. black and white only) images in either RAW or BMP format. Outputs text file reports in a sub-folder; the summary report uses a column format suitable for comparing images/treatments. Connectivity ratios (spanning pore volume fraction) are provided per principal axis of the image plus functional measures summarised by class (all objects in region, all spanning objects and all surface connected objects). The detailed report format provides functional measures per recorded object (only the largest and/or most highly connected or otherwise significant objects may be recorded due to storage limitations) and potentially allows individual objects to be identified in the optional output image. Two styles of output image are supported according to the number of bits requested; two or fewer bits specifies a connectivity class image in which the most highly connected objects are assigned the lowest numbered index (the background phase is always assigned the greatest available index). Specifying four or more bits creates an object discrimination image in which the largest and most highly connected objects are assigned unique indices; refer to the detailed report format for index values.

-res=# Specify image element resolution from which to calculate functional measures.
-bits=# Specify bits used for output image (1, 2, 4, or 8).
Internal processing requires a minimum of two bits => 4 distinct object classes.
Objects are stored as the first N-1 states {0, 1, .. } and background as the greatest valued state {(2^bits)-1}.

A colour palette appended to the raw image data maps the visual presentation of states as follows:

```
0 .. N-2    -> vivid colours
N-1 (2^bits-1)    -> transparent
```

-n=# specify connectivity neighbourhood (default 6 i.e. cube faces). Other values are 18 (faces + edges) and 26 (+ corners).

ImgView.exe

Requires volume or sliced images in RAW, BMP, TIFF or VOL/VGI format. No output files are generated. Two viewing modes are supported; surface rendering (giving the look of a "3D shell" bitmap image) and slice-proxy volume rendering (an approximation to true 3D volume rendering, the same approach is used by the Fiji/ImageJ volume renderer). Three techniques are implemented for volume rendering; iso-surface, gradient (magnitude) and laplacian.

Principal Interactive Controls

F1 help
T Technique (cyclic).
H Histogram of image intensity (toggle on/off). Clickable red bars apply upper&lower intensity cutoff for volume rendering.
W 3D Widgets (toggle on/off). Clickable 3D axes allow slice selection for surface rendering.

Command Line

-pal=none suppress colour palette binding; colour index treated as intensity.
-pal=filename extract colour palette from file (JASC-PAL text description assumed) and apply when the image is bound to graphics hardware.

Known Bugs and Limitations:

1) 3D axis widgets still do not work correctly all the time.
2) Maximum recommended image dimensions are (512,512,512) assuming 8-bit grey scale and a graphics hardware with 1GByte of VRAM. Larger amounts of VRAM do not seem to help with larger images: this is either due to a video hardware/driver design issue (possibly related to 3D texture filtering) or just another limitation of Win32 process memory.

vims.exe

Performs limited image file format conversion (*.BMP/*.PBM/*.txt <-> RAW) and mapping. Time series volume data files in floating point format (e.g. fungal biomass distribution) are mapped to a single 8bit precison 3D RAW format animation file compatible with ImgView.exe

Multiple scalar field merge is incorporated via list files; each line specifies a row of scalar fields ending with the pore/solid structure. For each element in the output image, an index is emitted identifying the dominant scalar field (or pore/solid structure). Dominance is determined using a standardised comparison of the scalar fields; standardisation is presently with respect to the mean plus two

standard deviations for each field. The first field is given index one and the last of N fields receives index N+1: zero is reserved for empty pore while the largest index N+2 is used for solid. A palette (colour look up table) can then be used to render the merged data set with colour coded features. Building an animation from a series of time points allows morphological dynamics to be interpreted.

-fmt=u8,bmp force output of 8bit BMP images
-fmt=txt " " ASCII text file

ImgFileOp.exe

Image processing tool providing either arithmetic, logical or special operations (not mixed) on images with identical dimensions.

Arithmetic operations (basic and linear combination):
img1 + img2 arithmetic sum
img1 - img2 arithmetic difference
img1 * img2 arithmetic product
img1 / img2 arithmetic quotient
img1 @ img2 absolute difference
Linear weightings are specified by preceding an image name by a number; the number must be a separate arguement and no '*' operator should be used eg:
0.95 img1 + 0.05 img2

Logical Operations
img1 img2 > value set img1 to zero where img2 exceeds value

Special Operations
1) Noise Model Mask
maskImg model.mnd.txt noiseImg Modulate noise image so as to fit Gaussian mixture model; Mask image controls spatial distribution of model components (table of gaussian distributions indexed by mask).

Appendix B – Published Work

Falconer R E, Houston A N, Otten W, Baveye P C. (2012) Emergent behavior of soil fungal dynamics: Influence of soil architecture and water distribution. Soil Science, Vol.177:2, pp.111-119.

Savage A, Katz E, Eberst A, Falconer R E, Houston A, Harrison D J, Bown J. (2012) Characterising the tumour morphological response to therapeutic intervention. Journal of Disease Models & Mechanisms, Vol.6:1, pp.252-260.

Houston A N, Otten W, Baveye P, Hapca S. (2013) Adaptive Window Indicator Kriging: A thresholding method for computed tomography images of porous media. Computers & Geosciences, Vol.54, pp.239-248.

Hapca SM, Houston AN, Otten W, Baveye PC. (2013) New Local Thresholding Method for Soil Images by Minimizing Grayscale Intra-Class Variance. Vadose Zone Journal, (in press).